



Ricardo Ribeiro Rodrigues

**A study on the electromagnetic
characterization of anisotropic materials in
cylindrical measurement cells using the
mode-matching method**

Dissertação de Mestrado

Dissertation presented to the Programa de Pós-graduação em Engenharia Elétrica of PUC-Rio in partial fulfillment of the requirements for the degree of Mestre em Engenharia Elétrica.

Advisor : Prof. Guilherme Simon da Rosa
Co-advisor: Prof. Rafael Abrantes Penchel

Rio de Janeiro
April 2022



Ricardo Ribeiro Rodrigues

**A study on the electromagnetic
characterization of anisotropic materials in
cylindrical measurement cells using the
mode-matching method**

Dissertation presented to the Programa de Pós-graduação em Engenharia Elétrica of PUC-Rio in partial fulfillment of the requirements for the degree of Mestre em Engenharia Elétrica. Approved by the Examination Committee.

Prof. Guilherme Simon da Rosa

Advisor

Centro de Estudos em Telecomunicações – PUC-Rio

Prof. Rafael Abrantes Penchel

Co-advisor

Universidade Estadual Paulista Júlio de Mesquita Filho –
UNESP

Prof. Fernando José da Silva Moreira

Universidade Federal de Minas Gerais – UFMG

Prof. Luiz Alencar Reis da Silva Mello

Centro de Estudos em Telecomunicações – PUC-Rio

Prof. José Ricardo Bergmann

Centro de Estudos em Telecomunicações – PUC-Rio

Rio de Janeiro, April the 8th, 2022

All rights reserved.

Ricardo Ribeiro Rodrigues

He received his B.S. degree in Electric Engineering from Pontifical Catholic University of Rio de Janeiro (PUC-Rio), Rio de Janeiro, Brazil, in 2020. He is currently pursuing a Master's degree in Applied Electromagnetism in the Center for Telecommunications Studies at PUC-Rio.

Bibliographic data

Ribeiro Rodrigues, Ricardo

A study on the electromagnetic characterization of anisotropic materials in cylindrical measurement cells using the mode-matching method / Ricardo Ribeiro Rodrigues; advisor: Guilherme Simon da Rosa; co-advisor: Rafael Abrantes Penchel. – 2022.

209 f: il. color. ; 30 cm

Dissertação (mestrado) - Pontifícia Universidade Católica do Rio de Janeiro, Departamento de Engenharia Elétrica, 2022.

Inclui bibliografia

1. Engenharia Elétrica – Teses. 2. Engenharia de Telecomunicações – Teses. 3. Meios anisotrópicos. 4. célula de medição. 5. técnica de casamento de modos. I. Simon da Rosa, Guilherme. II. Abrantes Penchel, Rafael. III. Pontifícia Universidade Católica do Rio de Janeiro. Departamento de Engenharia Elétrica. IV. Título.

CDD: 621.3

To my parents, for their support
and encouragement.

Acknowledgments

I would like to thank to PUC-Rio for the exemption of school fees offered by the Programa de Pós-Graduação em Engenharia Elétrica.

This study was financed in part by the Coordenação de Aperfeiçoamento de Pessoal de Nível Superior – Brasil (CAPES) - Finance Code 001.

Abstract

Ribeiro Rodrigues, Ricardo; Simon da Rosa, Guilherme (Advisor); Abrantes Penchel, Rafael (Co-Advisor). **A study on the electromagnetic characterization of anisotropic materials in cylindrical measurement cells using the mode-matching method.** Rio de Janeiro, 2022. 209p. Dissertação de Mestrado – Departamento de Engenharia Elétrica, Pontifícia Universidade Católica do Rio de Janeiro.

Measurement cells (MCs) are widely used in microwave engineering for the electromagnetic characterization of materials. In this work, we present a mode-matching technique (MMT) formulation for the electromagnetic characterization of MCs for uniaxial anisotropic materials. We present and validate a technique for modeling MCs with one- and two-ports via generalized scattering matrices (GSMs) extracted from the MMT. Since closed-form solutions are used for computing the coupling integrals of the GSMs, the present approach is a computationally-efficient alternative to modeling MCs when compared to usual brutal-force techniques (such as finite-elements, finite-volumes, and finite-difference solutions). An inverse algorithm is also presented to retrieve the constitutive parameters of complex media (lossy and anisotropic materials). Differently from the majority of the works using semi-analytical methods, the novelty of the present method rely on considering overmoded MCs. We present a series of numerical results that show that the inversion technique presented herein can properly retrieve the constitutive parameters of a sample material once the MC scattering parameters are known.

Keywords

Anisotropic media; measurement cell; mode-matching technique.

Resumo

Ribeiro Rodrigues, Ricardo; Simon da Rosa, Guilherme; Abrantes Penchel, Rafael. **Um estudo sobre a caracterização eletromagnética de materiais anisotrópicos em células de medição cilíndricas usando o método de casamento de modo.** Rio de Janeiro, 2022. 209p. Dissertação de Mestrado – Departamento de Engenharia Elétrica, Pontifícia Universidade Católica do Rio de Janeiro.

Células de medição (MCs) são amplamente utilizadas na engenharia de micro-ondas para a caracterização eletromagnética dos materiais. Neste trabalho, apresentamos uma formulação baseada na técnica de casamento de modos (MMT) para a caracterização eletromagnética de MCs para materiais anisotrópicos uniaxiais. Apresentamos e validamos uma técnica para modelagem de MCs com uma e duas portas por meio da de matrizes de espalhamento generalizadas (GSMs) extraídas do MMT. Uma vez que as soluções fechadas (isto é, não numéricas) são usadas para calcular as integrais de acoplamento das GSMs, a presente abordagem é uma alternativa computacionalmente eficiente para modelar MCs quando comparada às técnicas usuais de força bruta numérica (tais como soluções baseadas em elementos, volumes, ou diferenças finitas). Um algoritmo de inversão também é apresentado para recuperar os parâmetros constitutivos de meios complexos (materiais com perdas e anisotrópicos). Diferentemente da maioria dos trabalhos que utilizam métodos semi-analíticos, a novidade do presente método consiste em considerar MCs com seção transversal grande frente ao comprimento de onda, em vários modos podem ser progagantes. Apresentamos uma série de resultados numéricos que mostram que a técnica de inversão apresentada neste estudo pode recuperar adequadamente os parâmetros constitutivos de um material de amostra, uma vez que os parâmetros de espalhamento da MC são conhecidos.

Palavras-chave

Meios anisotrópicos; célula de medição; técnica de casamento de modos.

Table of contents

List of figures	11
List of tables	25
1 Introduction	32
1.1 General Introduction	32
1.2 Scientific Contributions	33
1.3 Dissertation Organization	34
2 Electromagnetic Characterization of Matter	35
2.1 Constitutive Relations	35
2.1.1 Linear Media	36
2.1.1.1 Isotropic, Bi-isotropic, Anisotropic and Bianisotropic Medium	36
2.1.1.2 Isotropic Medium	36
2.1.1.3 Bi-Isotropic Medium	36
2.1.1.4 Anisotropic Medium	37
2.1.1.5 Bianisotropic Medium	38
2.1.2 Lossy and Lossless Media	39
2.2 Electromagnetic Characterization	40
2.2.1 Resonant Methods	40
2.2.1.1 Cavity Resonator	40
2.2.2 Non Resonant Methods	41
2.2.2.1 Free Space	41
2.2.2.2 Transmission and Reflection Measurement	42
2.2.3 Material Parameters Extraction	44
3 Electromagnetic Modeling of Cylindrical Waveguides	47
3.1 Electromagnetic Fields in Uniform Cylindrical Waveguides	47
3.1.1 Homogeneous Waveguide	47
3.1.2 Inhomogeneous Waveguide	50
3.2 Mode-Matching Technique	50
3.2.1 PEC-Truncation Scattering Matrix	54
3.3 Perfectly Matched Layer for Representing Unbounded Domains	54
4 Determination of the Constitutive Parameters	57
4.1 Direct Problem	57
4.1.1 Two-Port Measurement Cells	58
4.1.2 One-Port Measurement Cells	61
4.1.3 Open-Ended Coaxial Measurement Cells	65
4.1.3.1 Relative Convergence Issues and Our Approach to Overcome Them	66
4.1.3.2 Solution for a PEC truncation	67
4.1.3.3 Solution for a PMC truncation	71
4.1.3.4 Solution for a combined PEC and PMC truncation	75

4.2	Inverse Problem	79
4.2.1	Graphical Comparisons	79
4.2.2	Functional Optimizations	79
4.2.2.1	fmincon and sqp algorithms	81
4.3	Study of local and global minimum	82
4.3.1	Basins of attraction	83
4.3.2	A discussion on the number of local minima	83
4.3.3	Mislead convergence due to wrong initial guess choice	87
5	Inverse Problem Results	90
5.1	Two-Port Measurement Cells	90
5.1.1	Heterogeneous Coaxial Waveguide	90
5.1.1.1	Lossless isotropic sample	91
5.1.1.2	Lossy isotropic sample	94
5.1.1.3	Lossless anisotropic sample	96
5.1.1.4	Anisotropic sample with isotropic loss	99
5.1.1.5	Anisotropic sample with anisotropic loss	104
5.1.2	Homogeneous Circular Waveguide	109
5.1.2.1	Lossless isotropic sample	109
5.1.2.2	Lossy isotropic sample	110
5.1.2.3	Lossless anisotropic sample	114
5.1.2.4	Anisotropic sample with isotropic loss	116
5.1.2.5	Anisotropic sample with anisotropic loss	122
5.1.3	Heterogeneous Circular Waveguide	127
5.1.3.1	Lossless isotropic sample	127
5.1.3.2	Lossy isotropic sample	128
5.1.3.3	Lossless anisotropic sample	130
5.1.3.4	Anisotropic sample with isotropic loss	133
5.1.3.5	Anisotropic sample with anisotropic loss	138
5.2	One-Port Measurement Cells	143
5.2.1	Heterogeneous Coaxial Waveguide	143
5.2.1.1	Lossless isotropic sample	143
5.2.1.2	Lossy isotropic sample	144
5.2.1.3	Lossless anisotropic sample	148
5.2.1.4	Anisotropic sample with isotropic loss	150
5.2.1.5	Anisotropic sample with anisotropic loss	154
5.2.2	Homogeneous Circular Waveguide	160
5.2.2.1	Lossless isotropic sample	160
5.2.2.2	Lossy isotropic sample	161
5.2.2.3	Lossless anisotropic sample	165
5.2.2.4	Anisotropic sample with isotropic loss	167
5.2.2.5	Anisotropic sample with anisotropic loss	171
5.2.3	Heterogeneous Circular Waveguide	177
5.2.3.1	Lossless isotropic sample	177
5.2.3.2	Lossy isotropic sample	178
5.2.3.3	Lossless anisotropic sample	182
5.2.3.4	Anisotropic sample with isotropic loss	184
5.2.3.5	Anisotropic sample with anisotropic loss	188
5.3	Open-ended Coaxial Measurement Cells	194

5.3.1	Homogeneous Circular Waveguide	194
5.3.1.1	Lossless isotropic sample	194
5.3.1.2	Lossless anisotropic sample	196
6	Conclusion	199
	Bibliography	200
7	Bibliography	201

List of figures

Figure 2.1	Behavior of the field in a linear isotropic media. Image obtained in [30].	37
Figure 2.2	Behavior of the field in a linear non isotropic media. Image obtained in [30].	38
Figure 2.3	Summary of the types of material discussed.	39
Figure 2.4	Cavity filled with a sample under test [55].	41
Figure 2.5	Free-space measurement setup for dielectric characterization. Image obtained in [55, 57–59].	42
Figure 2.6	Open-ended one-port MCs using coaxial probes in (a) and (b), and using rectangular probes in (c) and (d). Image obtained in [55].	43
Figure 2.7	Two-port MCs using (a) a rectangular waveguide, and (b) a coaxial transmission line. Image obtained in [55].	44
Figure 2.8	Integral admittance formulations for open-ended rectangular waveguides. Image obtained in [55].	45
Figure 3.1	Junction of two homogeneous coaxial waveguides. Image obtained in [66].	51
Figure 3.2	Structure with three regions. Image obtained in [66].	53
Figure 3.3	Geometry of an open-ended coaxial waveguide.	55
Figure 3.4	Equivalent problem used to emulate the open-ended coaxial waveguide.	56
Figure 4.1	Geometry of a cylindrical structure with tree waveguide regions. The PEC is represented by the hatched areas. The sample material is the dielectric partially filling region 2	59
Figure 4.2	Reflection coefficient in decibel for the fundamental mode in region 1 as a function of the frequency for the two-port measurement cell. The results from the present algorithm are indicated by the solid line while FIT results from [73] are the dashed-line.	59
Figure 4.3	Transmission coefficient in decibel for the fundamental mode in region 1 as a function of the frequency for the two-port measurement cell. The results from the present algorithm are indicated by the solid line while FIT results from [73] are the dashed-line.	60
Figure 4.4	Geometry of a cylindrical structure with tree waveguide regions, where region 3 is terminated by a PEC plate.	61
Figure 4.5	Reflection coefficient in decibel for the fundamental mode in region 1 as a function of the frequency for the first case. The results from the present algorithm are indicated by the solid line while FIT results from [73] are the dashed-line.	63

- Figure 4.6 Reflection coefficient in decibel for the fundamental mode in region 1 as a function of the frequency for the second case. The results from the present algorithm are indicated by the solid line while FIT results from [73] are the dashed-line. 63
- Figure 4.7 Reflection coefficient in decibel for the fundamental mode in region 1 as a function of the frequency for the third case. The results from the present algorithm are indicated by the solid line while FIT results from [73] are the dashed-line. 64
- Figure 4.8 Geometry of an open-ended coaxial waveguide. 65
- Figure 4.9 Geometry used to emulate the open-ended coaxial waveguide depicted in Fig. 4.8. 65
- Figure 4.10 Longitudinal wavenumbers k_z of regions 1 and 2 using the parameters shown in Tables 4.5 and 4.6 at frequency of 1 GHz when a PML is used with a PEC truncation. 68
- Figure 4.11 Reflection coefficient in decibel for the fundamental mode in region 1 as a function of the frequency for the open-ended coaxial measurement cell truncated by a PEC and $\epsilon_r = 2.55$. The results from the present algorithm are indicated by the solid line while FIT results from [73] are the dashed-line. 68
- Figure 4.12 Reflection coefficient in decibel for the fundamental mode in region 1 as a function of the frequency for the open-ended coaxial measurement cell truncated by a PEC and $\epsilon_r = 10$. The results from the present algorithm are indicated by the solid line while FIT results from [73] are the dashed-line. 69
- Figure 4.13 Reflection coefficient in decibel for the fundamental mode in region 1 as a function of the frequency for the open-ended coaxial measurement cell truncated by a PEC and $\epsilon_r = 1$. The results from the present algorithm are indicated by the solid line while FIT results from [73] are the dashed-line. 69
- Figure 4.14 Reflection coefficient in decibel for the fundamental mode in region 1 as a function of the frequency for the open-ended coaxial measurement cell truncated by a PEC and $\epsilon_r = 2.55$. The results from the present algorithm are indicated by the solid line, where the black line has $N_1 = 9$ and yellow has $N_1 = 12$, while FIT results from [73] are the dashed-line. 70
- Figure 4.15 Equivalent problem used in algorithm to validate the real situation. 71
- Figure 4.16 Longitudinal wavenumbers k_z of regions 1 and 2 using the parameters shown in Tables 4.5 and 4.6 at the frequency of 1 GHz when a PML is used with a PMC truncation. 72
- Figure 4.17 Reflection coefficient in decibel for the fundamental mode in region 1 as a function of the frequency for the open-ended coaxial measurement cell truncated by a PMC and $\epsilon_r = 2.55$. The results from the present algorithm are indicated by the solid line while FIT results from [73] are the dashed-line. 73

- Figure 4.18 Reflection coefficient in decibel for the fundamental mode in region 1 as a function of the frequency for the open-ended coaxial measurement cell truncated by a PMC and $\epsilon_r = 10$. The results from the present algorithm are indicated by the solid line while FIT results from [73] are the dashed-line. 73
- Figure 4.19 Reflection coefficient in decibel for the fundamental mode in region 1 as a function of the frequency for the open-ended coaxial measurement cell truncated by a PMC and $\epsilon_r = 1$. The results from the present algorithm are indicated by the solid line while FIT results from [73] are the dashed-line. 74
- Figure 4.20 Values of k_z of region 1 and 2 for its matching, using the parameters of Table 4.5 and 4.6 at the frequency of 1 GHz when using the combined PML+PEC+PMC truncation. 76
- Figure 4.21 Reflection coefficient in decibel for the fundamental mode in region 1 as a function of the frequency for the open-ended coaxial measurement cell and $\epsilon_r = 2.55$. The results from the present algorithm are indicated by the solid line while FIT results from [73] are the dashed-line 77
- Figure 4.22 Reflection coefficient in decibel for the fundamental mode in region 1 as a function of the frequency for the open-ended coaxial measurement cell and $\epsilon_r = 10$. The results from the present algorithm are indicated by the solid line while FIT results from [73] are the dashed-line 77
- Figure 4.23 Reflection coefficient in decibel for the fundamental mode in region 1 as a function of the frequency for the open-ended coaxial measurement cell and $\epsilon_r = 1$. The results from the present algorithm are indicated by the solid line while FIT results from [73] are the dashed-line 78
- Figure 4.24 Reflection coefficient in decibel for the fundamental mode in region 1 as a function of the frequency for the two-port coaxial measurement cell. The results from the present algorithm are indicated by the solid line while FIT results from [73] by the dashed-line. 80
- Figure 4.25 Example of local and global minimums of a function. Image obtained in [82]. 83
- Figure 4.26 The function minimum will be either $(0,0)$ or $(11/4, 11/4)$, if the initial guess is $x < 2$ or $x > 2$, respectively. Image obtained in [83]. 84
- Figure 4.27 Functional value considering $\epsilon_r = 2.55$, length $L = 10$ mm for first case. 84
- Figure 4.28 Functional value considering $\epsilon_r = 6$, length $L = 10$ mm for first case. 85
- Figure 4.29 Functional value considering $\epsilon_r = 2.55$, length $L = 30$ mm for first case. 85
- Figure 4.30 Functional value considering $\epsilon_r = 6$, length $L = 30$ mm for first case 86
- Figure 4.31 Functional value considering $\epsilon_r = 2.55$, length $L = 10$ mm for second case. 86

Figure 4.32 Functional value considering $\epsilon_r = 6$, length $L = 10$ mm for second case.	87
Figure 4.33 Functional value considering $\epsilon_r = 2.55$, length $L = 30$ mm for second case.	87
Figure 4.34 Functional value considering $\epsilon_r = 6$, length $L = 30$ mm for second case.	88
Figure 4.35 Functional value showing global minimum at $\epsilon_r = 2.51$ and others local minimums on $\epsilon_r = 5.51$ and $\epsilon_r = 8.51$.	88
Figure 4.36 Evolution of the optimization parameter as a function of the number of iterations. Convergence was achieved after 14 iterations at $\epsilon_r = 5.66$.	89
Figure 5.1 Evolution of the optimization parameter as a function of the number of iterations using linear functional. Convergence was achieved after 14 iterations at $\epsilon_{rs} = 2.55$.	92
Figure 5.2 Evolution of the optimization parameter as a function of the number of iterations using linear functional. Convergence was achieved after 14 iterations at $\epsilon_{rz} = 2.55$.	92
Figure 5.3 Evolution of the optimization parameter as a function of the number of iterations using decibel functional. Convergence was achieved after 11 iterations at $\epsilon_{rs} = 2.55$.	93
Figure 5.4 Evolution of the optimization parameter as a function of the number of iterations using decibel functional. Convergence was achieved after 11 iterations at $\epsilon_{rz} = 2.55$.	93
Figure 5.5 Evolution of the optimization parameter as a function of the number of iterations using linear functional. Convergence was achieved after 11 iterations at $\epsilon_r = 2.55$.	94
Figure 5.6 Evolution of the optimization parameter as a function of the number of iterations using linear functional. Convergence was achieved after 11 iterations at $\sigma = 0.02$.	95
Figure 5.7 Evolution of the optimization parameter as a function of the number of iterations using decibel functional. Convergence was achieved after 10 iterations at $\epsilon_{rs} = 2.55$.	95
Figure 5.8 Evolution of the optimization parameter as a function of the number of iterations using decibel functional. Convergence was achieved after 10 iterations at $\sigma = 0.02$.	96
Figure 5.9 Evolution of the optimization parameter as a function of the number of iterations using linear functional. Convergence was achieved after 15 iterations at $\epsilon_{rs} = 2.55$.	97
Figure 5.10 Evolution of the optimization parameter as a function of the number of iterations using linear functional. Convergence was achieved after 15 iterations at $\epsilon_{rz} = 3$.	97
Figure 5.11 Evolution of the optimization parameter as a function of the number of iterations using decibel functional. Convergence was achieved after 9 iterations at $\epsilon_{rs} = 2.55$.	98
Figure 5.12 Evolution of the optimization parameter as a function of the number of iterations using decibel functional. Convergence was achieved after 9 iterations at $\epsilon_{rz} = 3$.	98

Figure 5.13 Evolution of the optimization parameter as a function of the number of iterations using linear functional. Convergence was achieved after 27 iterations at $\epsilon_{rs} = 2.55$.	99
Figure 5.14 Evolution of the optimization parameter as a function of the number of iterations using linear functional. Convergence was achieved after 27 iterations at $\epsilon_{rz} = 3$.	100
Figure 5.15 Evolution of the optimization parameter as a function of the number of iterations using linear functional. Convergence was achieved after 27 iterations at $\sigma_s = 0.02$.	100
Figure 5.16 Evolution of the optimization parameter as a function of the number of iterations using linear functional. Convergence was achieved after 27 iterations at $\sigma_z = 0.02$.	101
Figure 5.17 Evolution of the optimization parameter as a function of the number of iterations using decibel functional. Convergence was achieved after 4 iterations at $\epsilon_{rs} = 2.57$.	101
Figure 5.18 Evolution of the optimization parameter as a function of the number of iterations using decibel functional. Convergence was achieved after 4 iterations at $\epsilon_{rz} = 2.89$.	102
Figure 5.19 Evolution of the optimization parameter as a function of the number of iterations using decibel functional. Convergence was achieved after 4 iterations at $\sigma_s = 0.02$.	102
Figure 5.20 Evolution of the optimization parameter as a function of the number of iterations using decibel functional. Convergence was achieved after 4 iterations at $\sigma_z = 0.02$.	103
Figure 5.21 Evolution of the optimization parameter as a function of the number of iterations using linear functional. Convergence was achieved after 23 iterations at $\epsilon_{rs} = 2.55$.	104
Figure 5.22 Evolution of the optimization parameter as a function of the number of iterations using linear functional. Convergence was achieved after 23 iterations at $\epsilon_{rz} = 3$.	105
Figure 5.23 Evolution of the optimization parameter as a function of the number of iterations using linear functional. Convergence was achieved after 23 iterations at $\sigma_s = 0.1$.	105
Figure 5.24 Evolution of the optimization parameter as a function of the number of iterations using linear functional. Convergence was achieved after 23 iterations at $\sigma_z = 0.02$.	106
Figure 5.25 Evolution of the optimization parameter as a function of the number of iterations using decibel functional. Convergence was achieved after 7 iterations at $\epsilon_{rs} = 2.56$.	106
Figure 5.26 Evolution of the optimization parameter as a function of the number of iterations using decibel functional. Convergence was achieved after 7 iterations at $\epsilon_{rz} = 3$.	107
Figure 5.27 Evolution of the optimization parameter as a function of the number of iterations using decibel functional. Convergence was achieved after 7 iterations at $\sigma_s = 0.1$.	107
Figure 5.28 Evolution of the optimization parameter as a function of the number of iterations using decibel functional. Convergence was achieved after 7 iterations at $\sigma_z = 0.02$.	108

Figure 5.29 Evolution of the optimization parameter as a function of the number of iterations using linear functional. Convergence was achieved after 7 iterations at $\epsilon_r = 2.55$.	109
Figure 5.30 Evolution of the optimization parameter as a function of the number of iterations using decibel functional. Convergence was achieved after 4 iterations at $\epsilon_r = 2.55$.	110
Figure 5.31 Evolution of the optimization parameter as a function of the number of iterations using linear functional. Convergence was achieved after 18 iterations at $\epsilon_r = 2.55$.	111
Figure 5.32 Evolution of the optimization parameter as a function of the number of iterations using linear functional. Convergence was achieved after 18 iterations at $\sigma = 0.02$.	112
Figure 5.33 Evolution of the optimization parameter as a function of the number of iterations using decibel functional. Convergence was achieved after 18 iterations at $\epsilon_r = 2.55$.	112
Figure 5.34 Evolution of the optimization parameter as a function of the number of iterations using decibel functional. Convergence was achieved after 18 iterations at $\sigma = 0.015$.	113
Figure 5.35 Evolution of the optimization parameter as a function of the number of iterations using linear functional. Convergence was achieved after 9 iterations at $\epsilon_{rs} = 2.53$.	114
Figure 5.36 Evolution of the optimization parameter as a function of the number of iterations using linear functional. Convergence was achieved after 9 iterations at $\epsilon_{rz} = 3.33$.	115
Figure 5.37 Evolution of the optimization parameter as a function of the number of iterations using decibel functional. Convergence was achieved after 3 iterations at $\epsilon_{rs} = 7.38$.	115
Figure 5.38 Evolution of the optimization parameter as a function of the number of iterations using decibel functional. Convergence was achieved after 3 iterations at $\epsilon_{rz} = 5.42$.	116
Figure 5.39 Evolution of the optimization parameter as a function of the number of iterations using linear functional. Convergence was achieved after 19 iterations at $\epsilon_{rs} = 2.55$.	117
Figure 5.40 Evolution of the optimization parameter as a function of the number of iterations using linear functional. Convergence was achieved after 19 iterations at $\epsilon_{rz} = 3$.	118
Figure 5.41 Evolution of the optimization parameter as a function of the number of iterations using linear functional. Convergence was achieved after 19 iterations at $\sigma_s = 0.01$.	118
Figure 5.42 Evolution of the optimization parameter as a function of the number of iterations using linear functional. Convergence was achieved after 19 iterations at $\sigma_z = 0.01$.	119
Figure 5.43 Evolution of the optimization parameter as a function of the number of iterations using decibel functional. Convergence was achieved after 5 iterations at $\epsilon_{rs} = 2.55$.	119
Figure 5.44 Evolution of the optimization parameter as a function of the number of iterations using decibel functional. Convergence was achieved after 5 iterations at $\epsilon_{rz} = 2.95$.	120

Figure 5.45 Evolution of the optimization parameter as a function of the number of iterations using decibel functional. Convergence was achieved after 5 iterations at $\sigma_s = 0.008$.	120
Figure 5.46 Evolution of the optimization parameter as a function of the number of iterations using decibel functional. Convergence was achieved after 5 iterations at $\sigma_z = 0.008$.	121
Figure 5.47 Evolution of the optimization parameter as a function of the number of iterations using linear functional. Convergence was achieved after 23 iterations at $\epsilon_{rs} = 2.55$.	122
Figure 5.48 Evolution of the optimization parameter as a function of the number of iterations using linear functional. Convergence was achieved after 23 iterations at $\epsilon_{rz} = 3$.	123
Figure 5.49 Evolution of the optimization parameter as a function of the number of iterations using linear functional. Convergence was achieved after 23 iterations at $\sigma_s = 0.01$.	123
Figure 5.50 Evolution of the optimization parameter as a function of the number of iterations using linear functional. Convergence was achieved after 23 iterations at $\sigma_z = 0.02$.	124
Figure 5.51 Evolution of the optimization parameter as a function of the number of iterations using decibel functional. Convergence was achieved after 8 iterations at $\epsilon_{rs} = 2.54$.	124
Figure 5.52 Evolution of the optimization parameter as a function of the number of iterations using decibel functional. Convergence was achieved after 8 iterations at $\epsilon_{rz} = 3.01$.	125
Figure 5.53 Evolution of the optimization parameter as a function of the number of iterations using decibel functional. Convergence was achieved after 8 iterations at $\sigma_s = 0.011$.	125
Figure 5.54 Evolution of the optimization parameter as a function of the number of iterations using decibel functional. Convergence was achieved after 8 iterations at $\sigma_z = 0.015$.	126
Figure 5.55 Evolution of the optimization parameter as a function of the number of iterations using linear functional. Convergence was achieved after 9 iterations at $\epsilon_r = 2.55$.	127
Figure 5.56 Evolution of the optimization parameter as a function of the number of iterations using linear functional. Convergence was achieved after 10 iterations at $\epsilon_r = 2.55$.	128
Figure 5.57 Evolution of the optimization parameter as a function of the number of iterations using linear functional. Convergence was achieved after 10 iterations at $\sigma = 0.02$.	129
Figure 5.58 Evolution of the optimization parameter as a function of the number of iterations using decibel functional. Convergence was achieved after 10 iterations at $\epsilon_r = 2.55$.	129
Figure 5.59 Evolution of the optimization parameter as a function of the number of iterations using decibel functional. Convergence was achieved after 10 iterations at $\sigma = 0.036$.	130
Figure 5.60 Evolution of the optimization parameter as a function of the number of iterations using linear functional. Convergence was achieved after 10 iterations at $\epsilon_{rs} = 2.55$.	131

- Figure 5.61 Evolution of the optimization parameter as a function of the number of iterations using linear functional. Convergence was achieved after 10 iterations at $\epsilon_{rz} = 3$. 131
- Figure 5.62 Evolution of the optimization parameter as a function of the number of iterations using decibel functional. Convergence was achieved after 3 iterations at $\epsilon_{rs} = 2.56$. 132
- Figure 5.63 Evolution of the optimization parameter as a function of the number of iterations using decibel functional. Convergence was achieved after 3 iterations at $\epsilon_{rz} = 2.99$. 132
- Figure 5.64 Evolution of the optimization parameter as a function of the number of iterations using linear functional. Convergence was achieved after 21 iterations at $\epsilon_{rs} = 2.55$. 133
- Figure 5.65 Evolution of the optimization parameter as a function of the number of iterations using linear functional. Convergence was achieved after 21 iterations at $\epsilon_{rz} = 3$. 134
- Figure 5.66 Evolution of the optimization parameter as a function of the number of iterations using linear functional. Convergence was achieved after 21 iterations at $\sigma_s = 0.018$. 134
- Figure 5.67 Evolution of the optimization parameter as a function of the number of iterations using linear functional. Convergence was achieved after 21 iterations at $\sigma_z = 0.02$. 135
- Figure 5.68 Evolution of the optimization parameter as a function of the number of iterations using decibel functional. Convergence was achieved after 3 iterations at $\epsilon_{rs} = 2.56$. 135
- Figure 5.69 Evolution of the optimization parameter as a function of the number of iterations using decibel functional. Convergence was achieved after 3 iterations at $\epsilon_{rz} = 2.99$. 136
- Figure 5.70 Evolution of the optimization parameter as a function of the number of iterations using decibel functional. Convergence was achieved after 3 iterations at $\sigma_s = 0.01$. 136
- Figure 5.71 Evolution of the optimization parameter as a function of the number of iterations using decibel functional. Convergence was achieved after 3 iterations at $\sigma_z = 0.01$. 137
- Figure 5.72 Evolution of the optimization parameter as a function of the number of iterations using linear functional. Convergence was achieved after 22 iterations at $\epsilon_{rs} = 2.55$. 138
- Figure 5.73 Evolution of the optimization parameter as a function of the number of iterations using linear functional. Convergence was achieved after 22 iterations at $\epsilon_{rz} = 3$. 139
- Figure 5.74 Evolution of the optimization parameter as a function of the number of iterations using linear functional. Convergence was achieved after 22 iterations at $\sigma_s = 0.01$. 139
- Figure 5.75 Evolution of the optimization parameter as a function of the number of iterations using linear functional. Convergence was achieved after 22 iterations at $\sigma_z = 0.02$. 140
- Figure 5.76 Evolution of the optimization parameter as a function of the number of iterations using decibel functional. Convergence was achieved after 3 iterations at $\epsilon_{rs} = 2.56$. 140

- Figure 5.77 Evolution of the optimization parameter as a function of the number of iterations using decibel functional. Convergence was achieved after 3 iterations at $\epsilon_{rz} = 2.99$. 141
- Figure 5.78 Evolution of the optimization parameter as a function of the number of iterations using decibel functional. Convergence was achieved after 3 iterations at $\sigma_s = 0.01$. 141
- Figure 5.79 Evolution of the optimization parameter as a function of the number of iterations using decibel functional. Convergence was achieved after 3 iterations at $\sigma_z = 0.01$. 142
- Figure 5.80 Evolution of the optimization parameter as a function of the number of iterations using linear functional. Convergence was achieved after 9 iterations at $\epsilon_r = 2.55$. 144
- Figure 5.81 Evolution of the optimization parameter as a function of the number of iterations using decibel functional. Convergence was achieved after 4 iterations at $\epsilon_r = 2.55$. 144
- Figure 5.82 Evolution of the optimization parameter as a function of the number of iterations using linear functional. Convergence was achieved after 16 iterations at $\epsilon_r = 2.55$. 145
- Figure 5.83 Evolution of the optimization parameter as a function of the number of iterations using linear functional. Convergence was achieved after 16 iterations at $\sigma = 0.01$. 146
- Figure 5.84 Evolution of the optimization parameter as a function of the number of iterations using decibel functional. Convergence was achieved after 3 iterations at $\epsilon_r = 2.58$. 146
- Figure 5.85 Evolution of the optimization parameter as a function of the number of iterations using decibel functional. Convergence was achieved after 3 iterations at $\sigma = 0.011$. 147
- Figure 5.86 Evolution of the optimization parameter as a function of the number of iterations using linear functional. Convergence was achieved after 14 iterations at $\epsilon_{rs} = 2.55$. 148
- Figure 5.87 Evolution of the optimization parameter as a function of the number of iterations using linear functional. Convergence was achieved after 14 iterations at $\epsilon_{rz} = 3$. 149
- Figure 5.88 Evolution of the optimization parameter as a function of the number of iterations using decibel functional. Convergence was achieved after 7 iterations at $\epsilon_{rs} = 2.55$. 149
- Figure 5.89 Evolution of the optimization parameter as a function of the number of iterations using decibel functional. Convergence was achieved after 7 iterations at $\epsilon_{rz} = 3$. 150
- Figure 5.90 Evolution of the optimization parameter as a function of the number of iterations using linear functional. Convergence was achieved after 24 iterations at $\epsilon_{rs} = 2.55$. 151
- Figure 5.91 Evolution of the optimization parameter as a function of the number of iterations using linear functional. Convergence was achieved after 24 iterations at $\epsilon_{rz} = 2.99$. 151
- Figure 5.92 Evolution of the optimization parameter as a function of the number of iterations using linear functional. Convergence was achieved after 24 iterations at $\sigma_s = 0.02$. 152

Figure 5.93 Evolution of the optimization parameter as a function of the number of iterations using linear functional. Convergence was achieved after 24 iterations at $\sigma_z = 0.02$.	152
Figure 5.94 Evolution of the optimization parameter as a function of the number of iterations using decibel functional. Convergence was achieved after 2 iterations at $\epsilon_{rs} = 2.51$.	153
Figure 5.95 Evolution of the optimization parameter as a function of the number of iterations using decibel functional. Convergence was achieved after 2 iterations at $\epsilon_{rz} = 3.01$.	153
Figure 5.96 Evolution of the optimization parameter as a function of the number of iterations using decibel functional. Convergence was achieved after 2 iterations at $\sigma_s = 0.01$.	154
Figure 5.97 Evolution of the optimization parameter as a function of the number of iterations using decibel functional. Convergence was achieved after 2 iterations at $\sigma_z = 0.01$.	154
Figure 5.98 Evolution of the optimization parameter as a function of the number of iterations using linear functional. Convergence was achieved after 21 iterations at $\epsilon_{rs} = 2.55$.	155
Figure 5.99 Evolution of the optimization parameter as a function of the number of iterations using linear functional. Convergence was achieved after 21 iterations at $\epsilon_{rz} = 3$.	156
Figure 5.100 Evolution of the optimization parameter as a function of the number of iterations using linear functional. Convergence was achieved after 21 iterations at $\sigma_s = 0.01$.	156
Figure 5.101 Evolution of the optimization parameter as a function of the number of iterations using linear functional. Convergence was achieved after 21 iterations at $\sigma_z = 0.02$.	157
Figure 5.102 Evolution of the optimization parameter as a function of the number of iterations using decibel functional. Convergence was achieved after 4 iterations at $\epsilon_{rs} = 2.57$.	157
Figure 5.103 Evolution of the optimization parameter as a function of the number of iterations using decibel functional. Convergence was achieved after 4 iterations at $\epsilon_{rz} = 2.98$.	158
Figure 5.104 Evolution of the optimization parameter as a function of the number of iterations using decibel functional. Convergence was achieved after 4 iterations at $\sigma_s = 0.012$.	158
Figure 5.105 Evolution of the optimization parameter as a function of the number of iterations using decibel functional. Convergence was achieved after 4 iterations at $\sigma_z = 0.013$.	159
Figure 5.106 Evolution of the optimization parameter as a function of the number of iterations using linear functional. Convergence was achieved after 9 iterations at $\epsilon_r = 2.55$.	160
Figure 5.107 Evolution of the optimization parameter as a function of the number of iterations using decibel functional. Convergence was achieved after 3 iterations at $\epsilon_r = 2.54$.	161
Figure 5.108 Evolution of the optimization parameter as a function of the number of iterations using linear functional. Convergence was achieved after 12 iterations at $\epsilon_r = 2.55$.	162

Figure 5.109	Evolution of the optimization parameter as a function of the number of iterations using linear functional. Convergence was achieved after 12 iterations at $\sigma = 0.01$.	163
Figure 5.110	Evolution of the optimization parameter as a function of the number of iterations using decibel functional. Convergence was achieved after 3 iterations at $\epsilon_r = 2.58$.	163
Figure 5.111	Evolution of the optimization parameter as a function of the number of iterations using decibel functional. Convergence was achieved after 3 iterations at $\sigma = 0.01$.	164
Figure 5.112	Evolution of the optimization parameter as a function of the number of iterations using linear functional. Convergence was achieved after 10 iterations at $\epsilon_{rs} = 2.55$.	165
Figure 5.113	Evolution of the optimization parameter as a function of the number of iterations using linear functional. Convergence was achieved after 10 iterations at $\epsilon_{rz} = 2.99$.	166
Figure 5.114	Evolution of the optimization parameter as a function of the number of iterations using decibel functional. Convergence was achieved after 3 iterations at $\epsilon_{rs} = 2.56$.	166
Figure 5.115	Evolution of the optimization parameter as a function of the number of iterations using decibel functional. Convergence was achieved after 3 iterations at $\epsilon_{rz} = 2.99$.	167
Figure 5.116	Evolution of the optimization parameter as a function of the number of iterations using linear functional. Convergence was achieved after 26 iterations at $\epsilon_{rs} = 2.55$.	168
Figure 5.117	Evolution of the optimization parameter as a function of the number of iterations using linear functional. Convergence was achieved after 26 iterations at $\epsilon_{rz} = 3$.	168
Figure 5.118	Evolution of the optimization parameter as a function of the number of iterations using linear functional. Convergence was achieved after 26 iterations at $\sigma_s = 0.01$.	169
Figure 5.119	Evolution of the optimization parameter as a function of the number of iterations using linear functional. Convergence was achieved after 26 iterations at $\sigma_z = 0.01$.	169
Figure 5.120	Evolution of the optimization parameter as a function of the number of iterations using decibel functional. Convergence was achieved after 3 iterations at $\epsilon_{rs} = 2.61$.	170
Figure 5.121	Evolution of the optimization parameter as a function of the number of iterations using decibel functional. Convergence was achieved after 3 iterations at $\epsilon_{rz} = 3.05$.	170
Figure 5.122	Evolution of the optimization parameter as a function of the number of iterations using decibel functional. Convergence was achieved after 3 iterations at $\sigma_s = 0.002$.	171
Figure 5.123	Evolution of the optimization parameter as a function of the number of iterations using decibel functional. Convergence was achieved after 3 iterations at $\sigma_z = 0.002$.	171
Figure 5.124	Evolution of the optimization parameter as a function of the number of iterations using linear functional. Convergence was achieved after 23 iterations at $\epsilon_{rs} = 2.55$.	172

Figure 5.125	Evolution of the optimization parameter as a function of the number of iterations using linear functional. Convergence was achieved after 23 iterations at $\epsilon_{rz} = 3$.	173
Figure 5.126	Evolution of the optimization parameter as a function of the number of iterations using linear functional. Convergence was achieved after 23 iterations at $\sigma_s = 0.01$.	173
Figure 5.127	Evolution of the optimization parameter as a function of the number of iterations using linear functional. Convergence was achieved after 23 iterations at $\sigma_z = 0.02$.	174
Figure 5.128	Evolution of the optimization parameter as a function of the number of iterations using decibel functional. Convergence was achieved after 4 iterations at $\epsilon_{rs} = 2.57$.	174
Figure 5.129	Evolution of the optimization parameter as a function of the number of iterations using decibel functional. Convergence was achieved after 4 iterations at $\epsilon_{rz} = 2.98$.	175
Figure 5.130	Evolution of the optimization parameter as a function of the number of iterations using decibel functional. Convergence was achieved after 4 iterations at $\sigma_s = 0.01$.	175
Figure 5.131	Evolution of the optimization parameter as a function of the number of iterations using decibel functional. Convergence was achieved after 4 iterations at $\sigma_z = 0.01$.	176
Figure 5.132	Evolution of the optimization parameter as a function of the number of iterations using linear functional. Convergence was achieved after 8 iterations at $\epsilon_r = 2.55$.	177
Figure 5.133	Evolution of the optimization parameter as a function of the number of iterations using decibel functional. Convergence was achieved after 4 iterations at $\epsilon_r = 2.55$.	178
Figure 5.134	Evolution of the optimization parameter as a function of the number of iterations using linear functional. Convergence was achieved after 5 iterations at $\epsilon_r = 2.53$.	179
Figure 5.135	Evolution of the optimization parameter as a function of the number of iterations using linear functional. Convergence was achieved after 5 iterations at $\sigma = 0.015$.	180
Figure 5.136	Evolution of the optimization parameter as a function of the number of iterations using decibel functional. Convergence was achieved after 3 iterations at $\epsilon_r = 2.58$.	180
Figure 5.137	Evolution of the optimization parameter as a function of the number of iterations using decibel functional. Convergence was achieved after 3 iterations at $\sigma = 0.01$.	181
Figure 5.138	Evolution of the optimization parameter as a function of the number of iterations using linear functional. Convergence was achieved after 14 iterations at $\epsilon_{rs} = 2.72$.	182
Figure 5.139	Evolution of the optimization parameter as a function of the number of iterations using linear functional. Convergence was achieved after 14 iterations at $\epsilon_{rz} = 3.2$.	183
Figure 5.140	Evolution of the optimization parameter as a function of the number of iterations using decibel functional. Convergence was achieved after 7 iterations at $\epsilon_{rs} = 2.55$.	183

Figure 5.141	Evolution of the optimization parameter as a function of the number of iterations using decibel functional. Convergence was achieved after 7 iterations at $\epsilon_{rz} = 3$.	184
Figure 5.142	Evolution of the optimization parameter as a function of the number of iterations using linear functional. Convergence was achieved after 24 iterations at $\epsilon_{rs} = 2.55$.	185
Figure 5.143	Evolution of the optimization parameter as a function of the number of iterations using linear functional. Convergence was achieved after 24 iterations at $\epsilon_{rz} = 2.99$.	185
Figure 5.144	Evolution of the optimization parameter as a function of the number of iterations using linear functional. Convergence was achieved after 24 iterations at $\sigma_s = 0.02$.	186
Figure 5.145	Evolution of the optimization parameter as a function of the number of iterations using linear functional. Convergence was achieved after 24 iterations at $\sigma_z = 0.02$.	186
Figure 5.146	Evolution of the optimization parameter as a function of the number of iterations using decibel functional. Convergence was achieved after 2 iterations at $\epsilon_{rs} = 2.51$.	187
Figure 5.147	Evolution of the optimization parameter as a function of the number of iterations using decibel functional. Convergence was achieved after 2 iterations at $\epsilon_{rz} = 3.01$.	187
Figure 5.148	Evolution of the optimization parameter as a function of the number of iterations using decibel functional. Convergence was achieved after 2 iterations at $\sigma_s = 0.01$.	188
Figure 5.149	Evolution of the optimization parameter as a function of the number of iterations using decibel functional. Convergence was achieved after 2 iterations at $\sigma_z = 0.01$.	188
Figure 5.150	Evolution of the optimization parameter as a function of the number of iterations using linear functional. Convergence was achieved after 21 iterations at $\epsilon_{rs} = 2.55$.	189
Figure 5.151	Evolution of the optimization parameter as a function of the number of iterations using linear functional. Convergence was achieved after 21 iterations at $\epsilon_{rz} = 3.00$.	190
Figure 5.152	Evolution of the optimization parameter as a function of the number of iterations using linear functional. Convergence was achieved after 21 iterations at $\sigma_s = 0.01$.	190
Figure 5.153	Evolution of the optimization parameter as a function of the number of iterations using linear functional. Convergence was achieved after 21 iterations at $\sigma_z = 0.02$.	191
Figure 5.154	Evolution of the optimization parameter as a function of the number of iterations using decibel functional. Convergence was achieved after 2 iterations at $\epsilon_{rs} = 2.57$.	191
Figure 5.155	Evolution of the optimization parameter as a function of the number of iterations using decibel functional. Convergence was achieved after 4 iterations at $\epsilon_{rz} = 2.98$.	192
Figure 5.156	Evolution of the optimization parameter as a function of the number of iterations using decibel functional. Convergence was achieved after 4 iterations at $\sigma_s = 0.012$.	192

Figure 5.157	Evolution of the optimization parameter as a function of the number of iterations using decibel functional. Convergence was achieved after 4 iterations at $\sigma_z = 0.013$.	193
Figure 5.158	Evolution of the optimization parameter as a function of the number of iterations using linear functional. Convergence was achieved after 6 iterations at $\epsilon_r = 2.55$.	195
Figure 5.159	Evolution of the optimization parameter as a function of the number of iterations using decibel functional. Convergence was achieved after 4 iterations at $\epsilon_r = 2.55$.	195
Figure 5.160	Evolution of the optimization parameter as a function of the number of iterations using linear functional. Convergence was achieved after 10 iterations at $\epsilon_{rs} = 2.55$.	196
Figure 5.161	Evolution of the optimization parameter as a function of the number of iterations using linear functional. Convergence was achieved after 10 iterations at $\epsilon_{rz} = 3$.	197
Figure 5.162	Evolution of the optimization parameter as a function of the number of iterations using decibel functional. Convergence was achieved after 3 iterations at $\epsilon_{rs} = 2.58$.	197
Figure 5.163	Evolution of the optimization parameter as a function of the number of iterations using decibel functional. Convergence was achieved after 3 iterations at $\epsilon_{rz} = 2.99$.	198

List of tables

Table 2.1	Classification of materials.	40
Table 2.2	Advantages and drawbacks of the resonator cavity method. Image obtained in [53].	41
Table 2.3	Advantages and drawbacks of the free space method [53].	42
Table 2.4	Advantages and drawbacks of the one-port MCs [53].	43
Table 2.5	Advantages and drawbacks of two-port MCs [53].	44
Table 2.6	Relation between ϵ_r and S_{11} [55].	44
Table 2.7	Nicholson-Ross-Weird relations.	46
Table 4.1	Simulation parameters for the case depicted in Fig. 4.1.	58
Table 4.2	Simulation parameters for the case depicted in Fig. 4.4.	62
Table 4.3	Simulation parameters for the second case	62
Table 4.4	Simulation parameters for the third case	62
Table 4.5	Parameter of the PML	66
Table 4.6	Simulation parameters used to emulate an open-ended coaxial probe	66
Table 4.7	Geometric and constitutive parameters used on direct problem of a lossless isotropic sample placed in second waveguide of a two-port heterogeneous coaxial waveguide for graphic comparison problem	79
Table 4.8	Algorithms used in function <code>fmincon</code> [77].	82
Table 5.1	Geometric and constitutive parameters used on direct problem of a lossless isotropic sample placed in second waveguide of a two-port heterogeneous coaxial waveguide.	91
Table 5.2	Initial guess, CPU time, and the number of iterations to achieve convergence by using the parameters Table 5.1 using linear functional.	91
Table 5.3	Initial guess, CPU time, and the number of iterations to achieve convergence by using the parameters table 5.1 using decibel functional.	91
Table 5.4	Geometric and constitutive parameters used on direct problem of a lossy isotropic sample placed in second waveguide of a two-port heterogeneous coaxial waveguide.	94
Table 5.5	Initial guess, CPU time, and the number of iterations to achieve convergence by using the parameters Table 5.4 using linear functional.	94
Table 5.6	Initial guess, CPU time, and the number of iterations to achieve convergence by using the parameters Table 5.4 using decibel functional.	96
Table 5.7	Geometric and constitutive parameters used on direct problem of a lossless anisotropic sample placed in second waveguide of a two-port heterogeneous coaxial waveguide	96

Table 5.8	Initial guess, CPU time, and the number of iterations to achieve convergence by using the parameters Table 5.7 using linear functional.	97
Table 5.9	Initial guess, CPU time, and the number of iterations to achieve convergence by using the parameters Table 5.7 using decibel functional	98
Table 5.10	Geometric and constitutive parameters used on direct problem of a isotropic loss and anisotropic sample placed in second waveguide of a two-port heterogeneous coaxial waveguide	99
Table 5.11	Initial guess, CPU time, and the number of iterations to achieve convergence by using the parameters Table 5.10 using linear functional.	99
Table 5.12	Initial guess, CPU time, and the number of iterations to achieve convergence by using the parameters Table 5.10 using decibel functional.	101
Table 5.13	Geometric and constitutive parameters used on direct problem of a anisotropic lossy and anisotropic sample placed in second waveguide of a two-port heterogeneous coaxial waveguide	104
Table 5.14	Initial guess, CPU time, and the number of iterations to achieve convergence by using the parameters Table 5.13 using linear functional.	104
Table 5.15	Initial guess, CPU time, and the number of iterations to achieve convergence by using the parameters Table 5.13 using decibel functional.	106
Table 5.16	Geometric and constitutive parameters used on direct problem of a lossless isotropic sample placed in second waveguide of a two-port homogeneous circular waveguide	109
Table 5.17	Initial guess, CPU time, and the number of iterations to achieve convergence by using the parameters Table 5.16 using linear functional.	110
Table 5.18	Initial guess, CPU time, and the number of iterations to achieve convergence by using the parameters Table 5.16 using decibel functional.	110
Table 5.19	Geometric and constitutive parameters used on direct problem of a lossy isotropic sample placed in second waveguide of a two-port homogeneous circular waveguide	111
Table 5.20	Initial guess, CPU time, and the number of iterations to achieve convergence by using the parameters Table 5.19 using linear functional.	111
Table 5.21	Initial guess, CPU time, and the number of iterations to achieve convergence by using the parameters Table 5.19 using decibel functional.	111
Table 5.22	Geometric and constitutive parameters used on direct problem of a lossless anisotropic sample placed in second waveguide of a two-port homogeneous circular waveguide	114
Table 5.23	Initial guess, CPU time, and the number of iterations to achieve convergence by using the parameters Table 5.22 using linear functional.	115

Table 5.24 Initial guess, CPU time, and the number of iterations to achieve convergence by using the parameters Table 5.22 using decibel functional.	116
Table 5.25 Geometric and constitutive parameters used on direct problem of a isotropic lossy and anisotropic sample placed in second waveguide of a two-port homogeneous circular waveguide	117
Table 5.26 Initial guess, CPU time, and the number of iterations to achieve convergence by using the parameters Table 5.25 using linear functional.	117
Table 5.27 Initial guess, CPU time, and the number of iterations to achieve convergence by using the parameters Table 5.25 using decibel functional.	117
Table 5.28 Geometric and constitutive parameters used on direct problem of a anisotropic lossy and anisotropic sample placed in second waveguide of a two-port homogeneous circular waveguide	122
Table 5.29 Initial guess, CPU time, and the number of iterations to achieve convergence by using the parameters Table 5.28 using linear functional.	123
Table 5.30 Initial guess, CPU time, and the number of iterations to achieve convergence by using the parameters Table 5.28 using decibel functional.	124
Table 5.31 Geometric and constitutive parameters used on direct problem of a lossless isotropic sample placed in second waveguide of a two-port heterogeneous circular waveguide	127
Table 5.32 Initial guess, CPU time, and the number of iterations to achieve convergence by using the parameters Table 5.31 using linear functional.	128
Table 5.33 Geometric and constitutive parameters used on direct problem of a lossy isotropic sample placed in second waveguide of a two-port heterogeneous circular waveguide	128
Table 5.34 Initial guess, CPU time, and the number of iterations to achieve convergence by using the parameters Table 5.33 using linear functional.	129
Table 5.35 Initial guess, CPU time, and the number of iterations to achieve convergence by using the parameters Table 5.33 using decibel functional.	130
Table 5.36 Geometric and constitutive parameters used on direct problem of a lossless anisotropic sample placed in second waveguide of a two-port heterogeneous circular waveguide	130
Table 5.37 Initial guess, CPU time, and the number of iterations to achieve convergence by using the parameters Table 5.36 using linear functional.	131
Table 5.38 Initial guess, CPU time, and the number of iterations to achieve convergence by using the parameters Table 5.36 using decibel functional.	132
Table 5.39 Geometric and constitutive parameters used on direct problem of a isotropic lossy and anisotropic sample placed in second waveguide of a two-port heterogeneous circular waveguide	133

Table 5.40 Initial guess, CPU time, and the number of iterations to achieve convergence by using the parameters Table 5.39 using linear functional.	134
Table 5.41 Initial guess, CPU time, and the number of iterations to achieve convergence by using the parameters Table 5.39 using decibel functional.	135
Table 5.42 Geometric and constitutive parameters used on direct problem of an anisotropic lossy and anisotropic sample placed in second waveguide of a two-port heterogeneous circular waveguide	138
Table 5.43 Initial guess, CPU time, and the number of iterations to achieve convergence by using the parameters Table 5.42 using linear functional.	139
Table 5.44 Initial guess, CPU time, and the number of iterations to achieve convergence by using the parameters Table 5.42 using decibel functional.	140
Table 5.45 Geometric and constitutive parameters used on direct problem of a lossless isotropic sample placed in second waveguide of a one-port heterogeneous coaxial waveguide	143
Table 5.46 Initial guess, CPU time, and the number of iterations to achieve convergence by using the parameters Table 5.45 using linear functional.	143
Table 5.47 Initial guess, CPU time, and the number of iterations to achieve convergence by using the parameters Table 5.45 using decibel functional.	143
Table 5.48 Geometric and constitutive parameters used on direct problem of a lossy isotropic sample placed in second waveguide of a one-port heterogeneous coaxial waveguide	145
Table 5.49 Initial guess, CPU time, and the number of iterations to achieve convergence by using the parameters Table 5.48 using linear functional.	145
Table 5.50 Initial guess, CPU time, and the number of iterations to achieve convergence by using the parameters Table 5.48 using decibel functional.	145
Table 5.51 Geometric and constitutive parameters used on direct problem of a lossless anisotropic sample placed in second waveguide of a one-port heterogeneous coaxial waveguide	148
Table 5.52 Initial guess, CPU time, and the number of iterations to achieve convergence by using the parameters Table 5.51 using linear functional.	149
Table 5.53 Initial guess, CPU time, and the number of iterations to achieve convergence by using the parameters Table 5.51 using decibel functional.	150
Table 5.54 Geometric and constitutive parameters used on direct problem of a isotropic lossy and anisotropic sample placed in second waveguide of a one-port heterogeneous coaxial waveguide	150
Table 5.55 Initial guess, CPU time, and the number of iterations to achieve convergence by using the parameters Table 5.54 using linear functional.	152

Table 5.56 Initial guess, CPU time, and the number of iterations to achieve convergence by using the parameters Table 5.54 using decibel functional.	153
Table 5.57 Geometric and constitutive parameters used on direct problem of a anisotropic lossy and anisotropic sample placed in second waveguide of a one-port heterogeneous coaxial waveguide	155
Table 5.58 Initial guess, CPU time, and the number of iterations to achieve convergence by using the parameters Table 5.57 using linear functional.	155
Table 5.59 Initial guess, CPU time, and the number of iterations to achieve convergence by using the parameters Table 5.57 using decibel functional.	156
Table 5.60 Geometric and constitutive parameters used on direct problem of a lossless isotropic sample placed in second waveguide of a one-port homogeneous circular waveguide	160
Table 5.61 Initial guess, CPU time, and the number of iterations to achieve convergence by using the parameters Table 5.60 using linear functional.	161
Table 5.62 Initial guess, CPU time, and the number of iterations to achieve convergence by using the parameters Table 5.60 using decibel functional.	161
Table 5.63 Geometric and constitutive parameters used on direct problem of a lossy isotropic sample placed in second waveguide of a one-port homogeneous circular waveguide	162
Table 5.64 Initial guess, CPU time, and the number of iterations to achieve convergence by using the parameters Table 5.63 using linear functional.	162
Table 5.65 Initial guess, CPU time, and the number of iterations to achieve convergence by using the parameters Table 5.63 using decibel functional.	162
Table 5.66 Geometric and constitutive parameters used on direct problem of a lossless anisotropic sample placed in second waveguide of a one-port homogeneous circular waveguide	165
Table 5.67 Initial guess, CPU time, and the number of iterations to achieve convergence by using the parameters table 5.66 of Fig. 5.112 and Fig. 5.113 using linear functional	166
Table 5.68 Initial guess, CPU time, and the number of iterations to achieve convergence by using the parameters Table 5.66 using decibel functional.	167
Table 5.69 Geometric and constitutive parameters used on direct problem of a isotropic lossy and anisotropic sample placed in second waveguide of a one-port homogeneous circular waveguide	167
Table 5.70 Initial guess, CPU time, and the number of iterations to achieve convergence by using the parameters Table 5.69 using linear functional.	169
Table 5.71 Initial guess, CPU time, and the number of iterations to achieve convergence by using the parameters Table 5.69 using decibel functional.	170

Table 5.72 Geometric and constitutive parameters used on direct problem of a anisotropic lossy and anisotropic sample placed in second waveguide of a one-port homogeneous circular waveguide	172
Table 5.73 Initial guess, CPU time, and the number of iterations to achieve convergence by using the parameters Table 5.72 using linear functional.	172
Table 5.74 Initial guess, CPU time, and the number of iterations to achieve convergence by using the parameters Table 5.72 using decibel functional.	173
Table 5.75 Geometric and constitutive parameters used on direct problem of a lossless isotropic sample placed in second waveguide of a one-port heterogeneous circular waveguide	177
Table 5.76 Initial guess, CPU time, and the number of iterations to achieve convergence by using the parameters Table 5.75 using linear functional.	178
Table 5.77 Initial guess, CPU time, and the number of iterations to achieve convergence by using the parameters table 5.75 of Fig. 5.133 using decibel functional	178
Table 5.78 Geometric and constitutive parameters used on direct problem of a lossy isotropic sample placed in second waveguide of a one-port heterogeneous circular waveguide	179
Table 5.79 Initial guess, CPU time, and the number of iterations to achieve convergence by using the parameters Table 5.78 using linear functional.	179
Table 5.80 Initial guess, CPU time, and the number of iterations to achieve convergence by using the parameters Table 5.78 using decibel functional.	179
Table 5.81 Geometric and constitutive parameters used on direct problem of a lossless anisotropic sample placed in second waveguide of a one-port heterogeneous circular waveguide	182
Table 5.82 Initial guess, CPU time, and the number of iterations to achieve convergence by using the parameters Table 5.81 using linear functional.	183
Table 5.83 Initial guess, CPU time, and the number of iterations to achieve convergence by using the parameters Table 5.81 using decibel functional.	184
Table 5.84 Geometric and constitutive parameters used on direct problem of a isotropic lossy and anisotropic sample placed in second waveguide of a one-port heterogeneous circular waveguide	184
Table 5.85 Initial guess, CPU time, and the number of iterations to achieve convergence by using the parameters Table 5.84 using linear functional.	186
Table 5.86 Initial guess, CPU time, and the number of iterations to achieve convergence by using the parameters Table 5.84 using decibel functional.	187
Table 5.87 Geometric and constitutive parameters used on direct problem of a anisotropic lossy and anisotropic sample placed in second waveguide of a one-port heterogeneous circular waveguide	189

Table 5.88 Initial guess, CPU time, and the number of iterations to achieve convergence by using the parameters Table 5.87 using linear functional.	189
Table 5.89 Initial guess, CPU time, and the number of iterations to achieve convergence by using the parameters Table 5.87 using decibel functional.	190
Table 5.90 Geometric and constitutive parameters used on direct problem of a lossless isotropic sample placed in second waveguide of a one-ended homogeneous circular waveguide	194
Table 5.91 Initial guess, CPU time, and the number of iterations to achieve convergence by using the parameters Table 5.90 using linear functional.	194
Table 5.92 Initial guess, CPU time, and the number of iterations to achieve convergence by using the parameters Table 5.90 using decibel functional.	195
Table 5.93 Geometric and constitutive parameters used on direct problem of a lossless anisotropic sample placed in second waveguide of a one-ended homogeneous circular waveguide	196
Table 5.94 Initial guess, CPU time, and the number of iterations to achieve convergence by using the parameters Table 5.93 using linear functional.	196
Table 5.95 Initial guess, CPU time, and the number of iterations to achieve convergence by using the parameters Table 5.93 using decibel functional.	197

1 Introduction

1.1 General Introduction

The research on microwave measurement cells (MCs) for material characterization have been extensively explored in the past decades. The works in [1, 2] introduced the idea of two-port MCs using rectangular waveguides. These methodologies are today known as the Nicholson-Ross-Weir method [3]. In parallel, research on one-port coaxial probes were introduced in [4] as an alternative MC for determining the constitutive parameters of a sample material that could not be placed inside a waveguide or cavity. Such pioneering works in the decade of 1970 have inspired the research towards the electromagnetic characterization of matter.

MCs that employ resonators and cavities have been widely used and studied over the years, and although popular techniques, they present frequency-range limitation [5]. Open-ended circular [6], rectangular [7–9] and coaxial [10, 11] waveguides can be used as MCs to retrieve the properties of material by only using reflection coefficient measurements. Two port MCs with rectangular [12, 13], circular and coaxial [14] symmetries are typically used to host a sample material, and the measurements of the scattering (reflection and transmission) parameters are then used into inverse algorithms for retrieving the material properties. Another option is based on free-space measurements [15], and such approaches present large-frequency bandwidth characteristic.

In the majority of the MCs mentioned above, the measurement of the scattering parameters are used into simple formulas for obtaining the electric permittivity or magnetic permeability of a given sample. In general, only lossless isotropic materials are characterized, and the size of MC is limited in order to only one propagating mode be present at the operating frequency of interest. In this work, we explore further the capacities of the measurements cells for the analysis of anisotropic and lossy media. In order to retrieve the material properties, a two-step procedure is proposed. First we need an accurate electromagnetic model for simulating the scattering parameters of a

given MC on assuming the material permittivity and permeability are known. This *direct algorithm* is then used into an iterative optimization process (the *inverse algorithm*), in which a functional is minimized and then will provide the material properties which best resemble the measured scattering parameters.

The direct algorithm needed for large (overmoded) MCs can employ a numerical solution of the Maxwell's equations. For example, this step can properly be done via the finite-element method (FEM) [16, 17], finite-difference time domain (FDTD) [18, 19], or integral equation-based methods [20, 21]. Such methods, however, demand a high computational effort. In contrast to these *brute-force methods*, where Maxwell's equations are discretized into computational huge grids of cells or elements, some pseudo-analytical methods can take advantage on the geometry of the MCs for improving the efficient of the simulation model. Since the geometry of typical MCs are conforming with simple rectangular and cylindrical waveguides, the mode-matching technique (MMT) excels as an efficient solution [22, 23].

In this work, we explore a semi-analytic formulation of the MMT for analyzing the junctions between non-homogeneous-filled waveguides for representing MCs that will be classified into three categories: two-port MCs, one-port MCs, and one-port open-ended coaxial MCs. As a key differential, our method can model materials that does not fill the entire waveguide cross-section, rendering a versatile direct algorithm for solving the MC scattering parameters. We introduce a novel formulation for handling multi-mode open-ended MCs via an equivalent problem to mimic the radiation boundary conditions via a virtual waveguide whose fields are the superposition of those of a circular waveguide truncated with a perfect matched layer (PML) [24–28] backed by a perfect electric conductor (PEC) and by a perfect magnetic conductor (PMC).

1.2

Scientific Contributions

The scientific contributions of this work are listed bellow:

- The development of a direct process using MMT for two-port, one-port and open-ended coaxial MCs.
- The development of a novel radiation boundary condition to be integrated into the MMT for emulating the free-space via a sum of cylindrical harmonics.
- The development of algorithms for the inverse process of extracting the constitutive parameters of complex media via the scattering parameters of the MC.

- A study on global and local minima of the functionals used in the inverse process and they relations with the MC and sample sizes.

1.3

Dissertation Organization

This dissertation is organized as follows. In Chapter 2, the electromagnetic material characterization is reviewed in view of the constitutive relations of matter. We also present a review on the electromagnetic methods typically used in resonant and non-resonant MCs.

In Chapter 3, a derivation of fields inside homogeneous and inhomogeneous cylindrical waveguides are present, as well as a review of the MMT. In addition, a review of PML to represent unbounded domains is presented.

In Chapter 4, the direct problem for two-port, one-port and open-ended coaxial measurement cells is derived. In addition, some methodologies to solve the inverse problem will be presented. A study on global and local minima of the functionals is then presented.

Finally, in Chapter 5, simulation results of several inverse problems for exploring the ability of the presented methodology (to retrieve the constitutive parameters of a sample material inside a MC) are presented.

2

Electromagnetic Characterization of Matter

2.1

Constitutive Relations

Matter can be characterized in the electromagnetic theory according to its constitutive relations, that are usually classified as [29]:

- Linear or non linear;
- Bianisotropic, anisotropic, or Isotropic;
- Spatially and temporally homogeneous or spatially and temporally non homogeneous;
- Dispersive or non dispersive.

These materials will be described in more details in the following sections.

For a *linear*, bianisotropic, spatially and temporally varying, and dispersive medium, we can relate electromagnetic fields and flux densities via [30, 31]:

$$\mathbf{D}(\mathbf{r}, t) = \int_V \int_{-\infty}^t \bar{\bar{\epsilon}}(\mathbf{r}, \mathbf{r}', t, t') \cdot \mathbf{E}(\mathbf{r}', t') dt' dv' + \int_V \int_{-\infty}^t \bar{\bar{\xi}}(\mathbf{r}, \mathbf{r}', t, t') \cdot \mathbf{H}(\mathbf{r}', t') dt' dv' \quad (2-1)$$

$$\mathbf{B}(\mathbf{r}, t) = \int_V \int_{-\infty}^t \bar{\bar{\zeta}}(\mathbf{r}, \mathbf{r}', t, t') \cdot \mathbf{E}(\mathbf{r}', t') dt' dv' + \int_V \int_{-\infty}^t \bar{\bar{\mu}}(\mathbf{r}, \mathbf{r}', t, t') \cdot \mathbf{H}(\mathbf{r}', t') dt' dv' \quad (2-2)$$

where the constitutive parameters are given by the complex-valued tensors $\bar{\bar{\epsilon}}$ (electric permittivity) and $\bar{\bar{\mu}}$ (magnetic permeability). The magneto-electric coupling is expressed by the complex-valued tensors $\bar{\bar{\zeta}}$ and $\bar{\bar{\xi}}$ [32]. The upper limit for the time integrals is t and the spatial-integration is over the domain V , such that $|r - r'| \leq c(t - t')$ for causality [30]. From these equations, we observe that the constitutive parameters act as dyadic Green's functions. In short, a) the integrals over the volume V represent the spatially dispersivity, b) the time-integrals represent the temporally dispersivity, c) the tensors $\bar{\bar{\xi}}$ and $\bar{\bar{\zeta}}$ represent the bianisotropic characteristic of the medium, d) r' indicates the spatial variation of the medium, and e) t' indicates the temporally variation of the medium.

2.1.1

Linear Media

2.1.1.1

Isotropic, Bi-isotropic, Anisotropic and Bianisotropic Medium

Recent studies on the interaction between electromagnetic fields and complex media suggest the creation of new devices can be possible by using novel exotic materials [33]. They can be design to possess several unique electromagnetic properties and have numerous applications for photonics [34], optoelectronics [35], gigahertz devices [36], radar cross-section reduction [37, 38], antenna reconfiguration [39], biosensors [1] and terahertz plasmonic filters [40]. These complex materials can be classified as isotropic, bi-isotropic, anisotropic and bianisotropic due to their macroscopic electromagnetic properties [33, 41].

2.1.1.2

Isotropic Medium

These type of materials does not present constitutive parameters as a function of the orientation of the applied field. In other words, they present uniformity in all directions and have a high degree of spatial symmetry. The electromagnetic response of fields applied to those materials are not affected by rotations with respect to the field. Some examples of such materials are unstressed plastic/glass, water, air and fluids at rest [33]. In this type of media, we have $\bar{\xi} = \bar{\zeta} = \bar{0}$, $\bar{\epsilon} = \epsilon \bar{I}$ and $\bar{\mu} = \mu \bar{I}$, where \bar{I} is a 3×3 unity tensor [32]. From (2-1), (2-2), we can obtain [32]

$$\mathbf{D} = \epsilon \bar{I} \cdot \mathbf{E} \quad (2-3)$$

$$\mathbf{B} = \mu \bar{I} \cdot \mathbf{H} \quad (2-4)$$

where the permittivity is $\epsilon = \epsilon_r \epsilon_0$, which $\epsilon_0 \approx 8,85 \times 10^{-12}$ F/m and the permeability is $\mu = \mu_r \mu_0$, which $\mu_0 = 4\pi \times 10^{-7}$ H/m. Fig. 2.1 shows the behavior of an electromagnetic field when passing by a linear isotropic media, it is possible to observe that for this case, the field's polarization does not get affected by the media.

2.1.1.3

Bi-Isotropic Medium

Bi-isotropic materials have the an optical property that they can rotate the polarization of light in either refraction or transmission. This twist effect is caused by the chirality and *non-reciprocity* of the structure of the media,



Figure 2.1: Behavior of the field in a linear isotropic media. Image obtained in [30].

causing an unusual interaction between the electric and magnetic field of an electromagnetic wave [29]. Recently, materials with chirality have been considered for applications in microwave and infrared frequency ranges. Such materials can be constructed by embedding chiral objects, such as wire helices, Möbius strips, or irregular tetrahedrons, in a nonchiral host isotropic medium, as detailed in [42].

In bi-isotropic media, the electric and magnetic fields are coupled and their constitutive relations are as follows [29, 43]:

$$\mathbf{D} = \epsilon\mathbf{E} + \xi\mathbf{H} \quad (2-5)$$

$$\mathbf{B} = \mu\mathbf{H} + \zeta\mathbf{E} \quad (2-6)$$

where ξ and ζ can be related to the reciprocity χ and chirality κ via [29]

$$\chi - i\kappa = \frac{\xi}{\sqrt{\epsilon\mu}} \quad (2-7)$$

$$\chi + i\kappa = \frac{\zeta}{\sqrt{\epsilon\mu}} \quad (2-8)$$

The above give us the following constitutive relation for a bi-isotropic medium:

$$\mathbf{D} = \epsilon\mathbf{E} + (\chi - i\kappa)\sqrt{\epsilon\mu}\mathbf{H} \quad (2-9)$$

$$\mathbf{B} = \mu\mathbf{H} + (\chi + i\kappa)\sqrt{\epsilon\mu}\mathbf{E} \quad (2-10)$$

2.1.1.4

Anisotropic Medium

Anisotropic materials have its constitutive parameters as a function of the direction of the applied field, which means that they are sensitive to the direction of the field.

For anisotropic media, we have $\bar{\bar{\xi}} = \bar{\bar{\zeta}} = \bar{\bar{0}}$ and the relations between

fields and flux densities become [32]

$$\mathbf{D} = \bar{\bar{\epsilon}} \cdot \mathbf{E} \quad (2-11)$$

$$\mathbf{B} = \bar{\bar{\mu}} \cdot \mathbf{H} \quad (2-12)$$

where $\bar{\bar{\epsilon}}$ is the permittivity tensor and $\bar{\bar{\mu}}$ is the permeability tensor. The electric flux density \mathbf{D} and electric field intensity \mathbf{E} are not parallel to each other, as well as the magnetic flux density \mathbf{B} and the magnetic field intensity \mathbf{H} are not [32]. The field's behavior in a non isotropic media is depicted in Fig. 2.2. It is possible to observe that for this case, the electromagnetic's field polarization is affected by the media and changing its direction.

In Cartesian coordinates, for instance, a biaxial anisotropic material has

$$\bar{\bar{\epsilon}} = \begin{bmatrix} \epsilon_x & 0 & 0 \\ 0 & \epsilon_y & 0 \\ 0 & 0 & \epsilon_z \end{bmatrix} \quad \text{and} \quad \bar{\bar{\mu}} = \begin{bmatrix} \mu_x & 0 & 0 \\ 0 & \mu_y & 0 \\ 0 & 0 & \mu_z \end{bmatrix} \quad (2-13)$$

with $\epsilon_x \neq \epsilon_y \neq \epsilon_z$. For uniaxial anisotropy, we have [32]

$$\bar{\bar{\epsilon}} = \begin{bmatrix} \epsilon & 0 & 0 \\ 0 & \epsilon & 0 \\ 0 & 0 & \epsilon_z \end{bmatrix} \quad \text{and} \quad \bar{\bar{\mu}} = \begin{bmatrix} \mu & 0 & 0 \\ 0 & \mu & 0 \\ 0 & 0 & \mu_z \end{bmatrix} \quad (2-14)$$

The special case with $\epsilon_x = \epsilon_y = \epsilon_z$ and $\mu_x = \mu_y = \mu_z$ classifies the medium as isotropic.

2.1.1.5

Bianisotropic Medium

Bianisotropic materials have a cross-coupling between the electric and magnetic fields [32]. In the presence of an electric or a magnetic field, a



Figure 2.2: Behavior of the field in a linear non isotropic media. Image obtained in [30].

bianisotropic medium becomes polarized and magnetized simultaneously. The relations between fields and flux densities become

$$\mathbf{D} = \bar{\bar{\epsilon}} \cdot \mathbf{E} + \bar{\bar{\xi}} \cdot \mathbf{H} \quad (2-15)$$

$$\mathbf{B} = \bar{\bar{\mu}} \cdot \mathbf{H} + \bar{\bar{\zeta}} \cdot \mathbf{E} \quad (2-16)$$

where the electric and magnetic density flux depends both on \mathbf{E} and \mathbf{H} . As four material parameter tensors are necessary, the most general case requires 36 complex-valued parameters. In many applications, however, symmetry relations apply for reciprocal media, for instance, and the number of independent constitutive parameters is lesser.

A summary of the different types of material discussed in this section is presented in Fig. 2.3.

2.1.2

Lossy and Lossless Media

In general, the response of a material to external fields depends on the frequency. This is due the fact that material's polarization does not change instantaneously when the electric field is applied into it. Therefore, in the frequency domain, the permittivity is complex-valued and can be written as $\epsilon = \epsilon' - j\epsilon''$. Notice the time-harmonic factor $e^{j\omega t}$ is assumed. In general, ϵ' and ϵ'' are frequency-dependent parameters. The imaginary parcel of the permittivity can also be expressed in terms of the electrical conductivity σ (that also may be a frequency-dependent parameters) via $\epsilon'' = \sigma/\omega$ [44, 45].

	Direction Independent	Direction Dependent
No magneto-electric coupling	Isotropic $\mathbf{D} = \epsilon \cdot \mathbf{E}$ $\mathbf{B} = \mu \cdot \mathbf{H}$	Anisotropic $\mathbf{D} = \bar{\bar{\epsilon}} \cdot \mathbf{E}$ $\mathbf{B} = \bar{\bar{\mu}} \cdot \mathbf{H}$
Magneto-electric coupling	Bi-isotropic $\mathbf{D} = \epsilon \cdot \mathbf{E} + \xi \cdot \mathbf{H}$ $\mathbf{B} = \mu \cdot \mathbf{H} + \zeta \cdot \mathbf{E}$	Bi-anisotropic $\mathbf{D} = \bar{\bar{\epsilon}} \cdot \mathbf{E} + \bar{\bar{\xi}} \cdot \mathbf{H}$ $\mathbf{B} = \bar{\bar{\mu}} \cdot \mathbf{H} + \bar{\bar{\zeta}} \cdot \mathbf{E}$

Figure 2.3: Summary of the types of material discussed.

The materials can be classified into four categories according to the ratio of the imaginary and real parts of the permittivity: lossless, low-loss, lossy, and high-loss medium according to Table 2.1.

Table 2.1: Classification of materials.

$\sigma/(\omega\epsilon')$	Characteristics
0	perfect dielectric lossless medium
$\ll 1$	good dielectric low-loss medium
≈ 1	lossy propagation medium
$\gg 1$	poor dielectric high-loss medium

2.2

Electromagnetic Characterization

In this section, we will present a review of some methods for material characterization using MCs. There are many techniques that uses either time domain (TD) [1, 46–49] or frequency domain (FD) [50–52] methodologies. The following subsections will be focused on resonant and non resonant techniques at microwave frequencies. Comprehensive details of other methods can be found in [5, 53].

2.2.1

Resonant Methods

2.2.1.1

Cavity Resonator

This technique is used normally to characterize homogeneous dielectric material due to its simplicity [54]. For this material characterization method, a resonator is filled with a material under test as show in Fig. 2.4. The presence of the sample will produce a broadening of the resonance curve and also a shift on its frequency when compared to the resonator without any material. From this measurements, the properties of the dielectric can be obtained. This technique is a good choice when the sample is a low-loss material. Notice, however, this MC only works well if the sample produces a small deviation on the resonating frequency. Otherwise, additional (larger or smaller) MCs should be employed. Table 2.2 lists some advantages and drawbacks of cavity-resonator MCs.

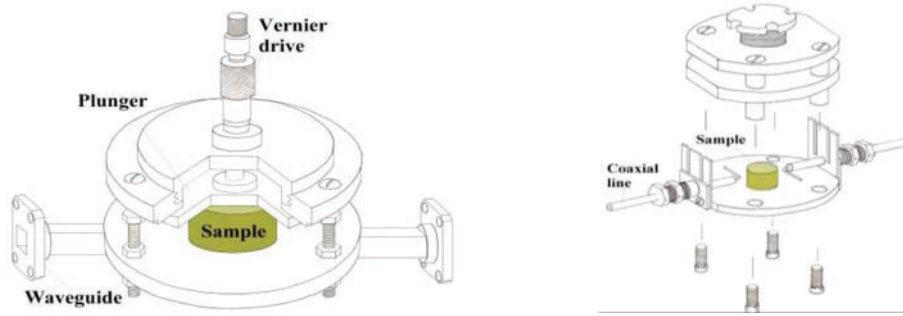


Figure 2.4: Cavity filled with a sample under test [55].

Table 2.2: Advantages and drawbacks of the resonator cavity method. Image obtained in [53].

Advantages	Drawbacks
<ul style="list-style-type: none"> • Support for both solids and liquids • Most accurate method • Suitable for low loss materials • No repetitive calibration procedures are required • High temperature capability • Best for low loss materials 	<ul style="list-style-type: none"> • Measurements at only single or at resonant frequency • Suitable for small size samples

2.2.2

Non Resonant Methods

2.2.2.1

Free Space

The so-called free-space measurement technique uses a horn antenna for far-field sensing as depicted in Fig. 2.5 where we can observe two circular horn setup placed in both sides of the sample and perpendicular to it's plane. Also, rectangular horns in three different configurations: first, similar to circular, however, with a dielectric bar on it's center, second, two horns oblique to sample's plane with a metal plate behind the it and third, one horn placed perpendicular to sample with a metal plate behind. Those are a non-contacting and non-destructive methodology, and usually is employed at high-frequencies when the sample is very large when compared to the working wavelength. This technique could be used at low frequencies but with severe limitations concerning the size of the sample material [56].

Since the antennas are not in contact with the material under test, free-space characterizations methods excel in the measurement of high-temperature samples [60]. The technique, however, is lacking in accuracy since precise distance measurements are mandatory. Table 2.3 lists some advantages and

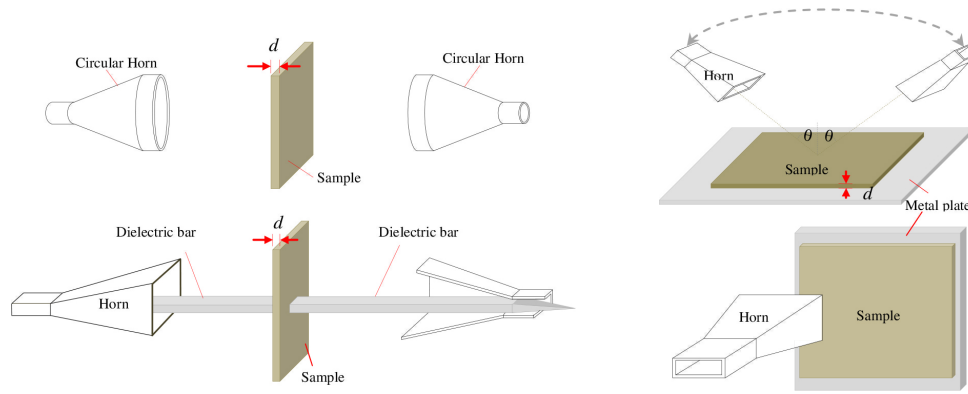


Figure 2.5: Free-space measurement setup for dielectric characterization. Image obtained in [55, 57–59].

drawbacks of this method.

Table 2.3: Advantages and drawbacks of the free space method [53].

Advantages	Drawbacks
<ul style="list-style-type: none"> • Wide frequency range • Non-contacting • Easy sample preparation • Moderate accuracy for high-loss and low-loss • Best for large flat and solid materials • Useful for high temperature 	<ul style="list-style-type: none"> • Diffraction problem (from material edges) • Low end limited by practical sample size

2.2.2.2

Transmission and Reflection Measurement

Another class of non-resonant material characterization methodology uses waveguides for hosting a sample under test. Transmission and reflection (scattering) coefficient measurements are then used for retrieving the constitutive parameters of the sample. Typical, waveguides with rectangular, circular or coaxial cross-section are used, according to the geometry of the MC, it can be categorized as one- or two-ports. In the following, the working mechanisms of rectangular and coaxial MCs will be detailed. 1 A typical coaxial probe used as MC consists of two concentric conductors with radius a and b , and such dimensions imply that only the transverse electromagnetic (TEM) mode is propagating. A typical MC using rectangular waveguides consists of metallic pipe with width b and height a , and it is assumed that only the fundamental TE_{10} mode is propagating.

One-port MCs (as depicted in Fig. 2.6) are the most frequently used into the characterization of lossy materials at high frequencies [61]. The material

characterization is done via measurement data of the reflected parameters S_{11} (with both phase and magnitude information) that will allow us to obtain the material constitutive parameters. This is a simple method and has the advantage of having a broad frequency range, covering from 0.5 GHz to 110 GHz [61]. It is well known that this method performs badly on low-permittivity materials [54], and is only suitable for measuring the relative permittivity ϵ_r . Table 2.4 lists some of the advantages and drawbacks that rectangular MCs present.

Table 2.4: Advantages and drawbacks of the one-port MCs [53].

Advantages	Drawbacks
<ul style="list-style-type: none"> • Broadband frequency • Simple and convenient (nondestructive) • Best for semi-solids or liquids • Simple sample preparation • Isotropic and homogeneous material • High accuracy for high-loss materials 	<ul style="list-style-type: none"> • Air gaps causes errors • Repetitive calibrations needed

Two-port MCs allow to retrieve the parameters ϵ_r and μ_r of a material via measurements of reflection (S_{11}) and transmission (S_{21}) coefficients. A typical setup of such MCs using rectangular and coaxial waveguides is depicted in Fig. 2.7. Since the electromagnetic fields become confined into the waveguide, these MCs typically allow higher accuracy on the material characterization when compared with one-probe counterparts. The theory need to model such devices are derived in the pioneering work of Nicholson and Ross [1]. The main advantage of this characterization technique is that both ϵ_r and μ_r

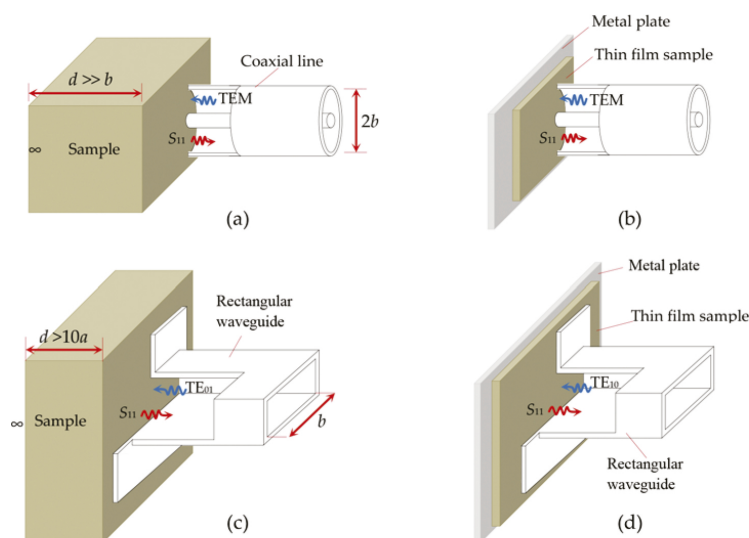


Figure 2.6: Open-ended one-port MCs using coaxial probes in (a) and (b), and using rectangular probes in (c) and (d). Image obtained in [55].

can be retrieved simultaneously [1, 2]. Further details on the advantages and drawbacks this MCs present are listed in Table 2.5.

Table 2.5: Advantages and drawbacks of two-port MCs [53].

Advantages	Drawbacks
<ul style="list-style-type: none"> • High frequency operation • Support for both solids and liquids • Anisotropic material supported 	<ul style="list-style-type: none"> • Cannot use below few GHz due to practical sample length limitation • Sample preparation is difficult (fills fixture cross section)

The math to extract the constitutive parameters of one- and two-ports MCs will be explored in the following.

2.2.3 Material Parameters Extraction

The relation between ϵ_r of a sample and the measured parameter $S_{11a_{sample}}$ of a one-port coaxial MC – with a semi-infinite sample (Fig. 2.6(a)) or with a sample backed by a metal plate (Fig. 2.6(b)) – was obtained via a transmission line model in the work in [62]. Table 2.6 reproduces the main results. Further details on the parameters Y_0 , C , γ_0 , and the coefficients a_1 , a_2 , a_3 can be found in [62–64]. Please note that the reference is considering the time-harmonic dependence in the form $e^{+j\omega t}$.

Table 2.6: Relation between ϵ_r and S_{11} [55].

Sample cases	Open-ended coaxial probe
Semi-infinite space sample (Fig. 2.6(a))	$\epsilon_r = \left(\frac{Y_0}{j\omega C}\right) \left(\frac{1-S_{11a_{sample}}}{1+S_{11a_{sample}}}\right)$
Thin sample backed by metal plate (Fig. 2.6(b))	$\epsilon_r = \left(\frac{Y_0}{j\omega C}\right) \left(\frac{1-S_{11a_{sample}}}{1+S_{11a_{sample}}}\right) \times (a_1 + a_2 e^{-d/M} + a_3 e^{-2d/M})$

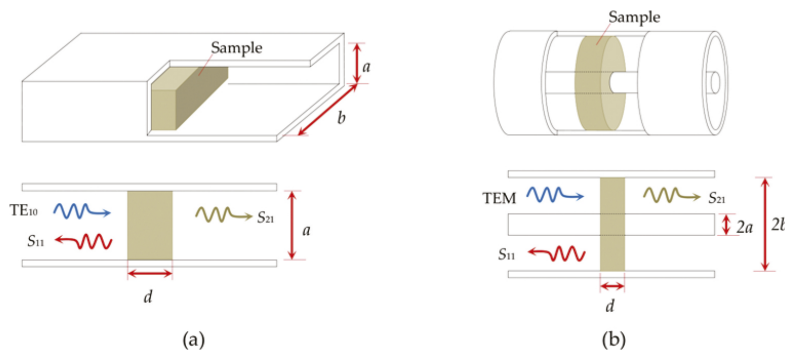


Figure 2.7: Two-port MCs using (a) a rectangular waveguide, and (b) a coaxial transmission line. Image obtained in [55].

The procedure for extracting the ϵ_r of a sample placed inside a rectangular MC is a bit more complicated. First, the measured reflection coefficient is transferred to the normalized admittance Y_a via equation $\tilde{Y}_{a_{sample}} = (1 - S_{11a_{sample}})/(1 + S_{11a_{sample}})$. The value of ϵ_r is then obtained through minimizing the difference between the *measured* normalized admittance $\tilde{Y}_{a_{sample}}$ and the *simulated* one \tilde{Y} . In [63, 64], a quasi-static model provided the formulas to \tilde{Y} shown in Fig. 2.8.

Please note that again the references are using the the time-harmonic dependence factor $e^{+j\omega t}$.

In case of two-port MCs hosting a lossy sample with $\epsilon_r = \epsilon'_r - j\epsilon''_r$ and $\mu_r = \mu'_r - j\mu''_r$, the measured scattering parameters can then fed the Nicholson-Ross-Weird (NRW) process [1, 2]. Pertinent formulas are presented in Fig. ?? for coaxial and rectangular waveguides MCs. For further details, please see [55].

The methods reported above are relatively easily to implement and widely used today. They are, however, restricted to MCs with only one propagation mode. Such mono-mode requirement has a downside effect on the operational bandwidth of the MC. In the following chapter, we will explore semi-analytical solutions for large (overmoded) MCs that remove such constraints. In addition, the model supports lossy uniaxial anisotropic materials, where the sample does not necessarily cover the entire MC cross-section.

Sample cases	Open-ended rectangular waveguide
Semi-infinite space sample (Figure 5c)	$\tilde{Y} = \frac{j8b}{a\gamma_o} \int_0^a \int_0^b \left\{ (a-x) \left\{ D_1(b-y) \cos \frac{\pi y}{b} + D_2 \sin \frac{\pi y}{b} \right\} \times \frac{\exp(-jk_1 \sqrt{x^2 + y^2})}{\sqrt{x^2 + y^2}} \right\} dx dy$
Thin sample backed by metal plate (Figure 5d)	<p>where $D_1 = \frac{1}{b^2} \left(\frac{k_1^2}{4\pi} - \frac{\pi}{4b^2} \right)$, $D_2 = \frac{1}{\pi b} \left(\frac{k_1^2}{4\pi} + \frac{\pi}{4b^2} \right)$, and $k_1 = \frac{2\pi f}{c} \sqrt{\epsilon_r}$</p> $\tilde{Y} = \frac{j8b}{a\gamma_o} \int_0^a \int_0^b \chi \frac{\exp(-jk_1 \sqrt{x^2 + y^2})}{\sqrt{x^2 + y^2}} dx dy$ $+ \frac{j16b}{a\gamma_o} \sum_{n=1}^{\infty} \int_0^a \int_0^b \chi \frac{\exp(-jk_1 \sqrt{x^2 + y^2 + 4n^2 d^2})}{\sqrt{x^2 + y^2 + 4n^2 d^2}} dx dy$ <p>where $\chi = (a-x) \left\{ D_1(b-y) \cos \frac{\pi y}{b} + D_2 \sin \frac{\pi y}{b} \right\}$</p>

Figure 2.8: Integral admittance formulations for open-ended rectangular waveguides. Image obtained in [55].

Table 2.7: Nicholson-Ross-Weird relations.

Waveguide factors	Explicit Equations
Coaxial: $\zeta = 1$	$\epsilon_r = j\zeta \left(\frac{1-\Gamma}{1+\Gamma} \right) \left(\frac{c}{2\pi fd} \right) \ln \left(\frac{1}{T} \right)$
Rectangular: $\zeta = \sqrt{k_0^2 - \left(\frac{\pi}{b} \right)^2}$	$\mu_r = j\frac{1}{\zeta} \left(\frac{1+\Gamma}{1-\Gamma} \right) \left\{ \frac{c}{2\pi fd} \ln \left(\frac{1}{T} \right) \right\}$

3

Electromagnetic Modeling of Cylindrical Waveguides

3.1

Electromagnetic Fields in Uniform Cylindrical Waveguides

In this chapter, we will derive the electromagnetic fields inside inhomogeneous anisotropic cylindrical waveguides, following the mathematical formalism presented in [22, Ch. 3], [65, 66]. Closed-form field solutions are obtained to model radially-layered circular waveguides in terms of cylindrical harmonics. A mode-matching technique (MMT) formulation is used to modeling MCs for uniaxial anisotropic materials. As in the rest of this work, differently from used on chapter 2, we will consider the time-harmonic dependence in the form $e^{-j\omega t}$.

3.1.1

Homogeneous Waveguide

Maxwell's equation in an anisotropic and homogeneous medium can be expressed in the frequency domain as

$$\nabla \times \mathbf{E} = i\omega \bar{\bar{\mu}} \cdot \mathbf{H}, \quad (3-1)$$

$$\nabla \times \mathbf{H} = -i\omega \bar{\bar{\epsilon}} \cdot \mathbf{E} + \mathbf{J}, \quad (3-2)$$

$$\nabla \cdot (\bar{\bar{\epsilon}} \cdot \mathbf{E}) = \rho, \quad (3-3)$$

$$\nabla \cdot (\bar{\bar{\mu}} \cdot \mathbf{H}) = 0, \quad (3-4)$$

where the permeability and permittivity tensors expressed in cylindrical coordinates (ρ, ϕ, z) are given by

$$\bar{\bar{\epsilon}} = \begin{bmatrix} \epsilon_s & 0 & 0 \\ 0 & \epsilon_s & 0 \\ 0 & 0 & \epsilon_z \end{bmatrix} \quad \text{and} \quad \bar{\bar{\mu}} = \begin{bmatrix} \mu_s & 0 & 0 \\ 0 & \mu_s & 0 \\ 0 & 0 & \mu_z \end{bmatrix}. \quad (3-5)$$

The subscript s indicates the coordinates transversal to z and

$$\epsilon_{\{s,z\}} = \epsilon_0 \epsilon_{r\{s,z\}} + i \frac{\sigma_{\{s,z\}}}{\omega}, \quad (3-6)$$

$$\mu_{\{s,z\}} = \mu_0 \mu_{r\{s,z\}}, \quad (3-7)$$

where σ is the electrical conductivity of the medium and may be expressed as the following tensor

$$\bar{\sigma} = \begin{bmatrix} \sigma_s & 0 & 0 \\ 0 & \sigma_s & 0 \\ 0 & 0 & \sigma_z \end{bmatrix}. \quad (3-8)$$

After some mathematical manipulations reported in [65, 66], we obtain the following wave equations for the axial electric and magnetic fields

$$\left(\nabla_s^2 + \frac{\epsilon_z}{\epsilon_s} \frac{\partial^2}{\partial z^2} + \omega^2 \mu_s \epsilon_z \right) E_z = 0, \quad (3-9)$$

$$\left(\nabla_s^2 + \frac{\mu_z}{\mu_s} \frac{\partial^2}{\partial z^2} + \omega^2 \mu_z \epsilon_s \right) H_z = 0, \quad (3-10)$$

These equations can be rewritten in a more compact fashion via

$$\left[\frac{1}{\rho} \frac{\partial}{\partial \rho} \left(\rho \frac{\partial}{\partial \rho} \right) + \frac{1}{\rho^2} \frac{\partial^2}{\partial \phi^2} + \frac{p_z}{p_s} \frac{\partial^2}{\partial z^2} + \omega^2 p_z \tilde{p}_s \right] \psi = 0, \quad (3-11)$$

where $\psi = \{E_z, H_z\}$, $p = \{\epsilon, \mu\}$ and $\tilde{p} = \{\mu, \epsilon\}$. Using the separation of variables method [67], we have that the solution is in the form

$$R_n \left(\sqrt{\frac{p_z}{p_s}} k_\rho \rho \right) \Phi(n\phi) Z(k_z z), \quad (3-12)$$

in which $R_n(\cdot)$ is the solution for the Bessel differential equation of order n , and $\Phi(n\phi)$ and $Z(k_z z)$ are harmonic functions. The values of n , k_ρ and k_z are determined by the boundary conditions enforcement.

The solution for ψ can then be written as a linear combination of the elementary function in (3-12), i.e.,

$$\psi = \sum_n \sum_{k_z} C_{n,k_z} R_n \left(\sqrt{\frac{p_z}{p_s}} k_\rho \rho \right) \Phi(n\phi) Z(k_z z), \quad (3-13)$$

where C_{n,k_z} are constants to be determined and

$$R_n \left(k_\rho^{e,h} \rho \right) = a^{e,h} H_n^{(1)}(k_\rho^{e,h} \rho) + b^{e,h} J_n(k_\rho^{e,h} \rho), \quad (3-14)$$

$$\Phi(n\phi) = e^{in\phi}, \text{ for } n = 0, \pm 1, \pm 2, \dots, \quad (3-15)$$

$$Z(k_z z) = e^{ik_z z}, \quad (3-16)$$

where $J_n(\cdot)$ and $H_n^{(1)}(\cdot)$ are first kind Bessel and Hankel functions of integer order n , $a^{e,h}$ and $b^{e,h}$ are modal amplitudes, $k_s^2 + k_z^2 = k_\rho^2$, and $k_\rho^{e,h} = (p_z/p_s)^{1/2} k_\rho$. The square-root branch-cut is selecting according to $\Im m(k_\rho^{e,h}) \geq 0$ and $\Im m(k_z) \geq 0$. The superscripts e, h indicate the correspondence for the axial electric and magnetic fields, respectively.

Following the matrix notation from [22, 65], longitudinal fields can be

written as

$$\begin{bmatrix} E_z \\ H_z \end{bmatrix} = \sum_{n=-\infty}^{\infty} \sum_{p=1}^{\infty} \begin{bmatrix} e_{z,np}(\rho) \\ h_{z,np}(\rho) \end{bmatrix} e^{in\phi} e^{ik_z z} \quad (3-17)$$

where p is related to the modal eigenvalues k_z and k_ρ . The ρ -dependent parcel of the fields are written as

$$\begin{bmatrix} e_z(\rho) \\ h_z(\rho) \end{bmatrix} = \bar{\bar{H}}_{zn}^{(1)}(k_\rho \rho) \bar{a} + \bar{\bar{J}}_{zn}(k_\rho \rho) \bar{b}, \quad (3-18)$$

where

$$\bar{\bar{G}}_{zn}(k_\rho \rho) = \begin{bmatrix} G_n(k_\rho^e \rho) & 0 \\ 0 & G_n(k_\rho^h \rho) \end{bmatrix}, \quad (3-19)$$

with $G_n = \{H_n^{(1)}, J_n\}$, and the vectors \bar{a} and \bar{b} (that combine the modal amplitudes) are arranged as

$$\bar{a} = \begin{bmatrix} a_{np}^e \\ a_{np}^h \end{bmatrix} \quad \text{and} \quad \bar{b} = \begin{bmatrix} b_{np}^e \\ b_{np}^h \end{bmatrix}. \quad (3-20)$$

Manipulating the Maxwell's equation in a source-free regions, the transversal fields can be written as [65, 66]:

$$\mathbf{E}_s = \frac{1}{k_\rho^2} [ik_z \nabla_s E_z + i\omega \mu_s \nabla_s \times (\hat{z} H_z)], \quad (3-21)$$

$$\mathbf{H}_s = \frac{1}{k_\rho^2} [ik_z \nabla_s H_z - i\omega \epsilon_s \nabla_s \times (\hat{z} E_z)], \quad (3-22)$$

where the ρ -dependent parcel is expressed as

$$\begin{bmatrix} e_{\phi,np}(\rho) \\ h_{\phi,np}(\rho) \end{bmatrix} = \bar{\bar{H}}_{\phi n}^{(1)}(k_\rho \rho) \bar{a} + \bar{\bar{J}}_{\phi n}(k_\rho \rho) \bar{b}, \quad (3-23)$$

$$\begin{bmatrix} e_{\rho,np}(\rho) \\ h_{\rho,np}(\rho) \end{bmatrix} = \bar{\bar{H}}_{\rho n}^{(1)}(k_\rho \rho) \bar{a} + \bar{\bar{J}}_{\rho n}(k_\rho \rho) \bar{b}, \quad (3-24)$$

where

$$\bar{\bar{G}}_{\phi n}(k_\rho \rho) = \frac{1}{k_\rho^2 \rho} \begin{bmatrix} -nk_z G_n(k_\rho^e \rho) & -i\omega \mu_s k_\rho^h \rho G_n'(k_\rho^h \rho) \\ i\omega \epsilon_s k_\rho^e \rho G_n'(k_\rho^e \rho) & -nk_z G_n(k_\rho^h \rho) \end{bmatrix}, \quad (3-25)$$

$$\bar{\bar{G}}_{\rho n}(k_\rho \rho) = \frac{1}{k_\rho^2 \rho} \begin{bmatrix} ik_z k_\rho^e \rho G_n'(k_\rho^e \rho) & -n\omega \mu_s G_n(k_\rho^h \rho) \\ n\omega \epsilon_s G_n(k_\rho^e \rho) & ik_z k_\rho^h \rho G_n'(k_\rho^h \rho) \end{bmatrix}. \quad (3-26)$$

In the above, $G_n'(\cdot)$ is denoting the derivative of $G_n(\cdot)$ with respect to its argument.

3.1.2 Inhomogeneous Waveguide

Consider now a waveguide with N radial layers defined by the radii $\{\rho_0, \rho_1, \dots, \rho_N\}$. The ρ -dependent parcel of the fields in the layer j can be written as

$$\begin{bmatrix} e_{j\alpha}(\rho) \\ h_{j\alpha}(\rho) \end{bmatrix} = \bar{\bar{H}}_{\alpha n}^{(1)}(k_{j\rho}\rho)\bar{a}_j + \bar{\bar{J}}_{\alpha n}(k_{j\rho}\rho)\bar{b}_j, \quad (3-27)$$

where $\alpha = \{\rho, \phi, z\}$ and j is the waveguide layer varying from 1 to N . Applying the boundary conditions of continuity of z - and ϕ -field components at the interfaces between layer j and its adjacency, we can obtain the determinantal characteristic equation is [65, 66]

$$f(k_z) = \det \left(\bar{I} - \bar{\bar{R}}_{j,j+1}^{(\rho)} \bar{\bar{R}}_{j,j-1}^{(\rho)} \right) = 0. \quad (3-28)$$

Where the generalized reflection matrices $\bar{\bar{R}}_{j,j+1}^{(\rho)}$ and $\bar{\bar{R}}_{j,j-1}^{(\rho)}$ are 2-by-2 matrix given by [22, 65]

$$\bar{\bar{R}}_{j,j\pm 1}^{(\rho)} = \bar{\bar{R}}_{j,j\pm 1}^{(\rho)} + \bar{\bar{T}}_{j\pm 1,j}^{(\rho)} \bar{\bar{R}}_{j\pm 1,j\pm 2}^{(\rho)} \left(\bar{I} - \bar{\bar{R}}_{j\pm 1,j}^{(\rho)} \bar{\bar{R}}_{j\pm 1,j\pm 2}^{(\rho)} \right)^{-1} \bar{\bar{T}}_{j,j\pm 1}^{(\rho)} \quad (3-29)$$

where \bar{I} is the identity matrix. The local transmission and reflection matrices are defined according to

$$\bar{\bar{R}}_{j,j+1}^{(\rho)} = \bar{D}_{ja}^{-1} \left[\bar{\bar{H}}_{\phi j+1,j} \bar{\bar{H}}_{zj,j} - \bar{\bar{H}}_{\phi j+1,j} \bar{\bar{H}}_{zj+1,j} \bar{\bar{H}}_{\phi j+1,j}^{-1} \bar{\bar{H}}_{\phi j,j} \right] \quad (3-30)$$

$$\bar{\bar{R}}_{j+1,j}^{(\rho)} = \bar{D}_{jb}^{-1} \left[\bar{\bar{J}}_{\phi j,j} \bar{\bar{J}}_{zj,j} \bar{\bar{J}}_{\phi j,j}^{-1} - \bar{\bar{J}}_{\phi j,j} \bar{\bar{J}}_{zj+1,j} \right] \quad (3-31)$$

$$\bar{\bar{T}}_{j,j+1}^{(\rho)} = \bar{D}_{jb}^{-1} \left[\bar{\bar{J}}_{\phi j,j} \bar{\bar{H}}_{zj,j} - \bar{\bar{J}}_{\phi j,j} \bar{\bar{J}}_{zj,j} \bar{\bar{J}}_{\phi j,j}^{-1} \bar{\bar{H}}_{\phi j,j} \right] \quad (3-32)$$

$$\bar{\bar{T}}_{j+1,j}^{(\rho)} = \bar{D}_{ja}^{-1} \left[\bar{\bar{H}}_{\phi j+1,j} \bar{\bar{H}}_{zj+1,j} \bar{\bar{H}}_{\phi j+1,j}^{-1} \bar{\bar{J}}_{\phi j+1,j} - \bar{\bar{H}}_{\phi j+1,j} \bar{\bar{J}}_{zj+1,j} \right] \quad (3-33)$$

$$\bar{D}_{ja} = \bar{\bar{H}}_{\phi j+1,j} \bar{\bar{H}}_{zj+1,j} \bar{\bar{H}}_{\phi j+1,j}^{-1} \bar{\bar{J}}_{\phi j,j} - \bar{\bar{H}}_{\phi j+1,j} \bar{\bar{J}}_{zj,j} \quad (3-34)$$

$$\bar{D}_{jb} = \bar{\bar{J}}_{\phi j,j} \bar{\bar{H}}_{zj+1,j} - \bar{\bar{J}}_{\phi j,j} \bar{\bar{J}}_{zj,j} \bar{\bar{J}}_{\phi j,j}^{-1} \bar{\bar{H}}_{\phi j+1,j} \quad (3-35)$$

And each value of k_z that satisfy the above equation 3-28 is a *modal solution* for the problem at hand. Once k_z is known, we can obtain the modal amplitudes \bar{a}_j and \bar{b}_j for each layer j . Further details can be found in [65].

3.2 Mode-Matching Technique

The mode-matching technique (MMT) is a semi-analytic method which allows us to analyze the junction between two connected waveguides [22, Ch. 6], [23], as depicted in Fig. 3.1. With this method we can obtain closed-form solutions for relating the forward and backward propagating waves at the $z = z_1$ and then extract a generalized scattering matrix (GSM) representation

of this junctions. Multi-region structures formed can be modeled by cascading the GSM matrices of each junction. Here, we will follow the mathematical procedures developed in [65, 66].

We start considering a homogeneous coaxial waveguide junction, as seen in Fig. 3.1, where S_a is the common aperture between the two waveguides, S_1 is the cross-section of region 1 and S_2 of region 2. In addition, we have $S_1 = S_a$, $S_2 = S_a + S_w$ and S_w is the surface of an impedance wall. As we will consider all walls as PECs, we have $Z_{2w} = 0$. As in [66], we also assume that $S_1 \in S_2$.

From [65], we have that the transversal fields derived in the previous section can be rewritten as

$$\mathbf{E}_{js} = \sum_{n=-\infty}^{\infty} \sum_{p=1}^{\infty} \left(a_{j,np}^+ e^{+ik_{jz,np}z} + a_{j,np}^- e^{-ik_{jz,np}z} \right) \mathbf{e}_{js,np}(\rho) e^{in\phi}, \quad \text{and} \quad (3-36)$$

$$\mathbf{H}_{js} = \sum_{n'=-\infty}^{\infty} \sum_{p'=1}^{\infty} \left(a_{j,n'p'}^+ e^{+ik_{jz,n'p'}z} - a_{j,n'p'}^- e^{-ik_{jz,n'p'}z} \right) \mathbf{h}_{js,n'p'}(\rho) e^{in\phi} \quad (3-37)$$

which can be simplified to

$$\mathbf{E}_{js} = \sum_m^{\infty} \left(A_{j,m}^+ + A_{j,m}^- \right) \mathbf{E}_{js,m} \quad \text{and} \quad (3-38)$$

$$\mathbf{H}_{js} = \sum_{m'}^{\infty} \left(A_{j,m'}^+ - A_{j,m'}^- \right) \mathbf{H}_{js,m'} \quad (3-39)$$

where $A_{j,m}^+$ and $A_{j,m}^-$ are the forward and backward modal amplitudes at the interface in $z = z_1$ expressed by $A_{j,m}^{\pm} = a_{j,m}^{\pm} e^{\pm ik_{jz,m}z_1}$ and j represents the region (1 or 2). Also, from [66], it can be shown that at the plane $z = z_1$, the

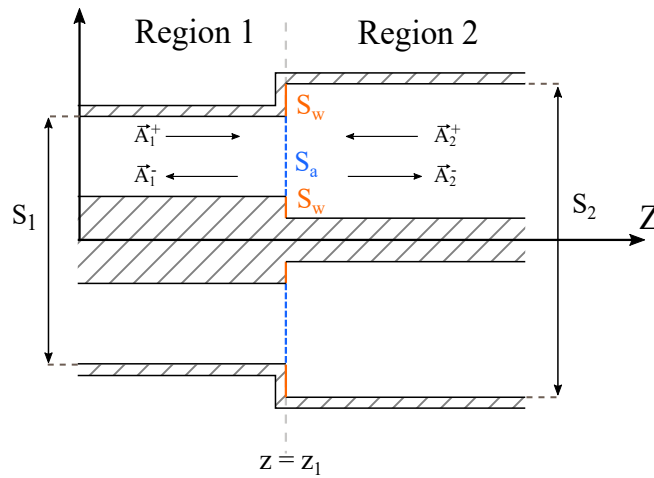


Figure 3.1: Junction of two homogeneous coaxial waveguides. Image obtained in [66].

following boundary conditions have to be satisfied:

$$\hat{z} \times \mathbf{E}_{2s} = \hat{z} \times \mathbf{E}_{1s}, \quad \text{in } S_a \quad (3-40)$$

$$\hat{z} \times \mathbf{H}_{2s} = \hat{z} \times \mathbf{H}_{1s}, \quad \text{in } S_a. \quad (3-41)$$

After some mathematical manipulations, we obtain the following GSM for relating incident and reflected waves [65, 66]:

$$\begin{bmatrix} \bar{A}_1^- \\ \bar{A}_2^+ \end{bmatrix} = \begin{bmatrix} \bar{\bar{S}}_{11} & \bar{\bar{S}}_{12} \\ \bar{\bar{S}}_{21} & \bar{\bar{S}}_{22} \end{bmatrix} \begin{bmatrix} \bar{A}_1^+ \\ \bar{A}_2^- \end{bmatrix} \quad (3-42)$$

where the scattering sub-matrices are

$$\bar{\bar{S}}_{11} = \left[\bar{\bar{Q}}_1 + \bar{\bar{X}}_{12}^t (\bar{\bar{Q}}_2)^{-1} \bar{\bar{X}}_{12} \right]^{-1} \left[\bar{\bar{Q}}_1 - \bar{\bar{X}}_{12}^t (\bar{\bar{Q}}_2)^{-1} \bar{\bar{X}}_{12} \right], \quad (3-43)$$

$$\bar{\bar{S}}_{12} = 2 \left[\bar{\bar{Q}}_1 + \bar{\bar{X}}_{12}^t (\bar{\bar{Q}}_2)^{-1} \bar{\bar{X}}_{12} \right]^{-1} \bar{\bar{X}}_{12}^t, \quad (3-44)$$

$$\bar{\bar{S}}_{21} = 2 \left[\bar{\bar{Q}}_2 + \bar{\bar{X}}_{12} (\bar{\bar{Q}}_1)^{-1} \bar{\bar{X}}_{12}^t \right]^{-1} \bar{\bar{X}}_{12}, \quad (3-45)$$

$$\bar{\bar{S}}_{22} = - \left[\bar{\bar{Q}}_2 + \bar{\bar{X}}_{12} (\bar{\bar{Q}}_1)^{-1} \bar{\bar{X}}_{12}^t \right]^{-1} \left[\bar{\bar{Q}}_2 - \bar{\bar{X}}_{12} (\bar{\bar{Q}}_1)^{-1} \bar{\bar{X}}_{12}^t \right]. \quad (3-46)$$

The expressions to determine the matrices $\bar{\bar{Q}}_1$, $\bar{\bar{Q}}_2$ and $\bar{\bar{X}}_{12}$ are obtained solving Lommel integrals and can be found with details in [65, 66, 68]. In the case where we have N_1 layers in region 1 and N_2 layers in region 2, some adjustments must be done to calculate these integrals.

Considering the case where the structure has more than two waveguide regions, as depicted in Fig. 3.2, the overall GSM can be calculated by cascading the intermediate GSM of a) the junction from regions 1 to 2, b) the GSM of the finite-length waveguide in region 2, and c) the junction from regions 2 to 3.

For a pair of subsequent GSMs denoted by $\bar{\bar{S}}^a$ and $\bar{\bar{S}}^b$, the resultant (cascaded) matrix $\bar{\bar{S}}^c$ is given by [23, 65, 66, 69]

$$\bar{\bar{S}}^c = \begin{bmatrix} \bar{\bar{S}}_{11}^c & \bar{\bar{S}}_{12}^c \\ \bar{\bar{S}}_{21}^c & \bar{\bar{S}}_{22}^c \end{bmatrix}, \quad (3-47)$$

where

$$\bar{\bar{S}}_{11}^c = \bar{\bar{S}}_{12}^a \left(\bar{\bar{I}} - \bar{\bar{S}}_{11}^b \bar{\bar{S}}_{22}^a \right)^{-1} \bar{\bar{S}}_{11}^b \bar{\bar{S}}_{21}^a + \bar{\bar{S}}_{11}^a, \quad (3-48)$$

$$\bar{\bar{S}}_{12}^c = \bar{\bar{S}}_{12}^a \left(\bar{\bar{I}} - \bar{\bar{S}}_{11}^b \bar{\bar{S}}_{22}^a \right)^{-1} \bar{\bar{S}}_{12}^b, \quad (3-49)$$

$$\bar{\bar{S}}_{21}^c = \bar{\bar{S}}_{21}^b \left(\bar{\bar{I}} - \bar{\bar{S}}_{22}^a \bar{\bar{S}}_{11}^b \right)^{-1} \bar{\bar{S}}_{21}^a, \quad (3-50)$$

$$\bar{\bar{S}}_{22}^c = \bar{\bar{S}}_{21}^b \left(\bar{\bar{I}} - \bar{\bar{S}}_{22}^a \bar{\bar{S}}_{11}^b \right)^{-1} \bar{\bar{S}}_{22}^a \bar{\bar{S}}_{12}^b + \bar{\bar{S}}_{22}^b, \quad (3-51)$$

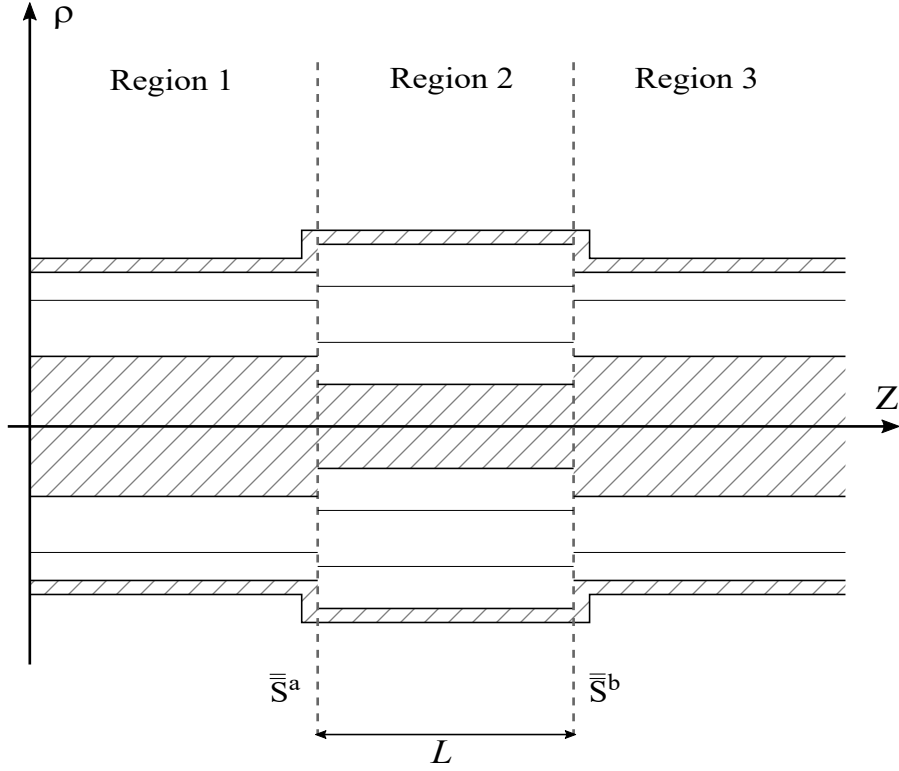


Figure 3.2: Structure with three regions. Image obtained in [66].

where the intermediary waveguide in region 2 has a scattering matrix associated to its length L and its eigenvalues k_z via [68]

$$\bar{\bar{S}}^g = \begin{bmatrix} \bar{0} & \bar{\bar{S}}_{12}^g \\ \bar{\bar{S}}_{12}^g & \bar{0} \end{bmatrix}, \quad (3-52)$$

where $\bar{\bar{S}}_{12}^g$ is a diagonal matrix that relates the axial propagation along the length L , whose elements are given by $\bar{\bar{S}}_{12}^g|_{m,m} = e^{ik_{2z,m}L}$. In addition, a normalization was made in this GSM matrix to ensure an independence from the field amplitudes according to [23, 70, 71]

$$\hat{\hat{S}}_{11}^c = \text{abs}(\bar{\bar{Q}}_1)^{1/2} \bar{\bar{S}}_{11}^c \text{abs}(\bar{\bar{Q}}_1)^{-1/2} \quad (3-53)$$

$$\hat{\hat{S}}_{12}^c = \text{abs}(\bar{\bar{Q}}_1)^{1/2} \bar{\bar{S}}_{12}^c \text{abs}(\bar{\bar{Q}}_2)^{-1/2} \quad (3-54)$$

$$\hat{\hat{S}}_{21}^c = \text{abs}(\bar{\bar{Q}}_2)^{1/2} \bar{\bar{S}}_{21}^c \text{abs}(\bar{\bar{Q}}_1)^{-1/2} \quad (3-55)$$

$$\hat{\hat{S}}_{22}^c = \text{abs}(\bar{\bar{Q}}_2)^{1/2} \bar{\bar{S}}_{22}^c \text{abs}(\bar{\bar{Q}}_2)^{-1/2}. \quad (3-56)$$

3.2.1 PEC-Truncation Scattering Matrix

In what follows we will obtain the scattering matrix of a PEC plate covering the waveguide cross-section for $z > z_{\text{PEC}}$. If the conductor is placed in region $j + 1$, the boundary conditions require the vanishing of transversal electric fields of region j at $z = z_{\text{PEC}}$, i.e., in view of (3-36)–(3-39), we must enforce

$$\mathbf{E}_{js}|_{z=z_{\text{PEC}}} = \sum_m^{\infty} \left(a_{j,m}^+ e^{+ik_{jz,m}z_{\text{PEC}}} + a_{j,m}^- e^{-ik_{jz,m}z_{\text{PEC}}} \right) \mathbf{E}_{js,m} \quad (3-57)$$

$$= \mathbf{0}. \quad (3-58)$$

Denoting $A_{j,m}^{+\text{PEC}} = a_{j,m}^+ e^{+ik_{jz,m}z_{\text{PEC}}}$ and $A_{j,m}^{-\text{PEC}} = a_{j,m}^- e^{-ik_{jz,m}z_{\text{PEC}}}$ as the forward and backward modal amplitudes at the PEC interface, respectively, the above requires $A_{j,m}^{-\text{PEC}} = -A_{j,m}^{+\text{PEC}}$. We can now establish a GSM representation of the PEC plate, similar to the canonical form in (3-42), given by

$$\begin{bmatrix} \bar{A}_j^{-\text{PEC}} \\ \bar{A}_{j+1}^{+\text{PEC}} \end{bmatrix} = \bar{\bar{S}}^{\text{PEC}} \begin{bmatrix} \bar{A}_j^{+\text{PEC}} \\ \bar{A}_{j+1}^{-\text{PEC}} \end{bmatrix}, \quad (3-59)$$

where

$$\bar{\bar{S}}^{\text{PEC}} = \begin{bmatrix} -\bar{\bar{I}} & \bar{\bar{0}} \\ \bar{\bar{0}} & \bar{\bar{0}} \end{bmatrix}. \quad (3-60)$$

3.3 Perfectly Matched Layer for Representing Unbounded Domains

The ordinary MMT we have explored before in Sec. 3.2 cannot be used for the analysis of an open-ended waveguide, as the one depicted in Fig. 3.3, because region 2 is a radially-unbounded domain and requires a dense spectrum of eigenvalue solutions. In short, the discrete sum of modal fields in (3-36) and (3-37) do not converge. We can, however, truncate the region 2 using an appropriated absorbing boundary condition at $\rho = r_N$ and then handling a discrete set of modal fields into the MMT formulation. We will use a perfectly matched layer (PML) [27, 28] to truncate our problem because the complex-coordinate stretching formulation of the PML enable us to reuse the closed-form eigenmode expressions and the MMT formulas already presented. The radial domain can be mapped according to [65, 72]

$$\tilde{\rho} = \begin{cases} \rho, & \text{for } \rho < r_{\text{PML}} \\ \rho + i \frac{\alpha_{\text{PML}}}{\omega} \frac{\rho - r_{\text{PML}}}{r_N - r_{\text{PML}}}, & \text{for } r_{\text{PML}} \leq \rho \leq r_N \end{cases}. \quad (3-61)$$

In the above, we consider the radial domain is truncated with a hard wall at $\rho = r_N$, and the PML spans over (the real-valued domain) $r_{\text{PML}} < \rho < r_N$. The positive and real-valued parameter α_{PML} is used here to confer an attenuation to outgoing waves inside the PML layer. Notice also the imaginary parcel of $\tilde{\rho}$ is normalized by ω in order to force an effective absorbance over the frequency.

Since closed-form formulas are available for solving fields and coupling in the MMT, the previously-derived equations can be reused under the analytical continuation in (3-61) [65], where the outermost radius of the waveguide becomes

$$r_N \rightarrow \tilde{r}_N = r'_N + ir''_N. \quad (3-62)$$

The value of $r'_N = r_N$ must be large enough to guarantee the attenuation of evanescent fields, while $r''_N = \alpha_{\text{PML}}/\omega$ must guarantee the effective absorbance of outgoing waves. Accordingly, the open-ended waveguide depicted in Fig. 3.3 can be mimicked by the equivalent structure shown in Fig. 3.4.

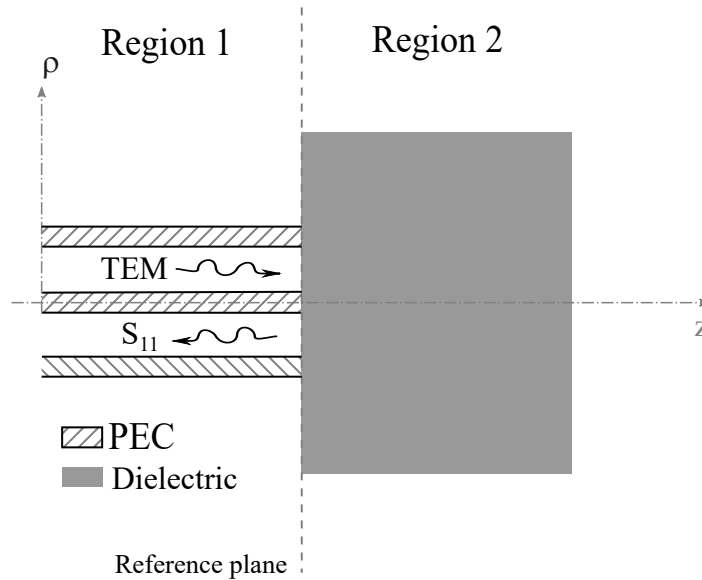


Figure 3.3: Geometry of an open-ended coaxial waveguide.

PUC-Rio - Certificação Digital N° 2012321/CA

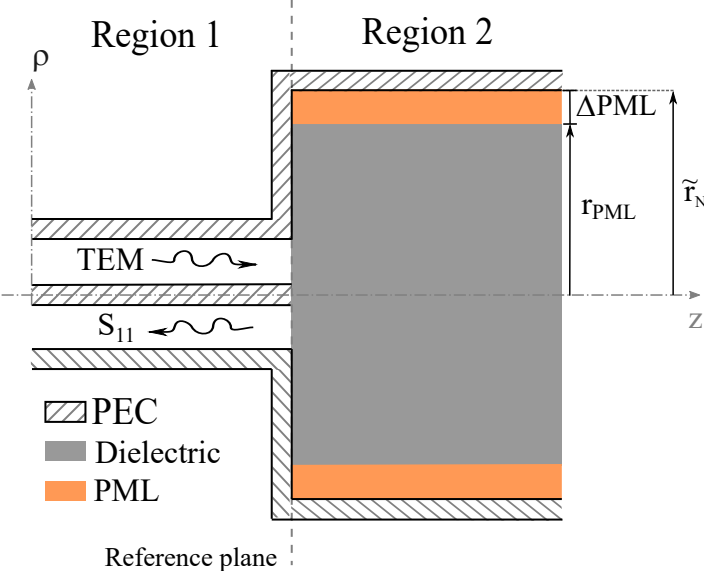


Figure 3.4: Equivalent problem used to emulate the open-ended coaxial waveguide.

4

Determination of the Constitutive Parameters of Complex Media

In this chapter, we will use the mode-matching solutions formulated in Chapter 3 for analyzing the electromagnetic fields along cylindrical structures formed by (a) the junction of sections of inhomogeneous-filled waveguides that represents a two-port measurement cell (see Fig. 4.1), (b) one-port measurement cells (see Fig. 4.4), and (c) open-ended coaxial measurement cells (see Fig. 4.8). The time-harmonic factor $e^{-i\omega t}$ is again assumed and suppressed.

We consider the waveguides used in the measurement cells are, in general, filled with non-magnetic anisotropic media characterized by the complex permittivity tensor $\bar{\bar{\epsilon}} = \epsilon_0 \bar{\bar{\epsilon}}_r + i\bar{\bar{\sigma}}/\omega$, where $\epsilon_0 \approx 8.85 \times 10^{-12}$ F/m and the relative permittivity and electrical conductivity represented in cylindrical coordinates are

$$\bar{\bar{\epsilon}}_r = \begin{bmatrix} \epsilon_{rs} & 0 & 0 \\ 0 & \epsilon_{rs} & 0 \\ 0 & 0 & \epsilon_{rz} \end{bmatrix}, \quad \bar{\bar{\sigma}} = \begin{bmatrix} \sigma_s & 0 & 0 \\ 0 & \sigma_s & 0 \\ 0 & 0 & \sigma_z \end{bmatrix}, \quad (4-1)$$

respectively. For convenience, subscripts s and z will be used to indicate components transversal and parallel to the axis z , respectively.

4.1

Direct Problem

In this section we present numerical results obtained from an implemented algorithm of the theory described in Chapters 2 and 3. We assume the measurement cells' geometry and media (permittivity and permeability) are known, and the scattering matrix are then be obtained. This *direct algorithm* will then be used in Section 4.2 into an iterative optimization process (the *inverse algorithm*) that finds the material parameters that best approach the measured scattering parameters.

4.1.1 Two-Port Measurement Cells

We first consider a two-port measurement cell as depicted in Fig. 4.1. To validate this case, we will consider a geometry with the parameters shown in Table 4.1

Table 4.1: Simulation parameters for the case depicted in Fig. 4.1.

Region	ρ_0 (mm)	ρ_1 (mm)	ρ_2 (mm)	ϵ_{rs} –	ϵ_{rz} –	σ_s (S/m)	σ_z (S/m)
1	1.84	2.00	5.00	1.00	1.00	0.00	0.00
2	1.84	3.92	6.00	2.55	3.00	0.10	0.02
3	1.84	2.00	5.00	1.00	1.00	0.00	0.00

The scattering parameters of a two-port MC can be solved on progressively cascading the GSMs that describe the longitudinal geometry. In case of a tree-region MC as depicted in Fig. 4.1 and according to Table 4.1, the overall resultant GSM relating the input and output regions can be symbolic represented by

$$\bar{\bar{S}}^{2\text{-ports}} = \bar{\bar{S}}^{1 \rightarrow 2} \star \bar{\bar{S}}^{g^2} \star \bar{\bar{S}}^{2 \rightarrow 3}, \quad (4-2)$$

where the symbol \star represents the cascading operation mathematically defined in (3-47), the generalized scattering matrix (GSM) are written as $\bar{\bar{S}}^{j \rightarrow j+1}$ for relating the junction between regions j and $j + 1$ and $\bar{\bar{S}}^{g^2}$ is scattering matrix associated with an uniform waveguide of finite longitudinal length L_2 . In this scenario, the sample material is partially filling region 2 and the reflection and transmission coefficient for the fundamental mode calculated via the finite integral technique (FIT) solver from [73] and via the MMT are compared in Fig. 4.2 and Fig. 4.3 respectively. We can observe that our technique has a good agreement towards the FIT.

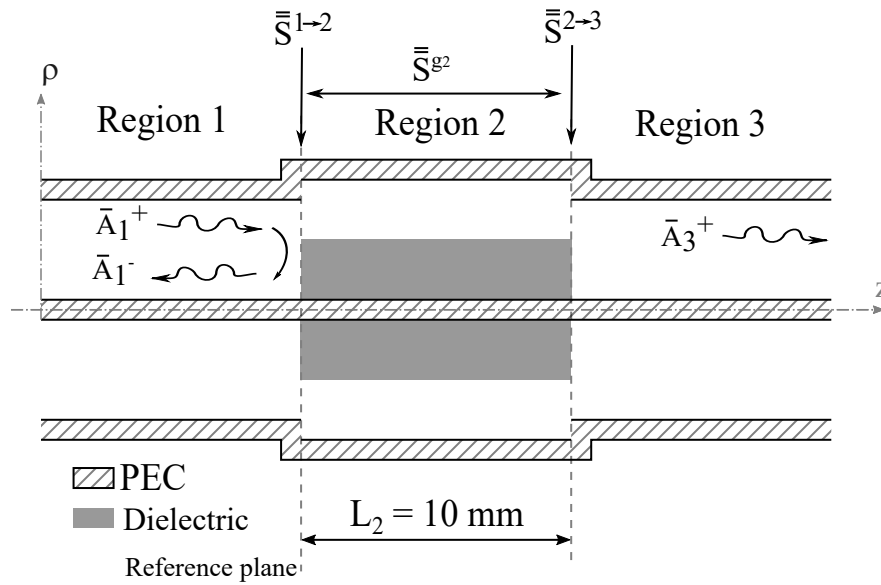


Figure 4.1: Geometry of a cylindrical structure with three waveguide regions. The PEC is represented by the hatched areas. The sample material is the dielectric partially filling region 2

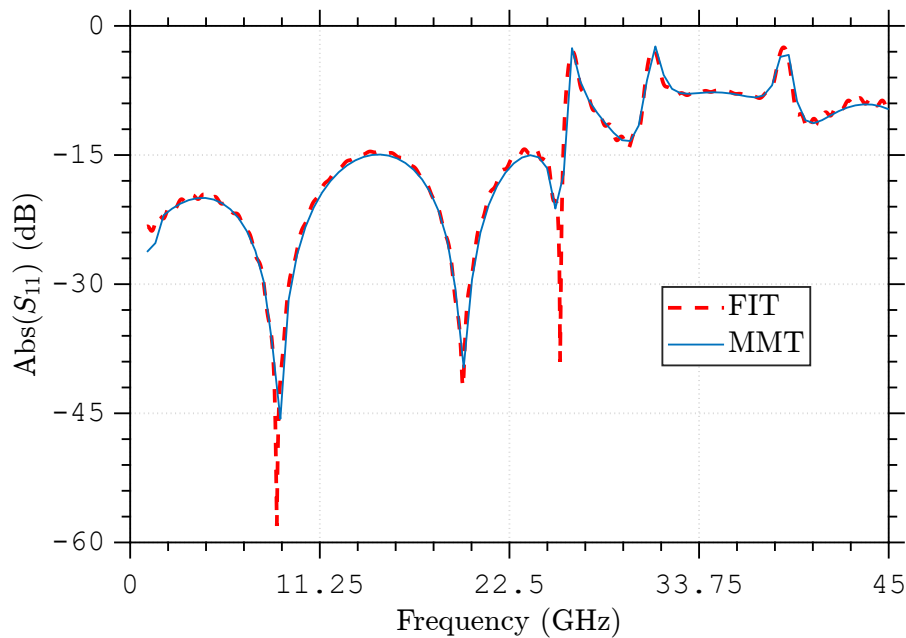


Figure 4.2: Reflection coefficient in decibel for the fundamental mode in region 1 as a function of the frequency for the two-port measurement cell. The results from the present algorithm are indicated by the solid line while FIT results from [73] are the dashed-line.

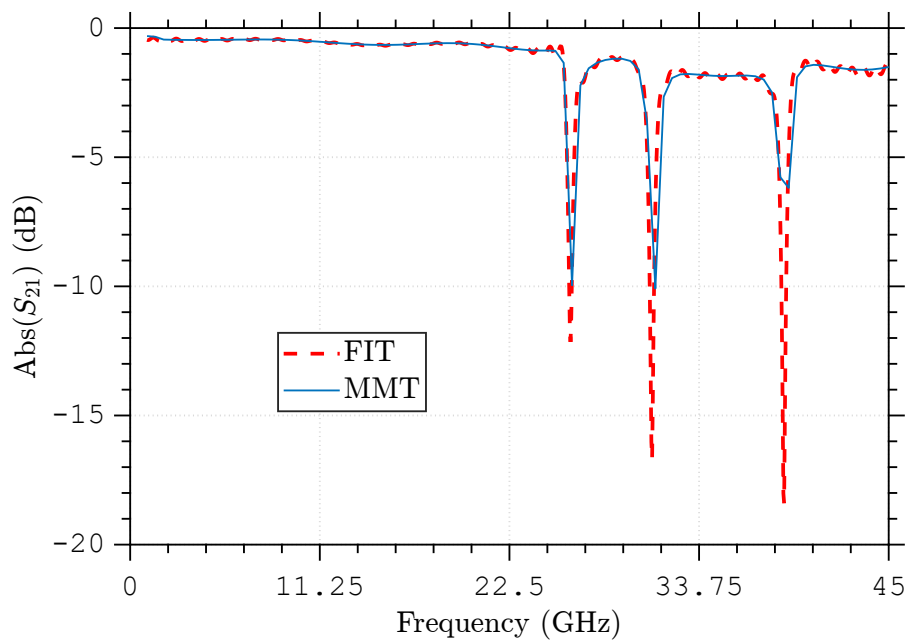


Figure 4.3: Transmission coefficient in decibel for the fundamental mode in region 1 as a function of the frequency for the two-port measurement cell. The results from the present algorithm are indicated by the solid line while FIT results from [73] are the dashed-line.

4.1.2 One-Port Measurement Cells

We consider now a one-port MC, as depicted Fig. 4.4. A simplified model setup, when compared to the two-port cell, is also possible when the output port is short-circuited by a PEC. The GSM matrix representation of this cell is constructed by first cascading the GSM of the PEC place $\bar{\bar{S}}^{\text{PEC}}$ with $\bar{\bar{S}}^{g3}$ defined as a scattering matrix associated with an uniform waveguide of finite longitudinal length L_3 . According to the equations in (3-48), $\bar{\bar{S}}^{\text{PEC}}$ becomes $\bar{\bar{S}}^b$ and $\bar{\bar{S}}^{g3}$ will be $\bar{\bar{S}}^a$, yielding

$$\bar{\bar{S}}_{11}^c = \bar{\bar{S}}_{12}^{g3} \bar{\bar{S}}_{11}^{\text{PEC}} \bar{\bar{S}}_{21}^{g3}, \quad (4-3)$$

$$\bar{\bar{S}}_{12}^c = \bar{\bar{0}}, \quad (4-4)$$

$$\bar{\bar{S}}_{21}^c = \bar{\bar{0}}, \quad (4-5)$$

$$\bar{\bar{S}}_{22}^c = \bar{\bar{0}}. \quad (4-6)$$

Next, we cascade the resulting matrix with the GSM for two-port cell:

$$\bar{\bar{S}}_{11}^{1\text{-port}} = \bar{\bar{S}}_{12}^a \left(\bar{\bar{I}} - \bar{\bar{S}}_{11}^c \bar{\bar{S}}_{22}^a \right)^{-1} \bar{\bar{S}}_{11}^c \bar{\bar{S}}_{21}^a + \bar{\bar{S}}_{11}^a, \quad (4-7)$$

$$\bar{\bar{S}}_{12}^{1\text{-port}} = \bar{\bar{0}}, \quad (4-8)$$

$$\bar{\bar{S}}_{21}^{1\text{-port}} = \bar{\bar{0}}, \quad (4-9)$$

$$\bar{\bar{S}}_{22}^{1\text{-port}} = \bar{\bar{0}}, \quad (4-10)$$

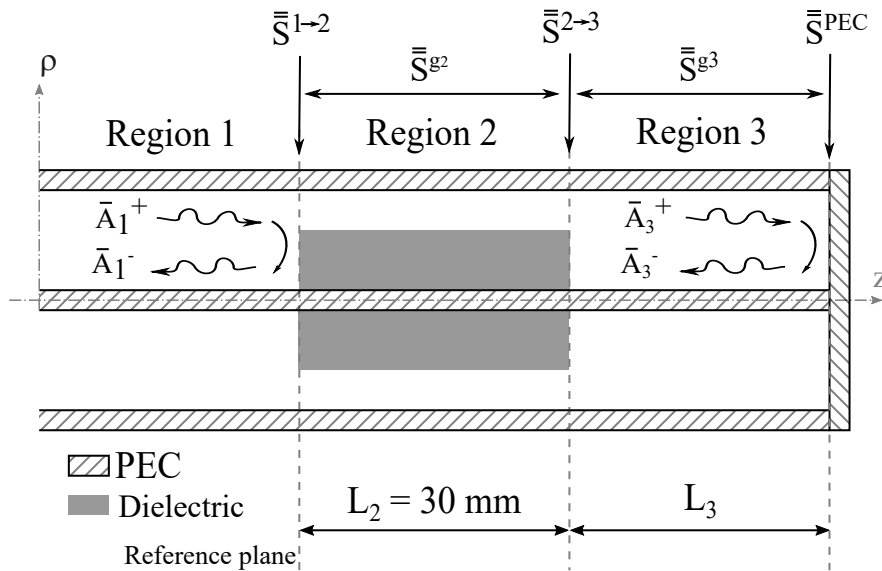


Figure 4.4: Geometry of a cylindrical structure with three waveguide regions, where region 3 is terminated by a PEC plate.

To validate the formulas above, we will consider a sample material inside a one-port MC in three different scenarios. The parameters of first layer (sample) of second region can be seen in Tables 4.2, 4.3 and 4.4, in all cases the second layer is filled with vacuum and lossless and the length of the third waveguide will vary in three different cases: first being $L_2 = 30$ mm, second 45 mm and third 60 mm, while the length of first region is fixed at $L_1 = 10$ mm. The validation results are presented for first scenario in Fig. 4.5, for second scenario in Fig. 4.6 and third scenario in Fig. 4.7. It is possible to observe that the comparison between MMT and FIT algorithms yields a good agreement providing a satisfactory validation results.

We can observe that in Fig. 4.5 the reflection coefficient in decibel becomes zero below 10 GHz because the transverse electromagnetic mode (fundamental transmission-line mode) will be completely reflected by the PEC plane. In contrast, the second propagation mode (TM_{01}) that becomes propagating above 10 GHz will be transmitted along the sampling material, reflected by the PEC plane, but a standing wave will remain. Similar observations also hold for results in Fig. 4.6 and in Fig. 4.7.

Table 4.2: Simulation parameters for the case depicted in Fig. 4.4.

Region	L(mm)	ρ_0 (mm)	ρ_1 (mm)	ρ_2 (mm)	ϵ_{rs1}	ϵ_{rz1}	σ_{s1}	σ_{z1}
1	10	6.3	13.6675	21.035	1.01	1	10^{-6}	10^{-6}
2	30	6.3	13.6675	21.035	2.55	2.55	10^{-6}	10^{-6}
3	30	6.3	13.6675	21.035	1.01	1	10^{-6}	10^{-6}

Table 4.3: Simulation parameters for the second case

Region	L(mm)	ρ_0 (mm)	ρ_1 (mm)	ρ_2 (mm)	ϵ_{rs1}	ϵ_{rz1}	σ_{s1}	σ_{z1}
1	10	6.3	13.6675	21.035	1.01	1	10^{-6}	10^{-6}
2	30	6.3	13.6675	21.035	2.55	2.55	10^{-6}	10^{-6}
3	45	6.3	13.6675	21.035	1.01	1	10^{-6}	10^{-6}

Table 4.4: Simulation parameters for the third case

Region	L(mm)	ρ_0 (mm)	ρ_1 (mm)	ρ_2 (mm)	ϵ_{rs1}	ϵ_{rz1}	σ_{s1}	σ_{z1}
1	10	6.3	13.6675	21.035	1.01	1.01	10^{-6}	10^{-6}
2	30	6.3	13.6675	21.035	2.55	2.55	10^{-6}	10^{-6}
3	60	6.3	13.6675	21.035	1.01	1.01	10^{-6}	10^{-6}

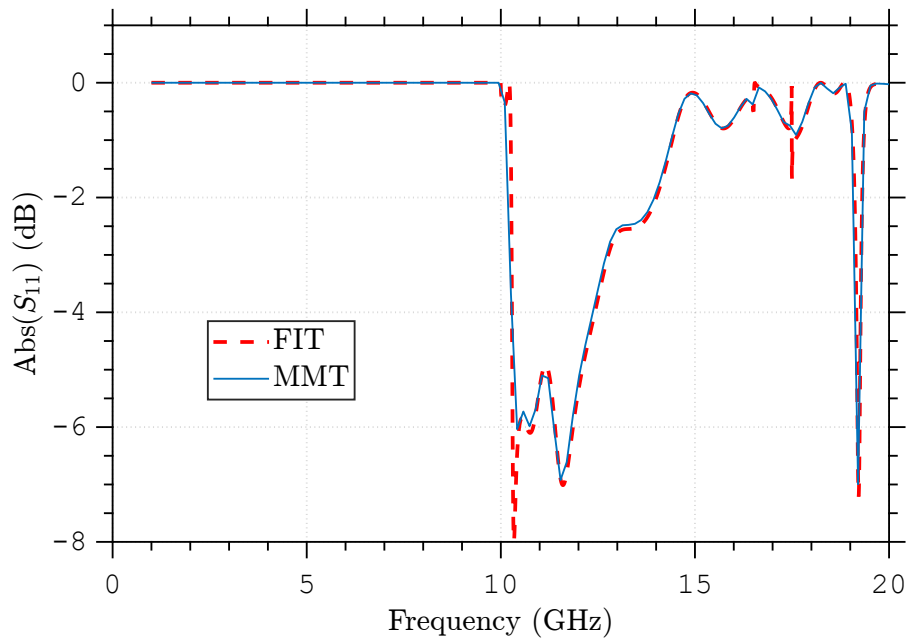


Figure 4.5: Reflection coefficient in decibel for the fundamental mode in region 1 as a function of the frequency for the first case. The results from the present algorithm are indicated by the solid line while FIT results from [73] are the dashed-line.

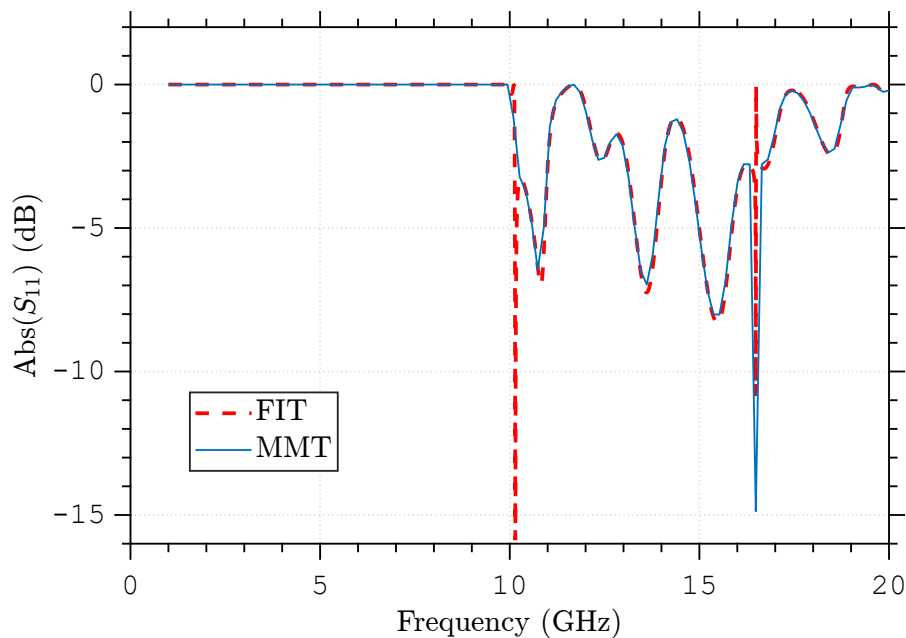


Figure 4.6: Reflection coefficient in decibel for the fundamental mode in region 1 as a function of the frequency for the second case. The results from the present algorithm are indicated by the solid line while FIT results from [73] are the dashed-line.

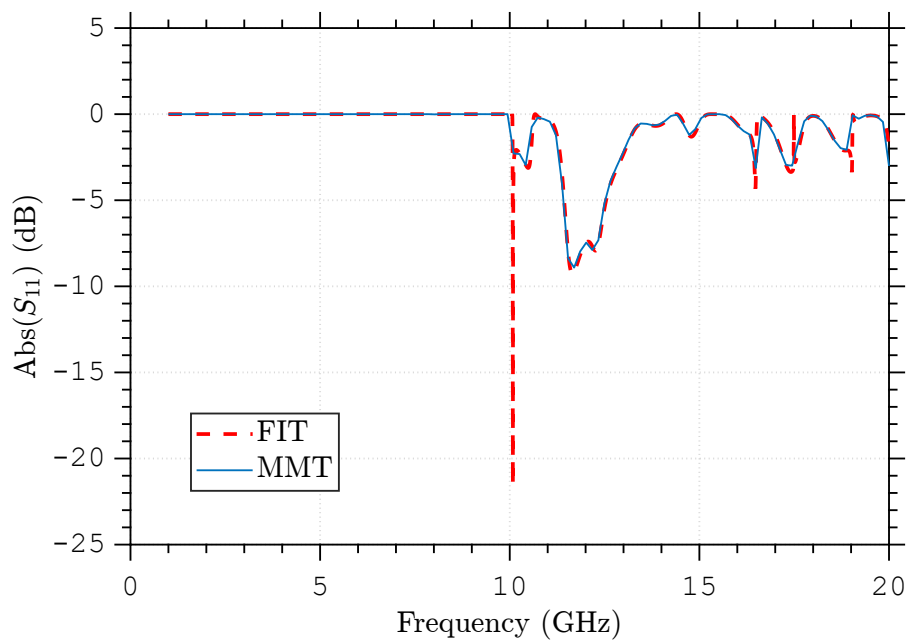


Figure 4.7: Reflection coefficient in decibel for the fundamental mode in region 1 as a function of the frequency for the third case. The results from the present algorithm are indicated by the solid line while FIT results from [73] are the dashed-line.

4.1.3 Open-Ended Coaxial Measurement Cells

To emulate an open-ended probe, as depicted in Fig. 4.8, we will use a PML layer in region 2 and the theory present in Section 3.3. In other words, we will model the equivalent problem depicted in Fig. 4.9, in which region 2 is now a radially-bounded circular waveguide. The complex-valued radius \tilde{r}_N introduces some issues to the MMT as will be detailed in the following sections.

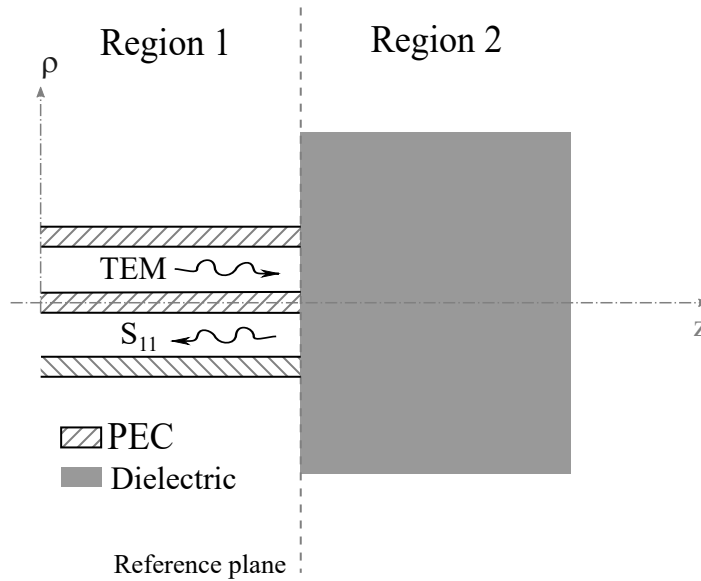


Figure 4.8: Geometry of an open-ended coaxial waveguide.

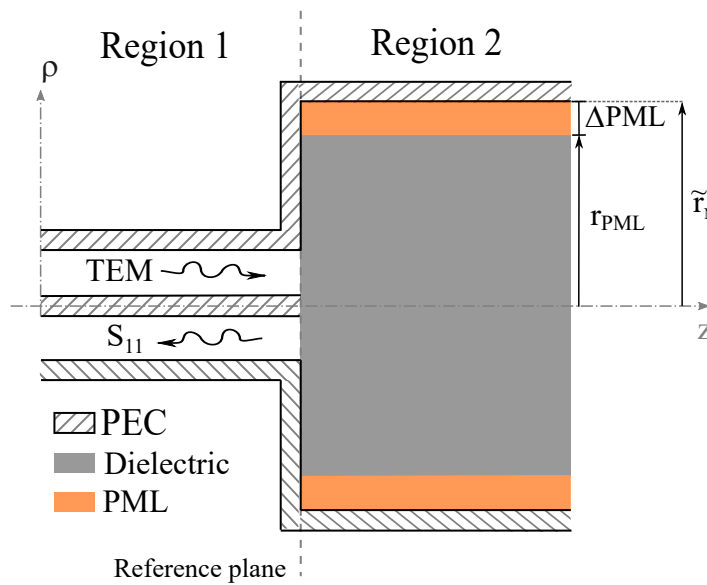


Figure 4.9: Geometry used to emulate the open-ended coaxial waveguide depicted in Fig. 4.8.

4.1.3.1

Relative Convergence Issues and Our Approach to Overcome Them

On computing the GSM at the junction between two regions, the MMT require the use of different number of modes in each waveguide. Usually, the number of modes in each region should be chosen proportional to the external waveguide radius [74]. Otherwise, the convergence is not guaranteed. Since the PML we are exploring confer a complex-valued radius for the waveguide in region 2 (see Fig. 4.9), the radius-ratio criterion above is no longer useful.

To avoid the relative convergence issues, we will match the rate of the longitudinal attenuation the modal fields present as the observation point depart from the junction. It has been implemented under the following terms:

1. The eigenvalues k_{1z} of region 1 are ordered by the ascendant of their imaginary parts.
2. We then select the most relevant modes (the first ones of the ordered list, taking care to include all the propagating modes in case of lossless medium). The number of modes in region 1 are denoted here as N_1 . Now, in order of importance, the first mode in region 1 is $k_{1z}(1)$, and the last is $k_{1z}(N_1)$.
3. A sorting procedure in the same terms of *step 1* is done for region 2, and we select all the eigenvalues k_{2z} in which the imaginary part are less than $\Im m[k_{1z}(N_1)]$. The number of selected modes in region 2 is denoted as N_2 . Notice that these relevant N_2 modes must include all the propagating modes in case of lossless medium. If not so, N_1 in *step 2* should be increased accordingly, and the present step should be rechecked.

In the numerical examples we will explore below, we consider operating frequencies in the range of 1 GHz to 20 GHz, and all the three-step process above is done for each operating frequency also the number of modes in first region was fixed $N_1 = 9$ and for second region, $N_2 = 50$ modes were calculated at first frequency to assure that the third step is successfully done.

Region	α	Polynomial order	δ_{PML} (mm)
2	0.5	1	10

Table 4.6: Simulation parameters used to emulate an open-ended coaxial probe

Region	ρ_0 (mm)	ρ_1 (mm)	ρ_2 (mm)	ϵ_{rs1}	ϵ_{rz1}	σ_{s1}	σ_{z1}
1	6.3	10	18	1.01	1.01	10^{-6}	10^{-6}
2	0	54	-	2.55	2.55	10^{-6}	10^{-6}

4.1.3.2

Solution for a PEC truncation

First we will consider a circular waveguide with radius \tilde{r}_N truncated by a perfect electric conductor (PEC) wall as depicted in Fig. 4.9. The boundary conditions enforcement needs that the tangential electrical fields vanish at $\rho = \tilde{r}_N$, i.e., $E_z = E_\phi = 0$ at the PEC surface. As $\rho = 0$ is in the domain, the non-singular field condition require the Hankel function in (3-18) and (3-23) be removed. Accordingly, we obtain

$$e_z(\tilde{r}_N) = J_n(k_\rho^e \tilde{r}_N) b_{np}^e = 0, \quad (4-11)$$

$$e_\phi(\tilde{r}_N) = \frac{1}{k_\rho^2 \tilde{r}_N} \left[-nk_z J_n(k_\rho^e \tilde{r}_N) b_{np}^e - i\omega \mu_s k_\rho^h \rho_1 J_n'(k_\rho^h \tilde{r}_N) b_{np}^h \right] = 0. \quad (4-12)$$

Observing equations (3-17), (3-18) and (3-20) we note that the amplitude b_{np}^e is proportional to E_z and b_{np}^h is proportional to H_z . As we have $H_z = 0$ for TM^z modes, the amplitude $b_{np}^h = 0$. In the same way, $E_z = 0$ for TE^z modes and consequently $b_{np}^e = 0$. Using this into (4-11) and (4-12), we have obtain the following characteristic equations:

$$J_n(k_\rho^e \tilde{r}_N) = 0, \quad \text{for } \text{TM}^z, \quad (4-13)$$

$$J_n'(k_\rho^h \tilde{r}_N) = 0, \quad \text{for } \text{TE}^z. \quad (4-14)$$

Feeding the above into the MMT formulas described in Chapter 3, we can now analyze the structure shown in Fig. 4.9. We consider this equivalent open-ended coaxial probe hosting a dielectric with the relative electric permittivity ϵ_r in region 2. The parameters used in PML and first and second region are displayed in Tables 4.5 and 4.6. The fundamental mode is exciting the waveguide in region 1, and we consider three different materials in region 2, with $\epsilon_r = 2.55$, $\epsilon_r = 10$, and $\epsilon_r = 1$. Fig. 4.10 shows the computed longitudinal wavenumbers k_z at the first frequency (1 GHz) for regions 1 and 2 when a PML is used with a PEC truncation. In this scenario at 1 GHz, we have 9 relevant modes in region 1 and 23 in region 2 that meet the criterion $\Im m(k_z) < 1100$. Figs. 4.11, Fig. 4.12 and Fig. 4.13 show the computed reflection coefficient in decibel for the fundamental mode in region 1 as a function of the frequency for the open-ended coaxial measurement cell. We compare our solution versus the FIT results, and some discrepancies can be noticed. Further investigation show the convergence of the MMT used with a PML backed by a PEC can improved by at the cost of increasing the number of modes in regions 1 and 2 following the criteria described above in Section 4.1.3.1 as can be noticed in Fig. 4.14 where the black line has $N_1 = 9$ and yellow line has $N_1 = 12$, it is possible

to observe that with higher number of modes in region 1 we obtain better convergence. We will next investigate other PML-based boundary condition for low computational cost.

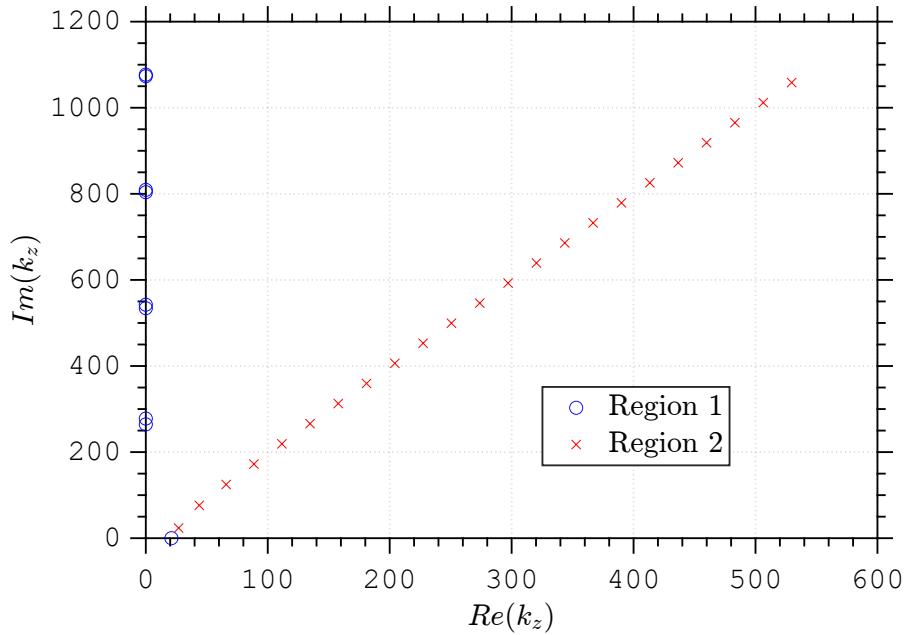


Figure 4.10: Longitudinal wavenumbers k_z of regions 1 and 2 using the parameters shown in Tables 4.5 and 4.6 at frequency of 1 GHz when a PML is used with a PEC truncation.

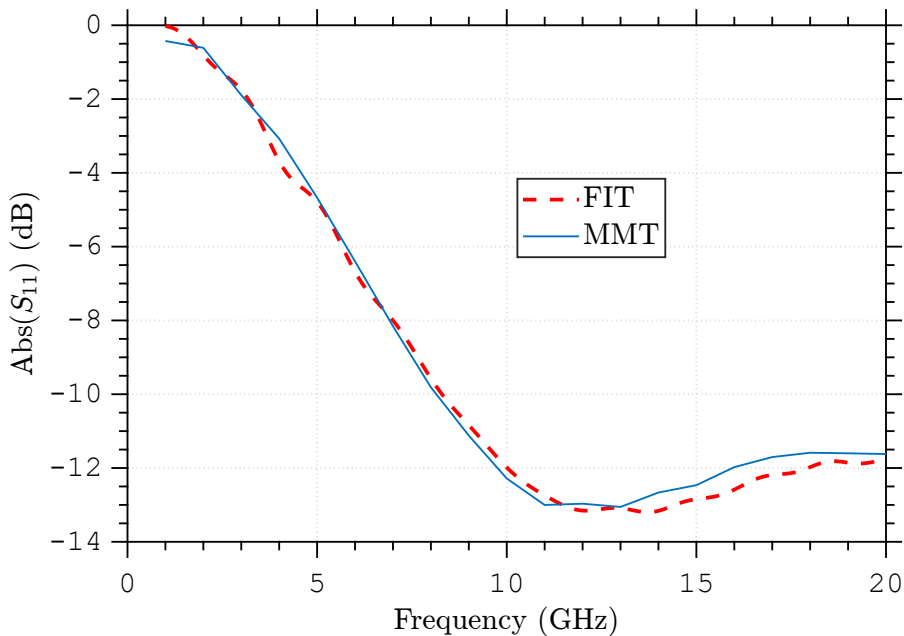


Figure 4.11: Reflection coefficient in decibel for the fundamental mode in region 1 as a function of the frequency for the open-ended coaxial measurement cell truncated by a PEC and $\epsilon_r = 2.55$. The results from the present algorithm are indicated by the solid line while FIT results from [73] are the dashed-line.

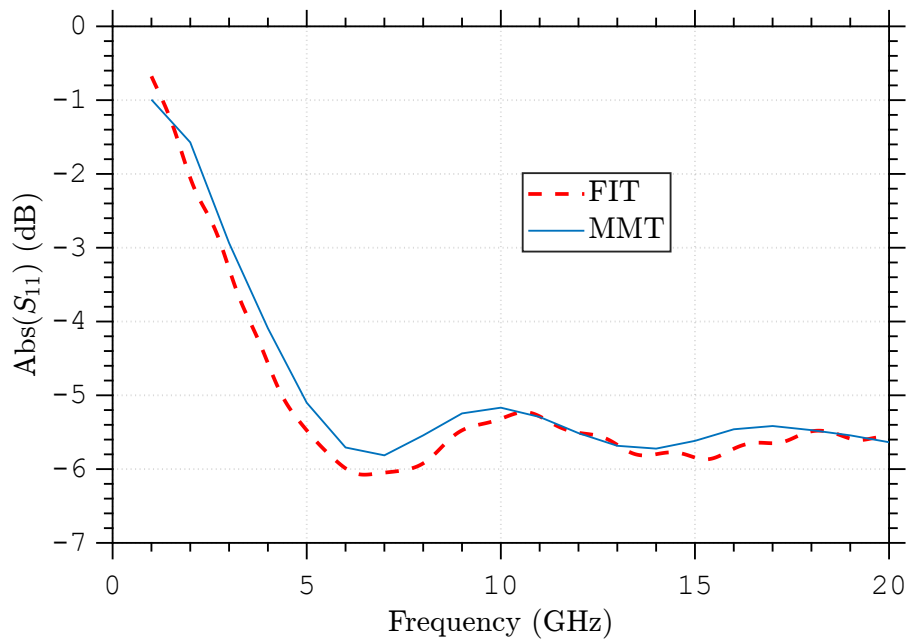


Figure 4.12: Reflection coefficient in decibel for the fundamental mode in region 1 as a function of the frequency for the open-ended coaxial measurement cell truncated by a PEC and $\epsilon_r = 10$. The results from the present algorithm are indicated by the solid line while FIT results from [73] are the dashed-line.

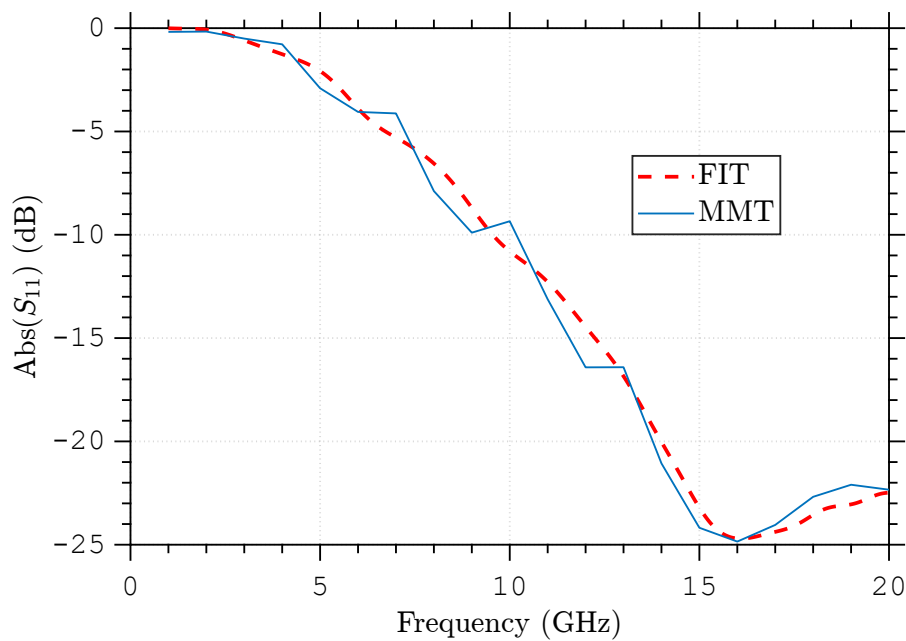


Figure 4.13: Reflection coefficient in decibel for the fundamental mode in region 1 as a function of the frequency for the open-ended coaxial measurement cell truncated by a PEC and $\epsilon_r = 1$. The results from the present algorithm are indicated by the solid line while FIT results from [73] are the dashed-line.

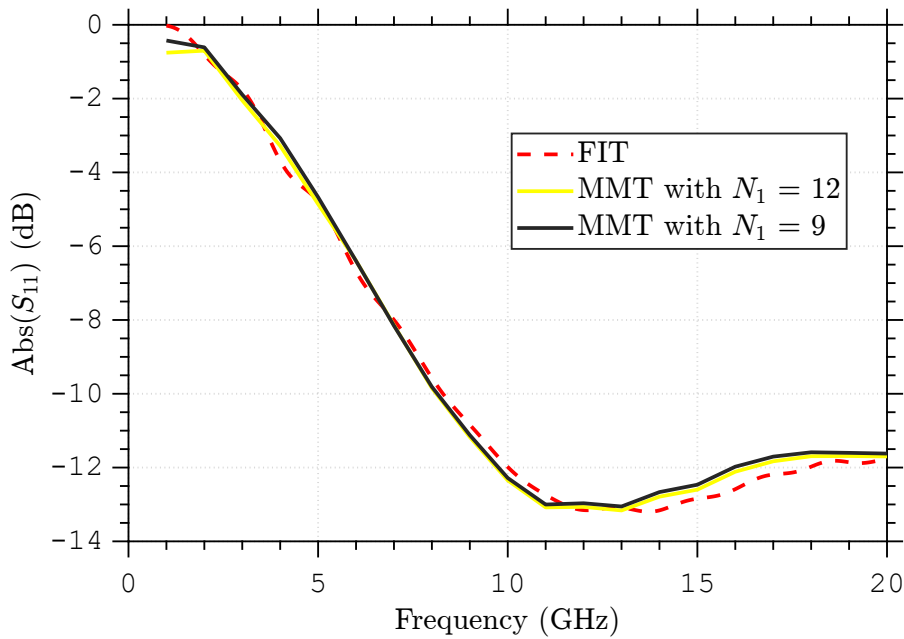


Figure 4.14: Reflection coefficient in decibel for the fundamental mode in region 1 as a function of the frequency for the open-ended coaxial measurement cell truncated by a PEC and $\epsilon_r = 2.55$. The results from the present algorithm are indicated by the solid line, where the black line has $N_1 = 9$ and yellow has $N_1 = 12$, while FIT results from [73] are the dashed-line.

4.1.3.3

Solution for a PMC truncation

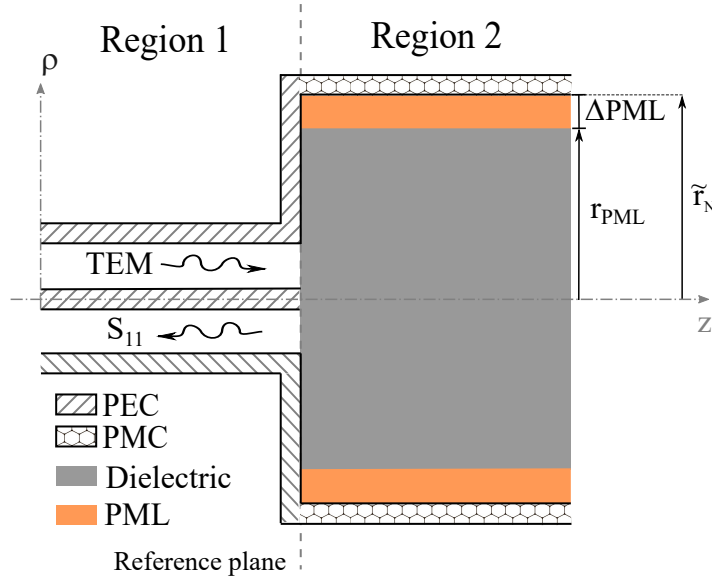


Figure 4.15: Equivalent problem used in algorithm to validate the real situation.

Considering the same circular waveguide as before in Section 4.1.3.2, but now radially truncated with a perfect magnetic conductor (PMC) wall as seen in Fig. 4.15. At $\rho = \tilde{r}_N$, we must enforce

$$h_z(\tilde{r}_N) = J_n(k_\rho^h \tilde{r}_N) b_{np}^h = 0, \quad (4-15)$$

$$h_\phi(\tilde{r}_N) = \frac{1}{k_\rho^2 \tilde{r}_N} \left[i\omega \epsilon_s k_\rho^e \tilde{r}_N J_n'(k_\rho^e \tilde{r}_N) b_{np}^e - n k_z J_n(k_\rho^h \tilde{r}_N) b_{np}^h \right] = 0. \quad (4-16)$$

We can then obtain the following characteristic equations:

$$J_n'(k_\rho^e \tilde{r}_N) = 0, \quad \text{for TM}^z, \quad (4-17)$$

$$J_n(k_\rho^h \tilde{r}_N) = 0, \quad \text{for TE}^z. \quad (4-18)$$

We consider again the structure shown in Fig. 4.9 but region 2 now is truncated by a PML backed by a PMC. The parameters of the PML and regions 1 and 2 are listed in Tables 4.5 and 4.6. The fundamental mode is exciting the waveguide in region 1, and we consider three different materials in region 2, with $\epsilon_r = 2.55$, $\epsilon_r = 10$, and $\epsilon_r = 1$. Fig. 4.16 shows the computed longitudinal wavenumbers k_z at the first frequency (1 GHz) for regions 1 and 2. In this scenario at 1 GHz, we have 9 relevant modes in region 1 and 22 in region 2 that meet the criterion $\Im m(k_z) < 1100$. Figs. 4.17, Fig. 4.18 and Fig. 4.19 show the computed reflection coefficient in decibel for the fundamental mode in region

1 as a function of the frequency for the open-ended coaxial measurement cell. We compare our solution versus the FIT results, and a relative agreement for the majority frequency range investigated is observed, but large discrepancies can be noticed at 1 GHz.

Similarly to the MTT+PML+PEC approach, we can verify the convergence of the MMT used with a PML backed by a PMC can improved by at the cost of at the cost of increasing the number of modes in regions 1 and 2. We will next investigate some features that PEC and PMC truncations present on examining a novel PML-based absorbing boundary condition to be integrated with the MMT.

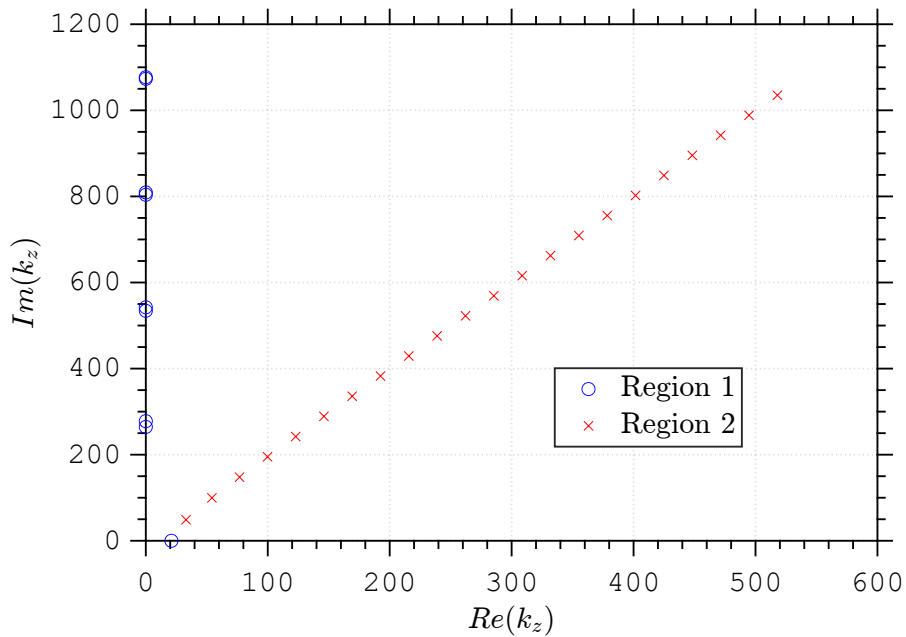


Figure 4.16: Longitudinal wavenumbers k_z of regions 1 and 2 using the parameters shown in Tables 4.5 and 4.6 at the frequency of 1 GHz when a PML is used with a PMC truncation.

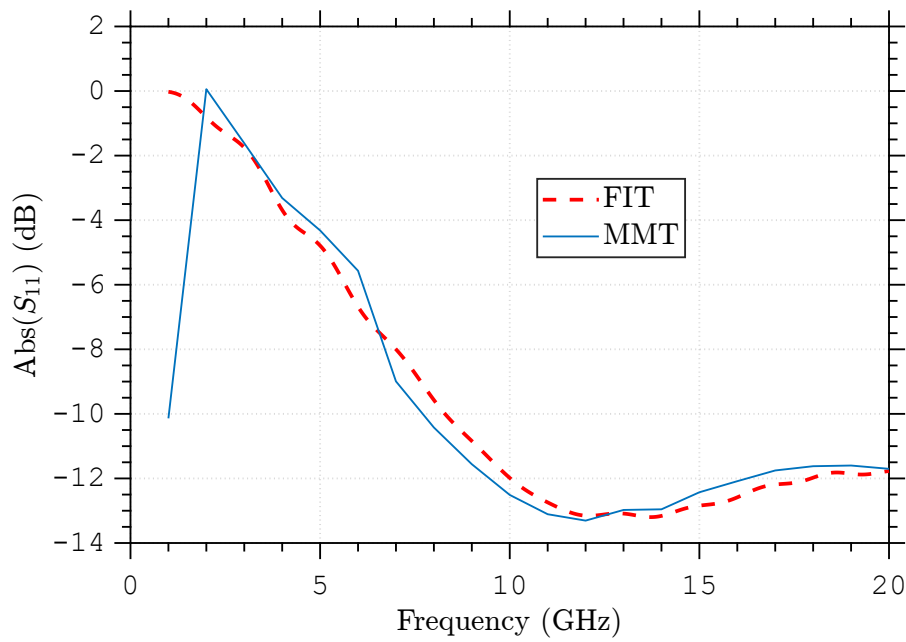


Figure 4.17: Reflection coefficient in decibel for the fundamental mode in region 1 as a function of the frequency for the open-ended coaxial measurement cell truncated by a PMC and $\epsilon_r = 2.55$. The results from the present algorithm are indicated by the solid line while FIT results from [73] are the dashed-line.

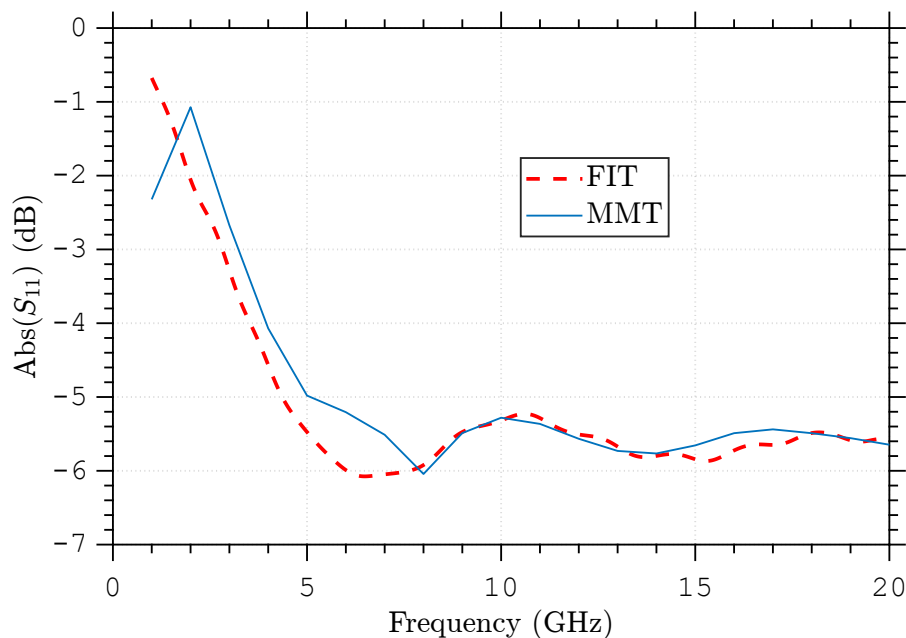


Figure 4.18: Reflection coefficient in decibel for the fundamental mode in region 1 as a function of the frequency for the open-ended coaxial measurement cell truncated by a PMC and $\epsilon_r = 10$. The results from the present algorithm are indicated by the solid line while FIT results from [73] are the dashed-line.

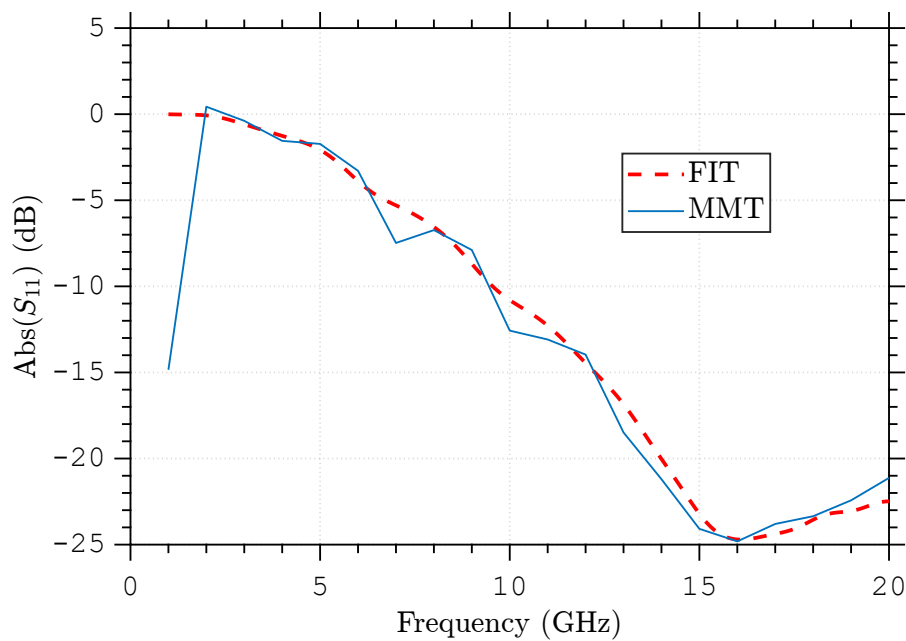


Figure 4.19: Reflection coefficient in decibel for the fundamental mode in region 1 as a function of the frequency for the open-ended coaxial measurement cell truncated by a PMC and $\epsilon_r = 1$. The results from the present algorithm are indicated by the solid line while FIT results from [73] are the dashed-line.

4.1.3.4

Solution for a combined PEC and PMC truncation

In order to improve the convergence of open-ended MCs and keeping the number of modal fields small as possible, we now investigate a combined boundary condition using both PEC and PMC truncations. For the geometry depicted in Fig. 4.9, we suppose the fields in region 2 assume the forms

$$\mathbf{E}_2 = \mathbf{E}_{\text{PEC}} + \mathbf{E}_{\text{PMC}}, \quad (4-19)$$

$$\mathbf{H}_2 = \mathbf{H}_{\text{PEC}} + \mathbf{H}_{\text{PMC}}, \quad (4-20)$$

where $\{\mathbf{E}_{\text{PEC}}, \mathbf{H}_{\text{PEC}}\}$ and $\{\mathbf{E}_{\text{PMC}}, \mathbf{H}_{\text{PMC}}\}$ are the fields corresponding to simulation problems where the PML is truncated by a PEC and by a PMC, respectively. In the perspective of the above (combined) fields, our mode-matching equations of Chapter 3 should be modified accordingly the conservation of reaction across the junction aperture plane. Since the self-reaction in region 2 now is computed using a pair of fields (of the PEC and the PMC truncations), we need to make $\bar{Q}_1 \rightarrow 2\bar{Q}_1$ in the original MMT equations.

To validate the above-described modified-MMT, we consider again the open-ended waveguide with the parameters shown in Tables 4.5 and 4.6. As before, we consider that the coaxial waveguide in region 1 (filled with vacuum) is radiating into the equivalent region 2 (non-magnetic and lossless medium) having the relative permittivities of $\epsilon_r = 2.55$, $\epsilon_r = 10$ and $\epsilon_r = 1$.

Fig. 4.20 shows the computed longitudinal wavenumbers k_z at the first frequency (1 GHz) for regions 1 and 2. In this scenario at 1 GHz, we have 9 relevant modes in region 1 and 45 in region 2 that meet the criterion $\Im m(k_z) < 1100$. Since the same criterion defined in Section 4.1.3.1 was used in this scenario, the number of mode in region 2 is the sum of the number of modes of the PEC and PMC cases. Besides that, the number of mode in region 1 kept as before. Figs. 4.21, Fig. 4.22 and Fig. 4.23 show the computed reflection coefficient in decibel for the fundamental mode in region 1 as a function of the frequency for the open-ended coaxial measurement cell. We again compare our solution versus the FIT results, and we observe the proposed modified-MMT provides better convergence when compared with the conventional PML+PEC and PML+PMC results presented before. Small discrepancies can be noticed, but gain now in small intensity when compared with those of conventional PMLs.

When comparing the cases for all scenarios, we can notice that the combined PEC and PMC yields better results, lowering the discrepancy that was obtained when we had PEC or PMC alone, this is due the fact that PEC

and PMC combined requires about twice the number of modes in region 2 as for PEC and PMC alone when fixing the number of modes for region 1. For $\epsilon_r = 2.55$ the problem on first frequency on PMC alone and the small error around frequency of 15 GHz for PEC alone was fixed by using PEC and PMC. As follows, for $\epsilon_r = 10$ the same problem on first frequency and also small discrepancy around the frequency of 5 GHz for both PEC and PMC alone, was also fixed. For final, $\epsilon_r = 1$, it is possible to noticed that around frequency 5 GHz to 10 GHz, the resonances behaviour in PEC or PMC alone has been mitigated when we combined PEC and PMC.

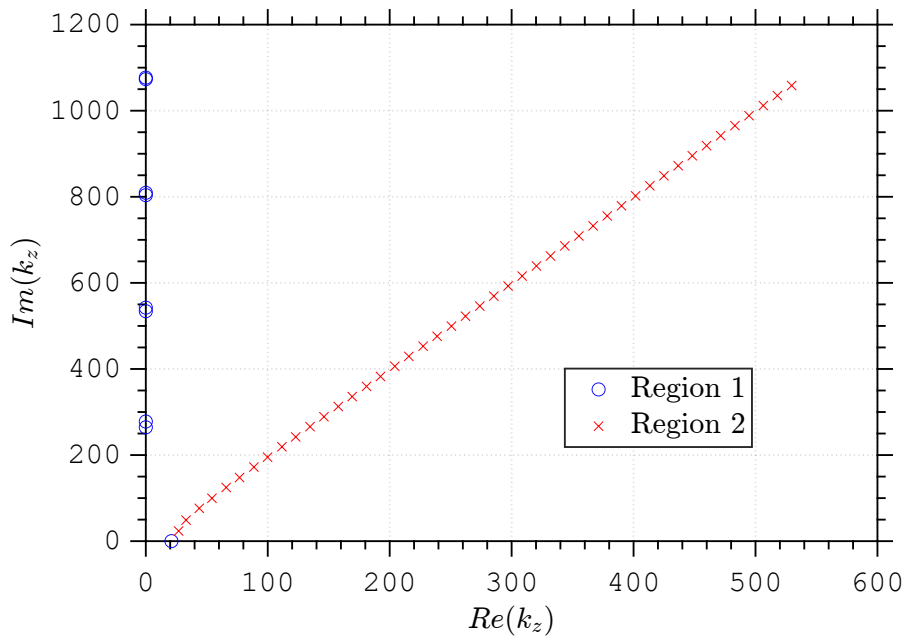


Figure 4.20: Values of k_z of region 1 and 2 for its matching, using the parameters of Table 4.5 and 4.6 at the frequency of 1 GHz when using the combined PML+PEC+PMC truncation.

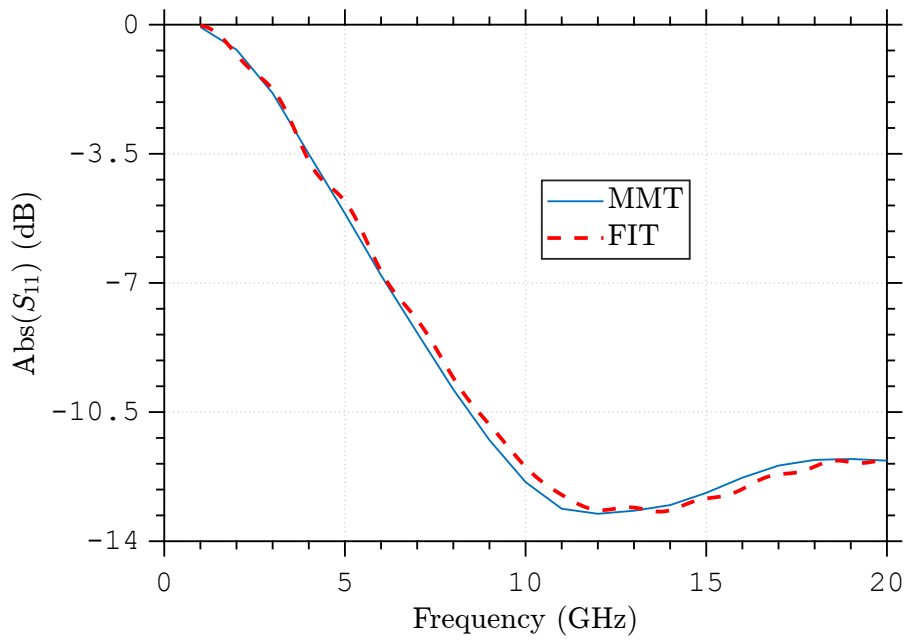


Figure 4.21: Reflection coefficient in decibel for the fundamental mode in region 1 as a function of the frequency for the open-ended coaxial measurement cell and $\epsilon_r = 2.55$. The results from the present algorithm are indicated by the solid line while FIT results from [73] are the dashed-line

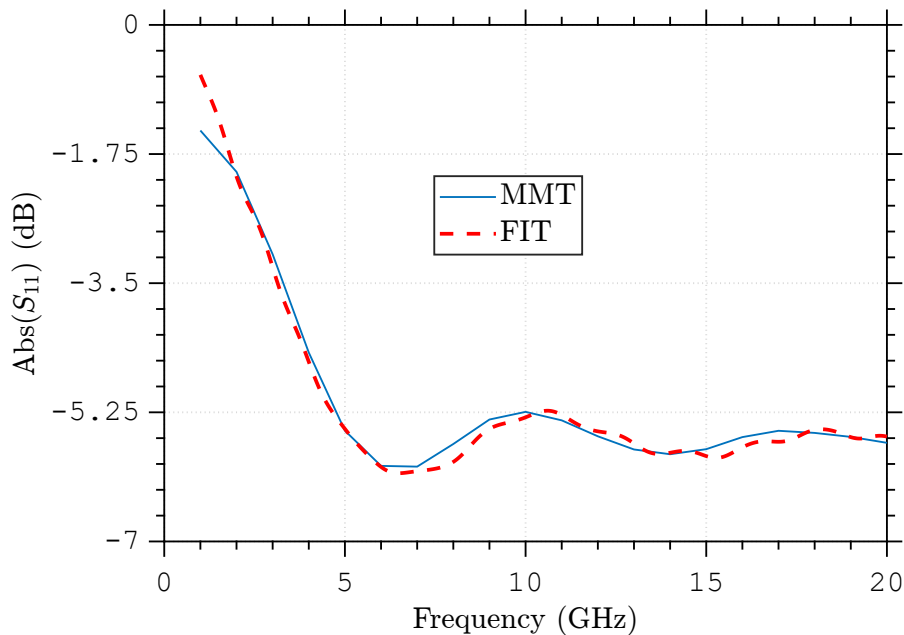


Figure 4.22: Reflection coefficient in decibel for the fundamental mode in region 1 as a function of the frequency for the open-ended coaxial measurement cell and $\epsilon_r = 10$. The results from the present algorithm are indicated by the solid line while FIT results from [73] are the dashed-line

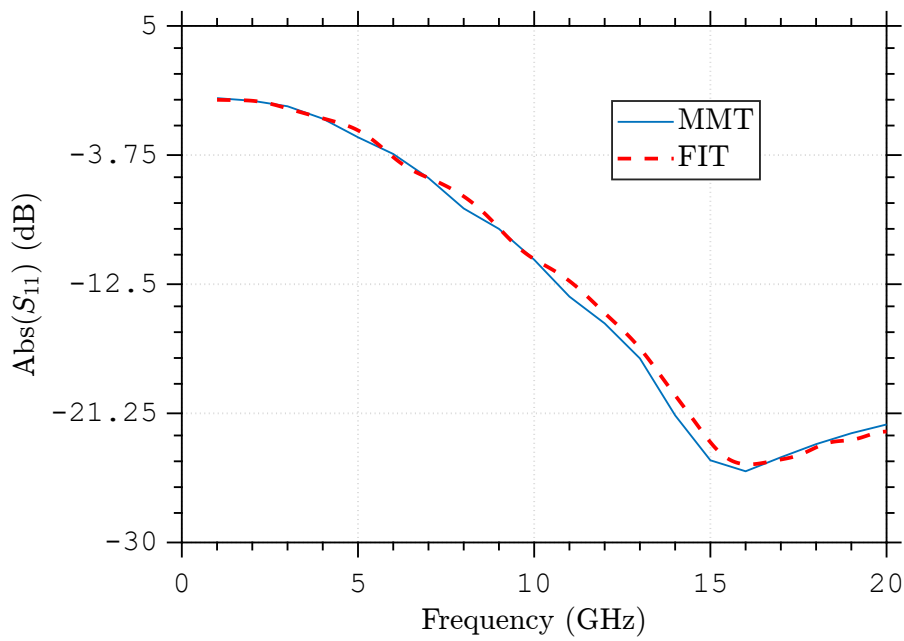


Figure 4.23: Reflection coefficient in decibel for the fundamental mode in region 1 as a function of the frequency for the open-ended coaxial measurement cell and $\epsilon_r = 1$. The results from the present algorithm are indicated by the solid line while FIT results from [73] are the dashed-line

4.2

Inverse Problem

In this section we will discuss two methodologies for determining the constitutive parameters of a sample inside a MC. The first one is based on direct graphical comparisons. The second employs optimization of functionals.

4.2.1

Graphical Comparisons

The graphic comparison method is considered a more simple process used in cases that the material under test is isotropic and lossless. In short, the reflection coefficient obtained from measurements using a vector network analyzer (VNA) is compared with a set of reference curves obtained via simulations. As an illustrative example of how this works, we assume here the FIT results act as those from an actual measurement of a sample with $\epsilon_r = 2.55$ placed inside a two-port MC with parameters described in table 4.7. Fig. 4.24 shows the corresponding S_{11} results as a function of the frequency. Then, we plot the results obtained via the presented MMT for $\epsilon_r = \{1.3, 2.55, 6.4\}$. We notice the curve with $\epsilon_r = 2.55$ is indeed the one that best fit, allowing us to characterize the sample material. Our MMT solutions considered a two-port MC with 10 modes in the first and third regions and 20 in the second region as seen in Fig. 4.1.

In more general cases, where the sample is anisotropic or lossy, this comparison procedure becomes prohibitively complex because of the huge database we need for all combinations of ϵ_{rs} , ϵ_{rz} , σ_s , σ_z , μ_{rs} , and μ_{rz} (also as a function of frequency!). For this reason, in next section we explore an inverse algorithm that instead minimize a functional into an optimization process.

Table 4.7: Geometric and constitutive parameters used on direct problem of a lossless isotropic sample placed in second waveguide of a two-port heterogeneous coaxial waveguide for graphic comparison problem

Region	L(mm)	ρ_0 (mm)	ρ_1 (mm)	ρ_2 (mm)	ϵ_{rs1}	ϵ_{rz1}	σ_{s1}	σ_{z1}
1	-	1.84	2.00	5.00	1.01	1.01	10^{-6}	10^{-6}
2	10	1.84	2.00	6.00	2.55	2.55	10^{-6}	10^{-6}
3	-	1.84	2.00	5.00	1.01	1.01	10^{-6}	10^{-6}

4.2.2

Functional Optimizations

In this work, two different functionals were developed. They are denoted as linear and decibel functional which will be described with more details in following subsections.

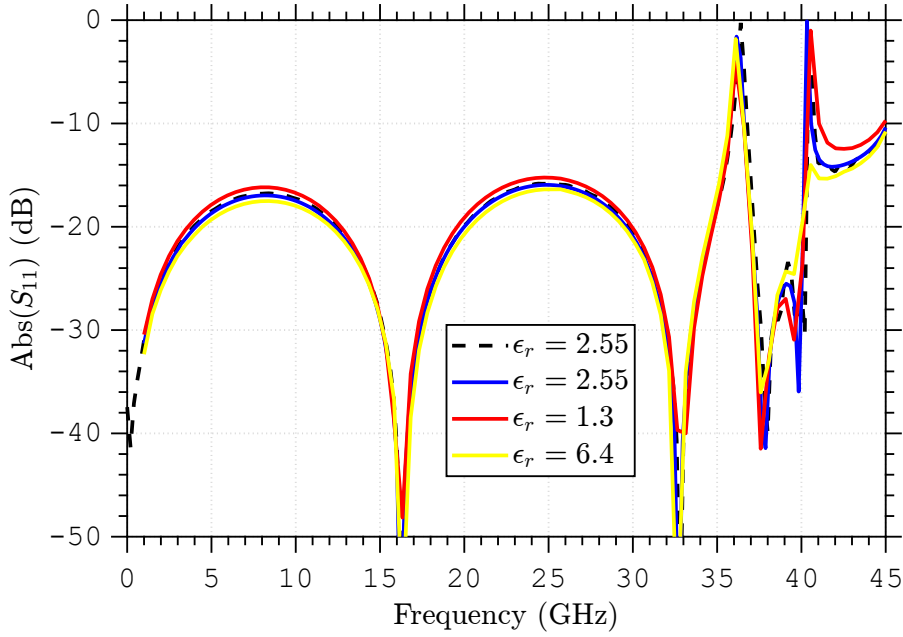


Figure 4.24: Reflection coefficient in decibel for the fundamental mode in region 1 as a function of the frequency for the two-port coaxial measurement cell. The results from the present algorithm are indicated by the solid line while FIT results from [73] by the dashed-line.

For both functionals, as a first step, we assume reflection and transmission parameters that represent the measurements of a given MC of interest are denoted as $S_{11,\text{meas}}(\omega)$ and $S_{21,\text{meas}}(\omega)$, respectively. The permittivity tensor $\bar{\bar{\epsilon}} = \epsilon_0 \bar{\bar{\epsilon}}_r + i\bar{\bar{\sigma}}/\omega$ tensor of the sample material placed inside a two-port MC can be obtained via the minimization of the functional

$$f^{2\text{-ports}}(\bar{\bar{\epsilon}}_r, \bar{\bar{\sigma}}) = \sum_{n=1}^N [\Delta S_{11}(\omega_n) + \Delta S_{21}(\omega_n)] \quad (4-21)$$

where

$$\Delta S_{11}(\omega) = |S_{11,\text{meas}}(\omega) - S_{11,\text{calc}}(\omega)| \quad (4-22)$$

$$\Delta S_{21}(\omega) = |S_{21,\text{meas}}(\omega) - S_{21,\text{calc}}(\omega)|. \quad (4-23)$$

The complex-valued functions $S_{11,\text{calc}}(\omega)$ and $S_{21,\text{calc}}(\omega)$ are obtained via the numerical implementation of the presented MMT.

As follows, we present the main difference of linear and decibel functionals, the linear case, equations (4-22) and (4-23) are calculated for the real and imaginary values of S_{11} and S_{12} , then a sum of those values are done. The decibel case, the same equations are calculated for amplitude and phase and then a sum of those values are done, however, the phase calculation is more complicated since the S-parameters measured and calculated must match. For

this, we used the following equations for phase matching before the sum is made.

$$\theta_{11, \text{calc}} = \angle(S_{11, \text{calc}}) \quad , \quad \theta_{21, \text{calc}} = \angle(S_{21, \text{calc}}) \quad (4-24)$$

$$\theta_{11, \text{meas}} = \angle(S_{11, \text{meas}}) \quad , \quad \theta_{21, \text{meas}} = \angle(S_{21, \text{meas}}) \quad (4-25)$$

$$\theta_{11, \text{calc}} = \theta_{11, \text{calc}} + |\theta_{11, \text{meas}}(\omega_1) - \theta_{11, \text{calc}}(\omega_1)| \quad (4-26)$$

$$\theta_{21, \text{calc}} = \theta_{21, \text{calc}} + |\theta_{21, \text{meas}}(\omega_1) - \theta_{21, \text{calc}}(\omega_1)| \quad (4-27)$$

Notice the functional in (4-21) uses a set of N frequency samples over the range of interest for filtering purposes. In case of a lossless sample, the electric conductivity tensor is zero.

For one-port and open-ended MCs, our functional is equal to (4-21) but the ΔS_{21} -terms are absent. The Matlab [75] function `fmincon` which will be described with more detailed in next section was used in the optimization process.

One of the major problems found in those algorithm was to proper choose an initial guess in order to avoid improper convergence to local minima instead of to the global one, and for this reason, the inverse process was divided into two steps. First, a set of simulations for ϵ_{rs} , ϵ_{rz} , σ_s and σ_z is performed by using a range of practical and reasonable values. We assume the relative permittivity ranges from 1 to 10, and the electrical conductivity from 10^{-6} S/m to 10 S/m. We then find the best initial guess for function `fmincon`. This approach have showed excellent results on preventing the optimization algorithm to fall into basis of attraction different from that of the global minimum.

4.2.2.1

`fmincon` and sqp algorithms

The `fmincon` algorithm finds a constrained minimum of a function with several variables starting at an initial guess [76]. The syntax used in our work follows the form `x = fmincon(fun, x0, A, b, Aeq, beq, lb, ub, nonlcon, options)`, where the algorithm starts at the initial guess vector \mathbf{x}_0 and attempts to find a \mathbf{x} that minimize the desired function `fun`, the linear inequalities constrains were not used, i.e. `A = b = Aeq = beq = nonlcon = []`, the terms `lb` and `ub` stands for lower and upper bond, respectively, such that `lb < x < ub` and the variable `options` specify the optimization options as the minimization algorithm, the Optimality Tolerance and the Step Tolerance. Some of these minimization algorithms are listed in the Table 4.8. In our case, we will use the sequential

quadratic programming (**sqp**).

Table 4.8: Algorithms used in function `fmincon` [77].

Algorithm	Description
<code>interior-point</code>	Handles large, sparse and small dense problems. The algorithm satisfies bounds at all iterations. It is a large-scale algorithm
<code>trust-region-reflective</code>	Requires you to provide a gradient, and allows only bounds or linear equality constraints. Handles large sparse and small dense problems efficiently. It is a large-scale algorithm
<code>sqp</code>	Satisfies bounds at all iterations. It is not a large-scale algorithm
<code>sqp-legacy</code>	Similar to <code>sqp</code> , but usually is slower and uses more memory
<code>active-set</code>	Can take large steps adding speed. Effective on some problems with non-smooth constraints. It is not a large-scale algorithm

The `sqp` methods represent the state of art in nonlinear programming methods. At each iteration, an approximation is made of the Hessian of the Lagrangian function using a quasi-Newton updating method, which is used to generate a sub-problem whose solution indicates the search direction for a line search procedure. The method can be seen with details in [78–81]. In general, the problem is described by equation (4-28) and the sub-problem by (4-29)

$$\min_s \{q(s), s \in N\}, \quad (4-28)$$

$$L(x, \lambda) = f(x) + \sum_{i=1}^m \lambda_i \cdot g_i(x), \quad (4-29)$$

which is based on a quadratic approximation of the Lagrangian function.

4.3

Study of local and global minimum

In this section a study on local and global minimums of the functionals will be presented. An example of local and global minimums of a function is depicted in Fig. 4.25. The functional studied is the one described in (4-21), using five frequencies equally spaced. This was made because one of the major problems found in the optimization algorithm used in inverse problem was to decide which was the best initial guess.

Some materials, with a given length, can present many local minimums. For this reason, the initial guess for the optimization has a fundamental

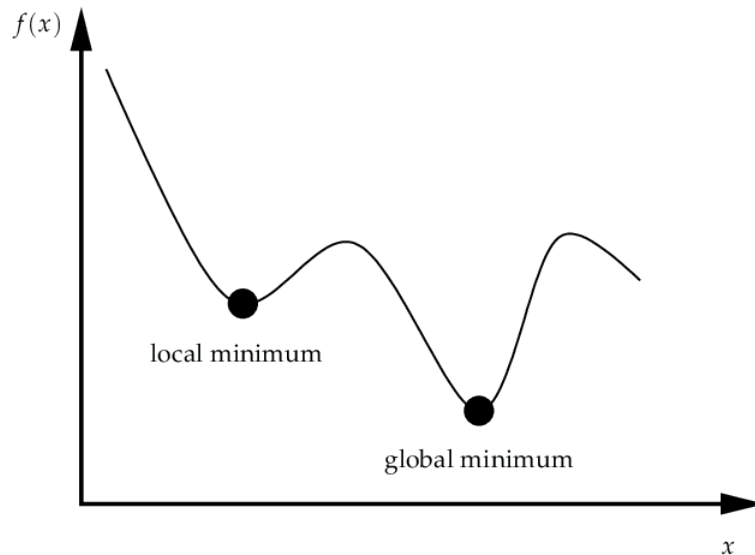


Figure 4.25: Example of local and global minimums of a function. Image obtained in [82].

importance to avoid an improper convergence to basins of attraction that does not correspond to the global minimum – which will be explained in next sub section.

4.3.1 Basins of attraction

Assuming our functional is denoted by $f(x(t))$, with the input variables $x(t) = \{\bar{\epsilon}(t), \bar{\mu}(t)\}$, the direction where the functional decrease more abruptly as the iteration t increases points to $\partial x(t)/\partial t$. This steepest descent path allows our functional to converge to a local minimum as t increases. In general, if more than one initial guess is chosen and are near each other, they tend to converge to the same minimum point. To illustrate, by considering a simplified functional with only one parameter (x), Fig. 4.26 shows a scenario with two minimums: one global and one local. The steepest descent paths, depicted as arrows, will led to one of them, depending on the initial guess chosen.

4.3.2 A discussion on the number of local minima

The study of the sample's parameters influence, such as length, height and permittivity, on the number of local minimums will be presented. This information is important since depending on those parameters our functional value will have only one local (global) or several local minumums. As consequence, we can design the sample for the less local minumums possible so our initial guess search algorithm converge faster to initial point.

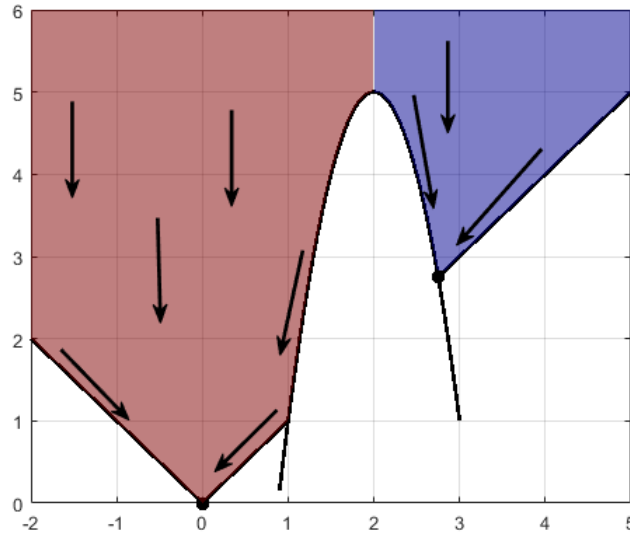


Figure 4.26: The function minimum will be either $(0,0)$ or $(11/4, 11/4)$, if the initial guess is $x < 2$ or $x > 2$, respectively. Image obtained in [83].

It is important to notice that, this study has been made considering five frequencies equally spaced over 1 GHz to 45 GHz, and on a two-port coaxial probe, as show in Fig. 4.1, and following the same parameters as in Table 4.1.

The first case will have the height of the sample fixed at 0.16 mm.

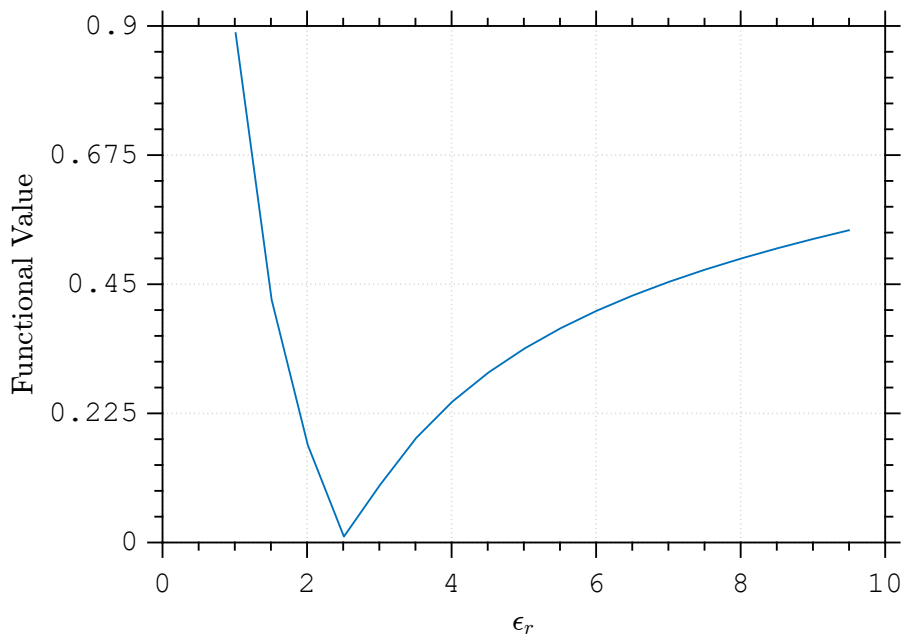


Figure 4.27: Functional value considering $\epsilon_r = 2.55$, length $L = 10$ mm for first case.

By analyzing the Figs. 4.27, 4.28, 4.29 and 4.30 for first case, it is possible to tell that in this particular situation, whenever the height is very small, the length and the relative permittivity does not affect the numbers of local

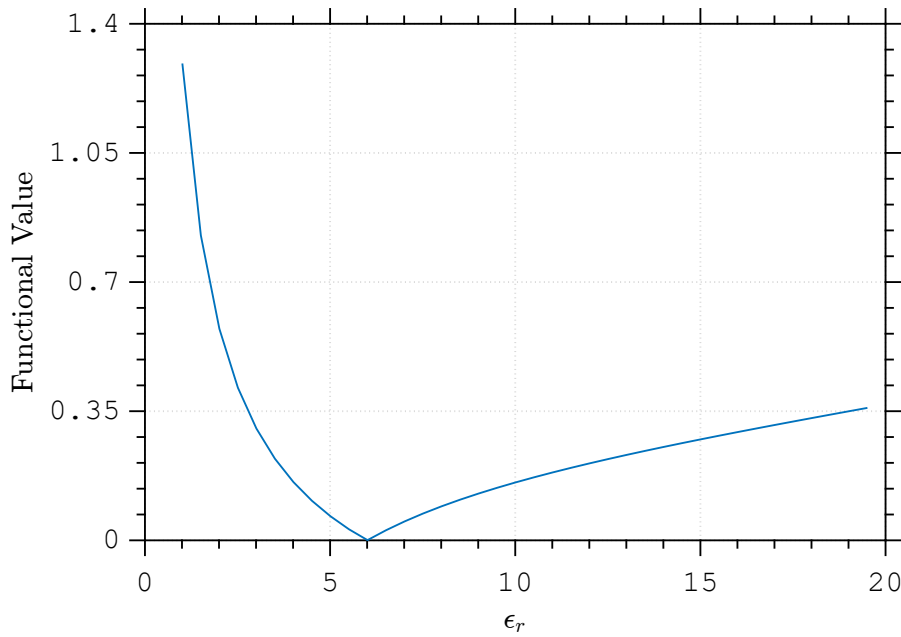


Figure 4.28: Functional value considering $\epsilon_r = 6$, length $L = 10$ mm for first case.

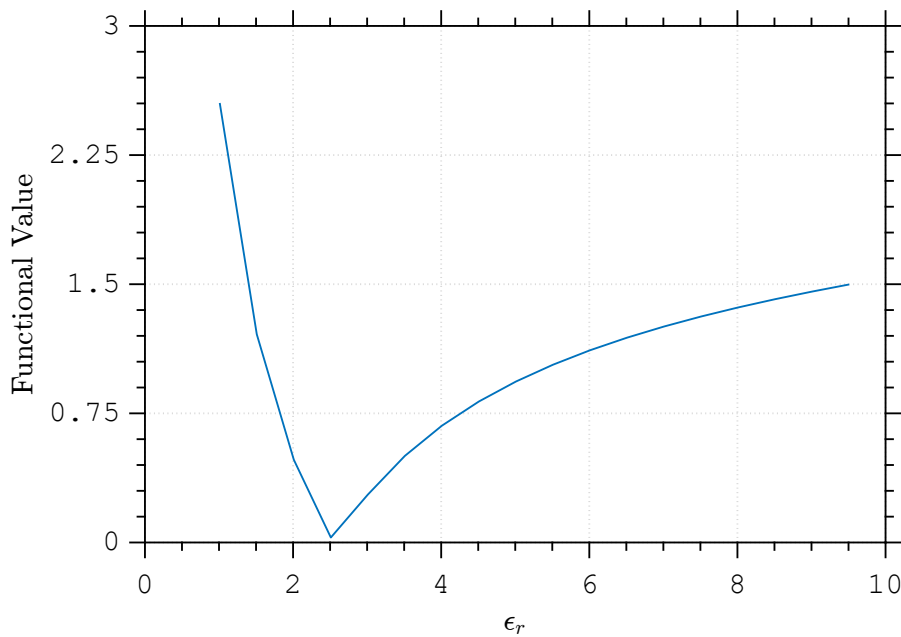


Figure 4.29: Functional value considering $\epsilon_r = 2.55$, length $L = 30$ mm for first case.

minima in the functional value. It is possible to notice that only one minimum is identified, meaning that, if any initial guess for ϵ_r is made in the 1 – 20 range, it will converge to the global minimum and yields the correct result.

The second case will be fixing the height of the sample at 1.56 mm. From analysing the Fig. 4.31, 4.32, 4.33 and 4.34 for second case, it is possible to tell that in this particular situation, the number of minimum of the functional does get affected by length difference and by the relative permittivity, as an

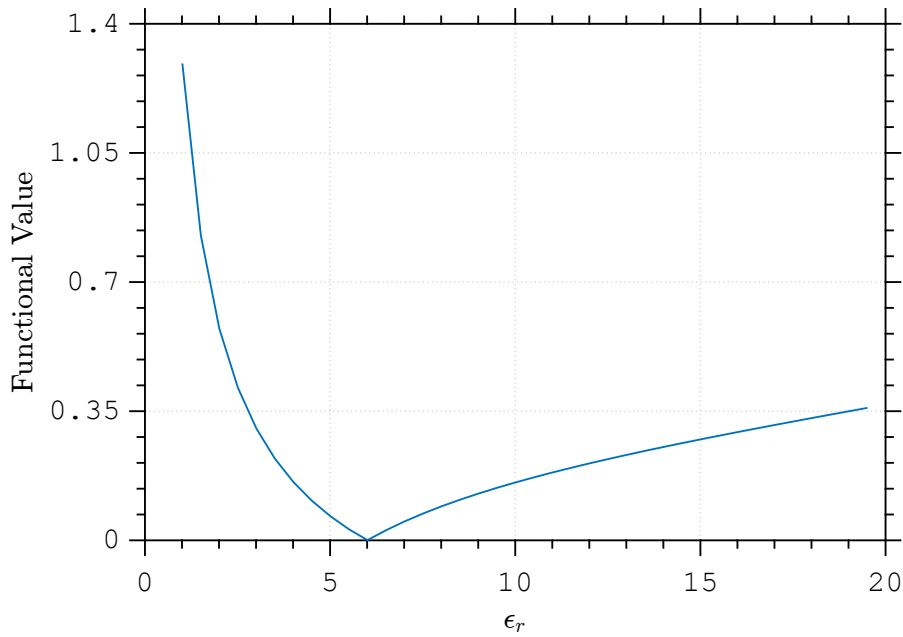


Figure 4.30: Functional value considering $\epsilon_r = 6$, length $L = 30$ mm for first case

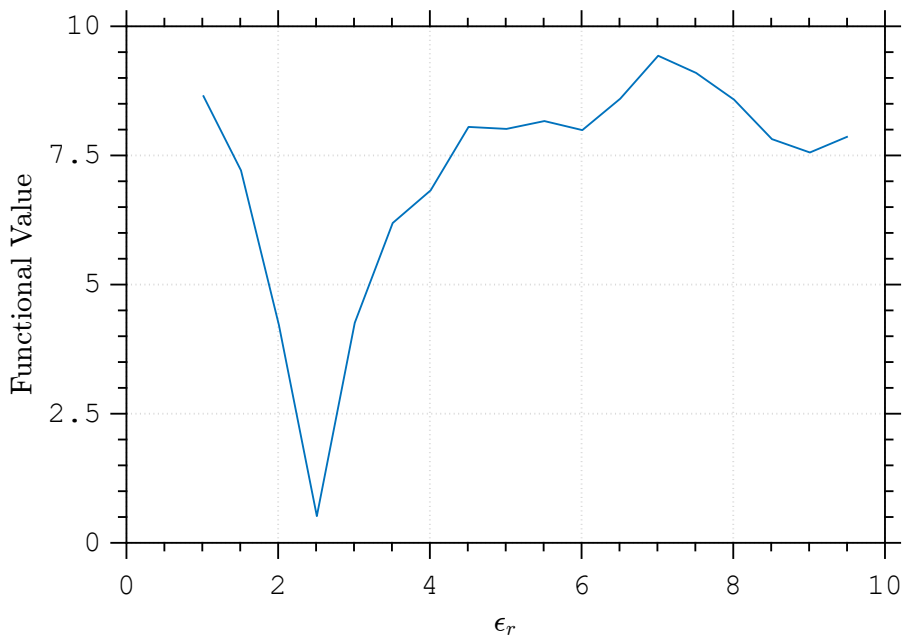


Figure 4.31: Functional value considering $\epsilon_r = 2.55$, length $L = 10$ mm for second case.

example, in Fig. 4.31 we have 3 minimums while Fig. 4.33 has 5. Also, when the length its kept the same and we just differ the ϵ_r , as an example, in Fig. 4.31 we have 3 minimums while in Fig. 4.32 we have 5.

As conclusion of this study, it is possible to affirm that in this particular situation where the 5 frequencies are equally spaced, the height samples affects the number of minimums of the functional and also when it is fixed and the length and relative permittivity varies, it also changes.

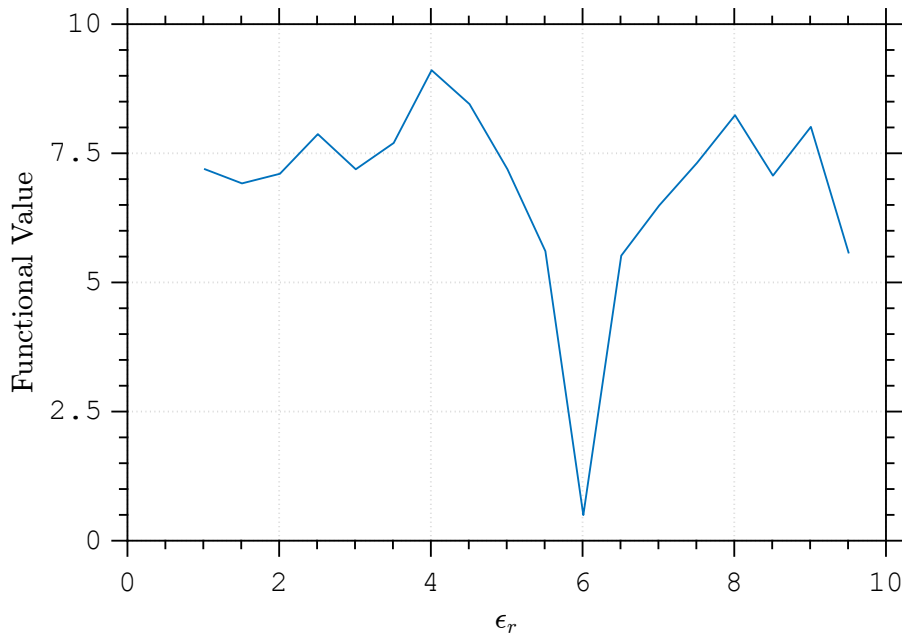


Figure 4.32: Functional value considering $\epsilon_r = 6$, length $L = 10$ mm for second case.

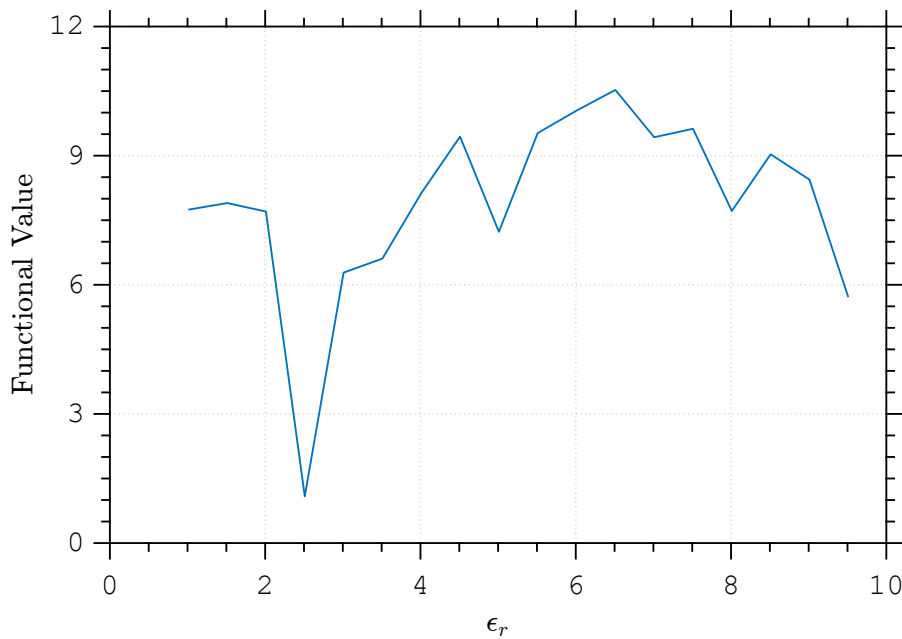


Figure 4.33: Functional value considering $\epsilon_r = 2.55$, length $L = 30$ mm for second case.

4.3.3

Mislead convergence due to wrong initial guess choice

In this section will be presented how important it is to choose a correct initial guess doing the search for global algorithm used before the optimization.

It was used a two-port coaxial line in this case, same as in Fig. 4.1, with an isotropic material with $\epsilon_r = 2.55$. As shown, since the initial guess was wrongly chosen, it converged to a mislead result, instead of $\epsilon_r = 2.55$, it

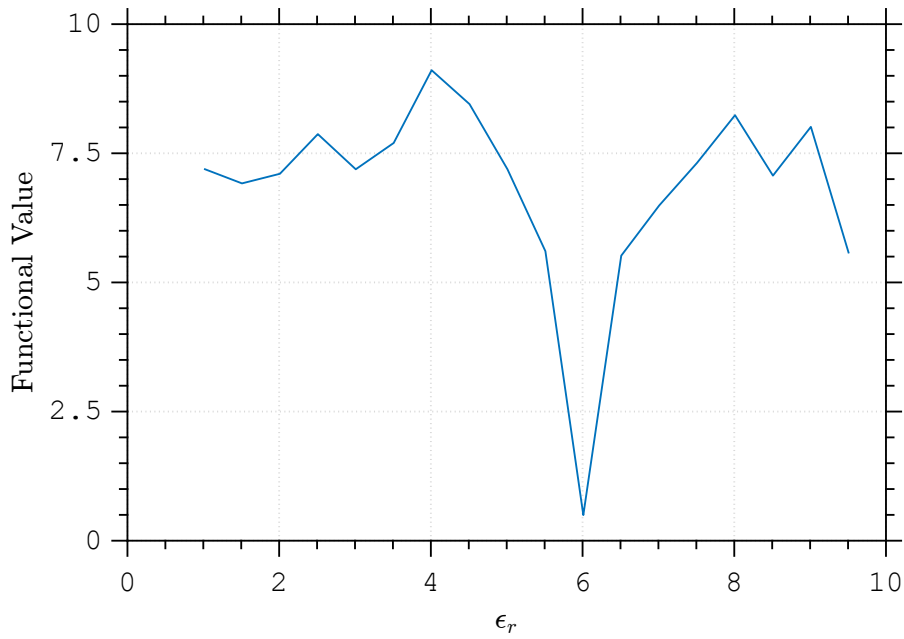


Figure 4.34: Functional value considering $\epsilon_r = 6$, length $L = 30$ mm for second case.

converged to $\epsilon_r = 5.66$. We will enforce that the initial guess is $\epsilon_r = 5.51$ and the answer should converge to the local minimum around this value.

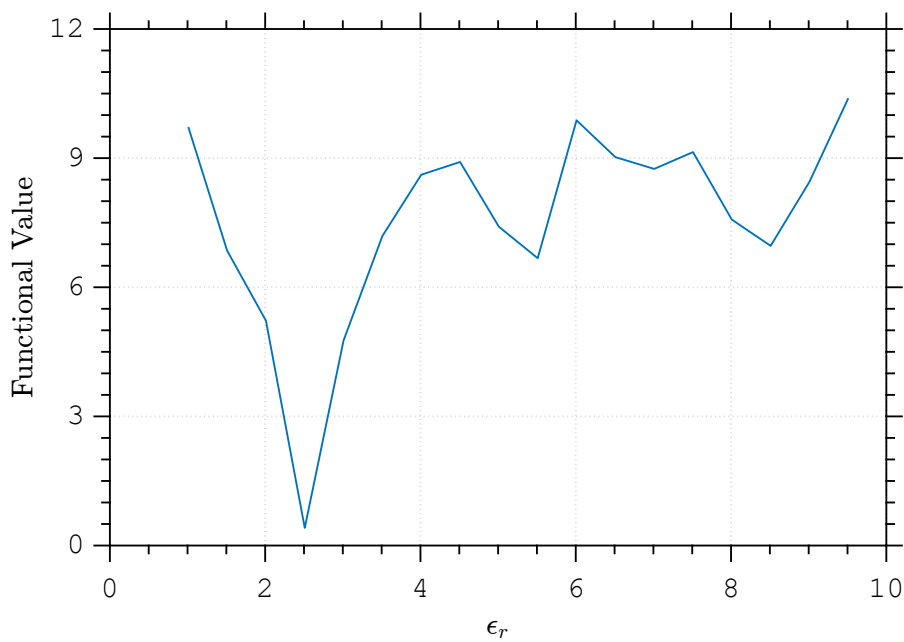


Figure 4.35: Functional value showing global minimum at $\epsilon_r = 2.51$ and others local minimums on $\epsilon_r = 5.51$ and $\epsilon_r = 8.51$.

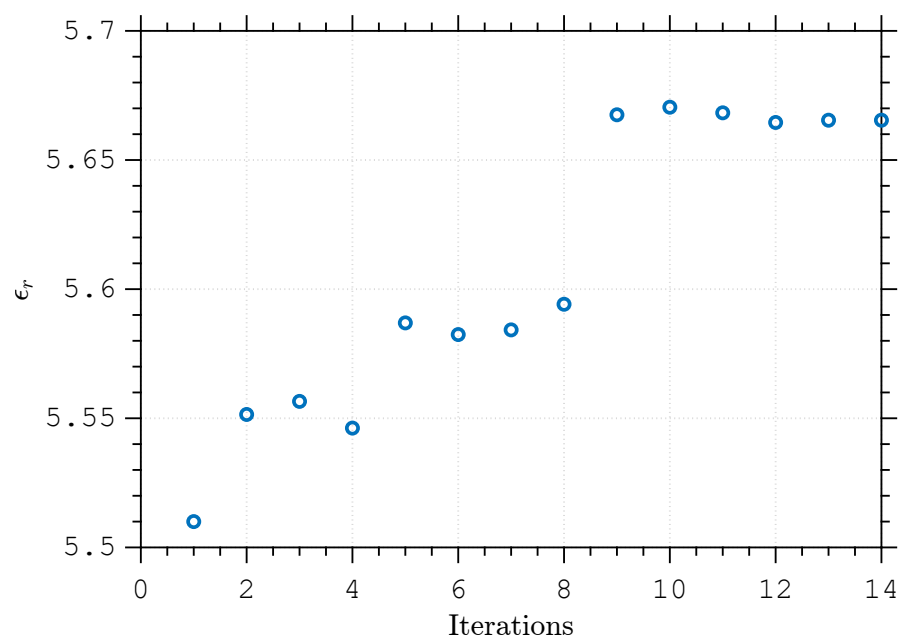


Figure 4.36: Evolution of the optimization parameter as a function of the number of iterations. Convergence was achieved after 14 iterations at $\epsilon_r = 5.66$.

5 Inverse Problem Results

In this chapter we will present simulation results of several inverse problems for exploring the ability of the previously-presented formulations to retrieve the constitutive parameters of a sample material inside a measurement cell.

Our MMT results were obtained using a Matlab code running on a PC with a 2.30-GHz Intel Core i7-10510U processor. In contrast, the FIT results were obtained using a dedicated HP Z800 Workstation with a dual quad-core 2.40-GHz Intel Xeon E5620 processor. We have used the standard options in the FIT solver of CST.

5.1 Two-Port Measurement Cells

For the inverse problem using two-port measurement cell it was considered that the material under test were categorized into following cases:

- lossless isotropic sample
- lossy isotropic sample
- lossless anisotropic sample
- anisotropic sample with isotropic loss
- anisotropic sample with anisotropic loss

Those cases were tested using heterogeneous coaxial waveguide, homogeneous circular waveguide and heterogeneous circular waveguide. The number of modes in region 1 and 3 were defined as 5 which was the smallest number to obtain convergence and in region 2, using the external waveguide ratio criteria [74], the number of modes were defined as 6.

5.1.1 Heterogeneous Coaxial Waveguide

Will be considered that the material under test is occupying the first layer, while second layer will be fulfilled with vacuum.

5.1.1.1

Lossless isotropic sample

The first simulation uses a lossless isotropic material in the second region. In this case, it was considered that the information about the material being isotropic was considered unknown to test if the algorithm was able to identify both ϵ_{rs} and ϵ_{rz} with the same values. The objective on this approach is to ensure that in cases where this information is unknown, our method is able to identify it nevertheless. The parameters used are in Table 5.1, for the linear functional, results are in Fig. 5.1 and 5.2, for the ϵ_{rs} and ϵ_{rz} , respectively. As the results were positives, for cases where the material is isotropic, we can work with one less parameter making the algorithm smoother.

Also, Table 5.2 presents the initial guess used by the optimization algorithm in the form $[\epsilon_{rs0} \ \epsilon_{rz0}]$, the time spent to find the results and the number of iterations necessary. We observe that the convergence was achieved after 14 iterations for a value near $\epsilon_{rs} = 2.55$ and $\epsilon_{rz} = 2.55$ which was the one used in the simulation.

Table 5.1: Geometric and constitutive parameters used on direct problem of a lossless isotropic sample placed in second waveguide of a two-port heterogeneous coaxial waveguide.

Region	L(mm)	ρ_0 (mm)	ρ_1 (mm)	ρ_2 (mm)	ϵ_{rs1}	ϵ_{rz1}	σ_{s1}	σ_{z1}
1	-	1.84	2.00	5.00	1.01	1.01	10^{-6}	10^{-6}
2	10	1.84	3.92	6.00	2.55	2.55	10^{-6}	10^{-6}
3	-	1.84	2.00	5.00	1.01	1.01	10^{-6}	10^{-6}

Table 5.2: Initial guess, CPU time, and the number of iterations to achieve convergence by using the parameters Table 5.1 using linear functional.

x_0	Time	Iterations
[2.51 2.51]	33 min 49 seconds	14

For the decibel functional, the results are present in Fig. 5.3 and 5.4. The information about the optimization algorithm are in Table 5.3. In this case, a lower number of iterations were necessary, although the time to converge was almost the same. We again observe that the convergence was achieved after 11 iterations for a value near $\epsilon_{rs} = 2.55$ and $\epsilon_{rz} = 2.55$ which was the one used in the simulation.

Table 5.3: Initial guess, CPU time, and the number of iterations to achieve convergence by using the parameters table 5.1 using decibel functional.

x_0	Time	Iterations
[2.51 2.51]	33 min 25 seconds	11

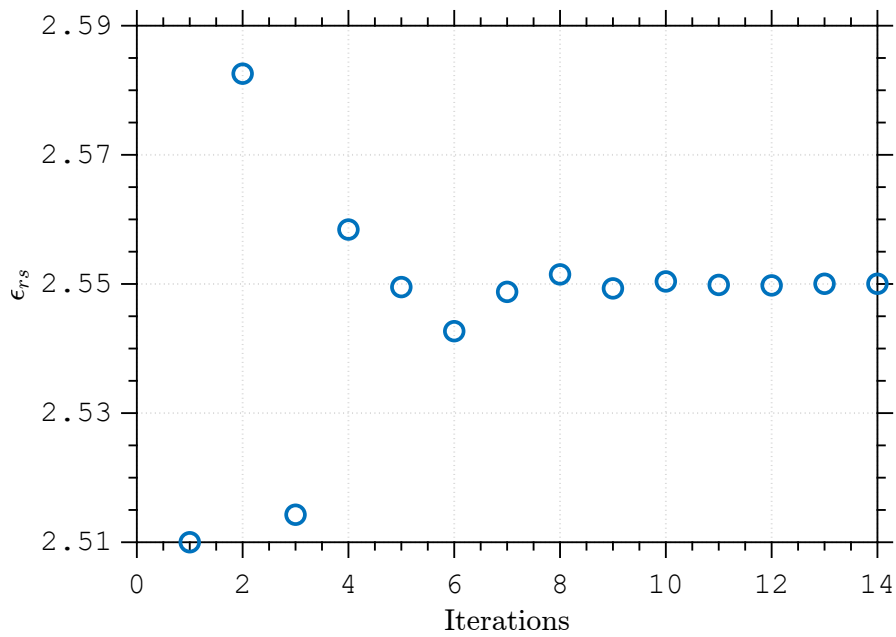


Figure 5.1: Evolution of the optimization parameter as a function of the number of iterations using linear functional. Convergence was achieved after 14 iterations at $\epsilon_{rs} = 2.55$.

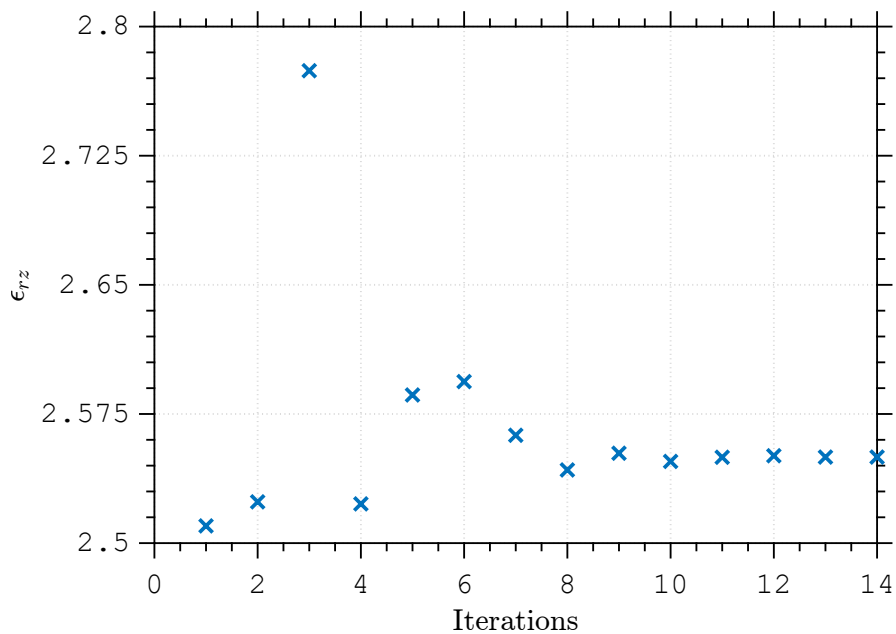


Figure 5.2: Evolution of the optimization parameter as a function of the number of iterations using linear functional. Convergence was achieved after 14 iterations at $\epsilon_{rz} = 2.55$.

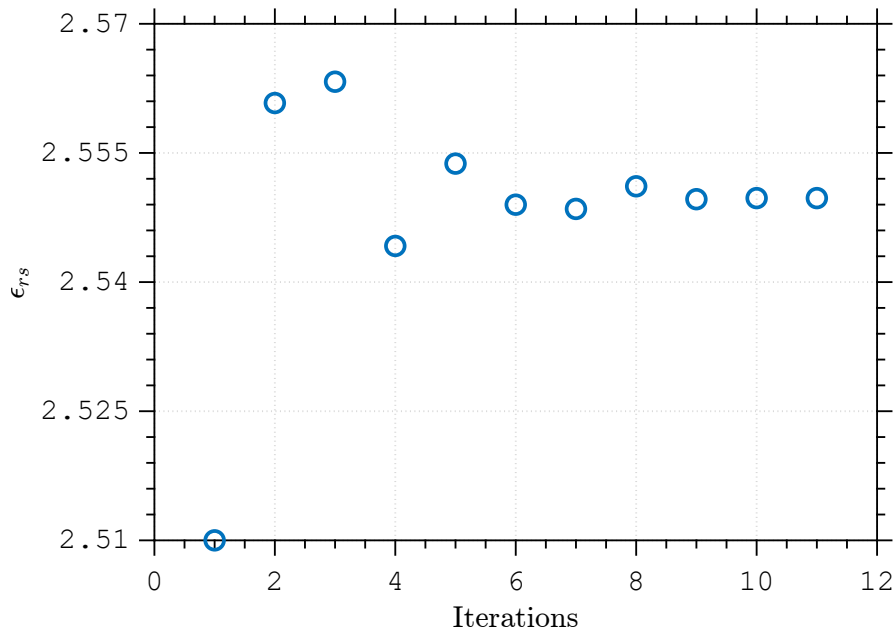


Figure 5.3: Evolution of the optimization parameter as a function of the number of iterations using decibel functional. Convergence was achieved after 11 iterations at $\epsilon_{rs} = 2.55$.

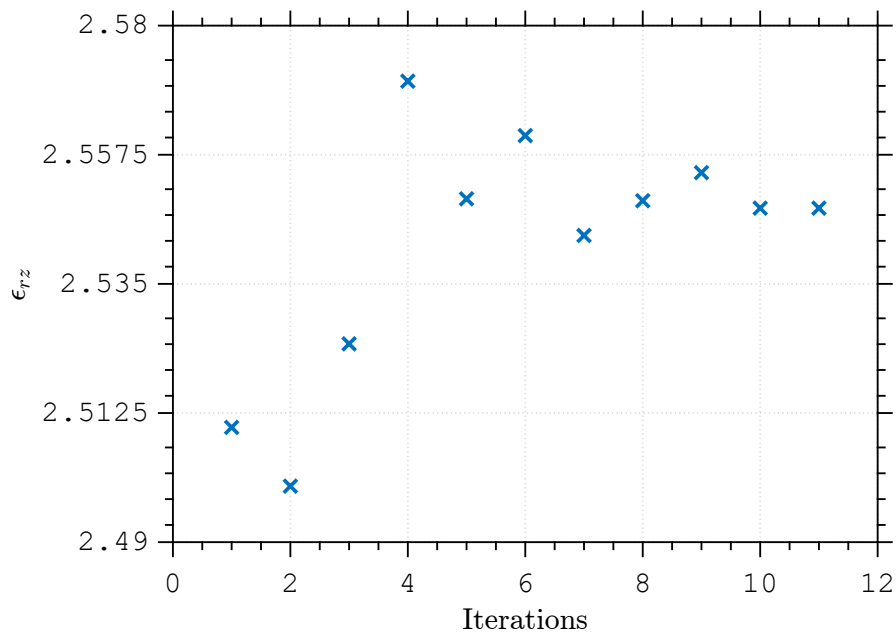


Figure 5.4: Evolution of the optimization parameter as a function of the number of iterations using decibel functional. Convergence was achieved after 11 iterations at $\epsilon_{rz} = 2.55$.

5.1.1.2

Lossy isotropic sample

The second case uses an isotropic material, with isotropic loss. As discussed in the previous case, as it was proved that our algorithm can find ϵ_{rs} equal to ϵ_{rz} for isotropic media, here we will not calculate them separately. The same observation is made to σ . Parameters are in Table 5.4. Results using the linear functional are in Fig. 5.5 and 5.6 and Table 5.5. The initial guess now has the format $x_0 = [\epsilon_r \ \sigma]$. We observe that the convergence was achieved after 11 iterations for a value near $\epsilon_r = 2.55$ and $\sigma = 0.02$ which was the one used in the simulation.

Table 5.4: Geometric and constitutive parameters used on direct problem of a lossy isotropic sample placed in second waveguide of a two-port heterogeneous coaxial waveguide.

Region	L(mm)	ρ_0 (mm)	ρ_1 (mm)	ρ_2 (mm)	ϵ_r	σ
1	-	1.84	2.00	5.00	1.01	10^{-6}
2	10	1.84	3.92	6.00	2.55	2×10^{-2}
3	-	1.84	2.00	5.00	1.01	10^{-6}

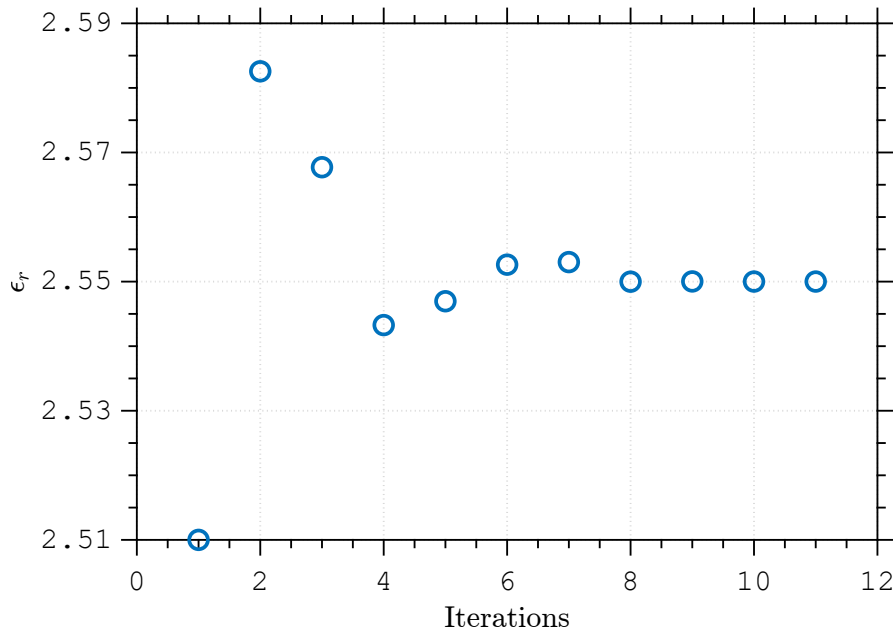


Figure 5.5: Evolution of the optimization parameter as a function of the number of iterations using linear functional. Convergence was achieved after 11 iterations at $\epsilon_r = 2.55$.

Table 5.5: Initial guess, CPU time, and the number of iterations to achieve convergence by using the parameters Table 5.4 using linear functional.

x_0	Time	Iterations
[2.51 0.01]	49 min 41 seconds	11

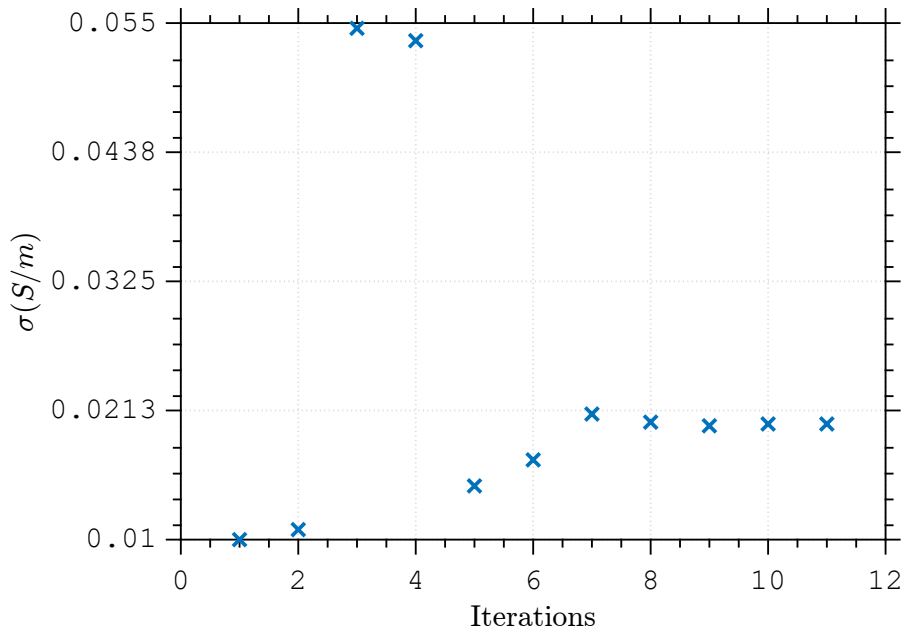


Figure 5.6: Evolution of the optimization parameter as a function of the number of iterations using linear functional. Convergence was achieved after 11 iterations at $\sigma = 0.02$.

For the decibel functions, results are in Fig. 5.7 and 5.8 and in Table 5.6. We observe that the convergence was achieved after 10 iterations for a value near $\epsilon_r = 2.55$ and $\sigma = 0.02$ which was the one used in the simulation.

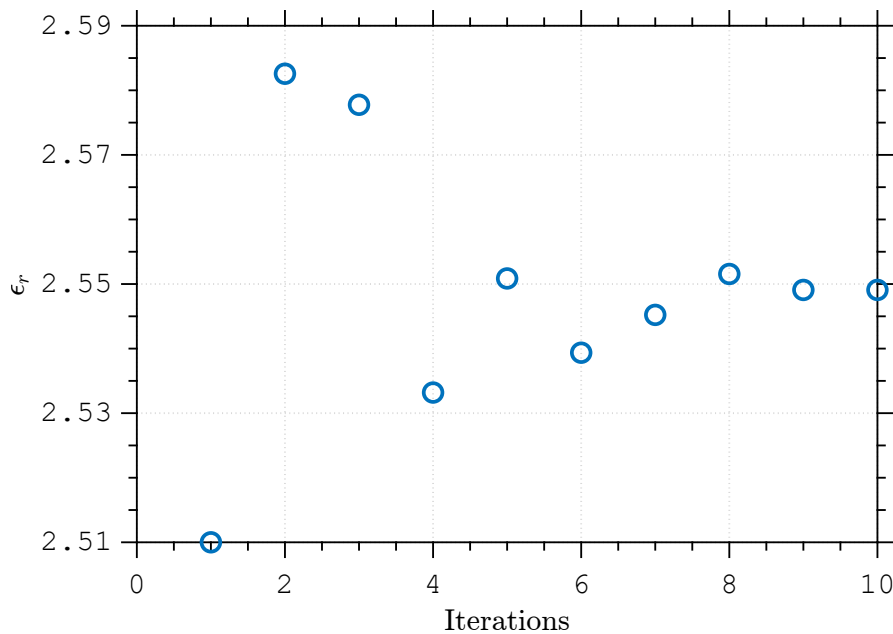


Figure 5.7: Evolution of the optimization parameter as a function of the number of iterations using decibel functional. Convergence was achieved after 10 iterations at $\epsilon_{rS} = 2.55$.

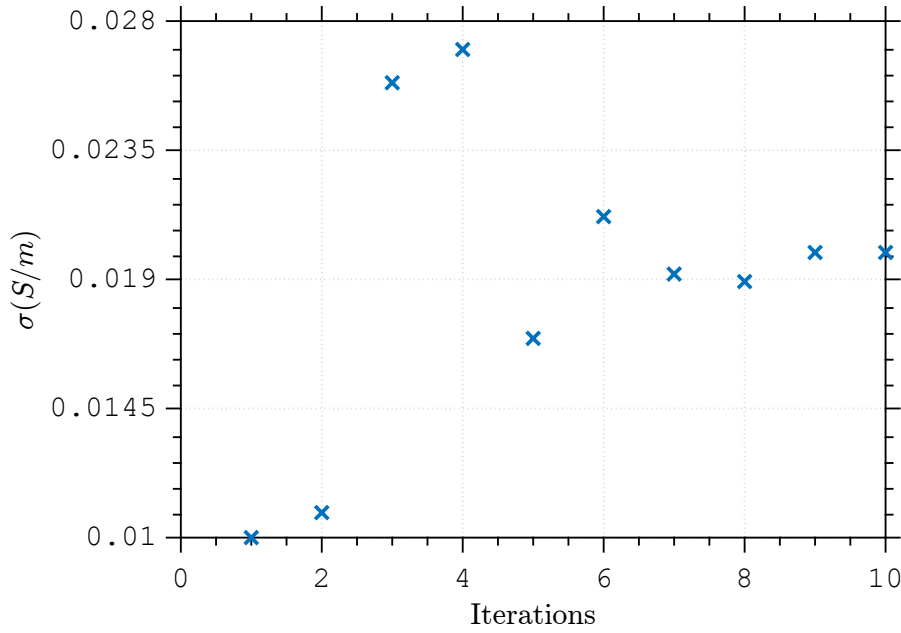


Figure 5.8: Evolution of the optimization parameter as a function of the number of iterations using decibel functional. Convergence was achieved after 10 iterations at $\sigma = 0.02$.

Table 5.6: Initial guess, CPU time, and the number of iterations to achieve convergence by using the parameters Table 5.4 using decibel functional.

x_0	Time	Iterations
[2.51 0.01]	30 min 7 seconds	10

5.1.1.3

Lossless anisotropic sample

The third case presents an anisotropic sample without losses. The parameters used are in Table 5.7 and results using the linear functional are in Fig. 5.9 and 5.10 and in Table 5.8. The initial guess are in the same format as in the lossless isotropic case. We observe that the convergence was achieved after 15 iterations for a value near $\epsilon_{rs} = 2.55$, $\epsilon_{rz} = 3$ which was the one used in the simulation.

Table 5.7: Geometric and constitutive parameters used on direct problem of a lossless anisotropic sample placed in second waveguide of a two-port heterogeneous coaxial waveguide

Region	L(mm)	ρ_0 (mm)	ρ_1 (mm)	ρ_2 (mm)	ϵ_{rs1}	ϵ_{rz1}	σ_{s1}	σ_{z1}
1	-	1.84	2.00	5.00	1.01	1.01	10^{-6}	10^{-6}
2	10	1.84	3.92	6.00	2.55	3.00	10^{-6}	10^{-6}
3	-	1.84	2.00	5.00	1.01	1.01	10^{-6}	10^{-6}

Results when using the decibel functional are in Fig. 5.11 and 5.12 and Table 5.9. We observe that the convergence was achieved after 9 iterations for a value near $\epsilon_{rs} = 2.55$, $\epsilon_{rz} = 3$ which was the one used in the simulation.

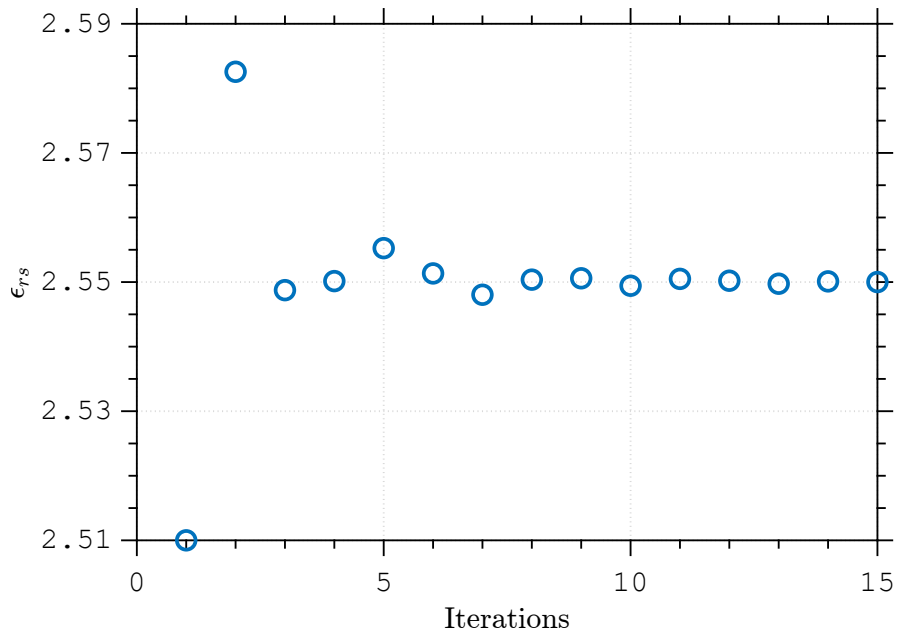


Figure 5.9: Evolution of the optimization parameter as a function of the number of iterations using linear functional. Convergence was achieved after 15 iterations at $\epsilon_{rs} = 2.55$.

PUC-Rio - Certificação Digital N° 2012321/CA

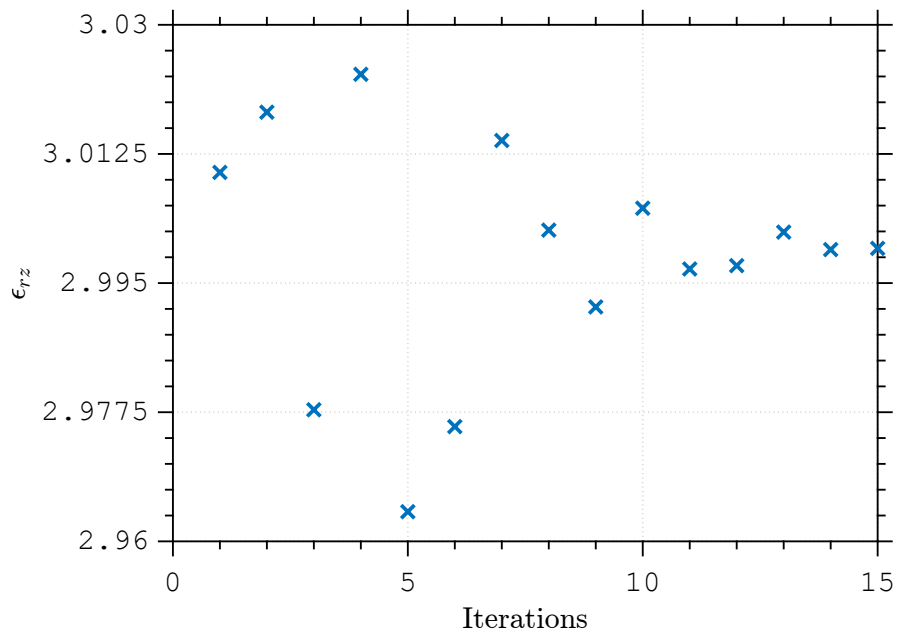


Figure 5.10: Evolution of the optimization parameter as a function of the number of iterations using linear functional. Convergence was achieved after 15 iterations at $\epsilon_{rz} = 3$.

Table 5.8: Initial guess, CPU time, and the number of iterations to achieve convergence by using the parameters Table 5.7 using linear functional.

x_0	Time	Iterations
[2.51 3.01]	105 min 45 seconds	15

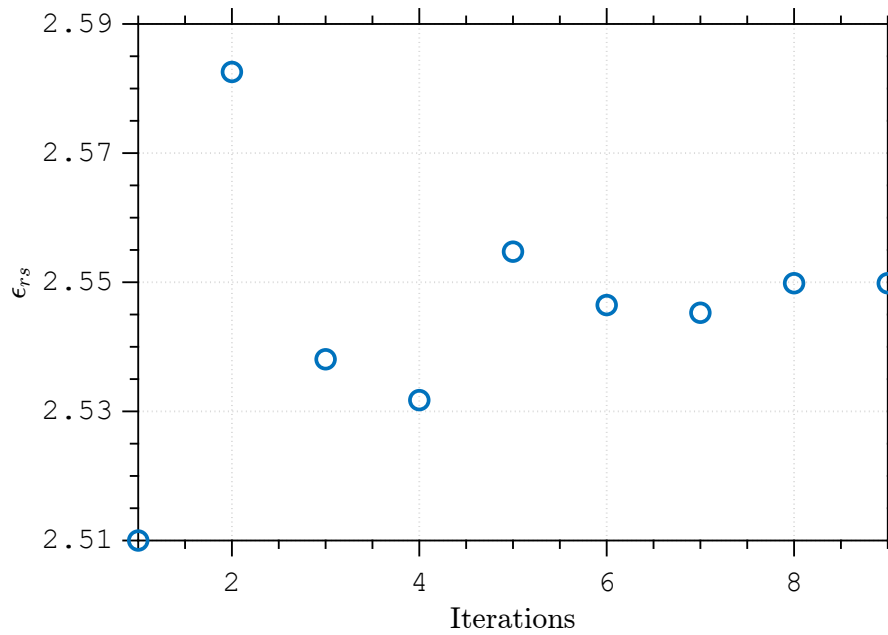


Figure 5.11: Evolution of the optimization parameter as a function of the number of iterations using decibel functional. Convergence was achieved after 9 iterations at $\epsilon_{rs} = 2.55$.

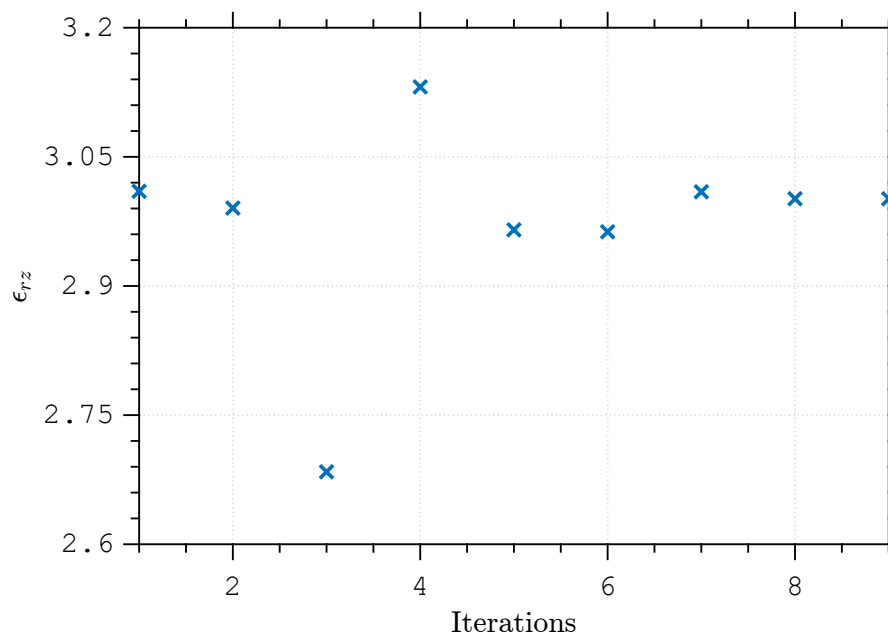


Figure 5.12: Evolution of the optimization parameter as a function of the number of iterations using decibel functional. Convergence was achieved after 9 iterations at $\epsilon_{rz} = 3$.

Table 5.9: Initial guess, CPU time, and the number of iterations to achieve convergence by using the parameters Table 5.7 using decibel functional

x_0	Time	Iterations
[2.51 3.01]	138 min 37 seconds	9

5.1.1.4

Anisotropic sample with isotropic loss

In this simulation we used an anisotropic material with isotropic loss. Parameters used are in Table 5.10. Results for the linear functional are in Fig. 5.13, 5.14, 5.15 and 5.16. Informations about the optimization algorithm are in Table 5.11. The initial guess has the format $x_0 = [\epsilon_{rs} \ \epsilon_{rz} \ \sigma_s \ \sigma_z]$. We observe that the convergence was achieved after 27 iterations for a value near $\epsilon_{rs} = 2.55$, $\epsilon_{rz} = 3$, $\sigma_s = 0.02$ and $\sigma_z = 0.02$ which was the one used in the simulation.

Table 5.10: Geometric and constitutive parameters used on direct problem of a isotropic loss and anisotropic sample placed in second waveguide of a two-port heterogeneous coaxial waveguide

Region	L(mm)	ρ_0 (mm)	ρ_1 (mm)	ρ_2 (mm)	ϵ_{rs1}	ϵ_{rz1}	σ_{s1}	σ_{z1}
1	-	1.84	2.00	5.00	1.01	1.01	10^{-6}	10^{-6}
2	10	1.84	3.92	6.00	2.55	3.00	2×10^{-2}	2×10^{-2}
3	-	1.84	2.00	5.00	1.01	1.01	10^{-6}	10^{-6}

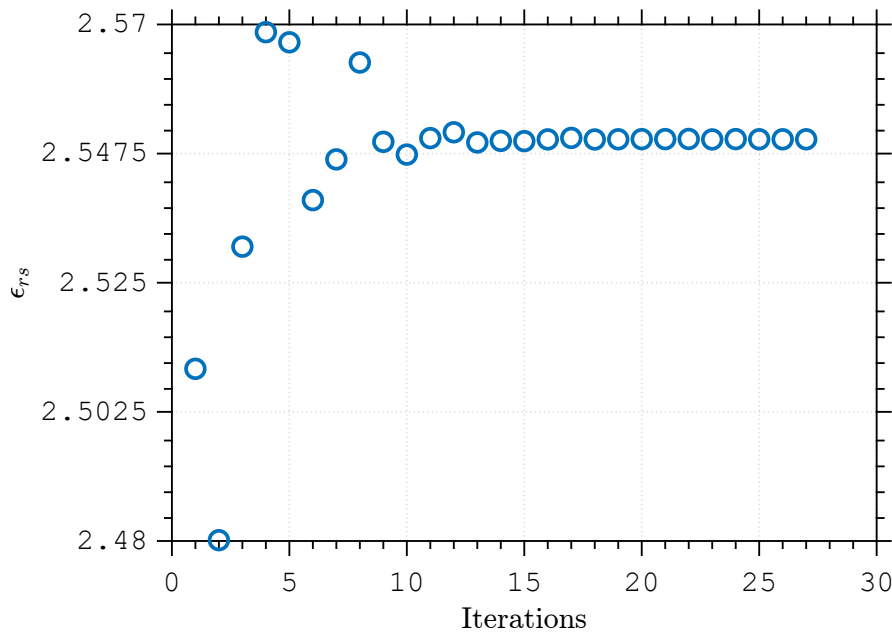


Figure 5.13: Evolution of the optimization parameter as a function of the number of iterations using linear functional. Convergence was achieved after 27 iterations at $\epsilon_{rs} = 2.55$.

Table 5.11: Initial guess, CPU time, and the number of iterations to achieve convergence by using the parameters Table 5.10 using linear functional.

x_0	Time	Iterations
[2.51 3.51 0.01 0.01]	153 min 2 seconds	27

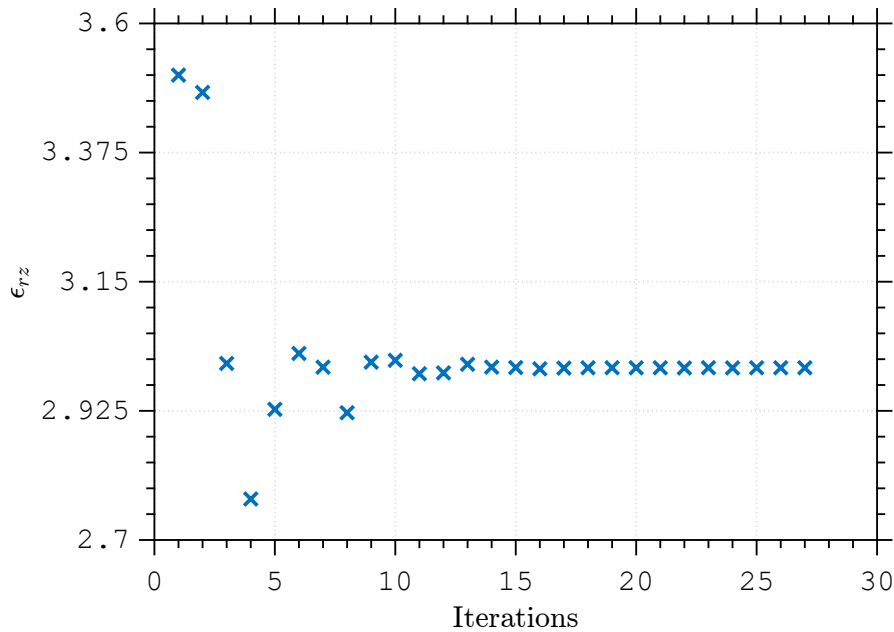


Figure 5.14: Evolution of the optimization parameter as a function of the number of iterations using linear functional. Convergence was achieved after 27 iterations at $\epsilon_{rz} = 3$.

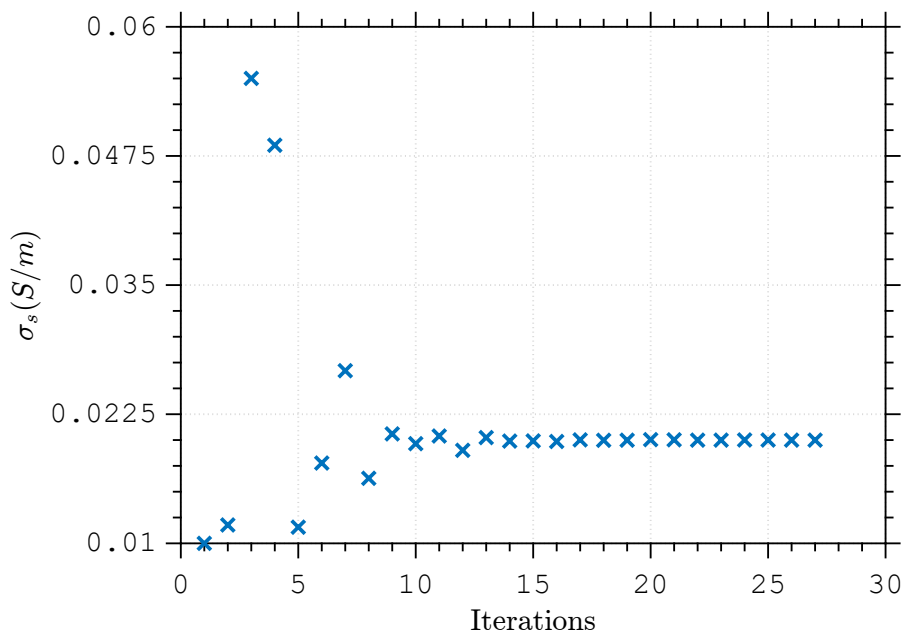


Figure 5.15: Evolution of the optimization parameter as a function of the number of iterations using linear functional. Convergence was achieved after 27 iterations at $\sigma_s = 0.02$.

For the decibel functional, the results obtained are in Fig. 5.17, 5.18, 5.19 and 5.20 and in Table 5.12. We observe that the convergence was achieved after 4 iterations for a value near $\epsilon_{rs} = 2.57$, $\epsilon_{rz} = 2.89$, $\sigma_s = 0.02$ and $\sigma_z = 0.02$ with a small difference from the ones used in simulation.

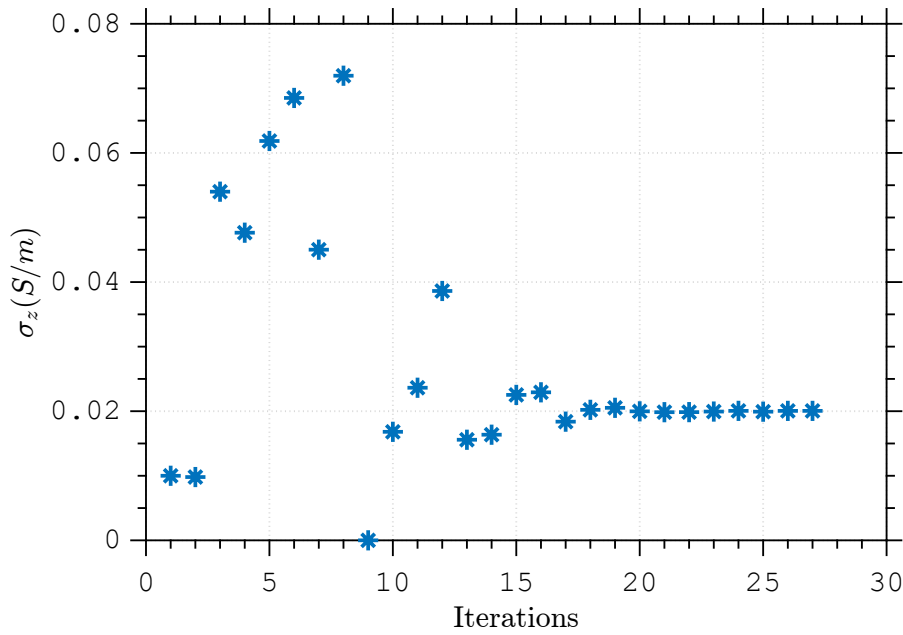


Figure 5.16: Evolution of the optimization parameter as a function of the number of iterations using linear functional. Convergence was achieved after 27 iterations at $\sigma_z = 0.02$.

PUC-Rio - Certificação Digital N° 2012321/CA

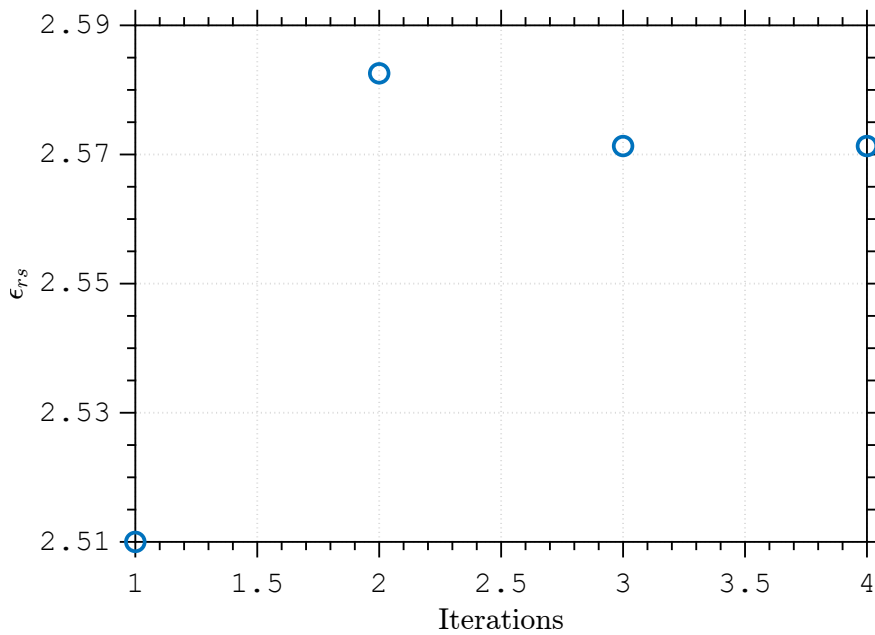


Figure 5.17: Evolution of the optimization parameter as a function of the number of iterations using decibel functional. Convergence was achieved after 4 iterations at $\epsilon_{rs} = 2.57$.

Table 5.12: Initial guess, CPU time, and the number of iterations to achieve convergence by using the parameters Table 5.10 using decibel functional.

x_0	Time	Iterations
[2.51 3.01 0.01 0.01]	197 min 41 seconds	4

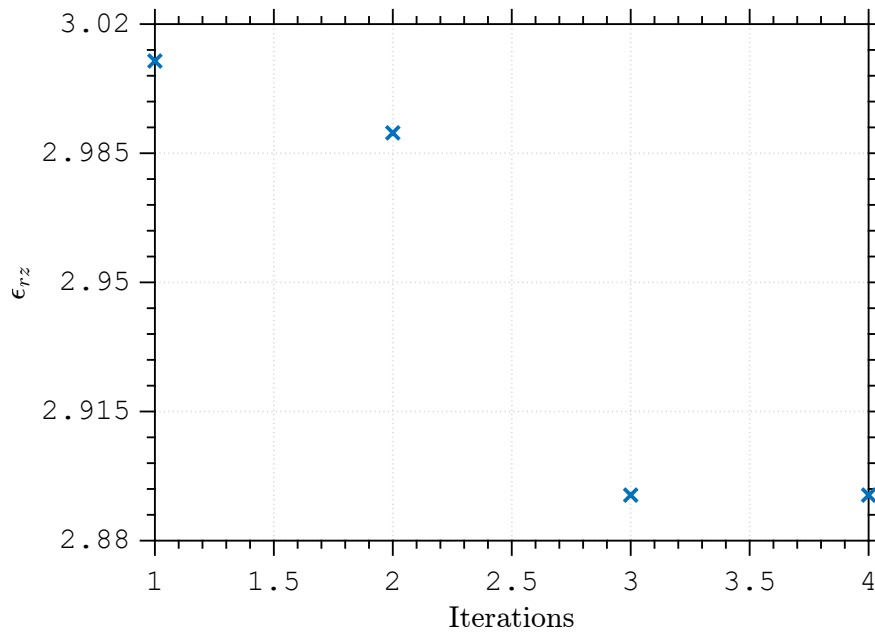


Figure 5.18: Evolution of the optimization parameter as a function of the number of iterations using decibel functional. Convergence was achieved after 4 iterations at $\epsilon_{rz} = 2.89$.

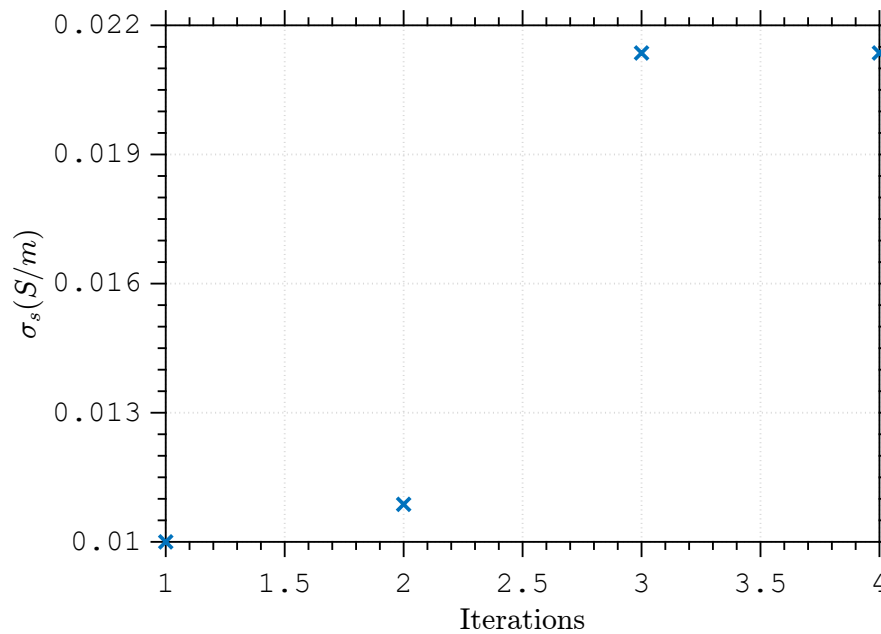


Figure 5.19: Evolution of the optimization parameter as a function of the number of iterations using decibel functional. Convergence was achieved after 4 iterations at $\sigma_s = 0.02$.

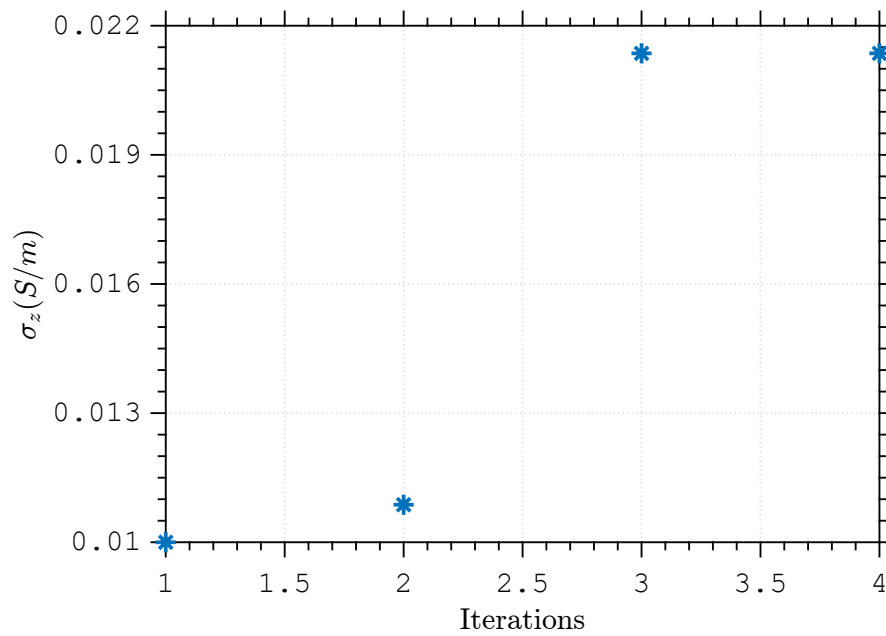


Figure 5.20: Evolution of the optimization parameter as a function of the number of iterations using decibel functional. Convergence was achieved after 4 iterations at $\sigma_z = 0.02$.

5.1.1.5 Anisotropic sample with anisotropic loss

The last case using an heterogeneous coaxial waveguide simulates an anisotropic material with anisotropic losses. Parameters are in Table 5.13. Results for the linear functional can be seen in Fig. 5.21, 5.22, 5.23 and 5.24 and in Table 5.14. The initial guess x_0 has the same format as the one presented in the previous case. We observe that the convergence was achieved after 21 iterations for a value near $\epsilon_{rs} = 2.55$, $\epsilon_{rz} = 3$, $\sigma_s = 0.1$ and $\sigma_z = 0.02$ which was the one used in the simulation.

Table 5.13: Geometric and constitutive parameters used on direct problem of a anisotropic lossy and anisotropic sample placed in second waveguide of a two-port heterogeneous coaxial waveguide

Region	L(mm)	ρ_0 (mm)	ρ_1 (mm)	ρ_2 (mm)	ϵ_{rs1}	ϵ_{rz1}	σ_{s1}	σ_{z1}
1	-	1.84	2.00	5.00	1.01	1.01	10^{-6}	10^{-6}
2	10	1.84	3.92	6.00	2.55	3.00	10^{-1}	2×10^{-2}
3	-	1.84	2.00	5.00	1.01	1.01	10^{-6}	10^{-6}

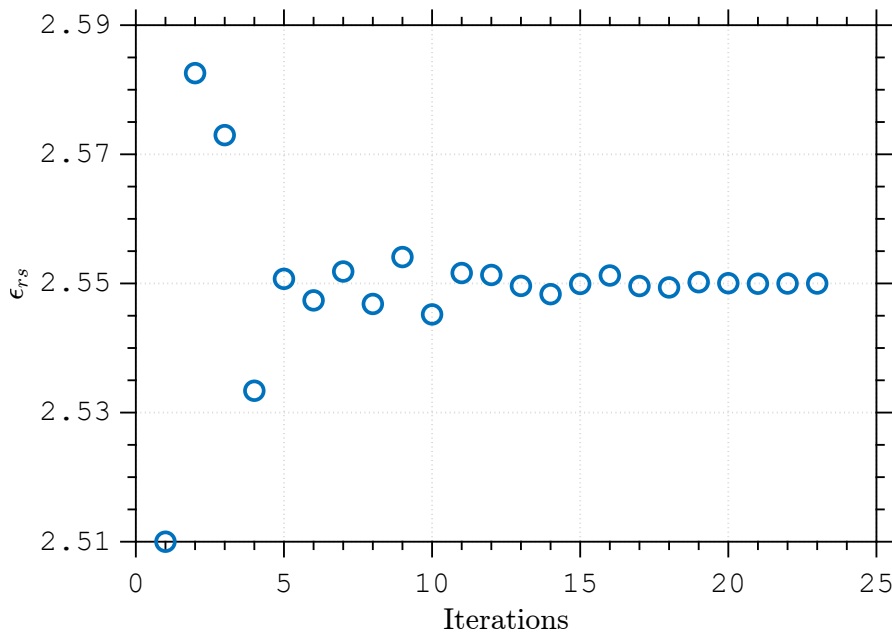


Figure 5.21: Evolution of the optimization parameter as a function of the number of iterations using linear functional. Convergence was achieved after 23 iterations at $\epsilon_{rs} = 2.55$.

Table 5.14: Initial guess, CPU time, and the number of iterations to achieve convergence by using the parameters Table 5.13 using linear functional.

x_0	Time	Iterations
[2.51 3.01 0.01 0.01]	135 min 25 seconds	23

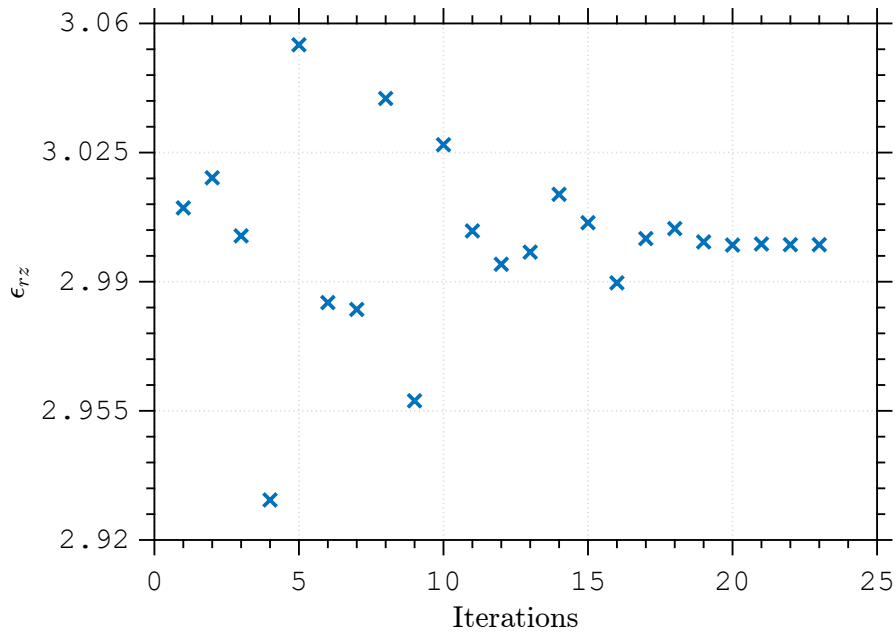


Figure 5.22: Evolution of the optimization parameter as a function of the number of iterations using linear functional. Convergence was achieved after 23 iterations at $\epsilon_{rz} = 3$.

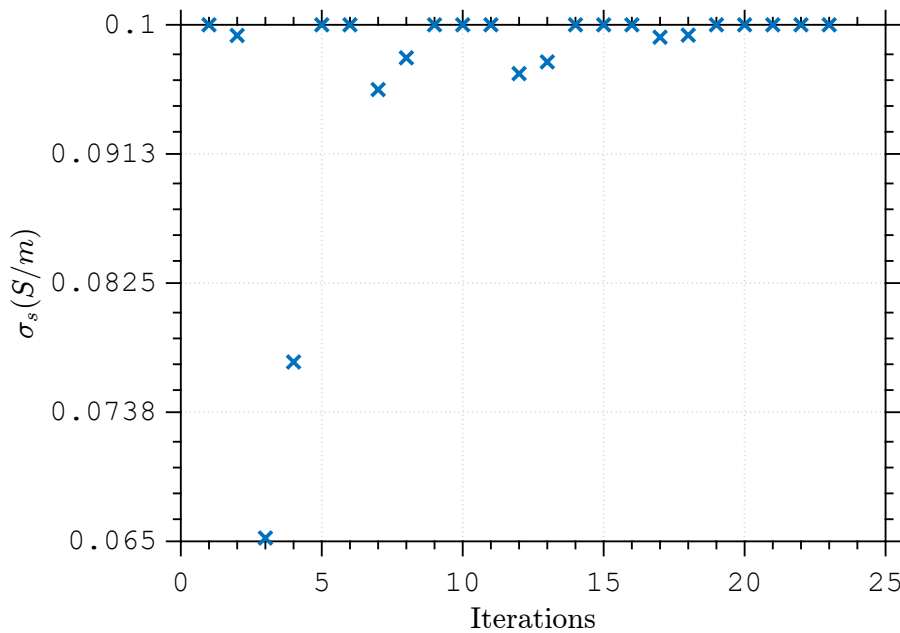


Figure 5.23: Evolution of the optimization parameter as a function of the number of iterations using linear functional. Convergence was achieved after 23 iterations at $\sigma_s = 0.1$.

Results using the decibel functional are in Fig. 5.25, 5.26, 5.27 and 5.28 and in Table 5.15. We observe that the convergence was achieved after 7 iterations for a value near $\epsilon_{rs} = 2.56$, $\epsilon_{rz} = 2.97$, $\sigma_s = 0.1$ and $\sigma_z = 0.02$ with a small difference from the ones used in simulation.

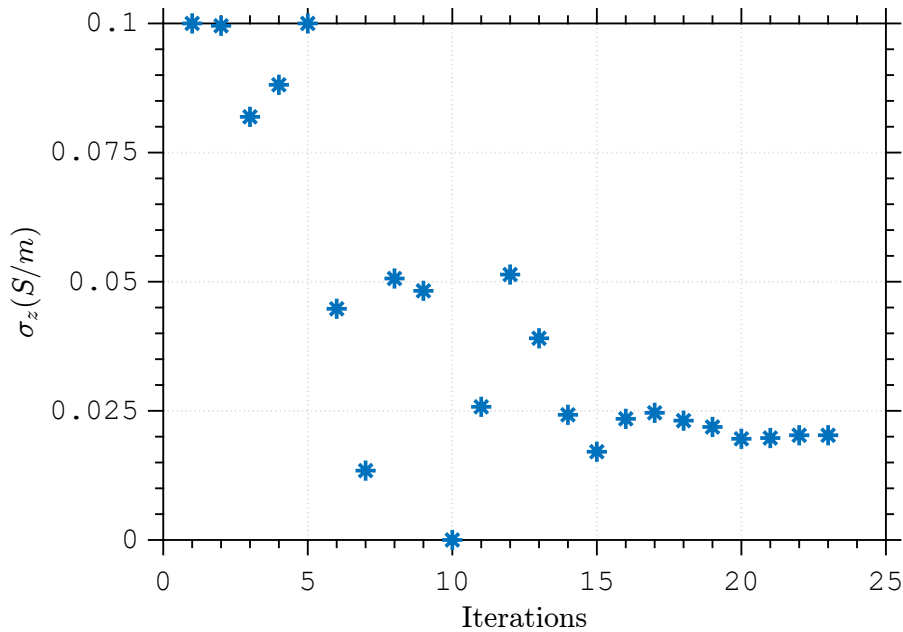


Figure 5.24: Evolution of the optimization parameter as a function of the number of iterations using linear functional. Convergence was achieved after 23 iterations at $\sigma_z = 0.02$.

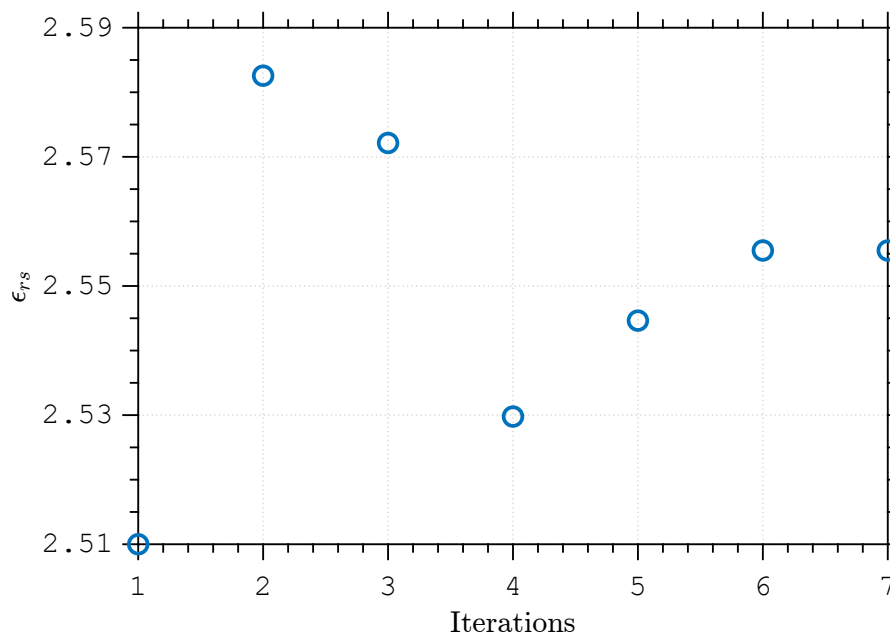


Figure 5.25: Evolution of the optimization parameter as a function of the number of iterations using decibel functional. Convergence was achieved after 7 iterations at $\epsilon_{rs} = 2.56$.

Table 5.15: Initial guess, CPU time, and the number of iterations to achieve convergence by using the parameters Table 5.13 using decibel functional.

x_0	Time	Iterations
[2.51 3.01 0.01 0.01]	204 min 41 seconds	7

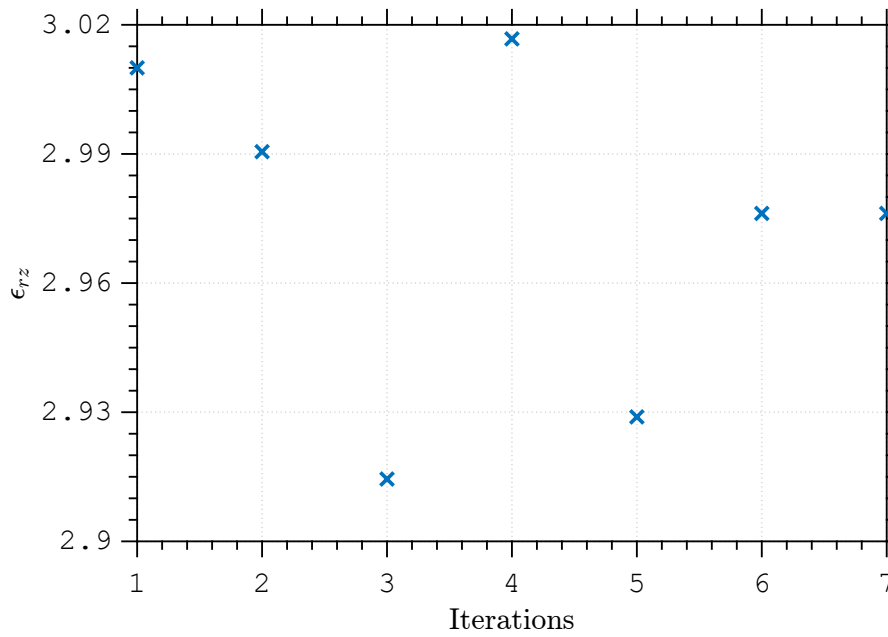


Figure 5.26: Evolution of the optimization parameter as a function of the number of iterations using decibel functional. Convergence was achieved after 7 iterations at $\epsilon_{rz} = 3$.

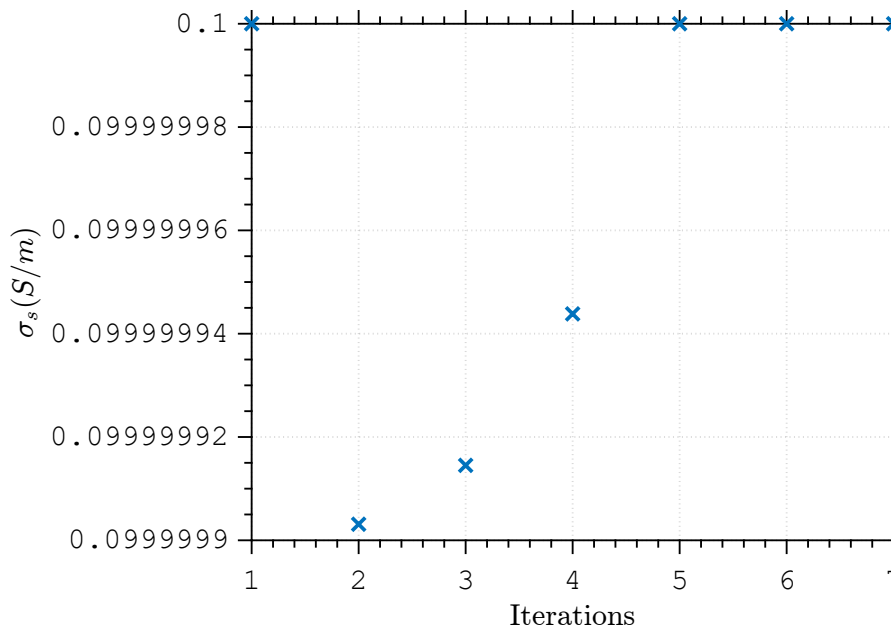


Figure 5.27: Evolution of the optimization parameter as a function of the number of iterations using decibel functional. Convergence was achieved after 7 iterations at $\sigma_s = 0.1$.

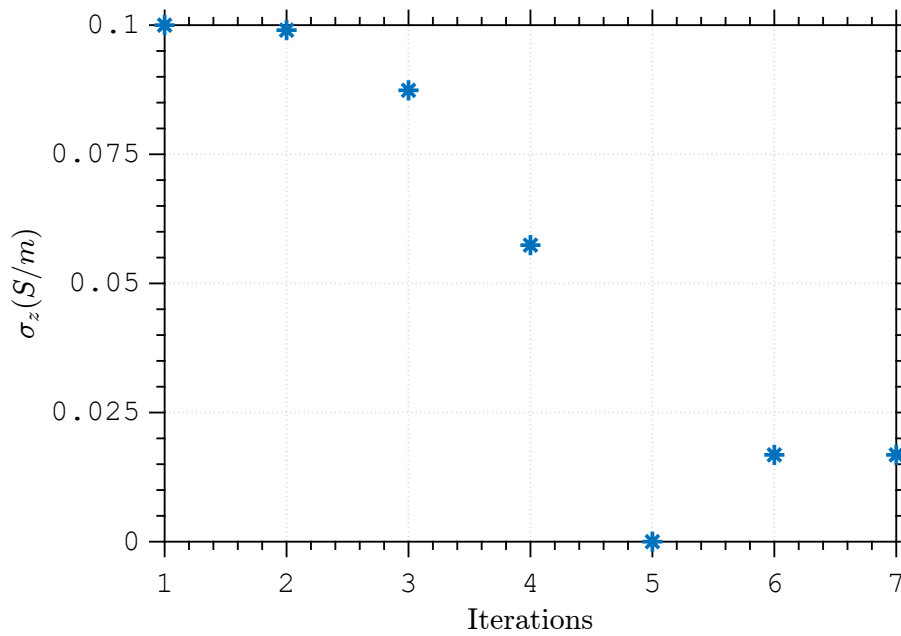


Figure 5.28: Evolution of the optimization parameter as a function of the number of iterations using decibel functional. Convergence was achieved after 7 iterations at $\sigma_z = 0.02$.

5.1.2 Homogeneous Circular Waveguide

Now, it will be considered that the material under test is occupying the entire waveguide in the second region.

5.1.2.1 Lossless isotropic sample

This first simulation used the parameters listed in Table 5.16. Results can be seen in Fig. 5.29 and in Table 5.17 for the linear functional while for the decibel one are in Fig. 5.30 and Table 5.18. We observe that the convergence was achieved after 7 iterations for linear functional and 4 iterations for decibel functional for a value near $\epsilon_r = 2.56$ for both with a small difference from the one used in simulation.

Table 5.16: Geometric and constitutive parameters used on direct problem of a lossless isotropic sample placed in second waveguide of a two-port homogeneous circular waveguide

Region	L(mm)	ρ_0 (mm)	ρ_1 (mm)	ρ_2 (mm)	ϵ_{rs1}	ϵ_{rz1}	σ_{s1}	σ_{z1}
1	-	1.84	2.00	5.00	1.01	1.01	10^{-6}	10^{-6}
2	10	0	6	-	2.55	2.55	10^{-6}	10^{-6}
3	-	1.84	2.00	5.00	1.01	1.01	10^{-6}	10^{-6}

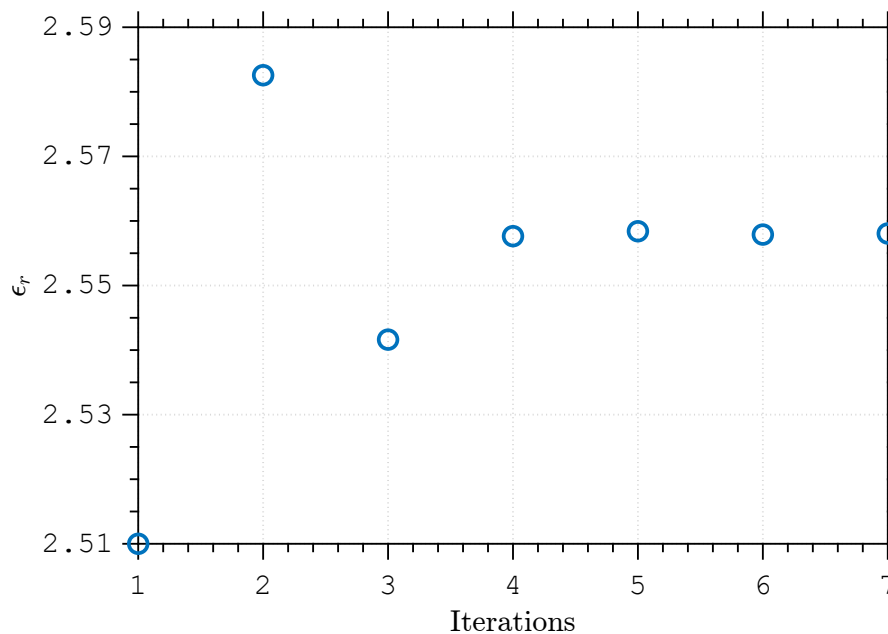


Figure 5.29: Evolution of the optimization parameter as a function of the number of iterations using linear functional. Convergence was achieved after 7 iterations at $\epsilon_r = 2.55$.

Table 5.17: Initial guess, CPU time, and the number of iterations to achieve convergence by using the parameters Table 5.16 using linear functional.

x_0	Time	Iterations
2.51	8 min 28 seconds	7

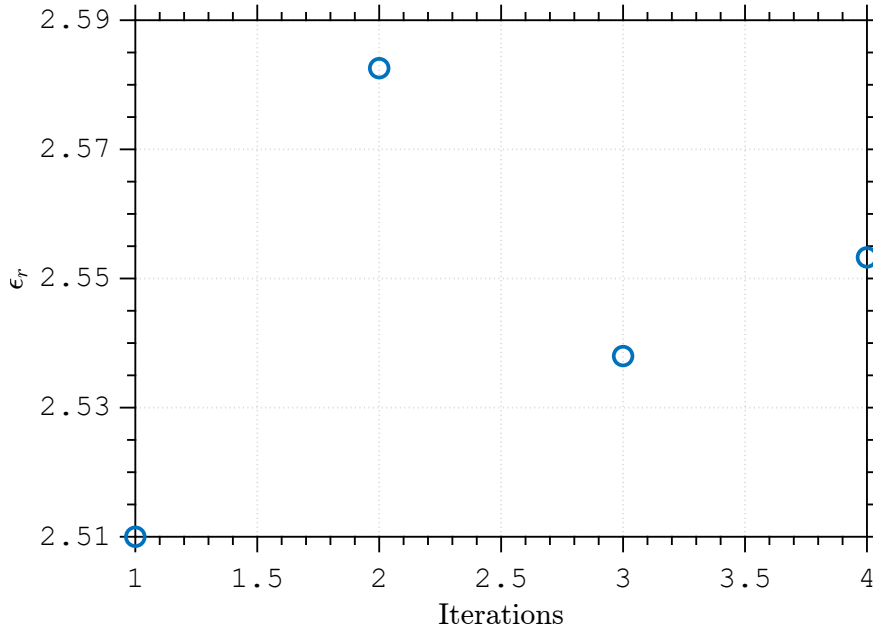


Figure 5.30: Evolution of the optimization parameter as a function of the number of iterations using decibel functional. Convergence was achieved after 4 iterations at $\epsilon_r = 2.55$.

Table 5.18: Initial guess, CPU time, and the number of iterations to achieve convergence by using the parameters Table 5.16 using decibel functional.

x_0	Time	Iterations
2.51	9 min 36 seconds	4

5.1.2.2

Lossy isotropic sample

For the lossy isotropic material, parameters can be observed in Table 5.19 and results for linear functional are in Fig. 5.31 and 5.32 and in Table 5.20. The decibel functional has its results on Fig. 5.33 and 5.34 and in Table 5.21. We observe that the convergence was achieved after 18 iterations for linear functional and 6 iterations for decibel functional for a value near $\epsilon_r = 2.55$ and $\sigma = 0.02$ for linear functional with a good convergence and $\epsilon_r = 2.55$ and $\sigma = 0.015$ for decibel functional with a small difference from the ones used in simulation.

Table 5.19: Geometric and constitutive parameters used on direct problem of a lossy isotropic sample placed in second waveguide of a two-port homogeneous circular waveguide

Region	L(mm)	ρ_0 (mm)	ρ_1 (mm)	ρ_2 (mm)	ϵ_{rs1}	ϵ_{rz1}	σ_{s1}	σ_{z1}
1	-	1.84	2.00	5.00	1.01	1.01	10^{-6}	10^{-6}
2	10	0	6	-	2.55	2.55	2×10^{-2}	2×10^{-2}
3	-	1.84	2.00	5.00	1.01	1.01	10^{-6}	10^{-6}

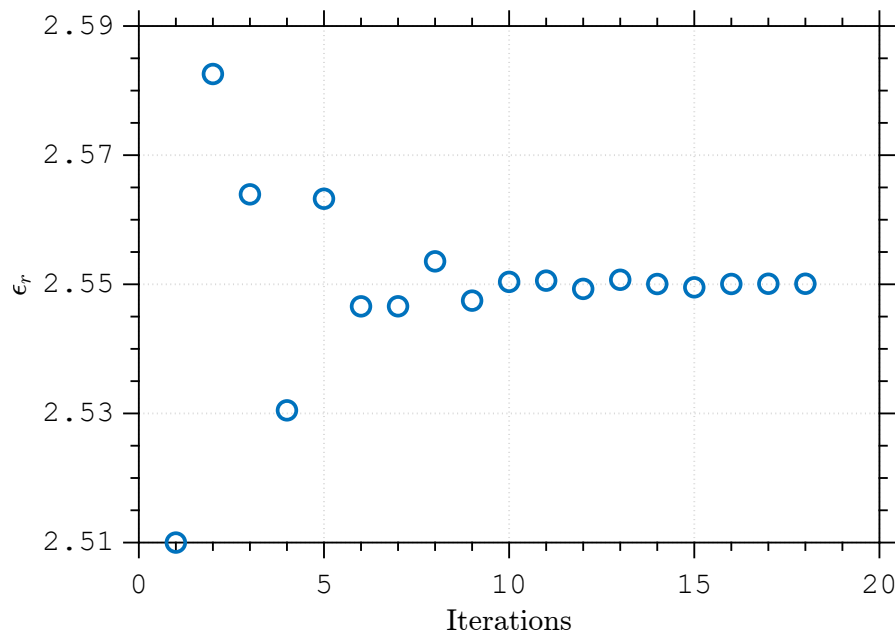


Figure 5.31: Evolution of the optimization parameter as a function of the number of iterations using linear functional. Convergence was achieved after 18 iterations at $\epsilon_r = 2.55$.

Table 5.20: Initial guess, CPU time, and the number of iterations to achieve convergence by using the parameters Table 5.19 using linear functional.

x_0	Time	Iterations
[2.51 0.01]	34 min 12 seconds	18

Table 5.21: Initial guess, CPU time, and the number of iterations to achieve convergence by using the parameters Table 5.19 using decibel functional.

x_0	Time	Iterations
[2.51 0.01]	32 min 53 seconds	6

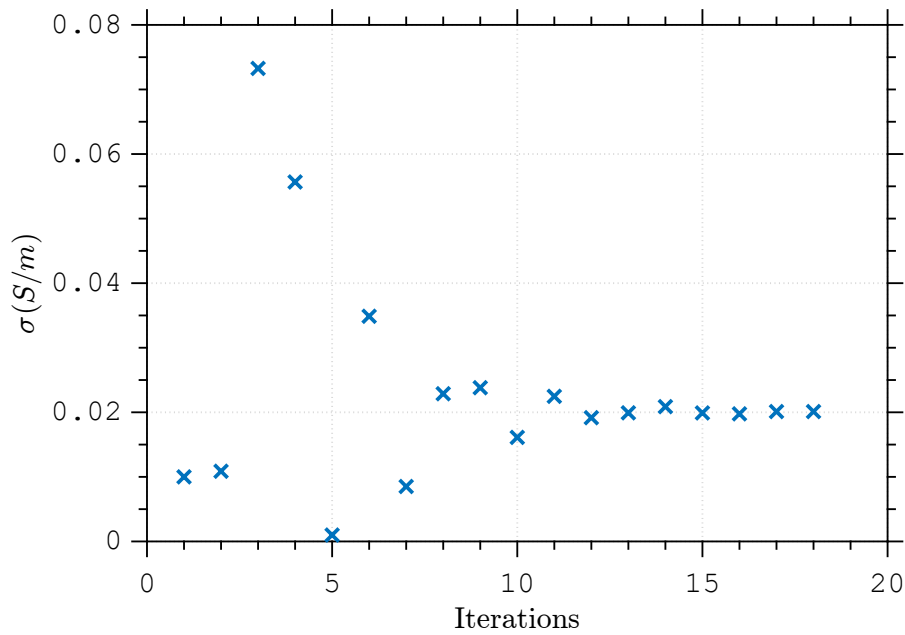


Figure 5.32: Evolution of the optimization parameter as a function of the number of iterations using linear functional. Convergence was achieved after 18 iterations at $\sigma = 0.02$.

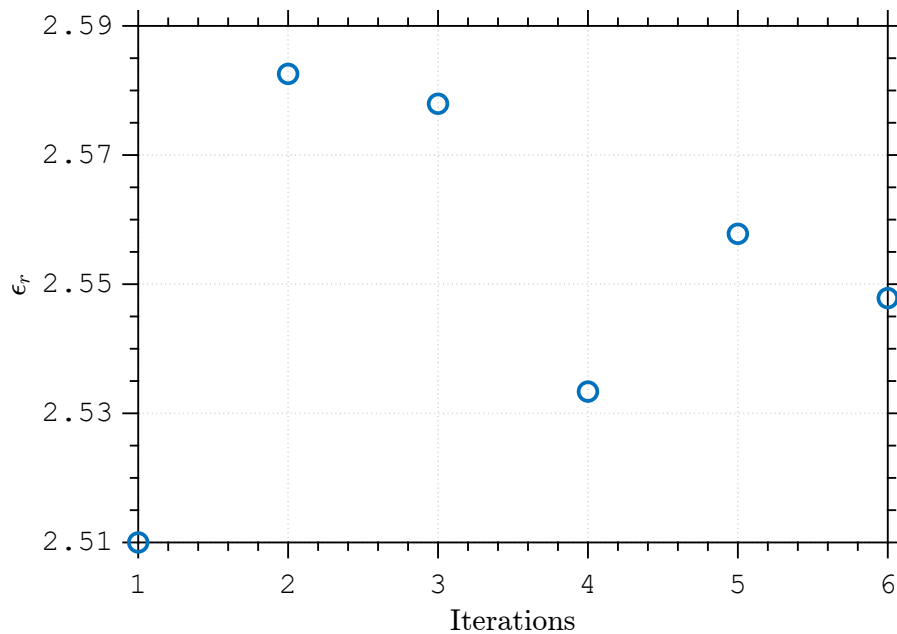


Figure 5.33: Evolution of the optimization parameter as a function of the number of iterations using decibel functional. Convergence was achieved after 18 iterations at $\epsilon_r = 2.55$.

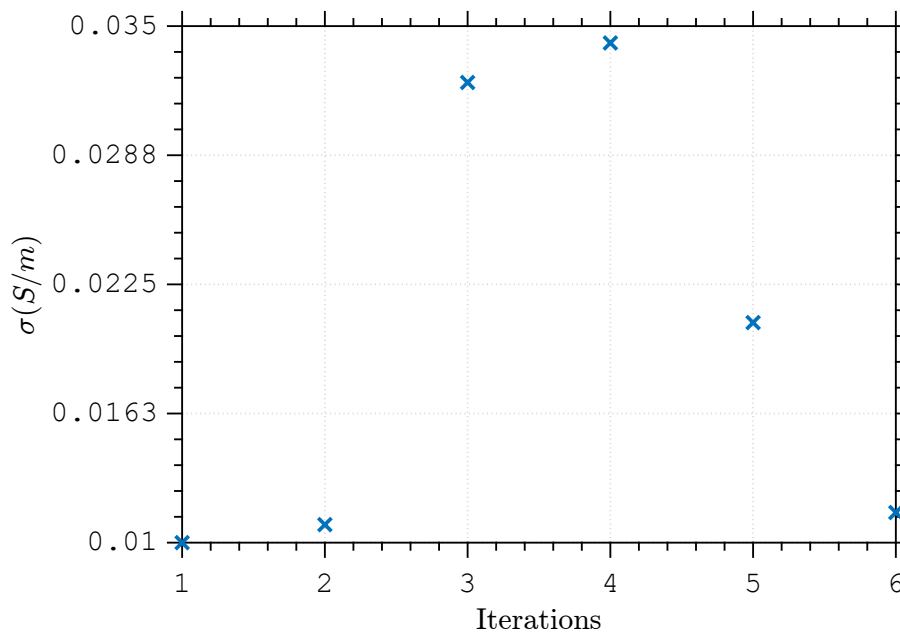


Figure 5.34: Evolution of the optimization parameter as a function of the number of iterations using decibel functional. Convergence was achieved after 18 iterations at $\sigma = 0.015$.

5.1.2.3

Lossless anisotropic sample

For this case, parameters can be seen in Table 5.22. Results for the linear functional are in Fig. 5.35 and 5.36 and in Table 5.23. For decibel functional they are in Fig. 5.37 and 5.38 and in Table 5.24. We observe that the convergence was achieved after 9 iterations for linear functional and 3 iterations for decibel functional for a value near $\epsilon_{rs} = 2.53$ and $\epsilon_{rz} = 3.33$ for linear functional with a small difference from the ones used in simulation and $\epsilon_{rs} = 7.38$ and $\epsilon_{rz} = 5.42$ for decibel functional with a large difference from the ones used in simulation

Table 5.22: Geometric and constitutive parameters used on direct problem of a lossless anisotropic sample placed in second waveguide of a two-port homogeneous circular waveguide

Region	L(mm)	ρ_0 (mm)	ρ_1 (mm)	ρ_2 (mm)	ϵ_{rs1}	ϵ_{rz1}	σ_{s1}	σ_{z1}
1	-	1.84	2.00	5.00	1.01	1.01	10^{-6}	10^{-6}
2	10	0	6	-	2.55	3	10^{-6}	10^{-6}
3	-	1.84	2.00	5.00	1.01	1.01	10^{-6}	10^{-6}

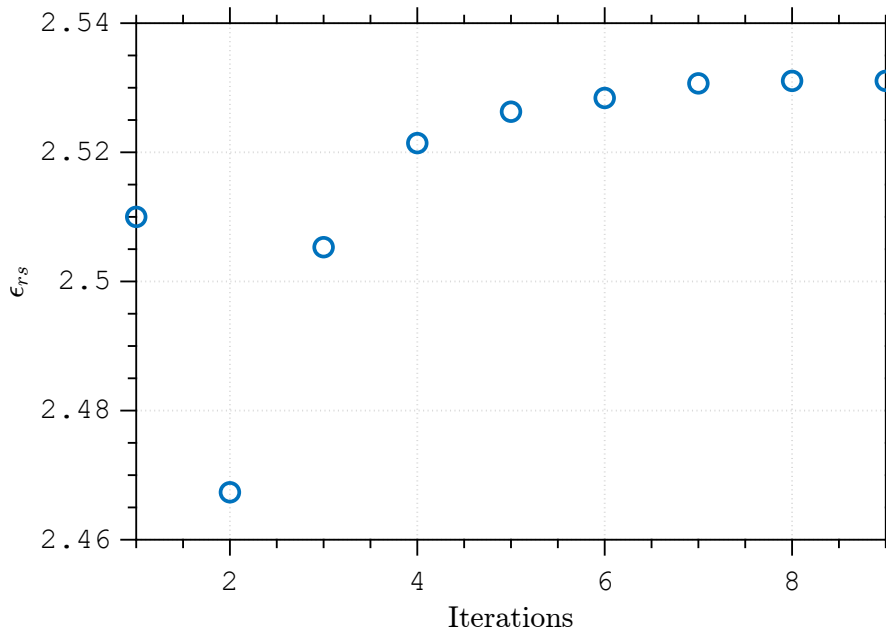


Figure 5.35: Evolution of the optimization parameter as a function of the number of iterations using linear functional. Convergence was achieved after 9 iterations at $\epsilon_{rs} = 2.53$.

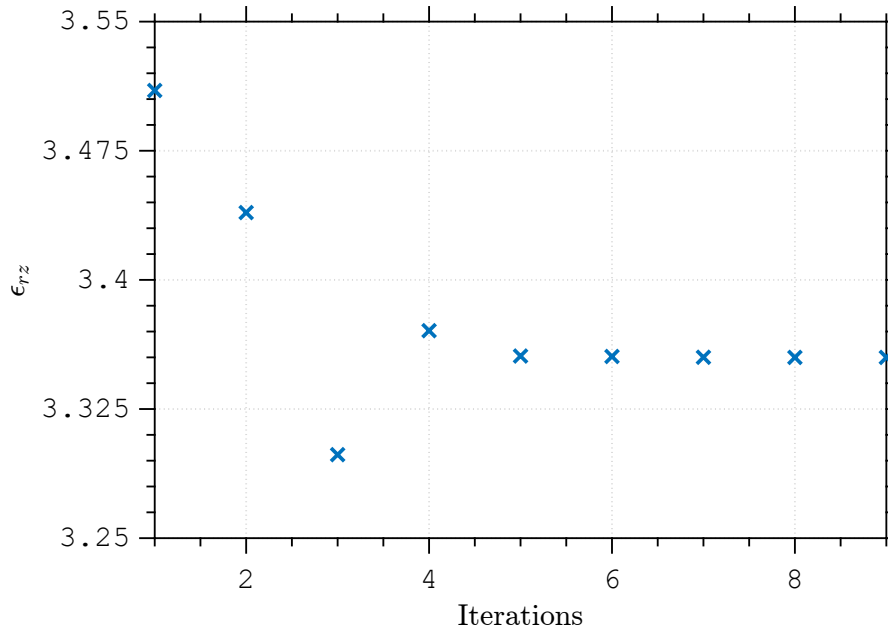


Figure 5.36: Evolution of the optimization parameter as a function of the number of iterations using linear functional. Convergence was achieved after 9 iterations at $\epsilon_{rz} = 3.33$.

Table 5.23: Initial guess, CPU time, and the number of iterations to achieve convergence by using the parameters Table 5.22 using linear functional.

x_0	Time	Iterations
[2.51 3.51]	122 min 15 seconds	9

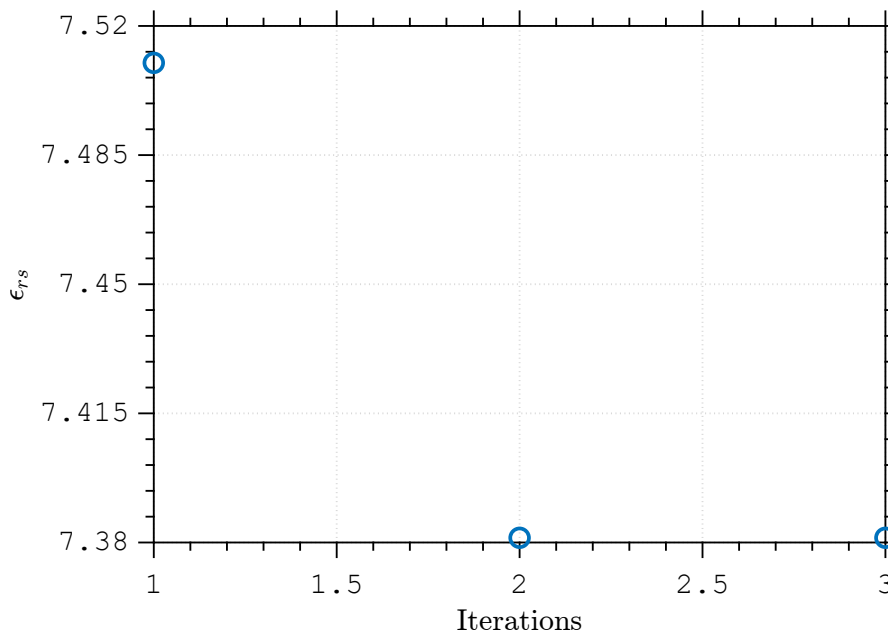


Figure 5.37: Evolution of the optimization parameter as a function of the number of iterations using decibel functional. Convergence was achieved after 3 iterations at $\epsilon_{rs} = 7.38$.

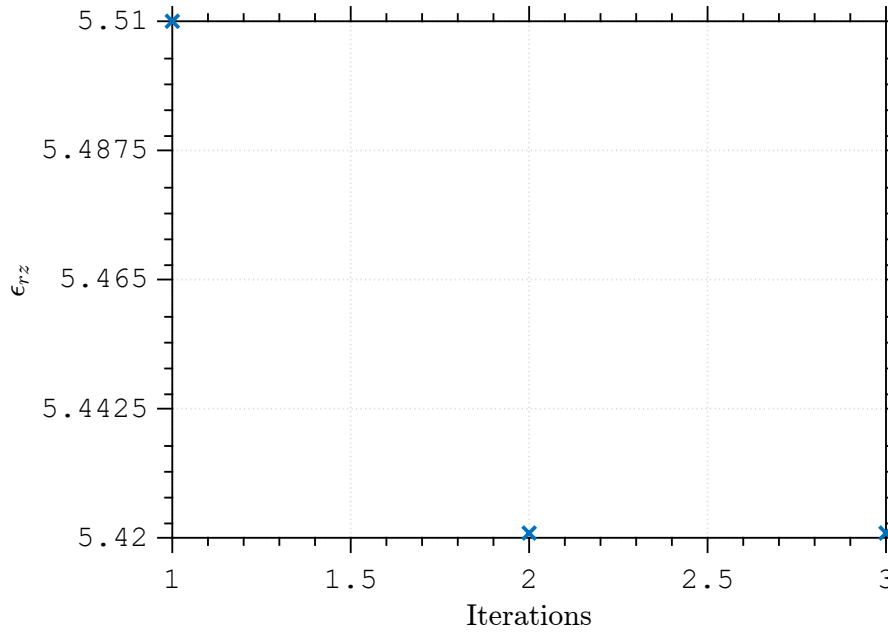


Figure 5.38: Evolution of the optimization parameter as a function of the number of iterations using decibel functional. Convergence was achieved after 3 iterations at $\epsilon_{rz} = 5.42$.

Table 5.24: Initial guess, CPU time, and the number of iterations to achieve convergence by using the parameters Table 5.22 using decibel functional.

x_0	Time	Iterations
[7.51 5.51]	116 min 34 seconds	3

5.1.2.4

Anisotropic sample with isotropic loss

The parameters used to simulate the measurement cell filled with an anisotropic medium with isotropic loss are in Table 5.25. For the linear functional, results are in Fig. 5.39, 5.40, 5.41 and 5.42 and in Table 5.26. For the decibel functional, they can be seen in Fig. 5.43, 5.44, 5.45 and 5.46 and in Table 5.27. We observe that the convergence was achieved after 19 iterations for linear functional and 5 iterations for decibel functional for a value near $\epsilon_{rs} = 2.55$, $\epsilon_{rz} = 3$, $\sigma_s = 0.01$ and $\sigma_z = 0.01$ for linear functional with a good convergence from the ones used in simulation and $\epsilon_{rs} = 2.55$, $\epsilon_{rz} = 2.95$, $\sigma_s = 0.008$ and $\sigma_z = 0.008$ for decibel functional with a small difference from the ones used in simulation

Table 5.25: Geometric and constitutive parameters used on direct problem of a isotropic lossy and anisotropic sample placed in second waveguide of a two-port homogeneous circular waveguide

Region	L(mm)	ρ_0 (mm)	ρ_1 (mm)	ρ_2 (mm)	ϵ_{rs1}	ϵ_{rz1}	σ_{s1}	σ_{z1}
1	-	1.84	2.00	5.00	1.01	1.01	10^{-6}	10^{-6}
2	10	0	6	-	2.55	3	10^{-2}	10^{-2}
3	-	1.84	2.00	5.00	1.01	1.01	10^{-6}	10^{-6}

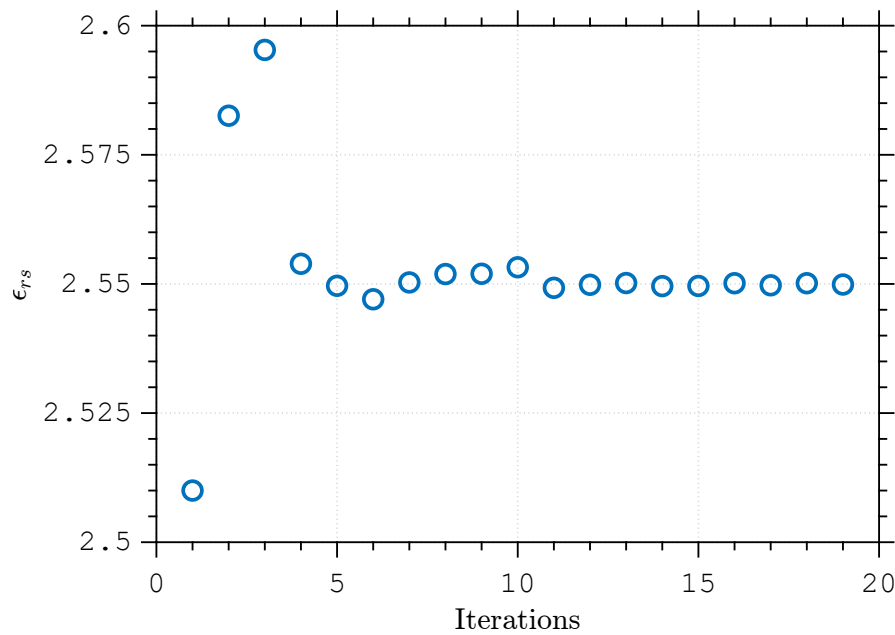


Figure 5.39: Evolution of the optimization parameter as a function of the number of iterations using linear functional. Convergence was achieved after 19 iterations at $\epsilon_{rs} = 2.55$.

Table 5.26: Initial guess, CPU time, and the number of iterations to achieve convergence by using the parameters Table 5.25 using linear functional.

x_0	Time	Iterations
[2.51 3.01 0.01 0.01]	121 min 9 seconds	19

Table 5.27: Initial guess, CPU time, and the number of iterations to achieve convergence by using the parameters Table 5.25 using decibel functional.

x_0	Time	Iterations
[2.51 3.01 0.01 0.01]	93 min 7 seconds	5

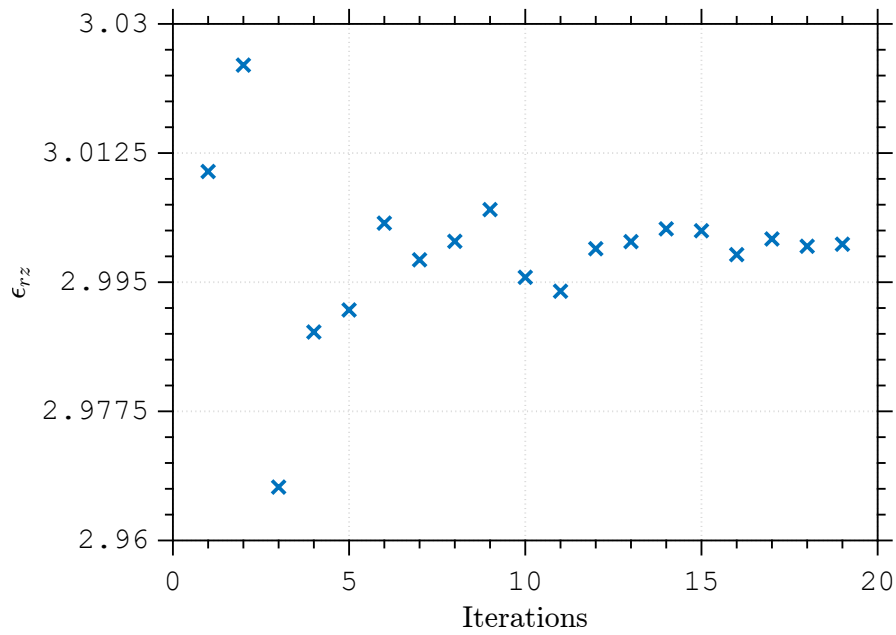


Figure 5.40: Evolution of the optimization parameter as a function of the number of iterations using linear functional. Convergence was achieved after 19 iterations at $\epsilon_{rz} = 3$.

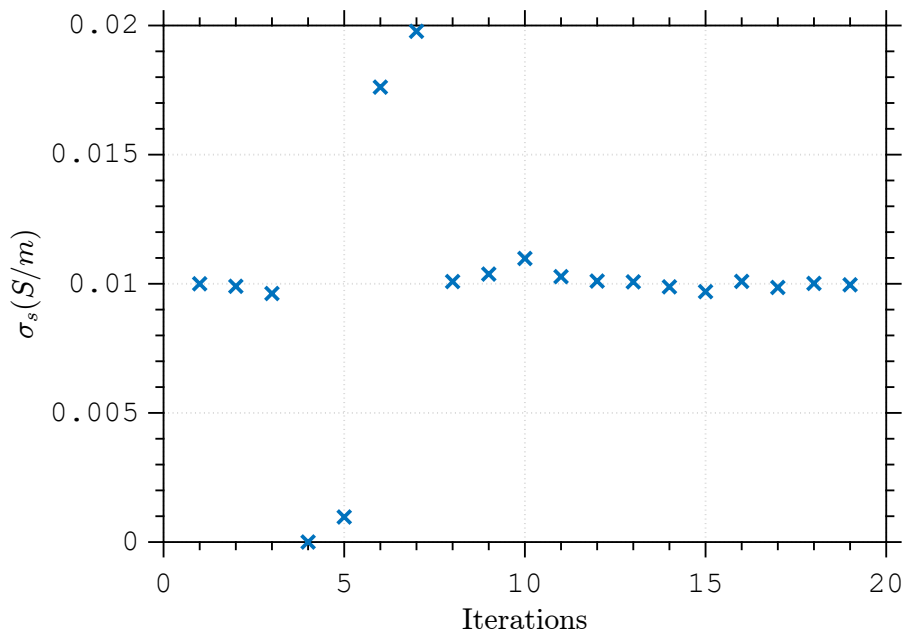


Figure 5.41: Evolution of the optimization parameter as a function of the number of iterations using linear functional. Convergence was achieved after 19 iterations at $\sigma_s = 0.01$.

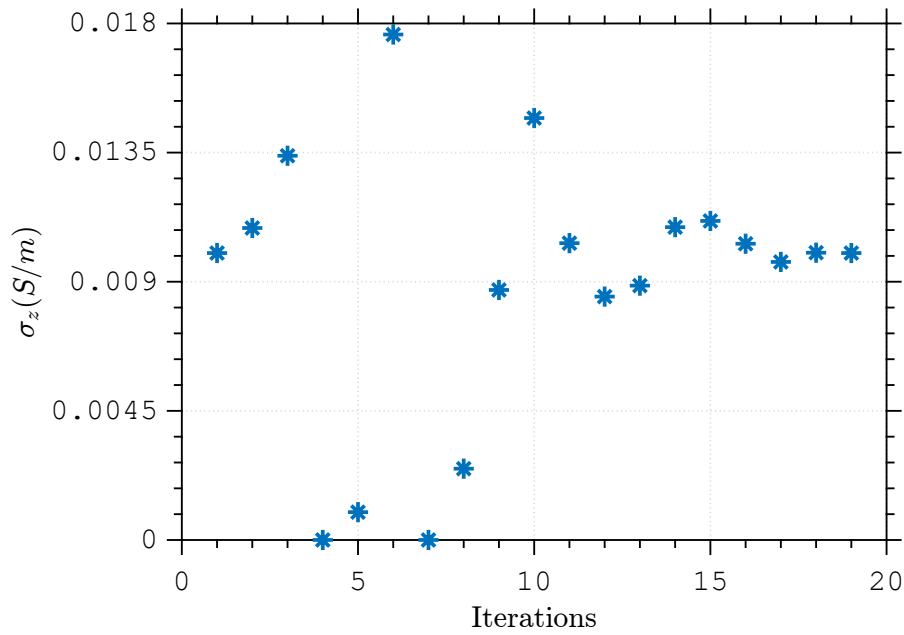


Figure 5.42: Evolution of the optimization parameter as a function of the number of iterations using linear functional. Convergence was achieved after 19 iterations at $\sigma_z = 0.01$.

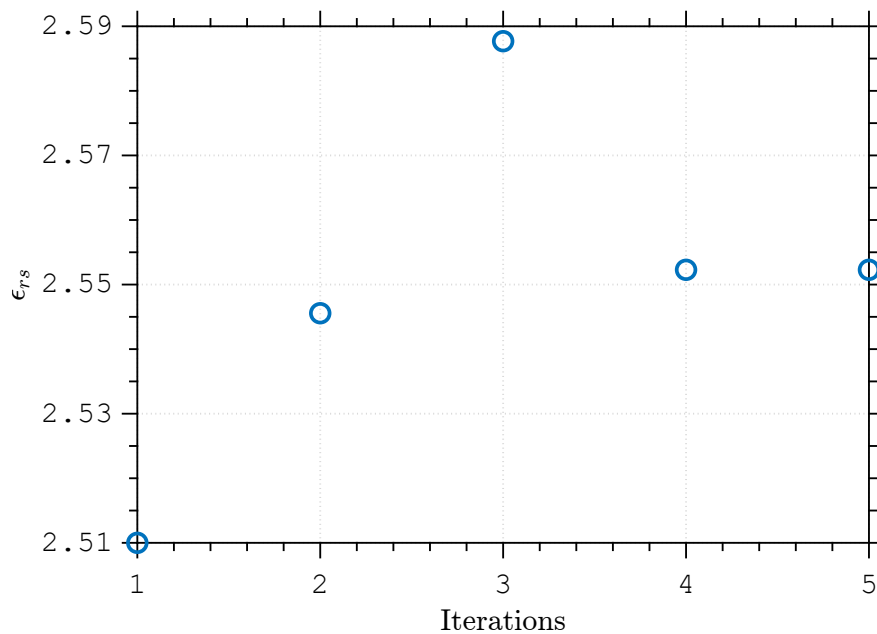


Figure 5.43: Evolution of the optimization parameter as a function of the number of iterations using decibel functional. Convergence was achieved after 5 iterations at $\epsilon_{rs} = 2.55$.

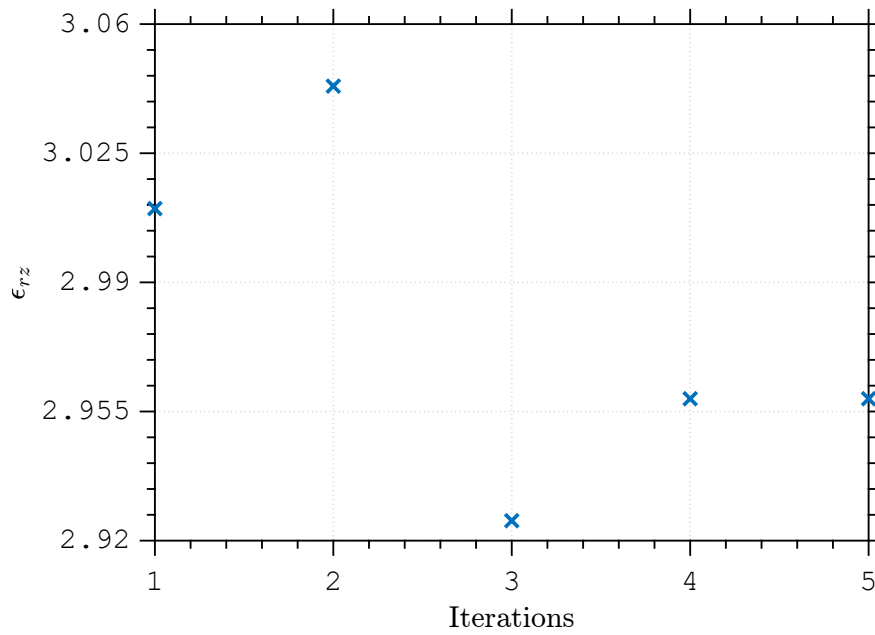


Figure 5.44: Evolution of the optimization parameter as a function of the number of iterations using decibel functional. Convergence was achieved after 5 iterations at $\epsilon_{rz} = 2.95$.

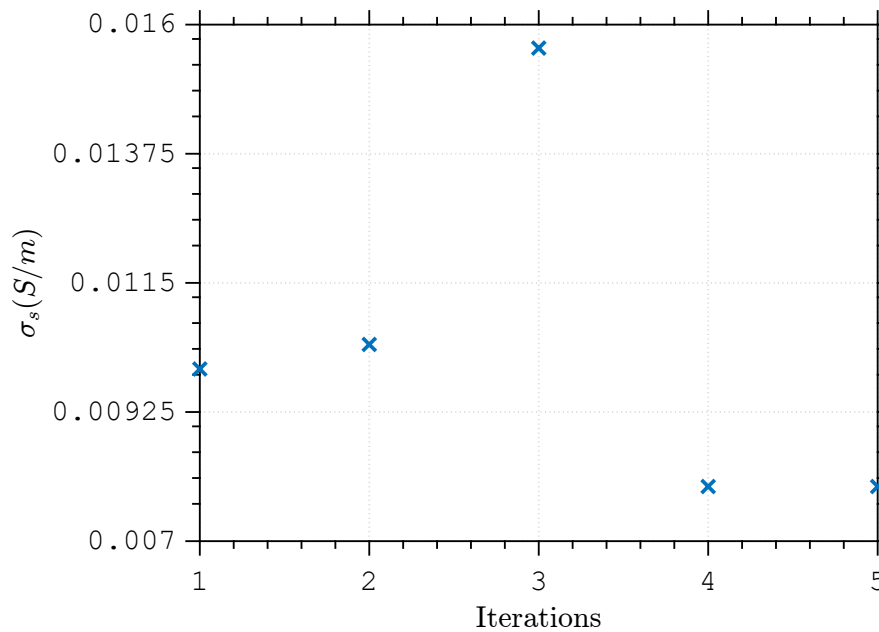


Figure 5.45: Evolution of the optimization parameter as a function of the number of iterations using decibel functional. Convergence was achieved after 5 iterations at $\sigma_s = 0.008$.

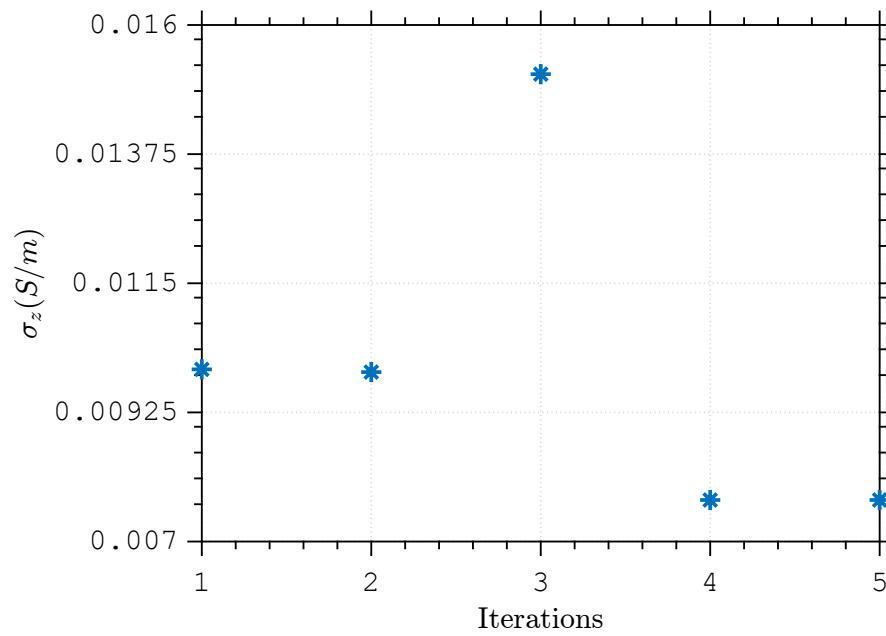


Figure 5.46: Evolution of the optimization parameter as a function of the number of iterations using decibel functional. Convergence was achieved after 5 iterations at $\sigma_z = 0.008$.

5.1.2.5

Anisotropic sample with anisotropic loss

Finally, for the last case, parameters are in Table 5.28 and results for linear functional are in Fig. 5.47, 5.48, 5.49 and 5.50 and in Table 5.29. The decibel functional has results presented in Fig. 5.51, 5.52, 5.53 and 5.54 and in Table 5.30. We observe that the convergence was achieved after 23 iterations for linear functional and 8 iterations for decibel functional for a value near $\epsilon_{rs} = 2.55$, $\epsilon_{rz} = 3$, $\sigma_s = 0.01$ and $\sigma_z = 0.02$ for linear functional with a good convergence from the ones used in simulation and $\epsilon_{rs} = 2.54$, $\epsilon_{rz} = 3.01$, $\sigma_s = 0.011$ and $\sigma_z = 0.015$ for decibel functional with a small difference from the ones used in simulation

Table 5.28: Geometric and constitutive parameters used on direct problem of a anisotropic lossy and anisotropic sample placed in second waveguide of a two-port homogeneous circular waveguide

Region	L(mm)	ρ_0 (mm)	ρ_1 (mm)	ρ_2 (mm)	ϵ_{rs1}	ϵ_{rz1}	σ_{s1}	σ_{z1}
1	-	1.84	2.00	5.00	1.01	1.01	10^{-6}	10^{-6}
2	10	0	6	-	2.55	3	10^{-2}	2×10^{-2}
3	-	1.84	2.00	5.00	1.01	1.01	10^{-6}	10^{-6}

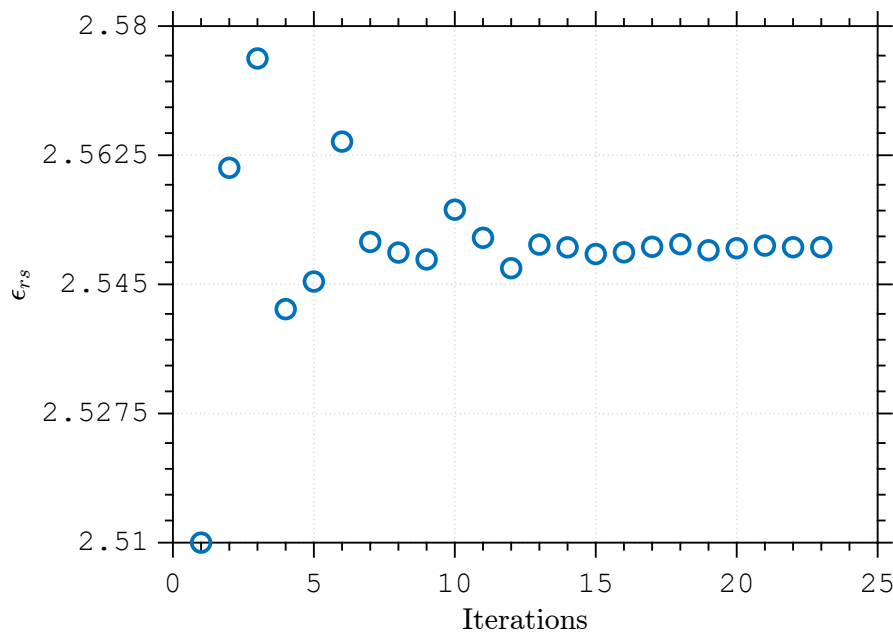


Figure 5.47: Evolution of the optimization parameter as a function of the number of iterations using linear functional. Convergence was achieved after 23 iterations at $\epsilon_{rs} = 2.55$.

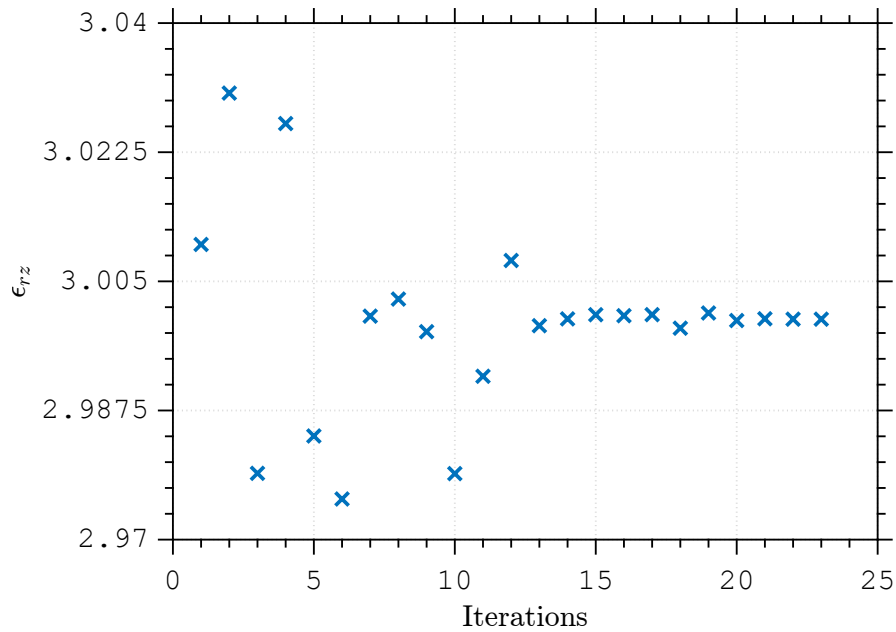


Figure 5.48: Evolution of the optimization parameter as a function of the number of iterations using linear functional. Convergence was achieved after 23 iterations at $\epsilon_{rz} = 3$.

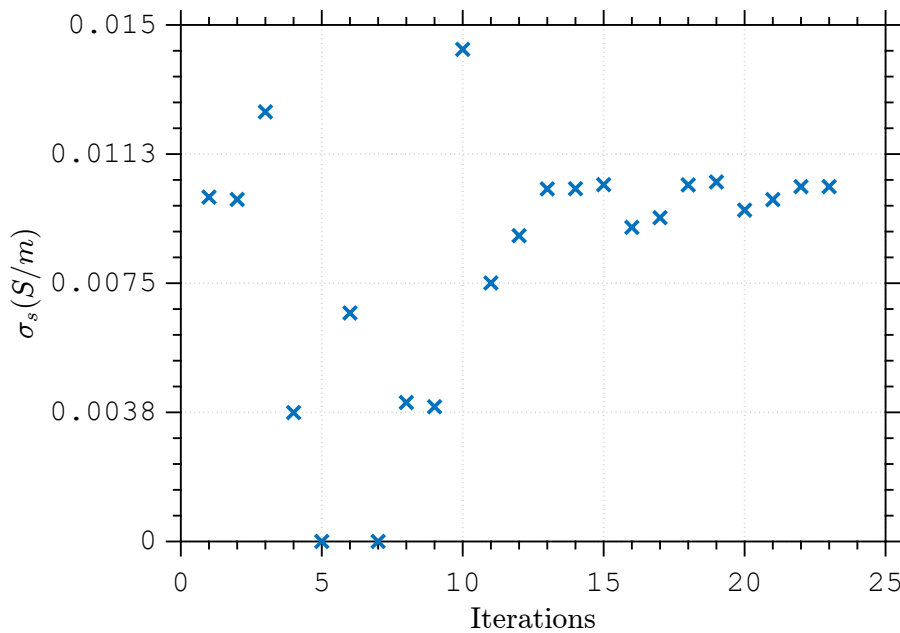


Figure 5.49: Evolution of the optimization parameter as a function of the number of iterations using linear functional. Convergence was achieved after 23 iterations at $\sigma_s = 0.01$.

Table 5.29: Initial guess, CPU time, and the number of iterations to achieve convergence by using the parameters Table 5.28 using linear functional.

x_0	Time	Iterations
[2.51 3.01 0.01 0.01]	143 min 55 seconds	23

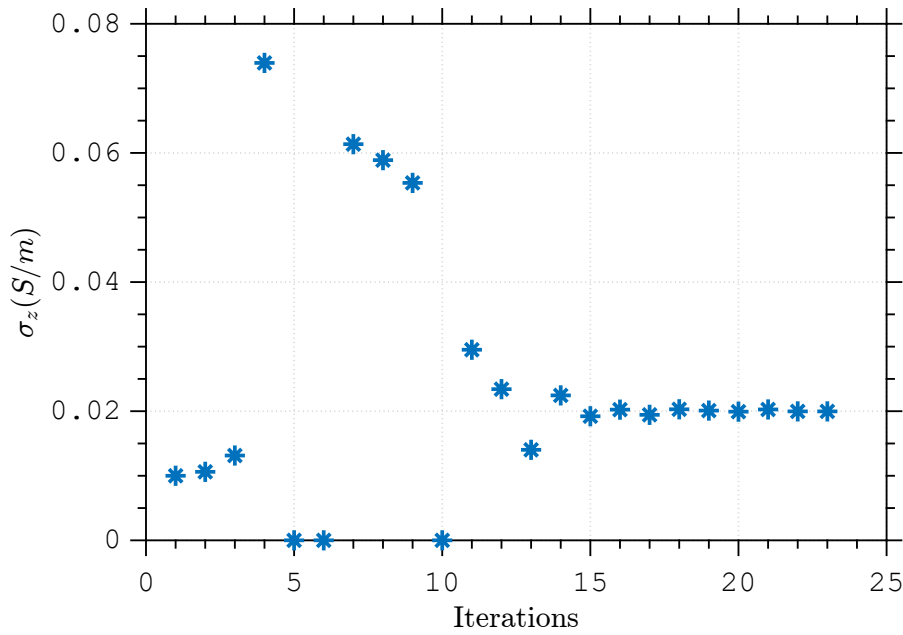


Figure 5.50: Evolution of the optimization parameter as a function of the number of iterations using linear functional. Convergence was achieved after 23 iterations at $\sigma_z = 0.02$.

PUC-Rio - Certificação Digital N° 2012321/CA

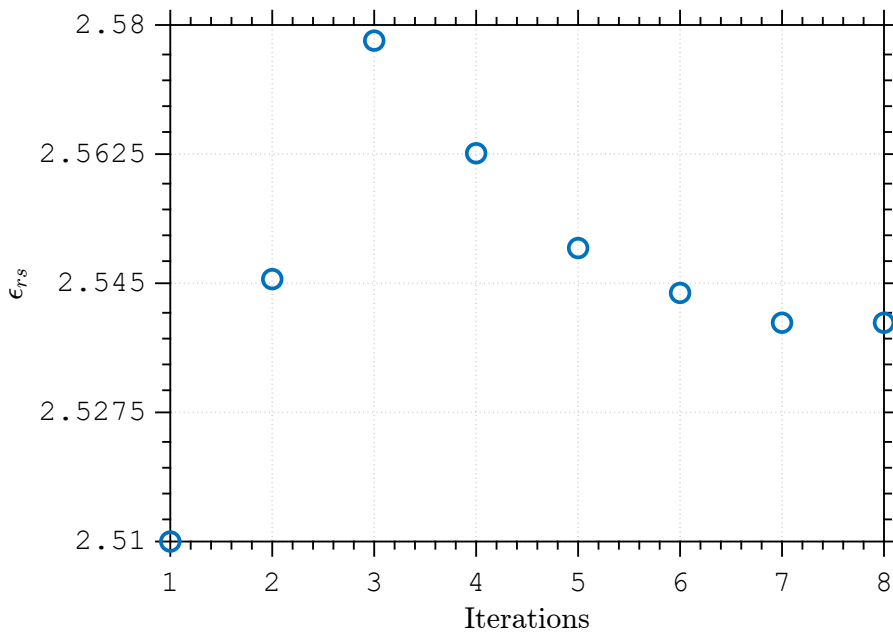


Figure 5.51: Evolution of the optimization parameter as a function of the number of iterations using decibel functional. Convergence was achieved after 8 iterations at $\epsilon_{rs} = 2.54$.

Table 5.30: Initial guess, CPU time, and the number of iterations to achieve convergence by using the parameters Table 5.28 using decibel functional.

x_0	Time	Iterations
[2.51 3.01 0.01 0.01]	101 min 44 seconds	8

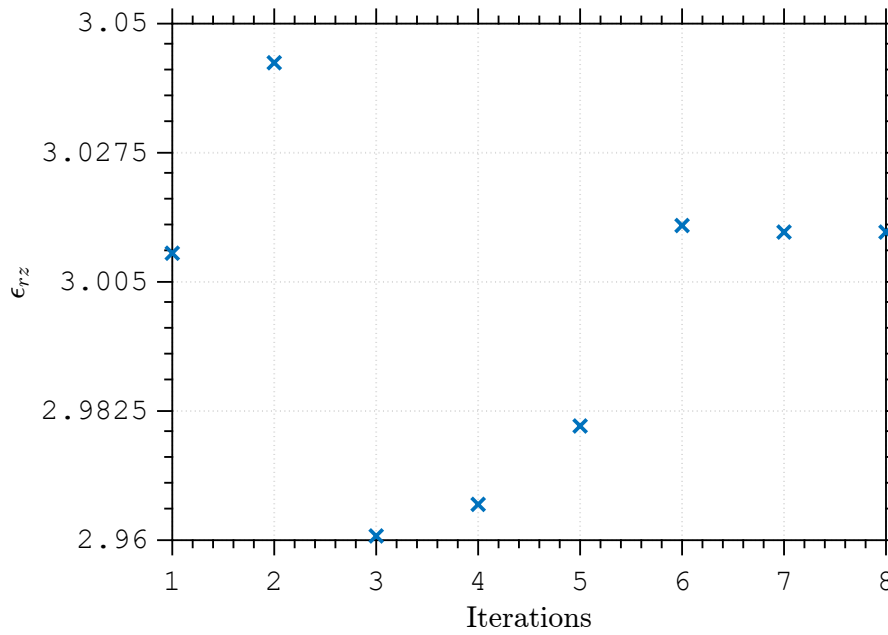


Figure 5.52: Evolution of the optimization parameter as a function of the number of iterations using decibel functional. Convergence was achieved after 8 iterations at $\epsilon_{rz} = 3.01$.

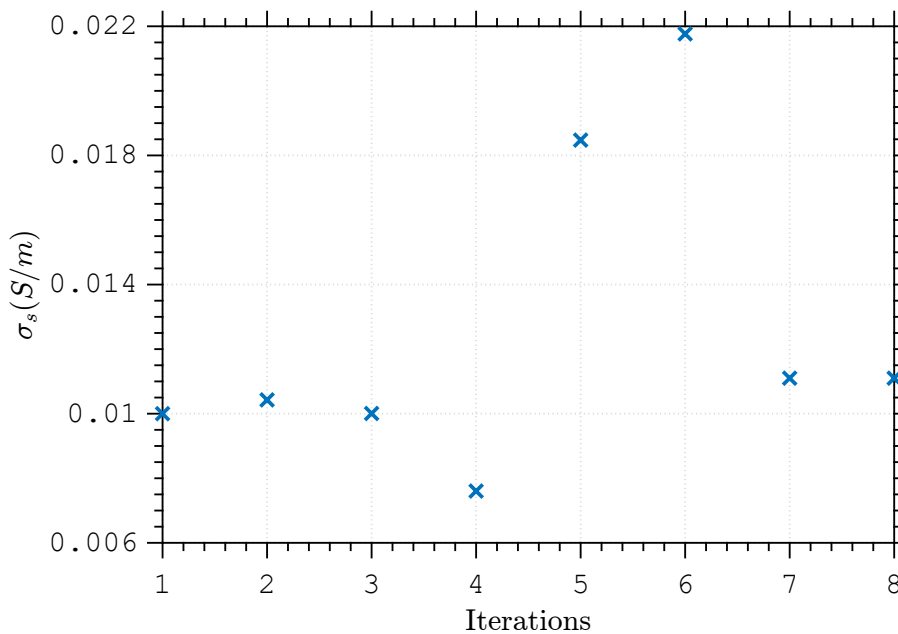


Figure 5.53: Evolution of the optimization parameter as a function of the number of iterations using decibel functional. Convergence was achieved after 8 iterations at $\sigma_s = 0.011$.

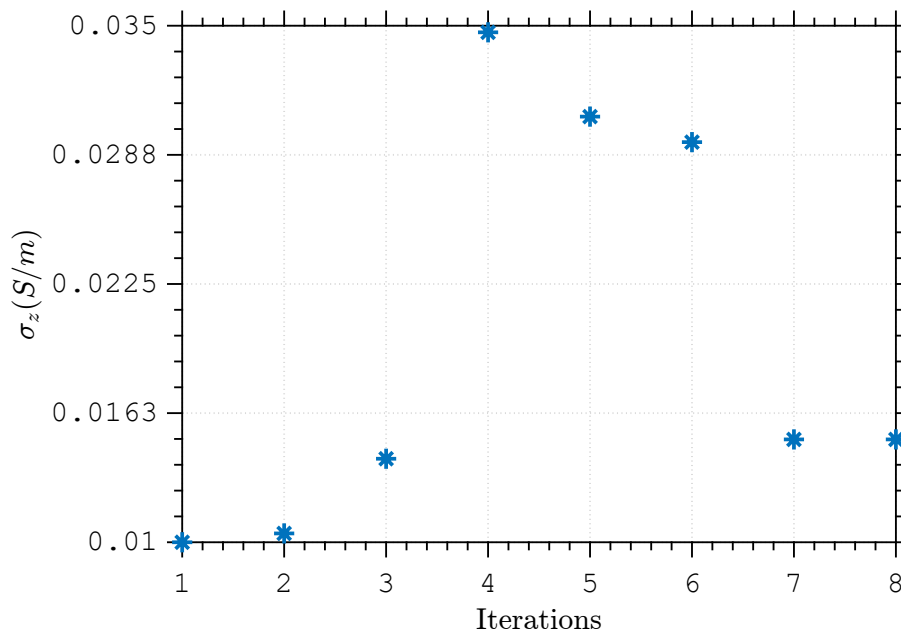


Figure 5.54: Evolution of the optimization parameter as a function of the number of iterations using decibel functional. Convergence was achieved after 8 iterations at $\sigma_z = 0.015$.

5.1.3 Heterogeneous Circular Waveguide

Now, the second region is a circular waveguide, where the material is in the first layer and second layer is filled with vacuum, 10 modes were used in this case.

5.1.3.1 Lossless isotropic sample

This simulation used the parameters in Table 5.31. Results can be seen in Fig. 5.55 and in Table 5.32. We observe that the convergence was achieved after 9 iterations for linear functional and 8 iterations for decibel functional for a value near $\epsilon_r = 2.55$ for linear functional with a good convergence from the ones used in simulation

Table 5.31: Geometric and constitutive parameters used on direct problem of a lossless isotropic sample placed in second waveguide of a two-port heterogeneous circular waveguide

Region	L(mm)	ρ_0 (mm)	ρ_1 (mm)	ρ_2 (mm)	ϵ_{rs1}	ϵ_{rz1}	σ_{s1}	σ_{z1}
1	-	1.84	2.00	5.00	1.01	1.01	10^{-6}	10^{-6}
2	10	0	3	6	2.55	2.55	10^{-6}	10^{-6}
3	-	1.84	2.00	5.00	1.01	1.01	10^{-6}	10^{-6}

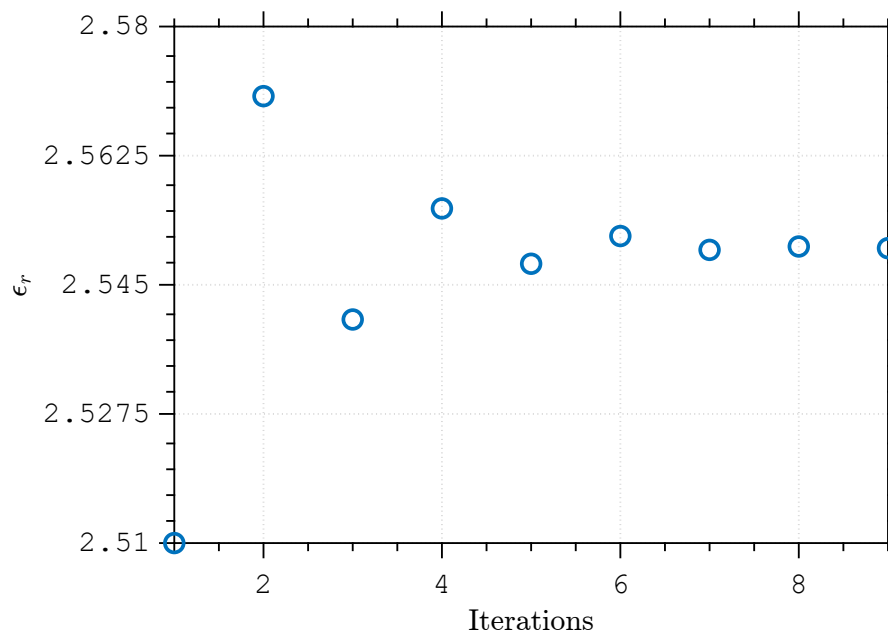


Figure 5.55: Evolution of the optimization parameter as a function of the number of iterations using linear functional. Convergence was achieved after 9 iterations at $\epsilon_r = 2.55$.

Table 5.32: Initial guess, CPU time, and the number of iterations to achieve convergence by using the parameters Table 5.31 using linear functional.

x_0	Time	Iterations
2.51	18 min 47 seconds	9

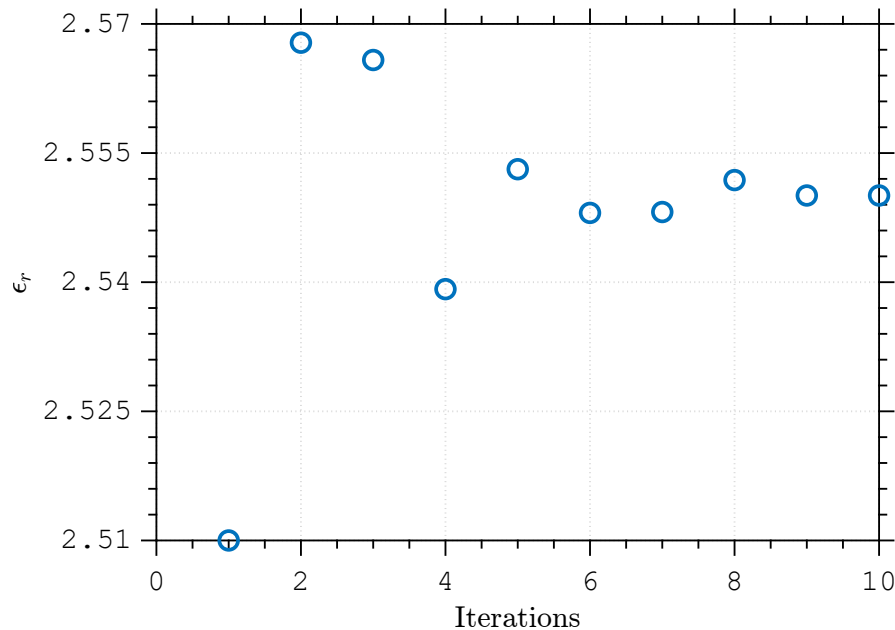
5.1.3.2

Lossy isotropic sample

For this case, parameters can be seen in Table 5.33 and results for linear functional are in Fig. 5.56 and 5.57 and in Table 5.34. The decibel functional has its results on Fig. 5.58 and 5.59 and in Table 5.35. We observe that the convergence was achieved after 10 iterations for linear functional and 4 iterations for decibel functional for a value near $\epsilon_r = 2.55$ and $\sigma = 0.02$ for linear functional with a good convergence from the ones used in simulation and $\epsilon_r = 2.55$ and $\sigma = 0.036$ for decibel functional with a small difference from the ones used in simulation

Table 5.33: Geometric and constitutive parameters used on direct problem of a lossy isotropic sample placed in second waveguide of a two-port heterogeneous circular waveguide

Region	L(mm)	ρ_0 (mm)	ρ_1 (mm)	ρ_2 (mm)	ϵ_{rs1}	ϵ_{rz1}	σ_{s1}	σ_{z1}
1	-	1.84	2.00	5.00	1.01	1.01	10^{-6}	10^{-6}
2	10	0	3	6	2.55	2.55	2×10^{-2}	2×10^{-2}
3	-	1.84	2.00	5.00	1.01	1.01	10^{-6}	10^{-6}

Figure 5.56: Evolution of the optimization parameter as a function of the number of iterations using linear functional. Convergence was achieved after 10 iterations at $\epsilon_r = 2.55$.

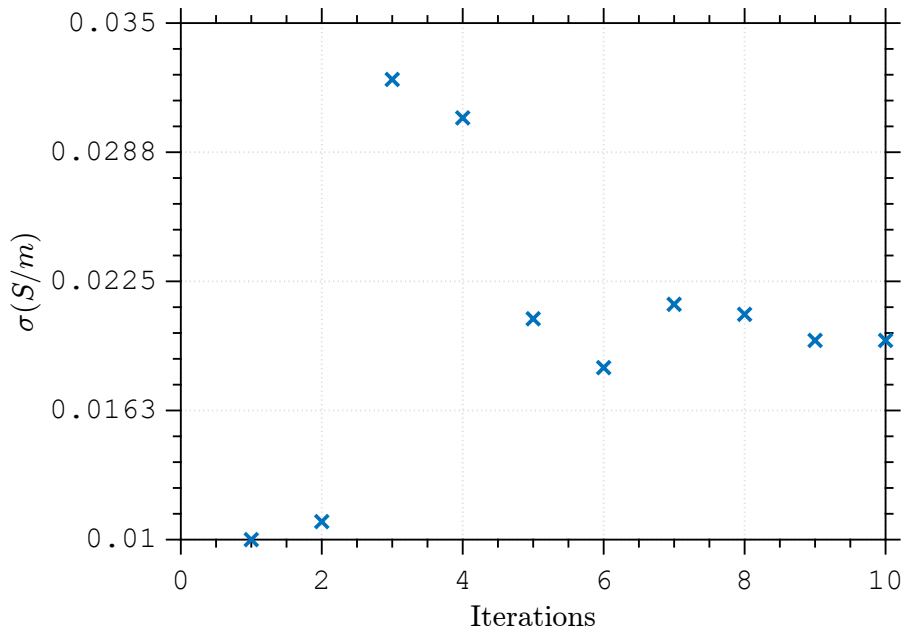


Figure 5.57: Evolution of the optimization parameter as a function of the number of iterations using linear functional. Convergence was achieved after 10 iterations at $\sigma = 0.02$.

Table 5.34: Initial guess, CPU time, and the number of iterations to achieve convergence by using the parameters Table 5.33 using linear functional.

x_0	Time	Iterations
[2.51 0.01]	70 min 26 seconds	10

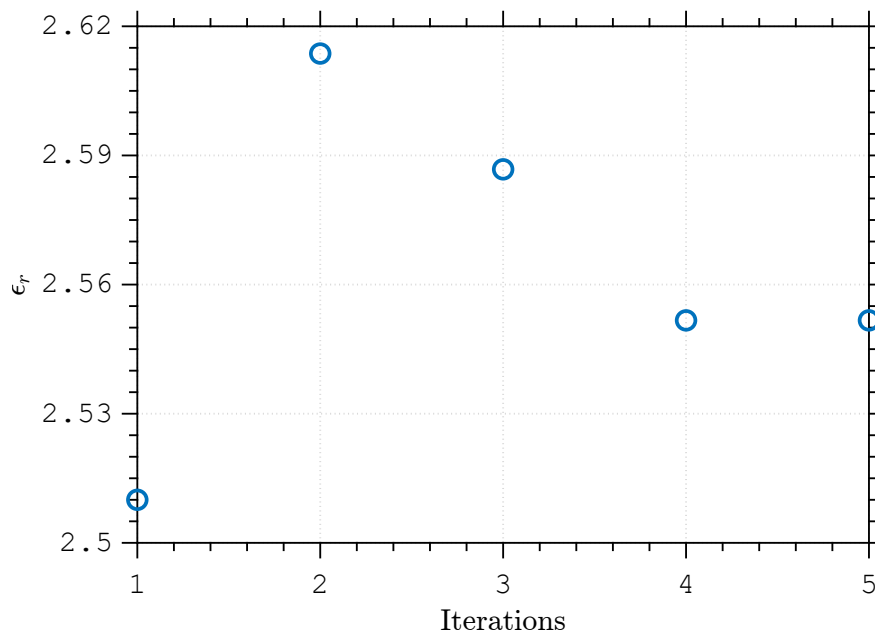


Figure 5.58: Evolution of the optimization parameter as a function of the number of iterations using decibel functional. Convergence was achieved after 10 iterations at $\epsilon_r = 2.55$.

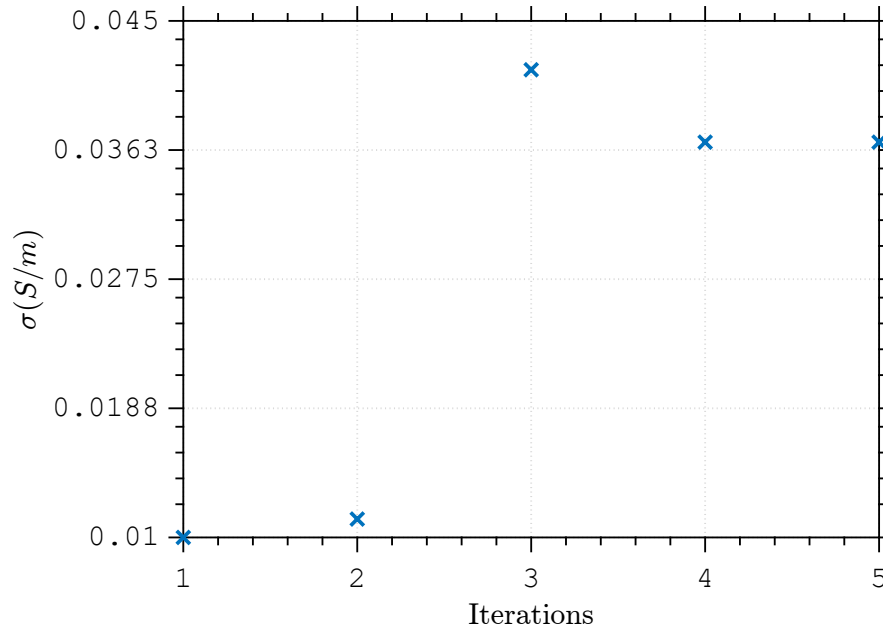


Figure 5.59: Evolution of the optimization parameter as a function of the number of iterations using decibel functional. Convergence was achieved after 10 iterations at $\sigma = 0.036$.

Table 5.35: Initial guess, CPU time, and the number of iterations to achieve convergence by using the parameters Table 5.33 using decibel functional.

x_0	Time	Iterations
[2.51 0.01]	197 min 41 seconds	4

5.1.3.3

Lossless anisotropic sample

For the lossless anisotropic material case, parameters are in Table 5.36. Results for the linear functional are in Fig. 5.60 and 5.61 and in Table 5.37. For decibel functional they are in Fig. 5.62 and 5.63 and in Table 5.38. We observe that the convergence was achieved after 10 iterations for linear functional and 3 iterations for decibel functional for a value near $\epsilon_{rs} = 2.55$ and $\epsilon_{rz} = 3$ for linear functional with a good convergence from the ones used in simulation and $\epsilon_{rs} = 2.56$ and $\epsilon_{rz} = 2.99$ for decibel functional with a small difference from the ones used in simulation

Table 5.36: Geometric and constitutive parameters used on direct problem of a lossless anisotropic sample placed in second waveguide of a two-port heterogeneous circular waveguide

Region	L(mm)	ρ_0 (mm)	ρ_1 (mm)	ρ_2 (mm)	ϵ_{rs1}	ϵ_{rz1}	σ_{s1}	σ_{z1}
1	-	1.84	2.00	5.00	1.01	1.01	10^{-6}	10^{-6}
2	10	0	3	6	2.55	3	10^{-6}	10^{-6}
3	-	1.84	2.00	5.00	1.01	1.01	10^{-6}	10^{-6}

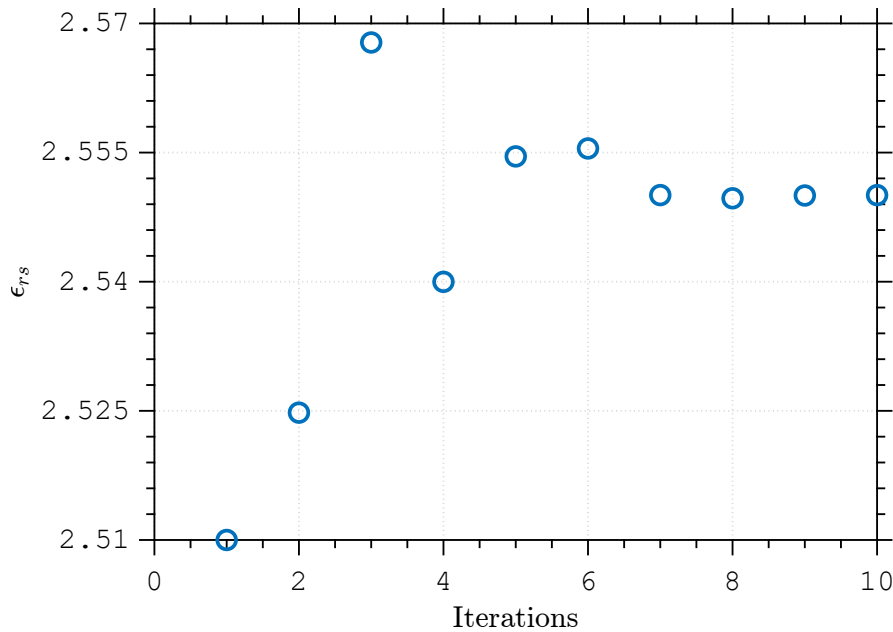


Figure 5.60: Evolution of the optimization parameter as a function of the number of iterations using linear functional. Convergence was achieved after 10 iterations at $\epsilon_{rs} = 2.55$.

PUC-Rio - Certificação Digital N° 2012321/CA

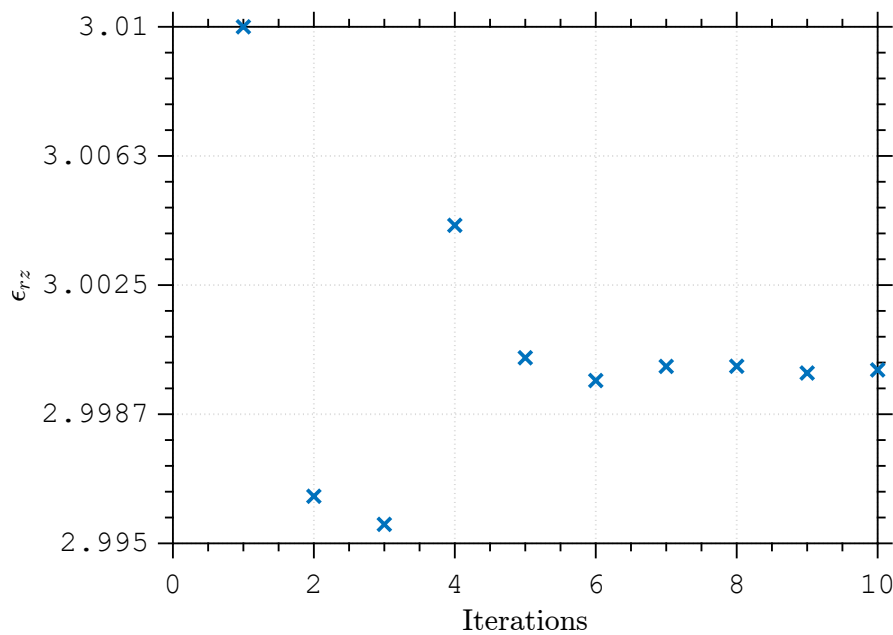


Figure 5.61: Evolution of the optimization parameter as a function of the number of iterations using linear functional. Convergence was achieved after 10 iterations at $\epsilon_{rz} = 3$.

Table 5.37: Initial guess, CPU time, and the number of iterations to achieve convergence by using the parameters Table 5.36 using linear functional.

x_0	Time	Iterations
[2.51 3.01]	166 min 5 seconds	10

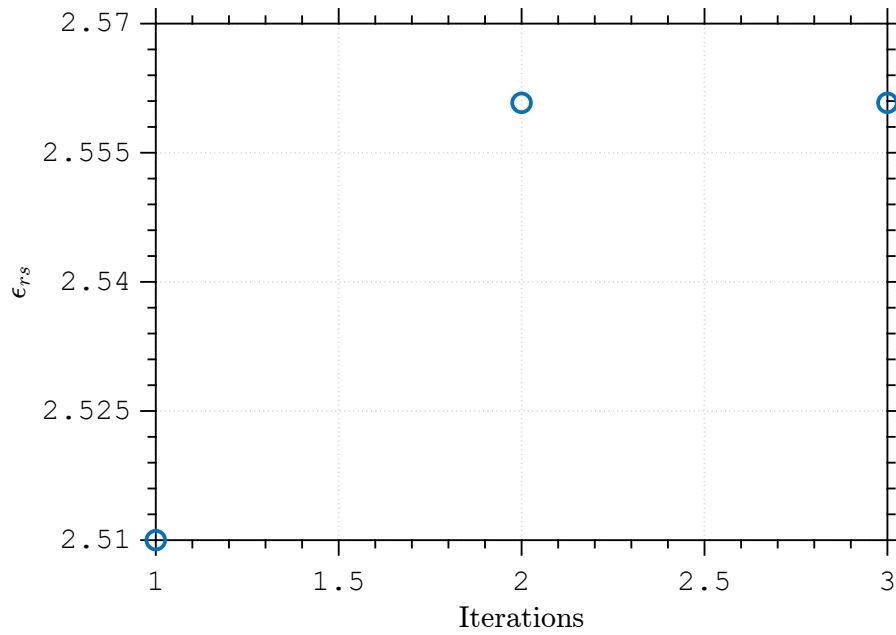


Figure 5.62: Evolution of the optimization parameter as a function of the number of iterations using decibel functional. Convergence was achieved after 3 iterations at $\epsilon_{rs} = 2.56$.

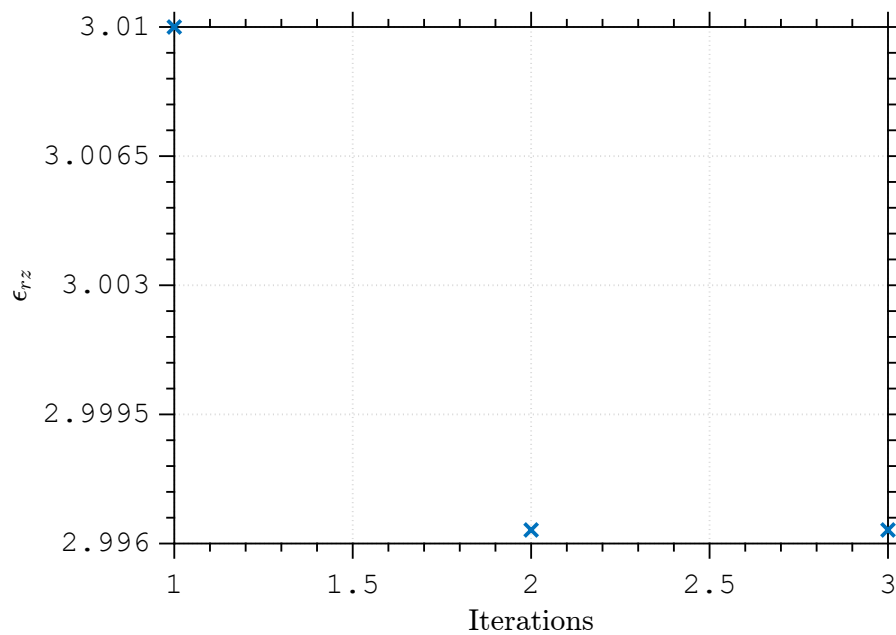


Figure 5.63: Evolution of the optimization parameter as a function of the number of iterations using decibel functional. Convergence was achieved after 3 iterations at $\epsilon_{rz} = 2.99$.

Table 5.38: Initial guess, CPU time, and the number of iterations to achieve convergence by using the parameters Table 5.36 using decibel functional.

x_0	Time	Iterations
[2.51 3.01]	152 min 33 seconds	3

5.1.3.4

Anisotropic sample with isotropic loss

In this simulation parameters used are in Table 5.39. Results for the linear functional are in Fig. 5.64, 5.65, 5.66 and 5.67 and Table 5.40. For the decibel one, results are in Fig. 5.68, 5.69, 5.70 and 5.71 and Table 5.41. We observe that the convergence was achieved after 21 iterations for linear functional and 3 iterations for decibel functional for a value near $\epsilon_{rs} = 2.55$, $\epsilon_{rz} = 3$, $\sigma_s = 0.018$ and $\sigma_z = 0.02$ for linear functional with a small difference from the ones used in simulation and $\epsilon_{rs} = 2.56$, $\epsilon_{rz} = 2.99$, $\sigma_s = 0.01$ and $\sigma_z = 0.01$ for decibel functional with a small difference from the ones used in simulation

Table 5.39: Geometric and constitutive parameters used on direct problem of a isotropic lossy and anisotropic sample placed in second waveguide of a two-port heterogeneous circular waveguide

Region	L(mm)	ρ_0 (mm)	ρ_1 (mm)	ρ_2 (mm)	ϵ_{rs1}	ϵ_{rz1}	σ_{s1}	σ_{z1}
1	-	1.84	2.00	5.00	1.01	1.01	10^{-6}	10^{-6}
2	10	0	3	6	2.55	3	2×10^{-2}	2×10^{-2}
3	-	1.84	2.00	5.00	1.01	1.01	10^{-6}	10^{-6}

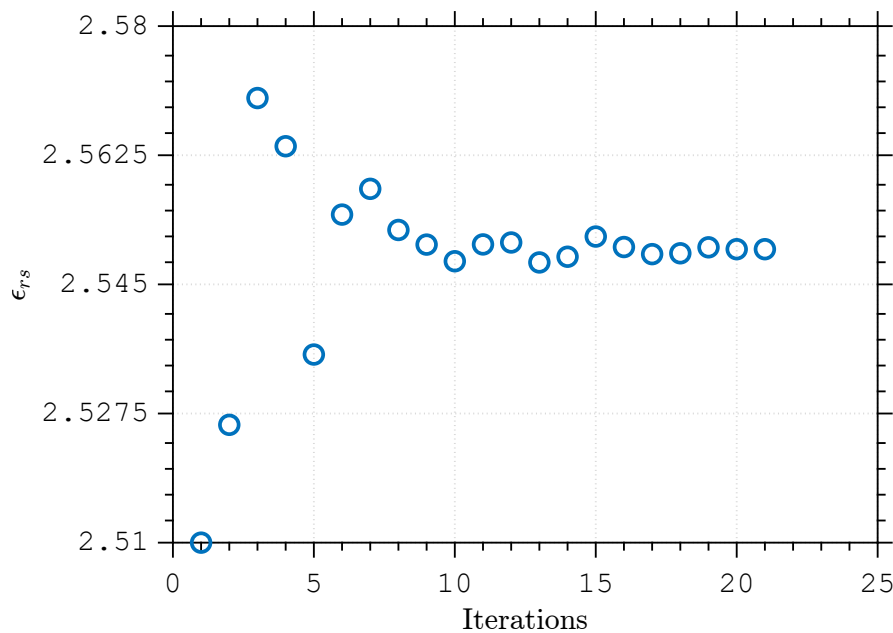


Figure 5.64: Evolution of the optimization parameter as a function of the number of iterations using linear functional. Convergence was achieved after 21 iterations at $\epsilon_{rs} = 2.55$.

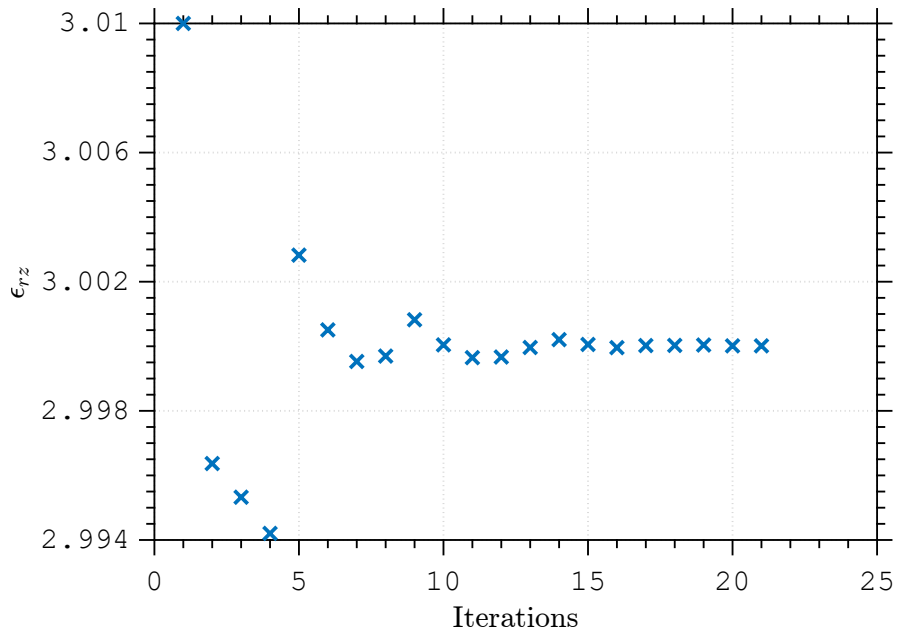


Figure 5.65: Evolution of the optimization parameter as a function of the number of iterations using linear functional. Convergence was achieved after 21 iterations at $\epsilon_{rz} = 3$.

PUC-Rio - Certificação Digital N° 2012321/CA

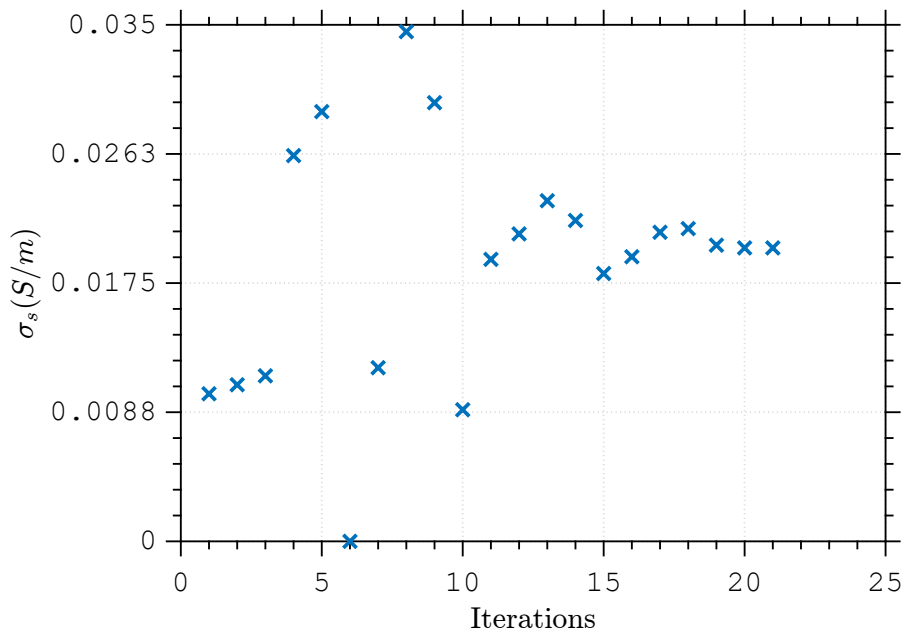


Figure 5.66: Evolution of the optimization parameter as a function of the number of iterations using linear functional. Convergence was achieved after 21 iterations at $\sigma_s = 0.018$.

Table 5.40: Initial guess, CPU time, and the number of iterations to achieve convergence by using the parameters Table 5.39 using linear functional.

x_0	Time	Iterations
[2.51 3.01 0.01 0.01]	230 min 30 seconds	21

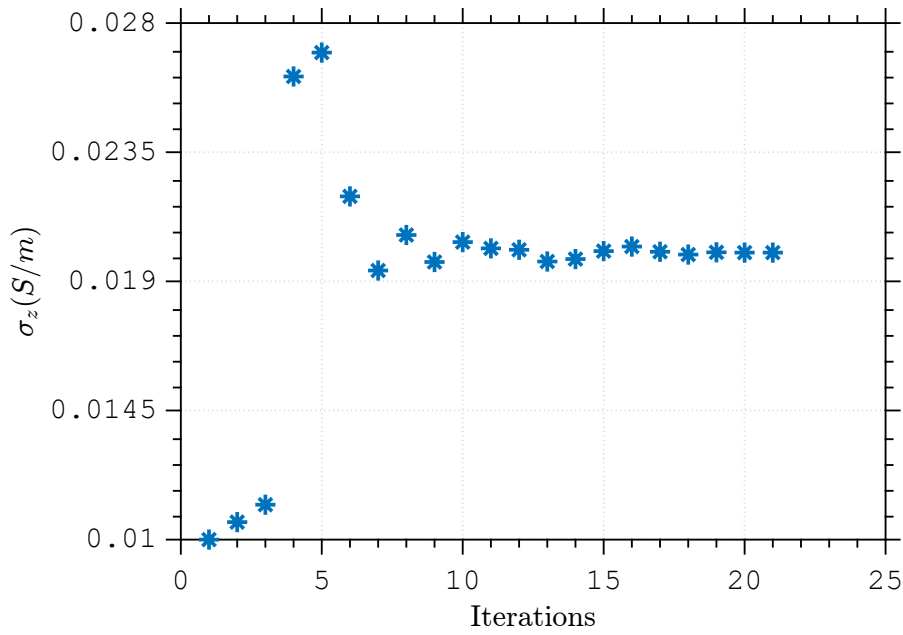


Figure 5.67: Evolution of the optimization parameter as a function of the number of iterations using linear functional. Convergence was achieved after 21 iterations at $\sigma_z = 0.02$.

PUC-Rio - Certificação Digital N° 2012321/CA

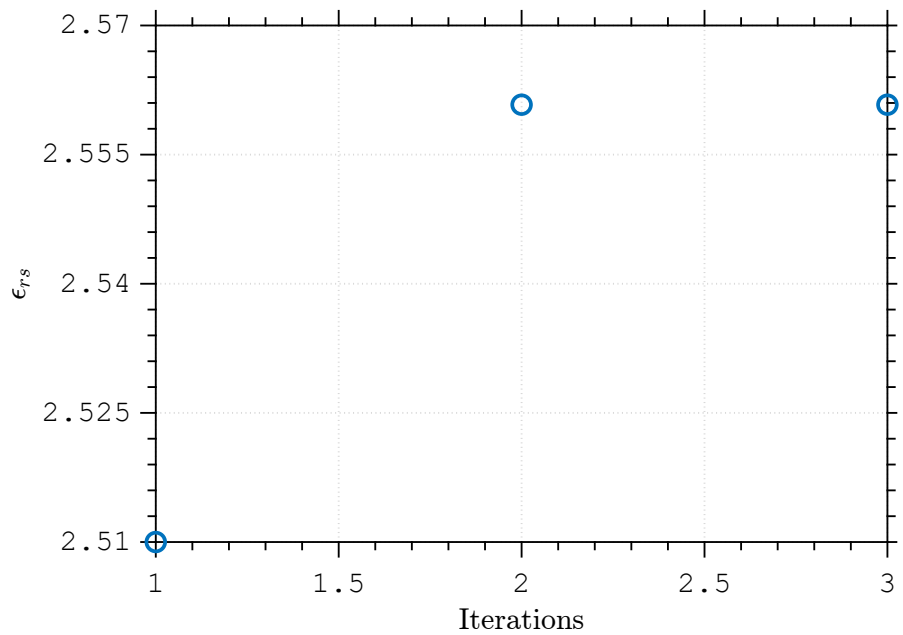


Figure 5.68: Evolution of the optimization parameter as a function of the number of iterations using decibel functional. Convergence was achieved after 3 iterations at $\epsilon_{rs} = 2.56$.

Table 5.41: Initial guess, CPU time, and the number of iterations to achieve convergence by using the parameters Table 5.39 using decibel functional.

x_0	Time	Iterations
[2.51 3.01 0.01 0.01]	166 min 46 seconds	3

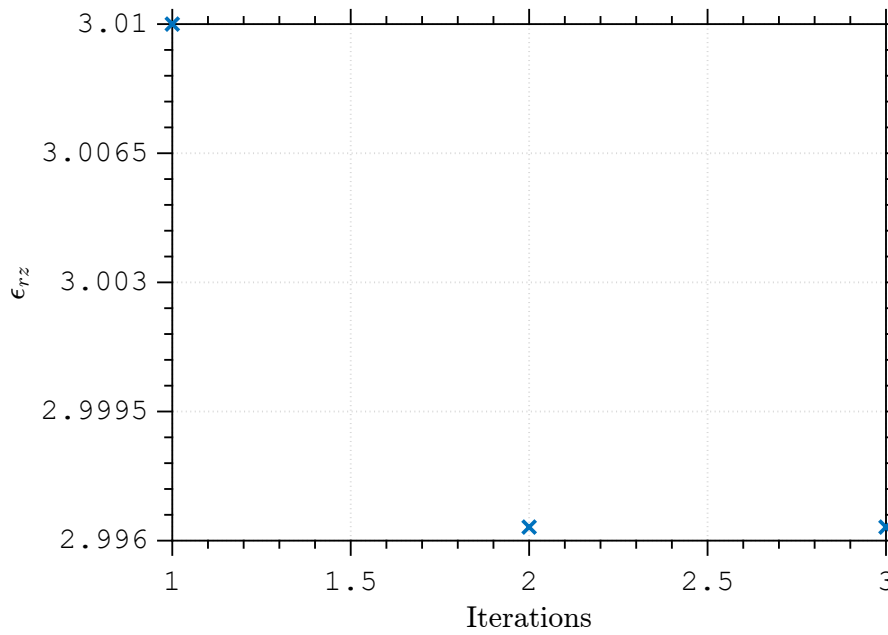


Figure 5.69: Evolution of the optimization parameter as a function of the number of iterations using decibel functional. Convergence was achieved after 3 iterations at $\epsilon_{rz} = 2.99$.

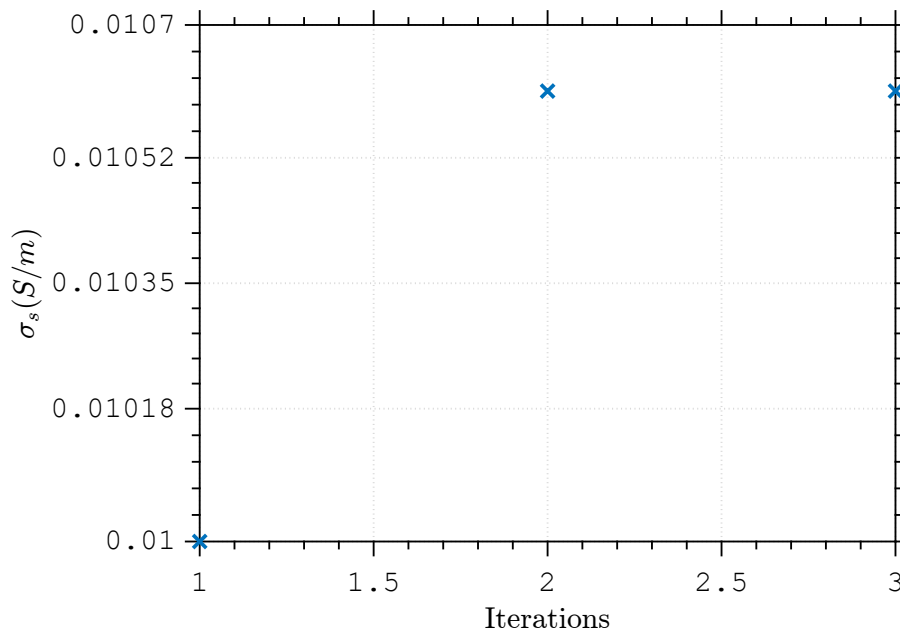


Figure 5.70: Evolution of the optimization parameter as a function of the number of iterations using decibel functional. Convergence was achieved after 3 iterations at $\sigma_s = 0.01$.

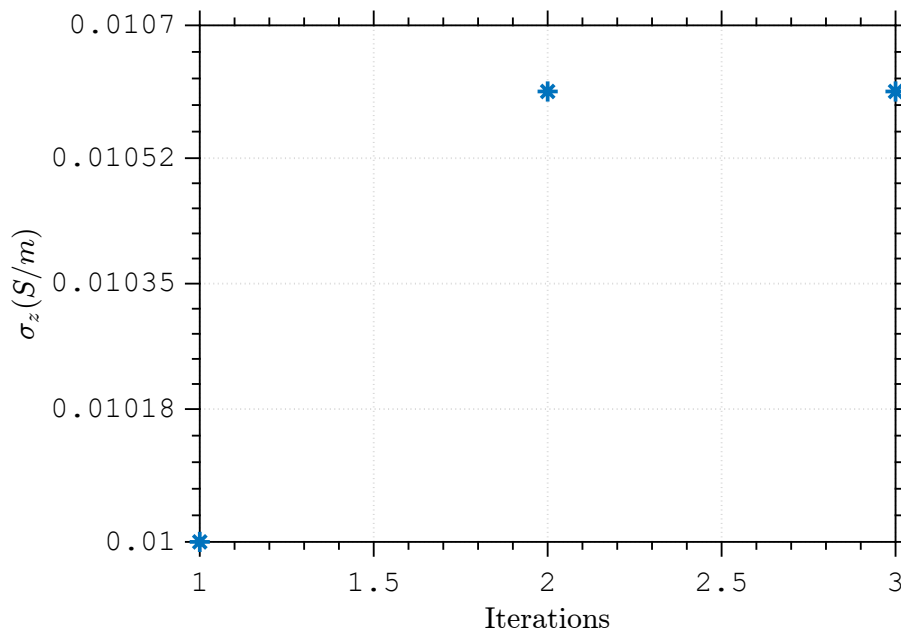


Figure 5.71: Evolution of the optimization parameter as a function of the number of iterations using decibel functional. Convergence was achieved after 3 iterations at $\sigma_z = 0.01$.

5.1.3.5

Anisotropic sample with anisotropic loss

The last case, with an lossy anisotropic material, parameters are in Table 5.42 and results for linear functional are in Fig. 5.72, 5.73, 5.74 and 5.75 and in Table 5.43. The decibel functional has results presented in Fig. 5.76, 5.77, 5.78 and 5.79 and in Table 5.44. We observe that the convergence was achieved after 22 iterations for linear functional and 3 iterations for decibel functional for a value near $\epsilon_{rs} = 2.55$, $\epsilon_{rz} = 3$, $\sigma_s = 0.01$ and $\sigma_z = 0.02$ for linear functional with a good convergence from the ones used in simulation and $\epsilon_{rs} = 2.56$, $\epsilon_{rz} = 2.99$, $\sigma_s = 0.01$ and $\sigma_z = 0.01$ for decibel functional with a small difference from the ones used in simulation

Table 5.42: Geometric and constitutive parameters used on direct problem of an anisotropic lossy and anisotropic sample placed in second waveguide of a two-port heterogeneous circular waveguide

Region	L(mm)	ρ_0 (mm)	ρ_1 (mm)	ρ_2 (mm)	ϵ_{rs1}	ϵ_{rz1}	σ_{s1}	σ_{z1}
1	-	1.84	2.00	5.00	1.01	1.01	10^{-6}	10^{-6}
2	10	0	3	6	2.55	2.55	10^{-2}	2×10^{-2}
3	-	1.84	2.00	5.00	1.01	1.01	10^{-6}	10^{-6}

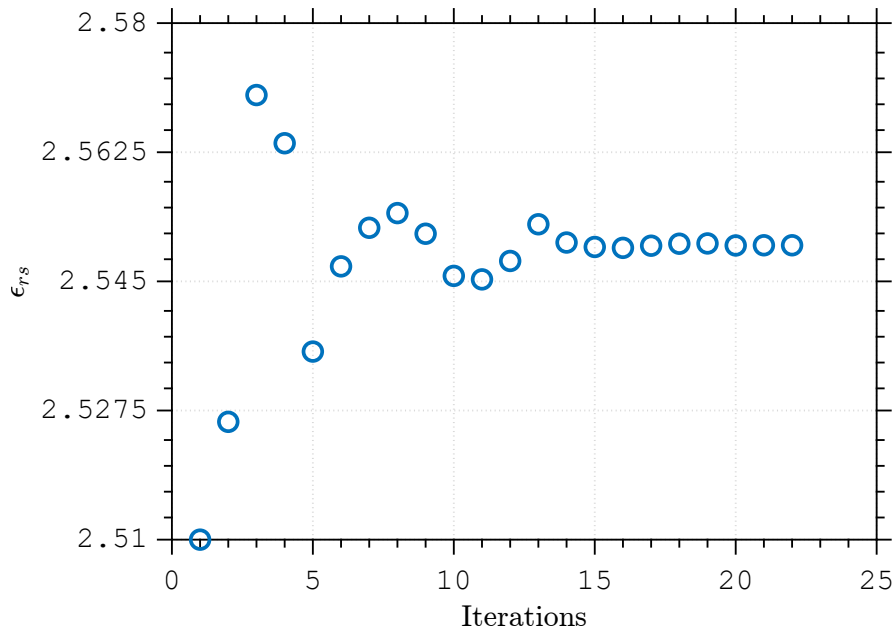


Figure 5.72: Evolution of the optimization parameter as a function of the number of iterations using linear functional. Convergence was achieved after 22 iterations at $\epsilon_{rs} = 2.55$.

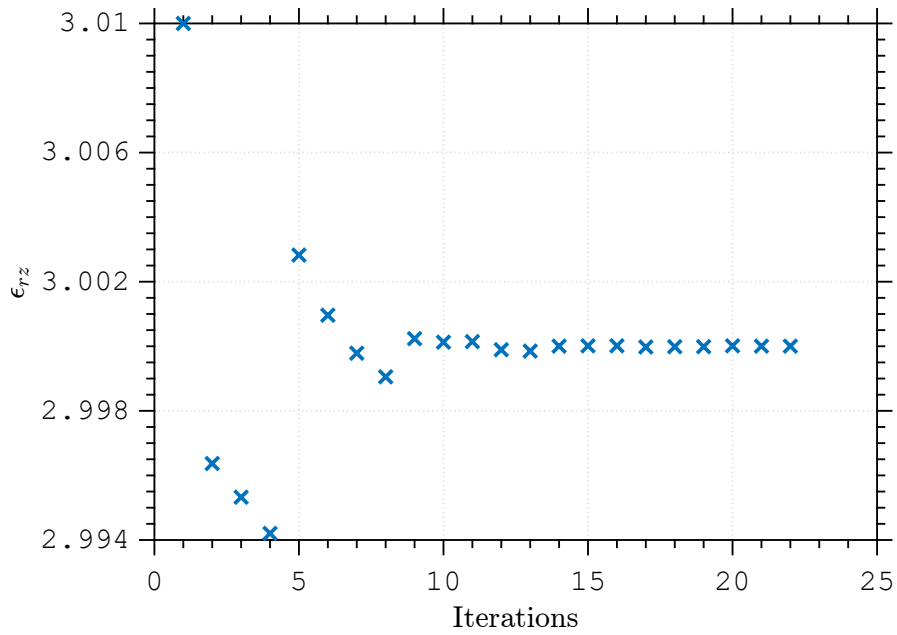


Figure 5.73: Evolution of the optimization parameter as a function of the number of iterations using linear functional. Convergence was achieved after 22 iterations at $\epsilon_{rz} = 3$.

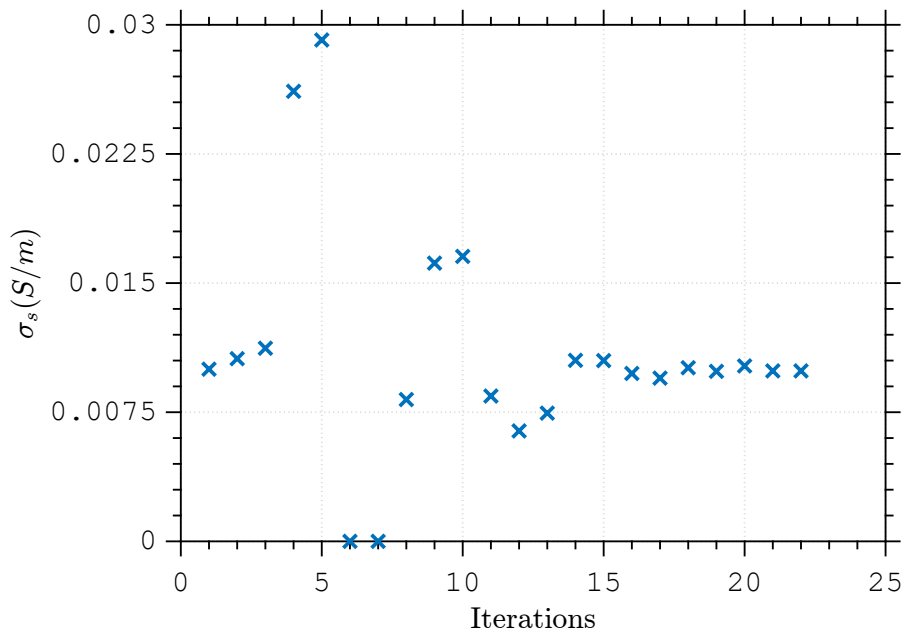


Figure 5.74: Evolution of the optimization parameter as a function of the number of iterations using linear functional. Convergence was achieved after 22 iterations at $\sigma_s = 0.01$.

Table 5.43: Initial guess, CPU time, and the number of iterations to achieve convergence by using the parameters Table 5.42 using linear functional.

x_0	Time	Iterations
[2.51 3.01 0.01 0.01]	229 min 31 seconds	22

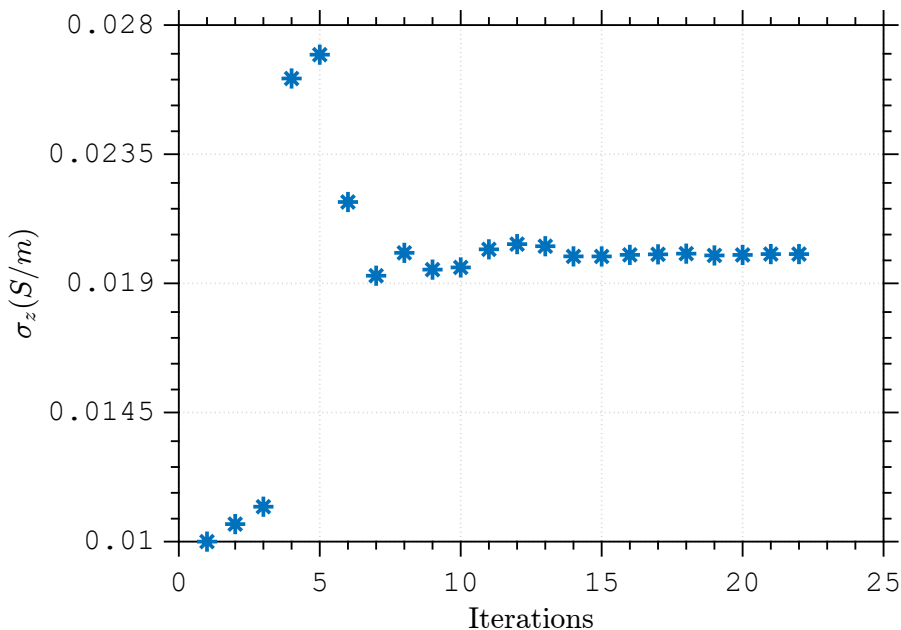


Figure 5.75: Evolution of the optimization parameter as a function of the number of iterations using linear functional. Convergence was achieved after 22 iterations at $\sigma_z = 0.02$.

PUC-Rio - Certificação Digital N° 2012321/CA

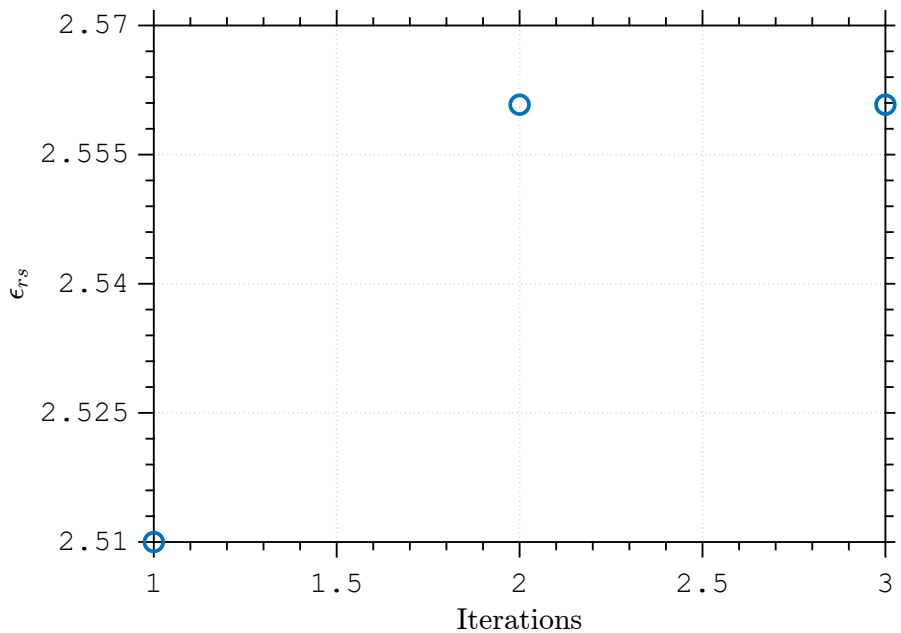


Figure 5.76: Evolution of the optimization parameter as a function of the number of iterations using decibel functional. Convergence was achieved after 3 iterations at $\epsilon_{rs} = 2.56$.

Table 5.44: Initial guess, CPU time, and the number of iterations to achieve convergence by using the parameters Table 5.42 using decibel functional.

x_0	Time	Iterations
[2.51 3.01 0.01 0.01]	160 min 51 seconds	3

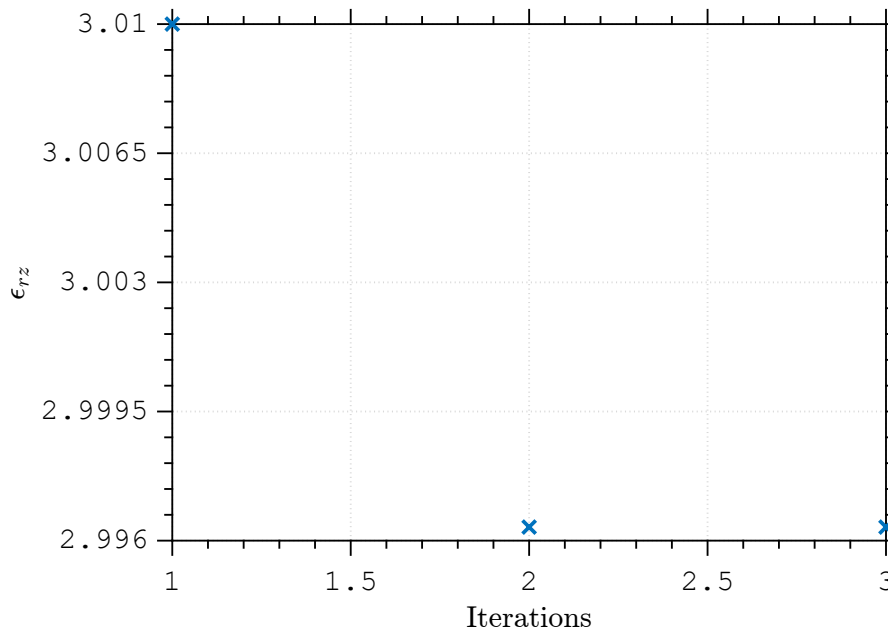


Figure 5.77: Evolution of the optimization parameter as a function of the number of iterations using decibel functional. Convergence was achieved after 3 iterations at $\epsilon_{rz} = 2.99$.

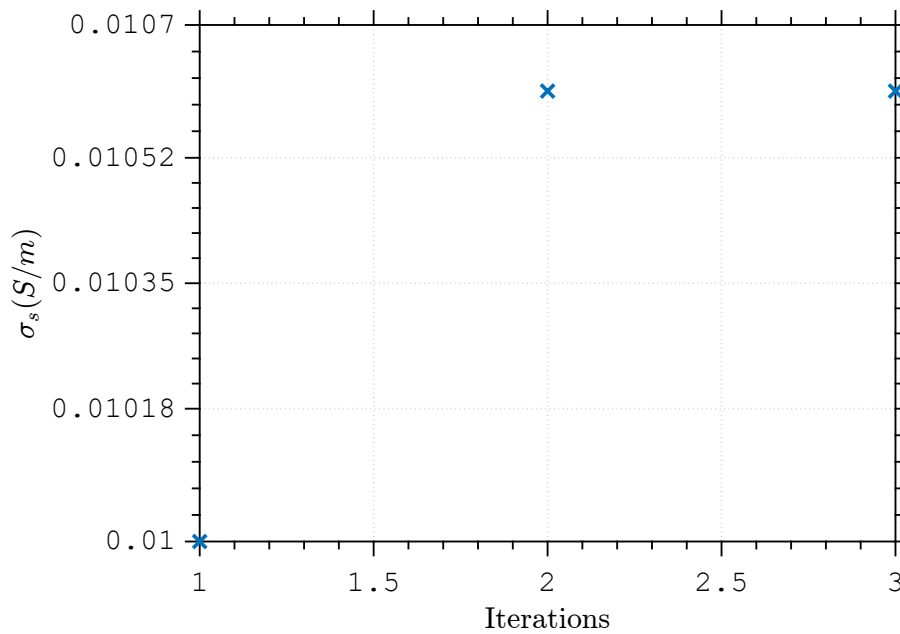


Figure 5.78: Evolution of the optimization parameter as a function of the number of iterations using decibel functional. Convergence was achieved after 3 iterations at $\sigma_s = 0.01$.

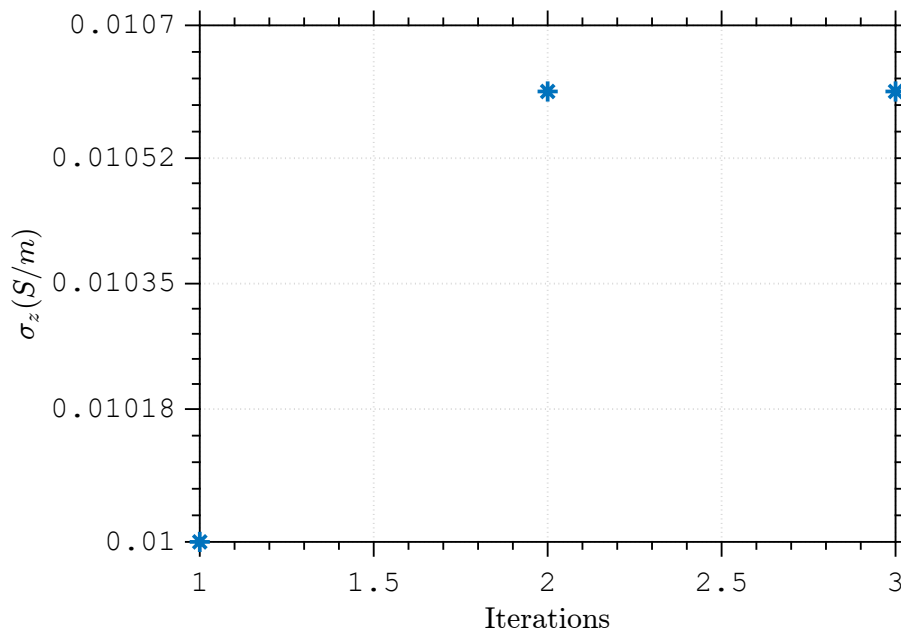


Figure 5.79: Evolution of the optimization parameter as a function of the number of iterations using decibel functional. Convergence was achieved after 3 iterations at $\sigma_z = 0.01$.

5.2

One-Port Measurement Cells

For the inverse problem using one-port measurement cell it was considered that the sample was categorized into the same cases as in the previous section. They were tested using the same three types of measurement cells as in the ones used in the two-ports scenarios.

5.2.1

Heterogeneous Coaxial Waveguide

The sample fills the first layer, while the second one is fullfilled with vacuum.

5.2.1.1

Lossless isotropic sample

This first simulation used the parameters listed in Table 5.45. Results can be seen in Fig. 5.80 and in Table 5.46 for the linear functional while for the decibel one they are in Fig. 5.81 and Table 5.47. We observe that the convergence was achieved after 9 iterations for linear functional and 4 iterations for decibel functional for a value near $\epsilon_r = 2.55$ for linear functional with a good convergence from the ones used in simulation and $\epsilon_r = 2.55$ for decibel functional with a good convergence from the ones used in simulation.

Table 5.45: Geometric and constitutive parameters used on direct problem of a lossless isotropic sample placed in second waveguide of a one-port heterogeneous coaxial waveguide

Region	L(mm)	ρ_0 (mm)	ρ_1 (mm)	ρ_2 (mm)	ϵ_{rs1}	ϵ_{rz1}	σ_{s1}	σ_{z1}
1	-	6.3	10	18	1.01	1.01	10^{-6}	10^{-6}
2	30	6.3	12.6	19	2.55	2.55	10^{-6}	10^{-6}
3	30	6.3	10	18	1.01	1.01	10^{-6}	10^{-6}

Table 5.46: Initial guess, CPU time, and the number of iterations to achieve convergence by using the parameters Table 5.45 using linear functional.

x_0	Time	Iterations
2.51	27 min 54 seconds	9

Table 5.47: Initial guess, CPU time, and the number of iterations to achieve convergence by using the parameters Table 5.45 using decibel functional.

x_0	Time	Iterations
2.51	20 min 55 seconds	4

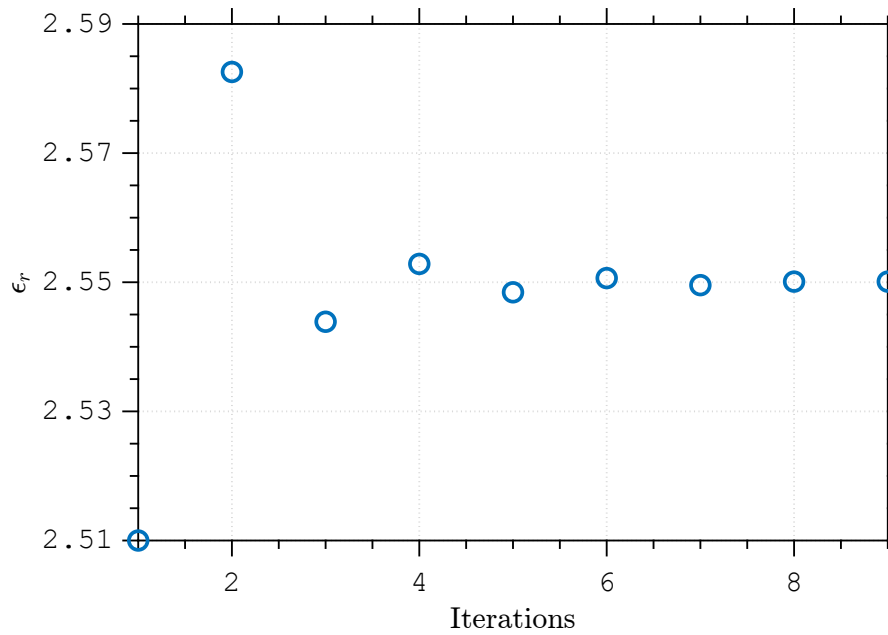


Figure 5.80: Evolution of the optimization parameter as a function of the number of iterations using linear functional. Convergence was achieved after 9 iterations at $\epsilon_r = 2.55$.

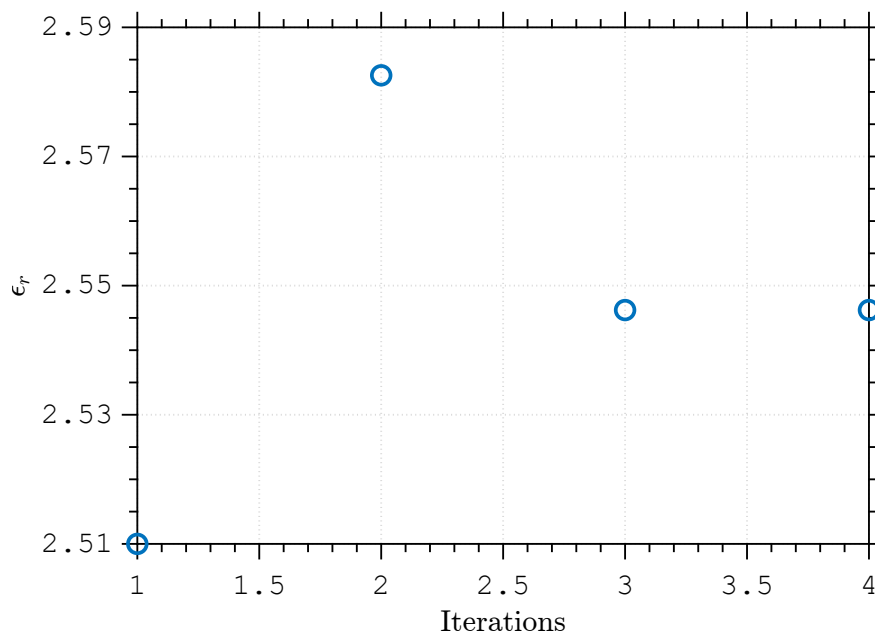


Figure 5.81: Evolution of the optimization parameter as a function of the number of iterations using decibel functional. Convergence was achieved after 4 iterations at $\epsilon_r = 2.55$.

5.2.1.2

Lossy isotropic sample

For this case, parameters can be seen in Table 5.48 and results for linear functional are in Fig. 5.82 and 5.83 and in Table 5.49. The decibel functional has its results on Fig. 5.84 and 5.85 and in Table 5.50. We observe that

the convergence was achieved after 16 iterations for linear functional and 3 iterations for decibel functional for a value near $\epsilon_r = 2.55$ and $\sigma = 0.01$ for linear functional with a good convergence from the ones used in simulation and $\epsilon_r = 2.58$ and $\sigma = 0.011$ for decibel functional with a small difference from the ones used in simulation

Table 5.48: Geometric and constitutive parameters used on direct problem of a lossy isotropic sample placed in second waveguide of a one-port heterogeneous coaxial waveguide

Region	L(mm)	ρ_0 (mm)	ρ_1 (mm)	ρ_2 (mm)	ϵ_{rs1}	ϵ_{rz1}	σ_{s1}	σ_{z1}
1	-	6.3	10	18	1.01	1.01	10^{-6}	10^{-6}
2	30	6.3	12.6	19	2.55	2.55	10^{-2}	10^{-2}
3	30	6.3	10	18	1.01	1.01	10^{-6}	10^{-6}

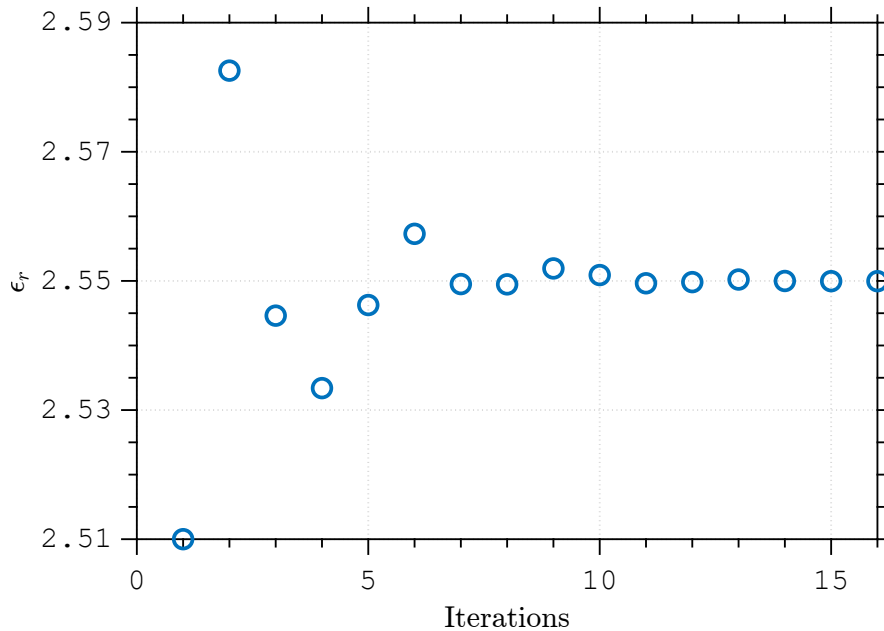


Figure 5.82: Evolution of the optimization parameter as a function of the number of iterations using linear functional. Convergence was achieved after 16 iterations at $\epsilon_r = 2.55$.

Table 5.49: Initial guess, CPU time, and the number of iterations to achieve convergence by using the parameters Table 5.48 using linear functional.

x_0	Time	Iterations
[2.51 0.01]	89 min 21 seconds	16

Table 5.50: Initial guess, CPU time, and the number of iterations to achieve convergence by using the parameters Table 5.48 using decibel functional.

x_0	Time	Iterations
[2.51 0.01]	53 min 27 seconds	3

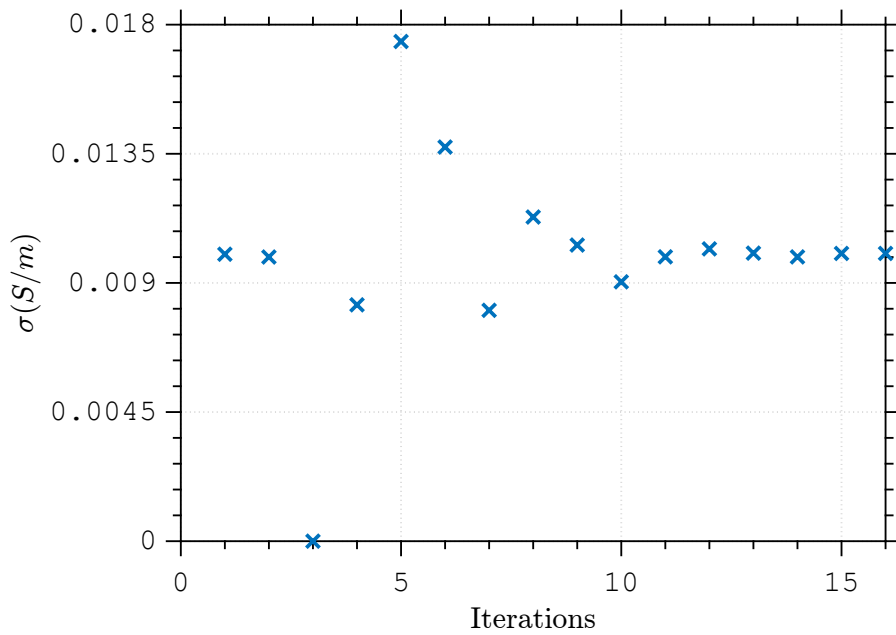


Figure 5.83: Evolution of the optimization parameter as a function of the number of iterations using linear functional. Convergence was achieved after 16 iterations at $\sigma = 0.01$.

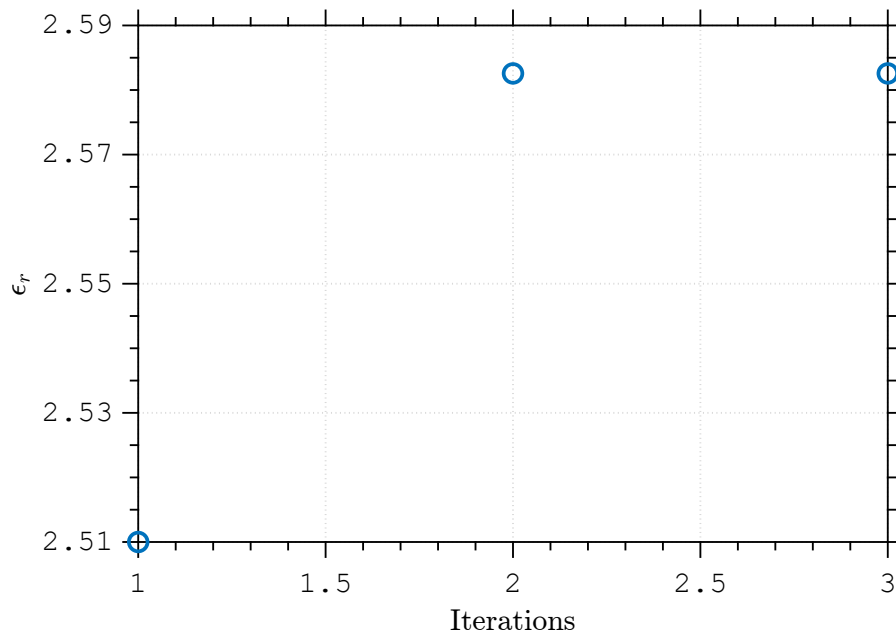


Figure 5.84: Evolution of the optimization parameter as a function of the number of iterations using decibel functional. Convergence was achieved after 3 iterations at $\epsilon_r = 2.58$.

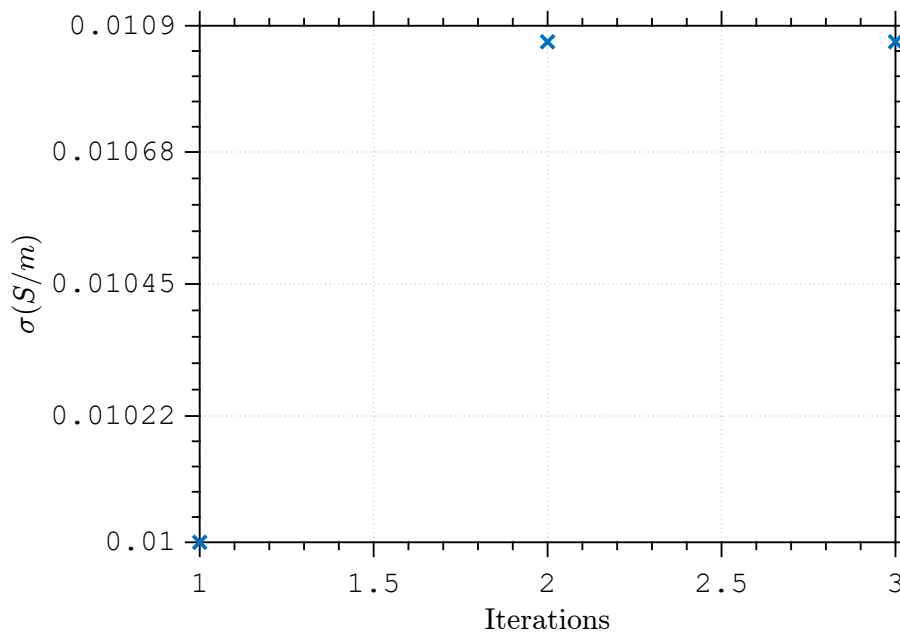


Figure 5.85: Evolution of the optimization parameter as a function of the number of iterations using decibel functional. Convergence was achieved after 3 iterations at $\sigma = 0.011$.

5.2.1.3 Lossless anisotropic sample

For the lossless anisotropic material case, parameters are in Table 5.51. Results for the linear functional are in Fig. 5.86 and 5.87 and in Table 5.52. For decibel functional they are in Fig. 5.88 and 5.89 and in Table 5.53. We observe that the convergence was achieved after 14 iterations for linear functional and 7 iterations for decibel functional for a value near $\epsilon_{rs} = 2.55$ and $\epsilon_{rz} = 3$ for linear functional with a good convergence from the ones used in simulation and $\epsilon_{rs} = 2.55$ and $\epsilon_{rz} = 3$ for decibel functional with a good convergence from the ones used in simulation

Table 5.51: Geometric and constitutive parameters used on direct problem of a lossless anisotropic sample placed in second waveguide of a one-port heterogeneous coaxial waveguide

Region	L(mm)	ρ_0 (mm)	ρ_1 (mm)	ρ_2 (mm)	ϵ_{rs1}	ϵ_{rz1}	σ_{s1}	σ_{z1}
1	-	6.3	10	18	1.01	1.01	10^{-6}	10^{-6}
2	30	6.3	12.6	19	2.55	3	10^{-6}	10^{-6}
3	30	6.3	10	18	1.01	1.01	10^{-6}	10^{-6}

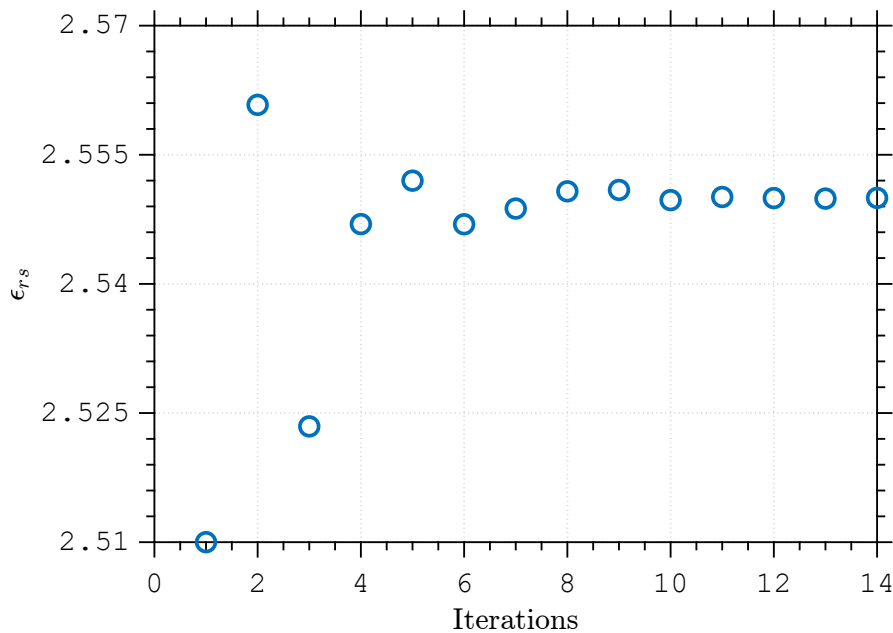


Figure 5.86: Evolution of the optimization parameter as a function of the number of iterations using linear functional. Convergence was achieved after 14 iterations at $\epsilon_{rs} = 2.55$.

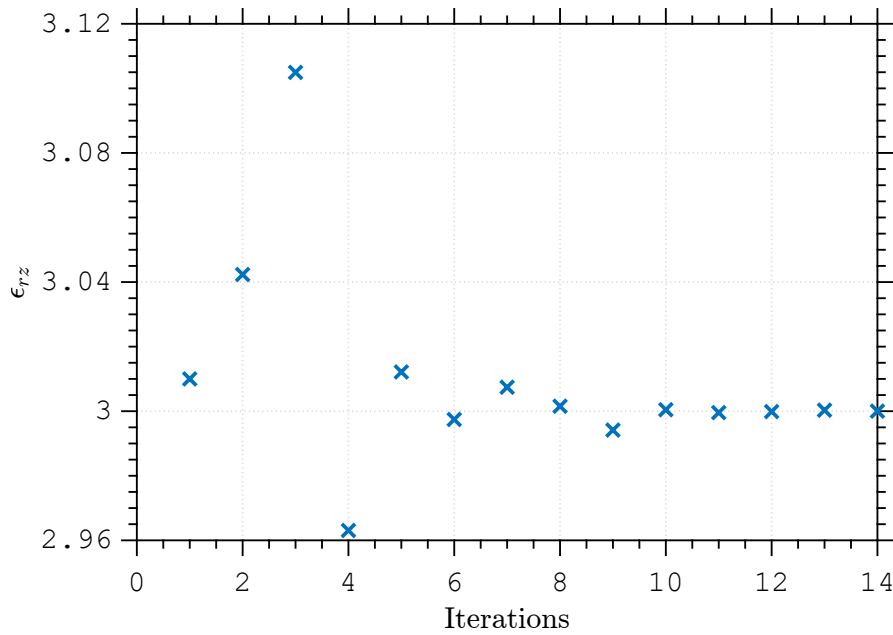


Figure 5.87: Evolution of the optimization parameter as a function of the number of iterations using linear functional. Convergence was achieved after 14 iterations at $\epsilon_{rz} = 3$.

Table 5.52: Initial guess, CPU time, and the number of iterations to achieve convergence by using the parameters Table 5.51 using linear functional.

x_0	Time	Iterations
[2.51 3.01]	243 min 18 seconds	14

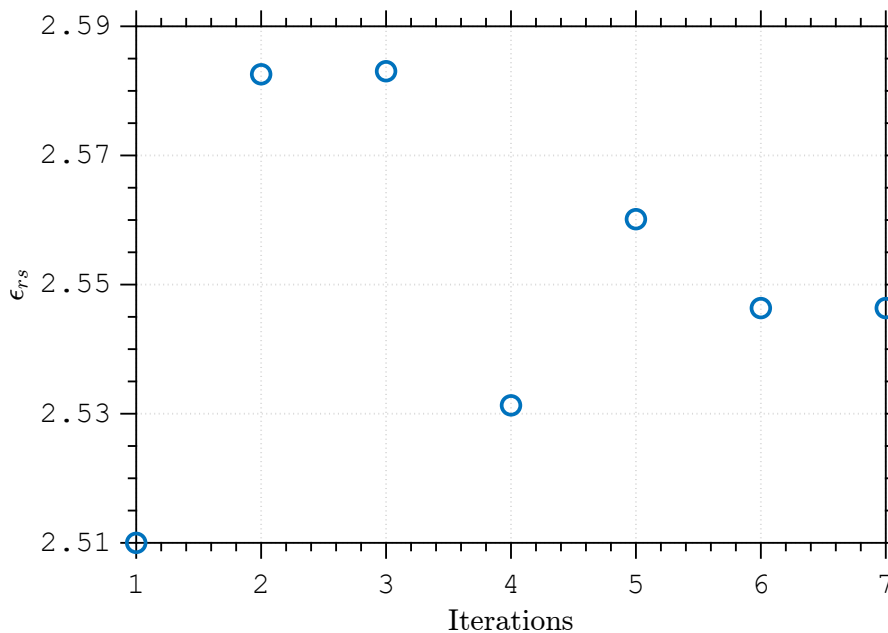


Figure 5.88: Evolution of the optimization parameter as a function of the number of iterations using decibel functional. Convergence was achieved after 7 iterations at $\epsilon_{rs} = 2.55$.

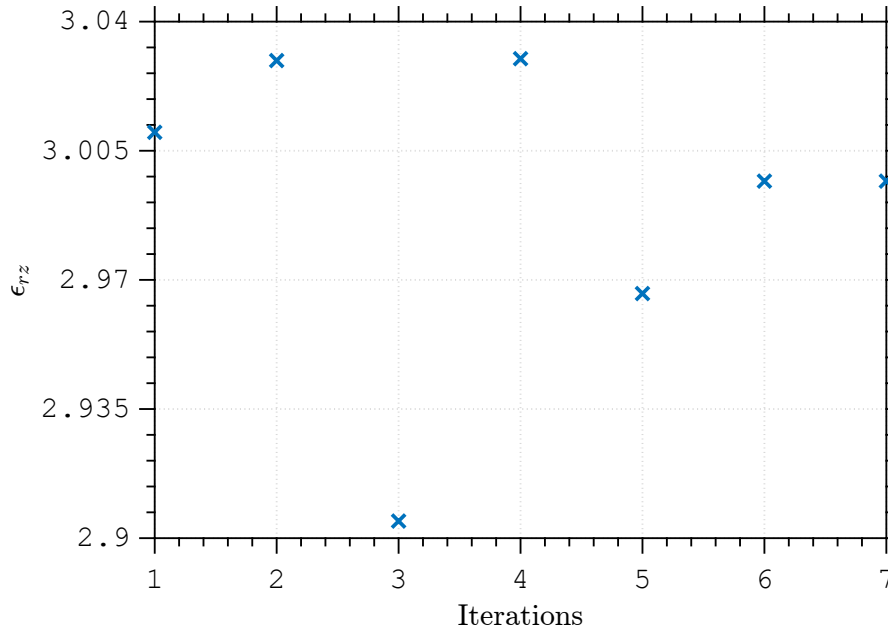


Figure 5.89: Evolution of the optimization parameter as a function of the number of iterations using decibel functional. Convergence was achieved after 7 iterations at $\epsilon_{rz} = 3$.

Table 5.53: Initial guess, CPU time, and the number of iterations to achieve convergence by using the parameters Table 5.51 using decibel functional.

x_0	Time	Iterations
[2.51 3.01]	213 min 3 seconds	7

5.2.1.4

Anisotropic sample with isotropic loss

In this simulation parameters used are in Table 5.54. Results for the linear functional are in Fig. 5.90, 5.91, 5.92 and 5.93 and Table 5.55. For the decibel one, results are in Fig. 5.94, 5.95, 5.96 and 5.97 and in Table 5.56. We observe that the convergence was achieved after 24 iterations for linear functional and 2 iterations for decibel functional for a value near $\epsilon_{rs} = 2.55$, $\epsilon_{rz} = 3$, $\sigma_s = 0.02$ and $\sigma_z = 0.02$ for linear functional with a good convergence from the ones used in simulation and $\epsilon_{rs} = 2.51$, $\epsilon_{rz} = 3.01$, $\sigma_s = 0.01$ and $\sigma_z = 0.01$ for decibel functional with a small difference from the ones used in simulation

Table 5.54: Geometric and constitutive parameters used on direct problem of a isotropic lossy and anisotropic sample placed in second waveguide of a one-port heterogeneous coaxial waveguide

Region	L(mm)	ρ_0 (mm)	ρ_1 (mm)	ρ_2 (mm)	ϵ_{rs1}	ϵ_{rz1}	σ_{s1}	σ_{z1}
1	-	6.3	10	18	1.01	1.01	10^{-6}	10^{-6}
2	30	6.3	12.6	19	2.55	3	2×10^{-2}	2×10^{-2}
3	30	6.3	10	18	1.01	1.01	10^{-6}	10^{-6}

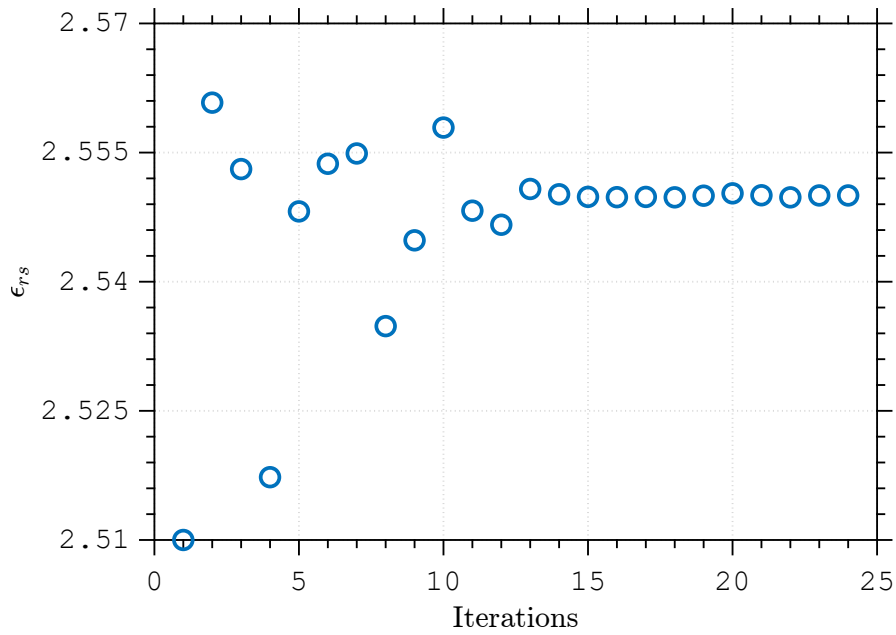


Figure 5.90: Evolution of the optimization parameter as a function of the number of iterations using linear functional. Convergence was achieved after 24 iterations at $\epsilon_{rs} = 2.55$.

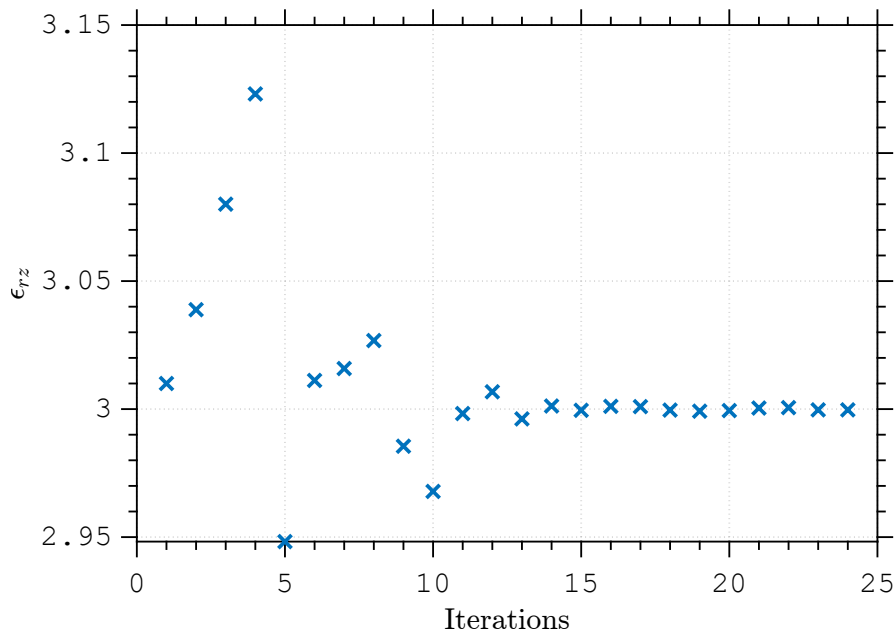


Figure 5.91: Evolution of the optimization parameter as a function of the number of iterations using linear functional. Convergence was achieved after 24 iterations at $\epsilon_{rz} = 2.99$.

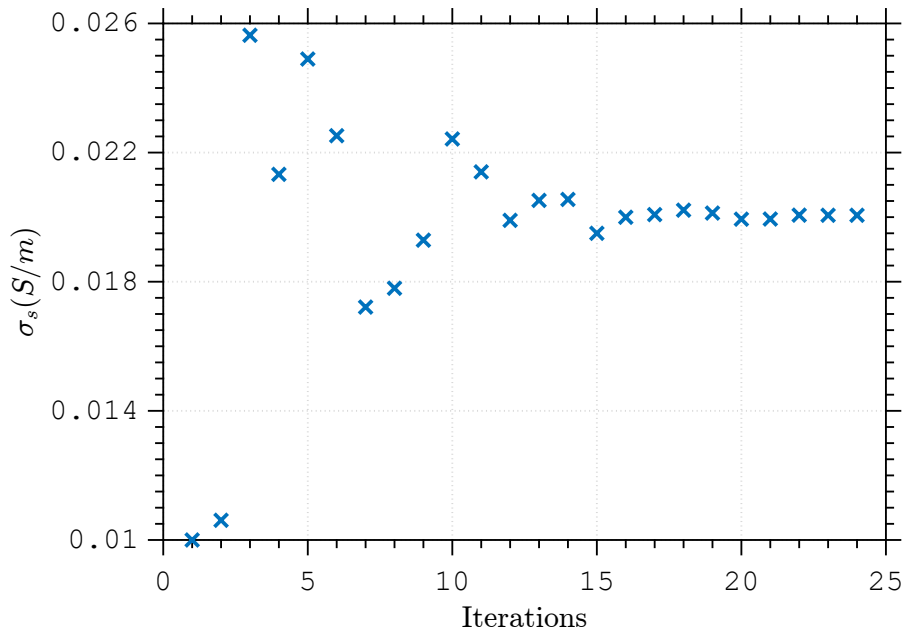


Figure 5.92: Evolution of the optimization parameter as a function of the number of iterations using linear functional. Convergence was achieved after 24 iterations at $\sigma_s = 0.02$.

PUC-Rio - Certificação Digital N° 2012321/CA

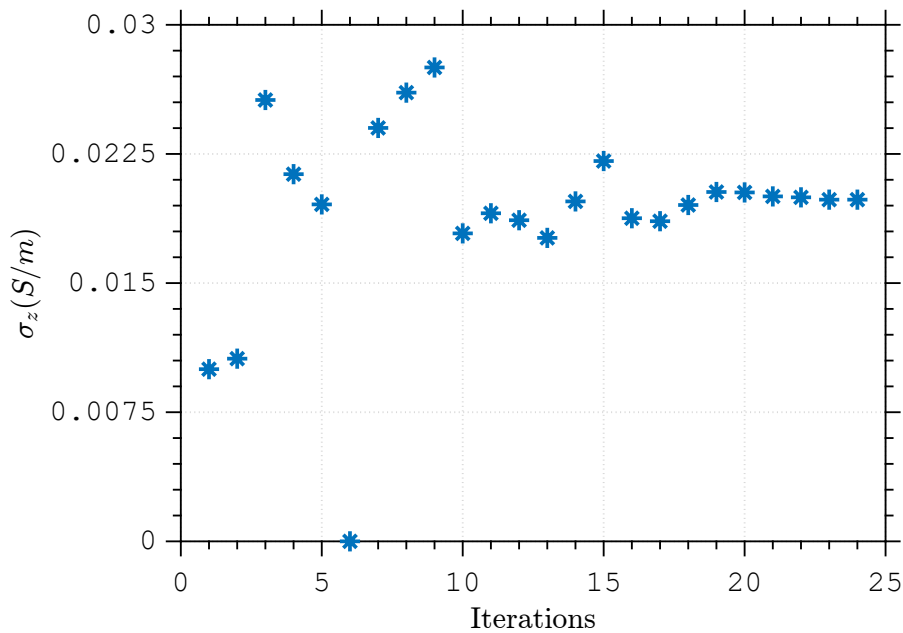


Figure 5.93: Evolution of the optimization parameter as a function of the number of iterations using linear functional. Convergence was achieved after 24 iterations at $\sigma_z = 0.02$.

Table 5.55: Initial guess, CPU time, and the number of iterations to achieve convergence by using the parameters Table 5.54 using linear functional.

x_0	Time	Iterations
[2.51 3.01 0.01 0.01]	230 min 53 seconds	24

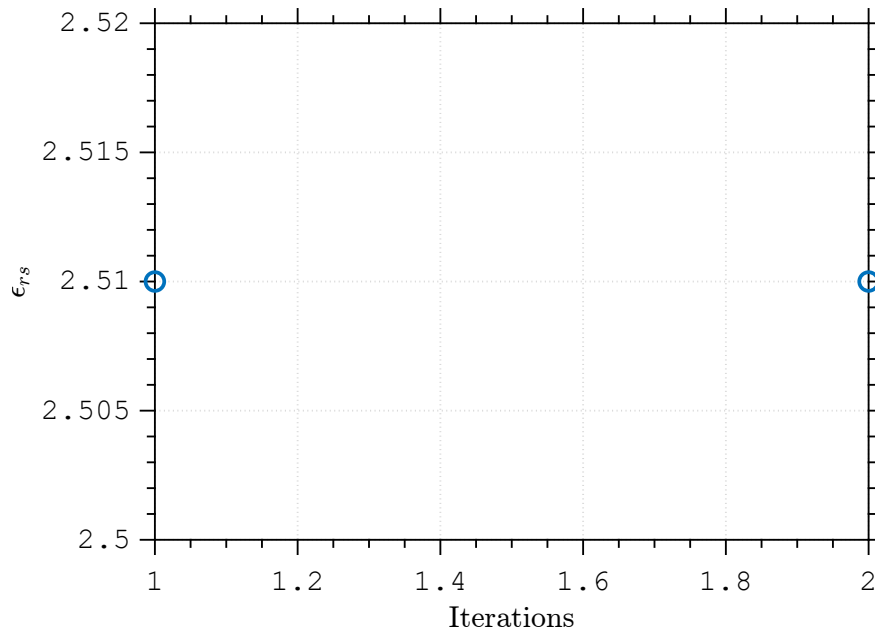


Figure 5.94: Evolution of the optimization parameter as a function of the number of iterations using decibel functional. Convergence was achieved after 2 iterations at $\epsilon_{rs} = 2.51$.

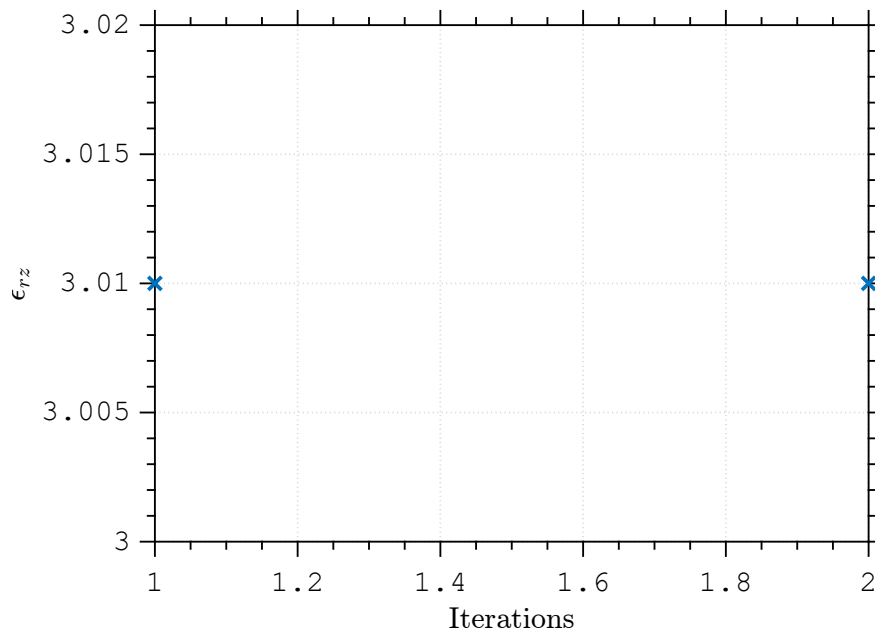


Figure 5.95: Evolution of the optimization parameter as a function of the number of iterations using decibel functional. Convergence was achieved after 2 iterations at $\epsilon_{rz} = 3.01$.

Table 5.56: Initial guess, CPU time, and the number of iterations to achieve convergence by using the parameters Table 5.54 using decibel functional.

x_0	Time	Iterations
[2.51 3.01 0.01 0.01]	156 min 33 seconds	2

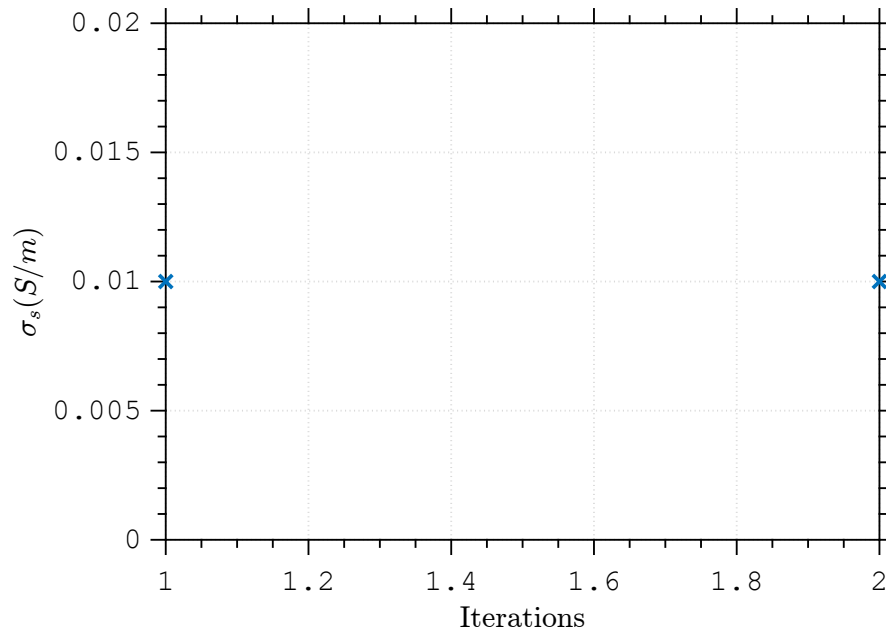


Figure 5.96: Evolution of the optimization parameter as a function of the number of iterations using decibel functional. Convergence was achieved after 2 iterations at $\sigma_s = 0.01$.

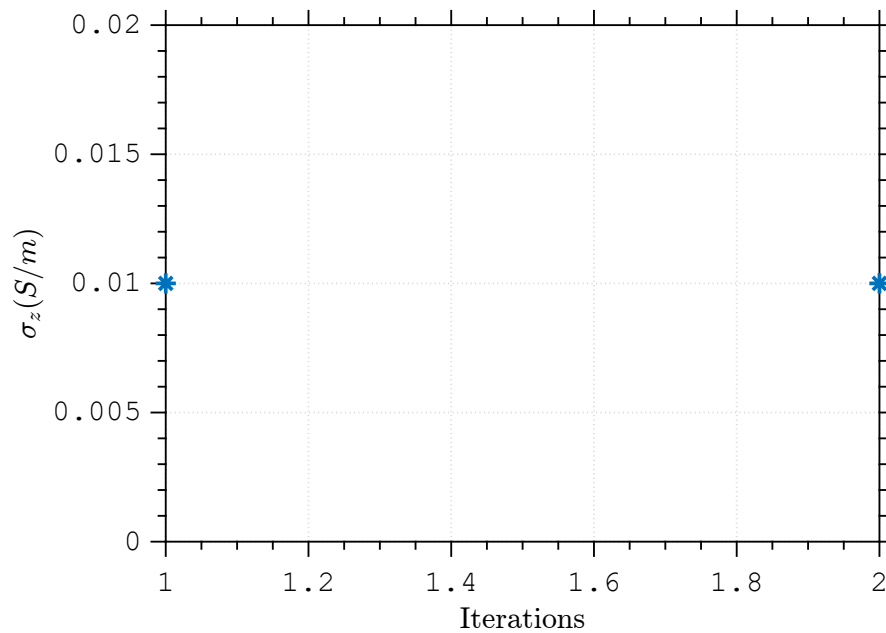


Figure 5.97: Evolution of the optimization parameter as a function of the number of iterations using decibel functional. Convergence was achieved after 2 iterations at $\sigma_z = 0.01$.

5.2.1.5

Anisotropic sample with anisotropic loss

The last case, with an lossy anisotropic material, parameters are in Table 5.57 and results for linear functional are in Fig. 5.98, 5.99, 5.100 and 5.101 and in Table 5.58. The decibel functional has results presented

in Fig. 5.102, 5.103, 5.104 and 5.105 and in Table 5.59. We observe that the convergence was achieved after 21 iterations for linear functional and 4 iterations for decibel functional for a value near $\epsilon_{rs} = 2.55$, $\epsilon_{rz} = 3$, $\sigma_s = 0.01$ and $\sigma_z = 0.02$ for linear functional with a good convergence from the ones used in simulation and $\epsilon_{rs} = 2.57$, $\epsilon_{rz} = 2.98$, $\sigma_s = 0.012$ and $\sigma_z = 0.013$ for decibel functional with a small difference from the ones used in simulation

Table 5.57: Geometric and constitutive parameters used on direct problem of a anisotropic lossy and anisotropic sample placed in second waveguide of a one-port heterogeneous coaxial waveguide

Region	L(mm)	ρ_0 (mm)	ρ_1 (mm)	ρ_2 (mm)	ϵ_{rs1}	ϵ_{rz1}	σ_{s1}	σ_{z1}
1	-	6.3	10	18	1.01	1.01	10^{-6}	10^{-6}
2	30	6.3	12.6	19	2.55	3	10^{-2}	2×10^{-2}
3	30	6.3	10	18	1.01	1.01	10^{-6}	10^{-6}

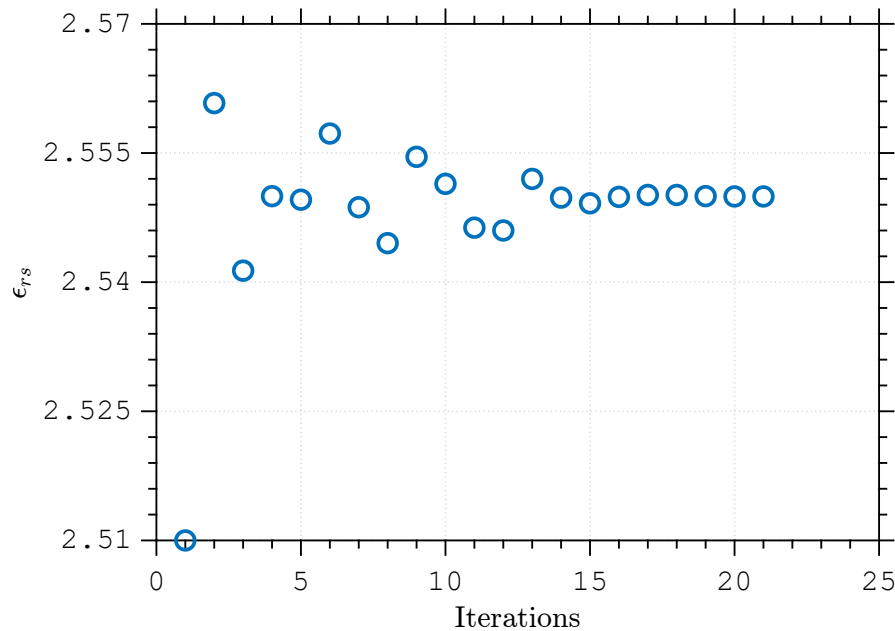


Figure 5.98: Evolution of the optimization parameter as a function of the number of iterations using linear functional. Convergence was achieved after 21 iterations at $\epsilon_{rs} = 2.55$.

Table 5.58: Initial guess, CPU time, and the number of iterations to achieve convergence by using the parameters Table 5.57 using linear functional.

x_0	Time	Iterations
[2.51 3.01 0.01 0.01]	217 min 14 seconds	21

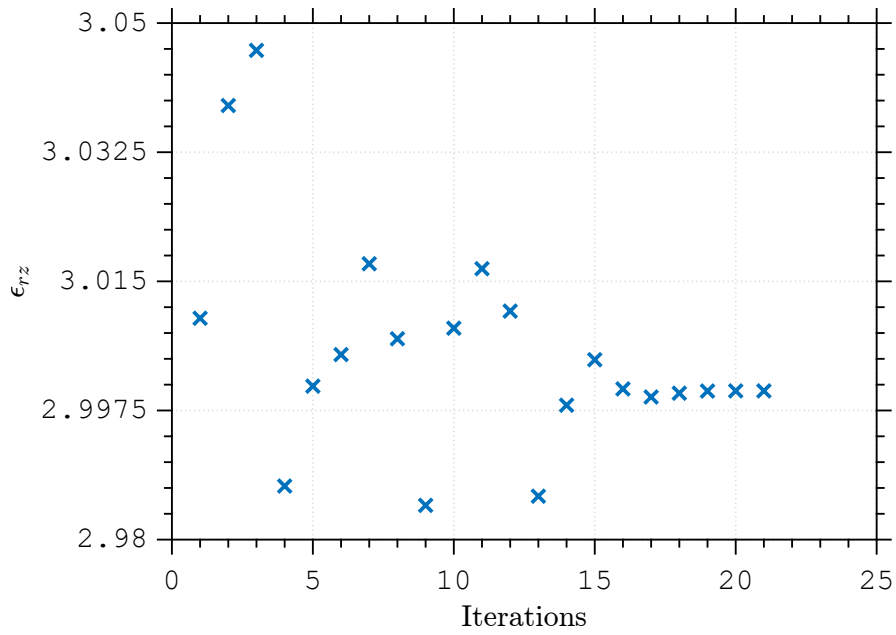


Figure 5.99: Evolution of the optimization parameter as a function of the number of iterations using linear functional. Convergence was achieved after 21 iterations at $\epsilon_{rz} = 3$.

PUC-Rio - Certificação Digital N° 2012321/CA

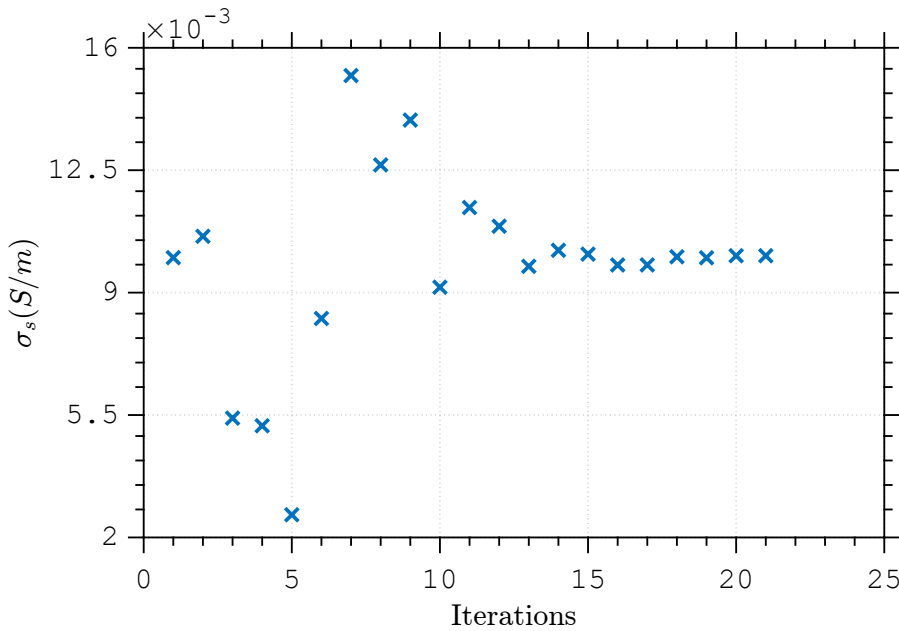


Figure 5.100: Evolution of the optimization parameter as a function of the number of iterations using linear functional. Convergence was achieved after 21 iterations at $\sigma_s = 0.01$.

Table 5.59: Initial guess, CPU time, and the number of iterations to achieve convergence by using the parameters Table 5.57 using decibel functional.

x_0	Time	Iterations
[2.51 3.01 0.01 0.01]	180 min 24 seconds	4

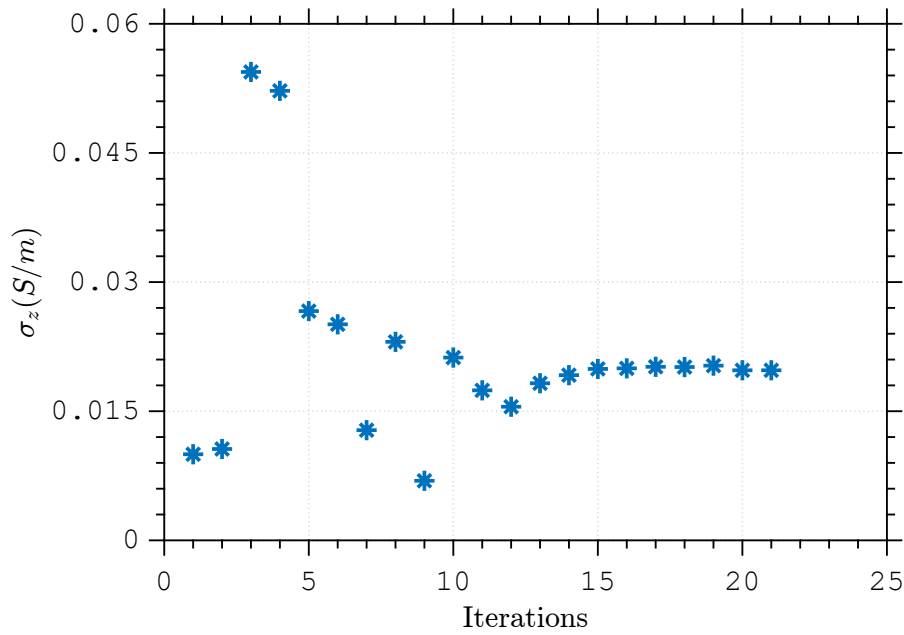


Figure 5.101: Evolution of the optimization parameter as a function of the number of iterations using linear functional. Convergence was achieved after 21 iterations at $\sigma_z = 0.02$.

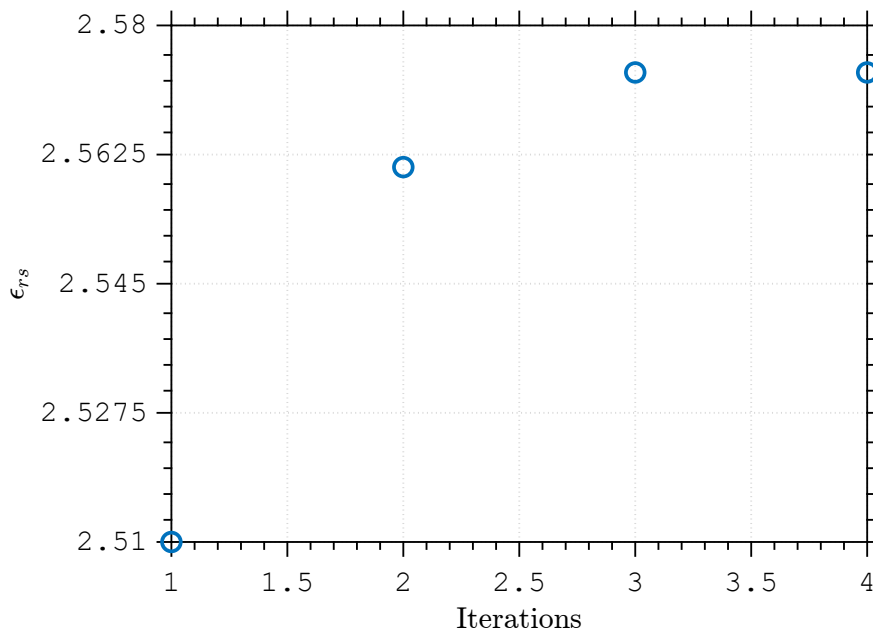


Figure 5.102: Evolution of the optimization parameter as a function of the number of iterations using decibel functional. Convergence was achieved after 4 iterations at $\epsilon_{rs} = 2.57$.

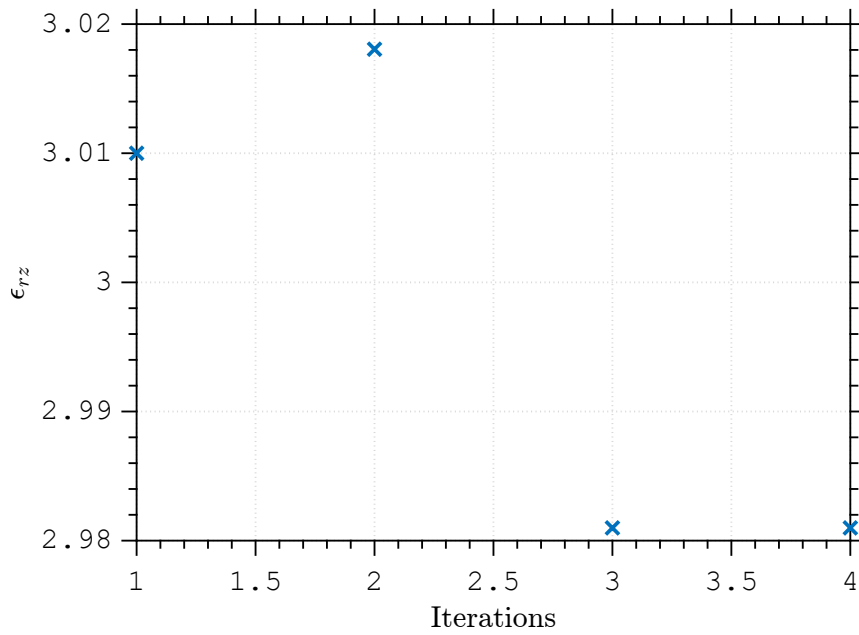


Figure 5.103: Evolution of the optimization parameter as a function of the number of iterations using decibel functional. Convergence was achieved after 4 iterations at $\epsilon_{rz} = 2.98$.

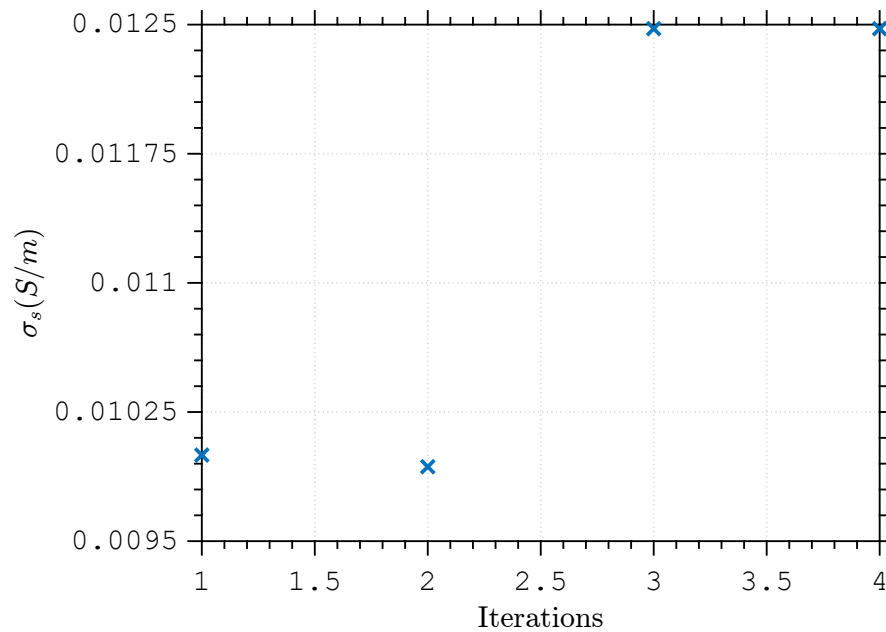


Figure 5.104: Evolution of the optimization parameter as a function of the number of iterations using decibel functional. Convergence was achieved after 4 iterations at $\sigma_s = 0.012$.

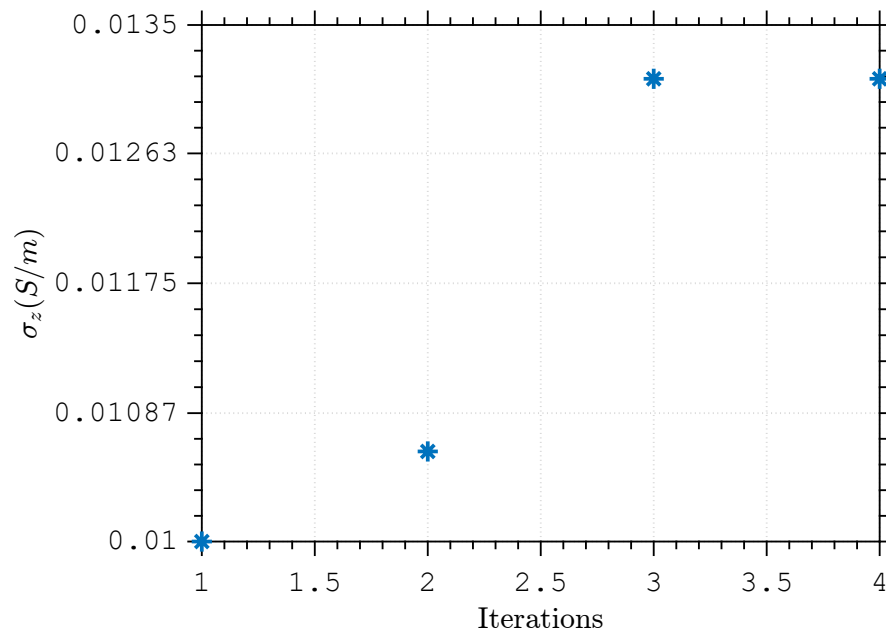


Figure 5.105: Evolution of the optimization parameter as a function of the number of iterations using decibel functional. Convergence was achieved after 4 iterations at $\sigma_z = 0.013$.

5.2.2 Homogeneous Circular Waveguide

As in the previous section, the material is occupying the entire waveguide in the second region.

5.2.2.1 Lossless isotropic sample

This first simulation used the parameters listed in Table 5.60. Results can be seen in Fig. 5.106 and in Table 5.61 for the linear functional while for the decibel one are in Fig. 5.107 and Table 5.62. We observe that the convergence was achieved after 9 iterations for linear functional and 3 iterations for decibel functional for a value near $\epsilon_r = 2.55$ for linear functional with a good convergence from the ones used in simulation and $\epsilon_r = 2.54$ for decibel functional with a good convergence from the ones used in simulation

Table 5.60: Geometric and constitutive parameters used on direct problem of a lossless isotropic sample placed in second waveguide of a one-port homogeneous circular waveguide

Region	L(mm)	ρ_0 (mm)	ρ_1 (mm)	ρ_2 (mm)	ϵ_{rs1}	ϵ_{rz1}	σ_{s1}	σ_{z1}
1	-	6.3	10	18	1.01	1.01	10^{-6}	10^{-6}
2	30	0	19	-	2.55	2.55	10^{-6}	10^{-6}
3	30	6.3	10	18	1.01	1.01	10^{-6}	10^{-6}

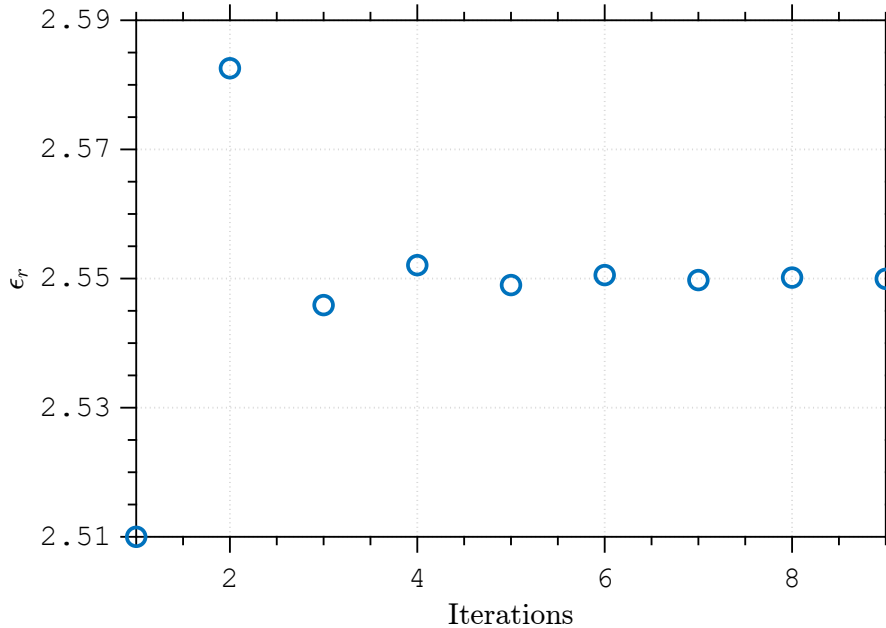


Figure 5.106: Evolution of the optimization parameter as a function of the number of iterations using linear functional. Convergence was achieved after 9 iterations at $\epsilon_r = 2.55$.

Table 5.61: Initial guess, CPU time, and the number of iterations to achieve convergence by using the parameters Table 5.60 using linear functional.

x_0	Time	Iterations
2.51	25 min 16 seconds	9

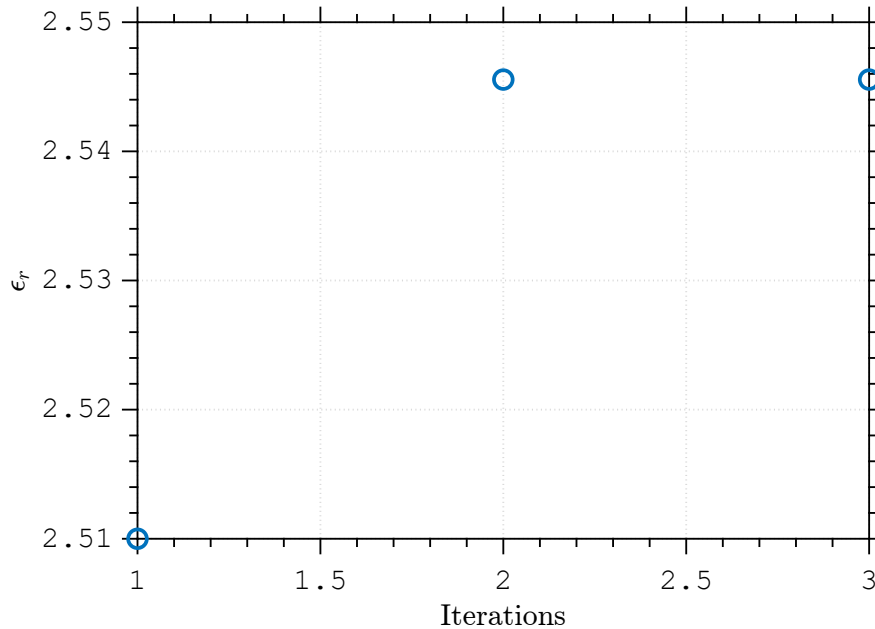


Figure 5.107: Evolution of the optimization parameter as a function of the number of iterations using decibel functional. Convergence was achieved after 3 iterations at $\epsilon_r = 2.54$.

Table 5.62: Initial guess, CPU time, and the number of iterations to achieve convergence by using the parameters Table 5.60 using decibel functional.

x_0	Time	Iterations
2.51	21 min 52 seconds	3

5.2.2.2

Lossy isotropic sample

For this case, parameters can be seen in Table 5.63 and results for linear functional are in Fig. 5.108 and 5.109 and in Table 5.64. The decibel functional has its results on Fig. 5.110 and 5.111 and in Table 5.65. We observe that the convergence was achieved after 12 iterations for linear functional and 3 iterations for decibel functional for a value near $\epsilon_r = 2.55$ and $\sigma = 0.01$ for linear functional with a good convergence from the ones used in simulation and $\epsilon_r = 2.58$ and $\sigma = 0.011$ for decibel functional with a small difference from the ones used in simulation.

Table 5.63: Geometric and constitutive parameters used on direct problem of a lossy isotropic sample placed in second waveguide of a one-port homogeneous circular waveguide

Region	L(mm)	ρ_0 (mm)	ρ_1 (mm)	ρ_2 (mm)	ϵ_{rs1}	ϵ_{rz1}	σ_{s1}	σ_{z1}
1	-	6.3	10	18	1.01	1.01	10^{-6}	10^{-6}
2	30	0	19	-	2.55	2.55	10^{-2}	10^{-2}
3	30	6.3	10	18	1.01	1.01	10^{-6}	10^{-6}

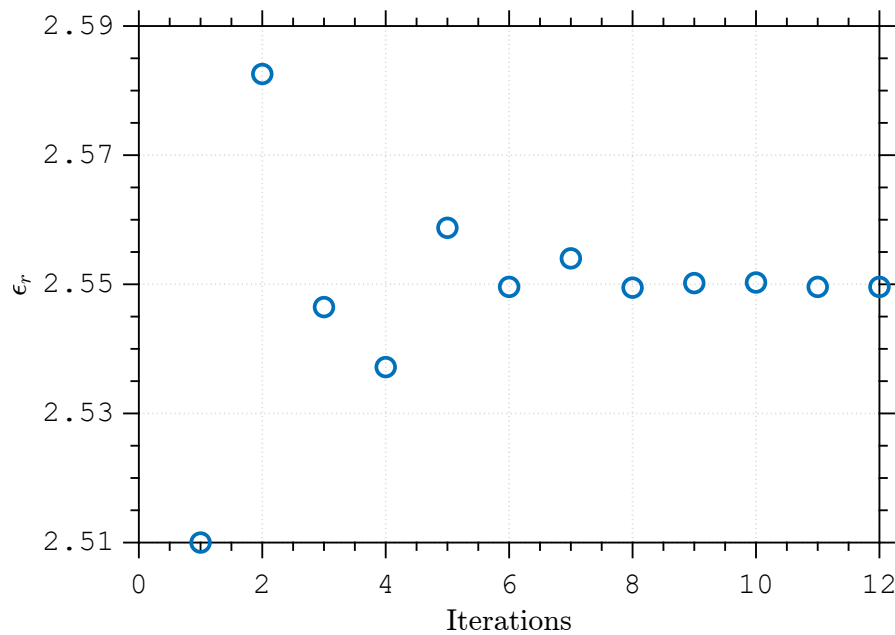


Figure 5.108: Evolution of the optimization parameter as a function of the number of iterations using linear functional. Convergence was achieved after 12 iterations at $\epsilon_r = 2.55$.

Table 5.64: Initial guess, CPU time, and the number of iterations to achieve convergence by using the parameters Table 5.63 using linear functional.

x_0	Time	Iterations
[2.51 0.01]	67 min 8 seconds	12

Table 5.65: Initial guess, CPU time, and the number of iterations to achieve convergence by using the parameters Table 5.63 using decibel functional.

x_0	Time	Iterations
[2.51 0.01]	47 min 56 seconds	3

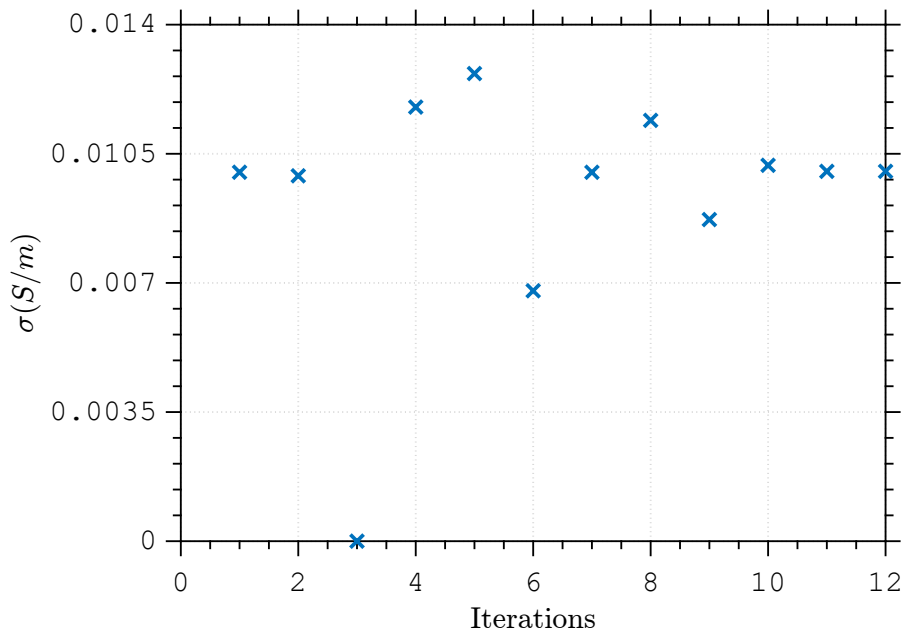


Figure 5.109: Evolution of the optimization parameter as a function of the number of iterations using linear functional. Convergence was achieved after 12 iterations at $\sigma = 0.01$.

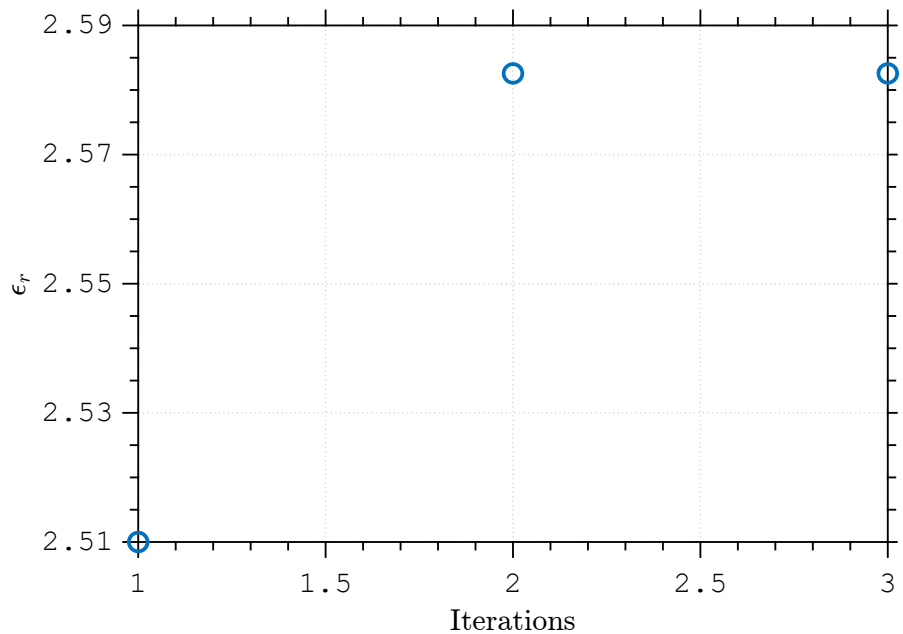


Figure 5.110: Evolution of the optimization parameter as a function of the number of iterations using decibel functional. Convergence was achieved after 3 iterations at $\epsilon_r = 2.58$.

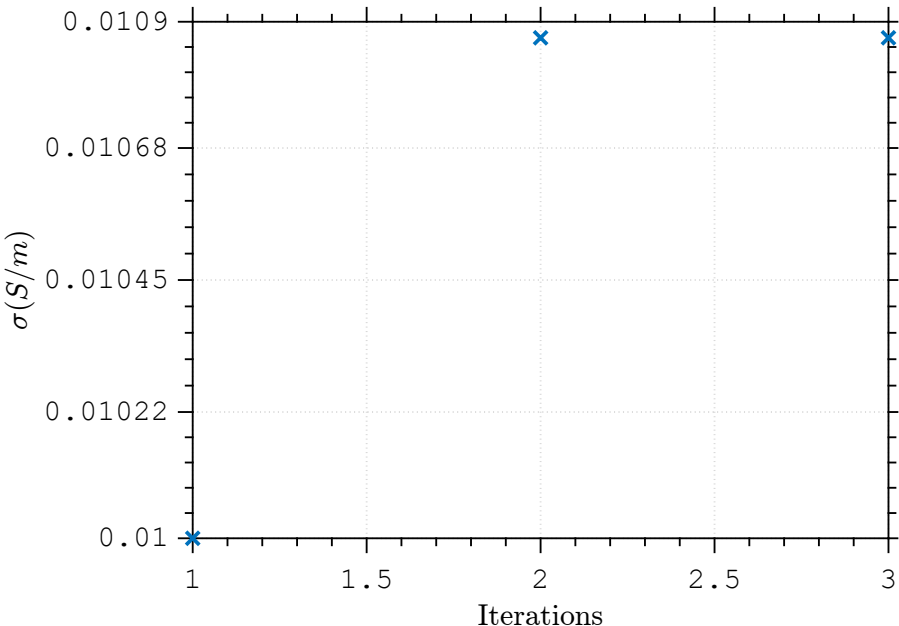


Figure 5.111: Evolution of the optimization parameter as a function of the number of iterations using decibel functional. Convergence was achieved after 3 iterations at $\sigma = 0.01$.

5.2.2.3

Lossless anisotropic sample

For the lossless anisotropic material case, parameters are in Table 5.66. Results for the linear functional are in Fig. 5.112 and 5.113 and in Table 5.67. For decibel functional they are in Fig. 5.114 and 5.115 and in Table 5.68. We observe that the convergence was achieved after 10 iterations for linear functional and 3 iterations for decibel functional for a value near $\epsilon_{rs} = 2.55$ and $\epsilon_{rz} = 2.99$ for linear functional with a small difference from the ones used in simulation and $\epsilon_{rs} = 2.56$ and $\epsilon_{rz} = 2.99$ for decibel functional with a small difference from the ones used in simulation

Table 5.66: Geometric and constitutive parameters used on direct problem of a lossless anisotropic sample placed in second waveguide of a one-port homogeneous circular waveguide

Region	L(mm)	ρ_0 (mm)	ρ_1 (mm)	ρ_2 (mm)	ϵ_{rs1}	ϵ_{rz1}	σ_{s1}	σ_{z1}
1	-	6.3	10	18	1.01	1.01	10^{-6}	10^{-6}
2	30	0	19	-	2.55	3	10^{-6}	10^{-6}
3	30	6.3	10	18	1.01	1.01	10^{-6}	10^{-6}

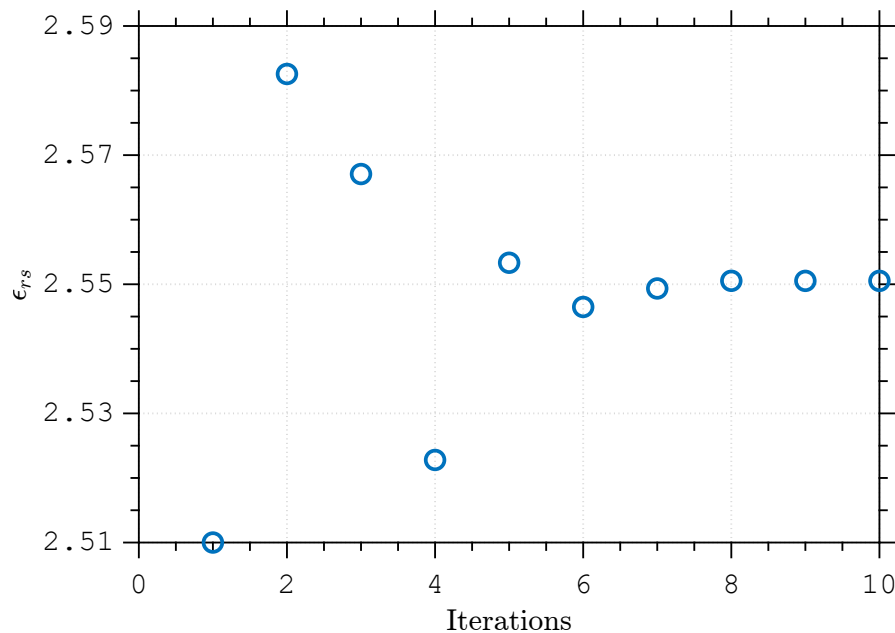


Figure 5.112: Evolution of the optimization parameter as a function of the number of iterations using linear functional. Convergence was achieved after 10 iterations at $\epsilon_{rs} = 2.55$.

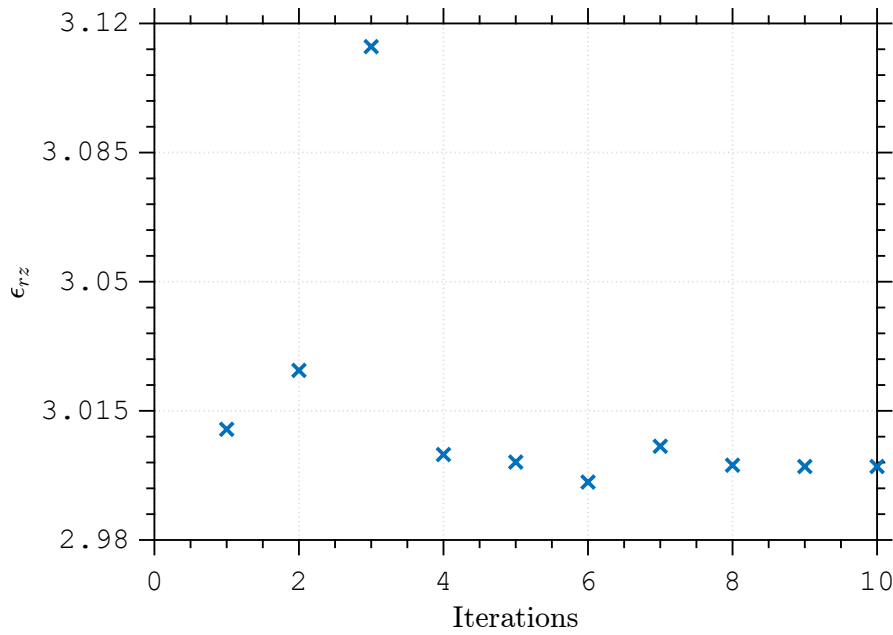


Figure 5.113: Evolution of the optimization parameter as a function of the number of iterations using linear functional. Convergence was achieved after 10 iterations at $\epsilon_{rz} = 2.99$.

Table 5.67: Initial guess, CPU time, and the number of iterations to achieve convergence by using the parameters table 5.66 of Fig. 5.112 and Fig. 5.113 using linear functional

x_0	Time	Iterations
[2.51 3.01]	195 min 12 seconds	10

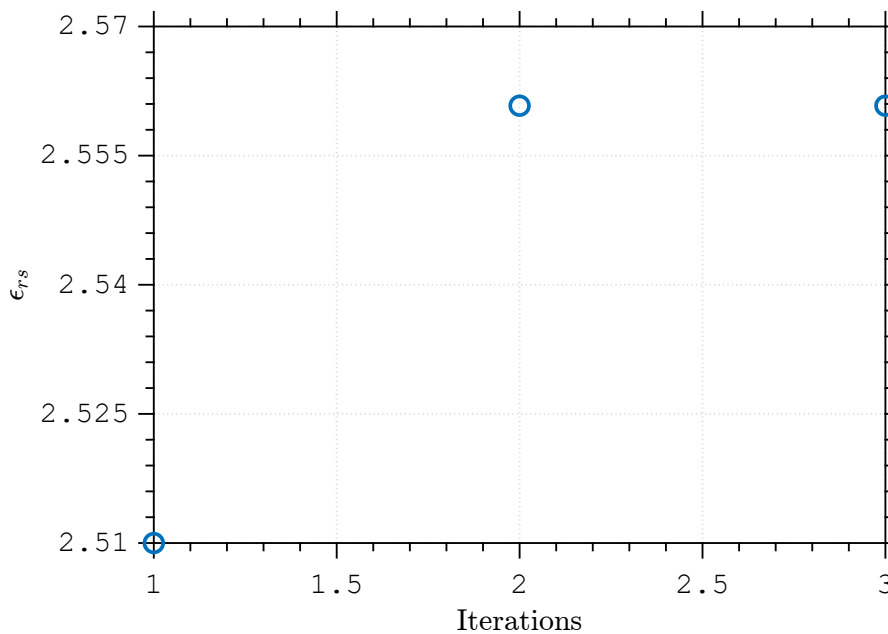


Figure 5.114: Evolution of the optimization parameter as a function of the number of iterations using decibel functional. Convergence was achieved after 3 iterations at $\epsilon_{rs} = 2.56$.

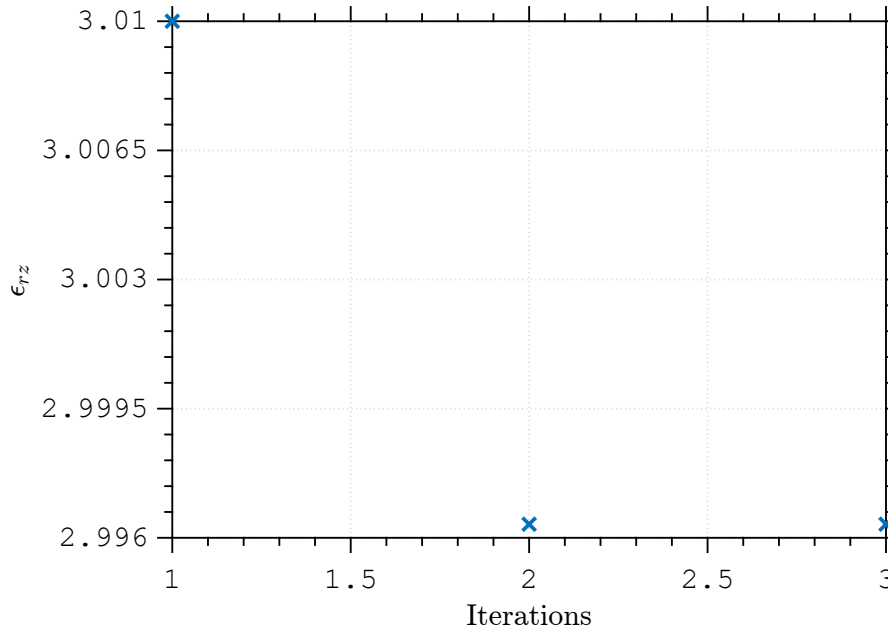


Figure 5.115: Evolution of the optimization parameter as a function of the number of iterations using decibel functional. Convergence was achieved after 3 iterations at $\epsilon_{rz} = 2.99$.

Table 5.68: Initial guess, CPU time, and the number of iterations to achieve convergence by using the parameters Table 5.66 using decibel functional.

x_0	Time	Iterations
[2.51 3.01]	178 min 11 seconds	3

5.2.2.4

Anisotropic sample with isotropic loss

In this simulation parameters used are in Table 5.69. Results for the linear functional are in Fig. 5.116, 5.117, 5.118 and 5.119 and Table 5.70. For the decibel one, results are in Fig. 5.120, 5.121, 5.122 and 5.123 and Table 5.71. We observe that the convergence was achieved after 26 iterations for linear functional and 3 iterations for decibel functional for a value near $\epsilon_{rs} = 2.55$, $\epsilon_{rz} = 3$, $\sigma_s = 0.01$ and $\sigma_z = 0.01$ for linear functional with a good convergence from the ones used in simulation and $\epsilon_{rs} = 2.61$, $\epsilon_{rz} = 3.05$, $\sigma_s = 0.002$ and $\sigma_z = 0.002$ for decibel functional with a relative difference from the ones used in simulation

Table 5.69: Geometric and constitutive parameters used on direct problem of a isotropic lossy and anisotropic sample placed in second waveguide of a one-port homogeneous circular waveguide

Region	L(mm)	ρ_0 (mm)	ρ_1 (mm)	ρ_2 (mm)	ϵ_{rs1}	ϵ_{rz1}	σ_{s1}	σ_{z1}
1	-	6.3	10	18	1.01	1.01	10^{-6}	10^{-6}
2	30	0	19	-	2.55	3	10^{-2}	10^{-2}
3	30	6.3	10	18	1.01	1.01	10^{-6}	10^{-6}

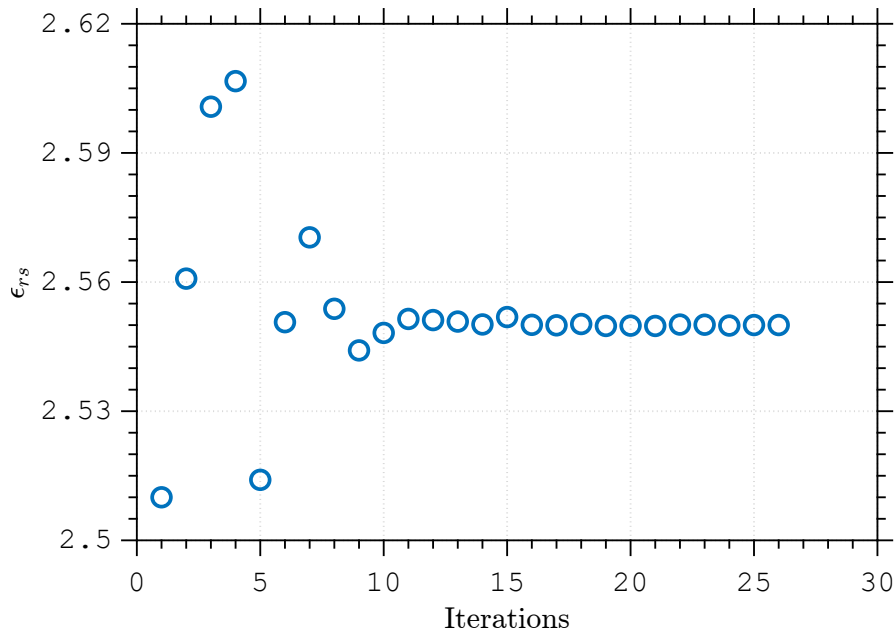


Figure 5.116: Evolution of the optimization parameter as a function of the number of iterations using linear functional. Convergence was achieved after 26 iterations at $\epsilon_{rs} = 2.55$.

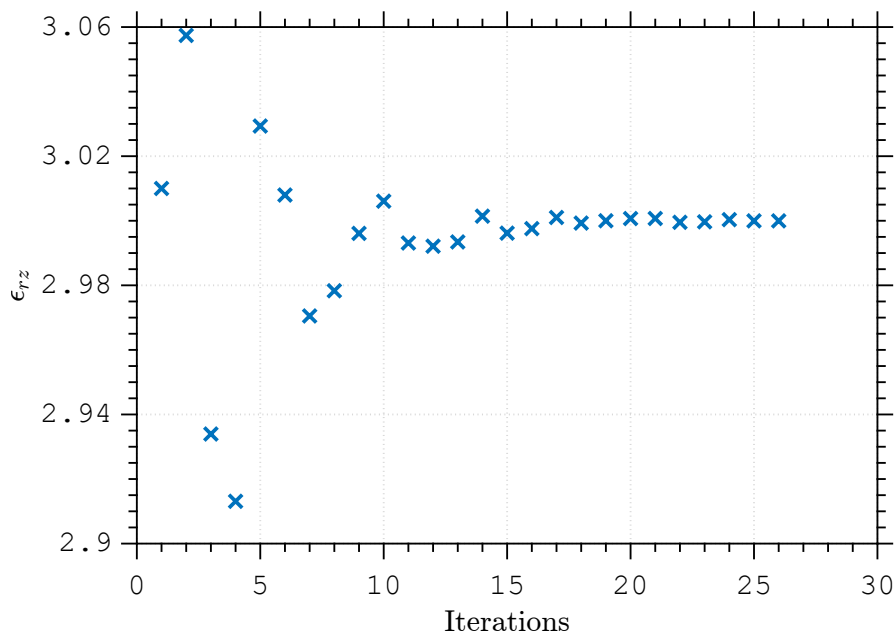


Figure 5.117: Evolution of the optimization parameter as a function of the number of iterations using linear functional. Convergence was achieved after 26 iterations at $\epsilon_{rz} = 3$.

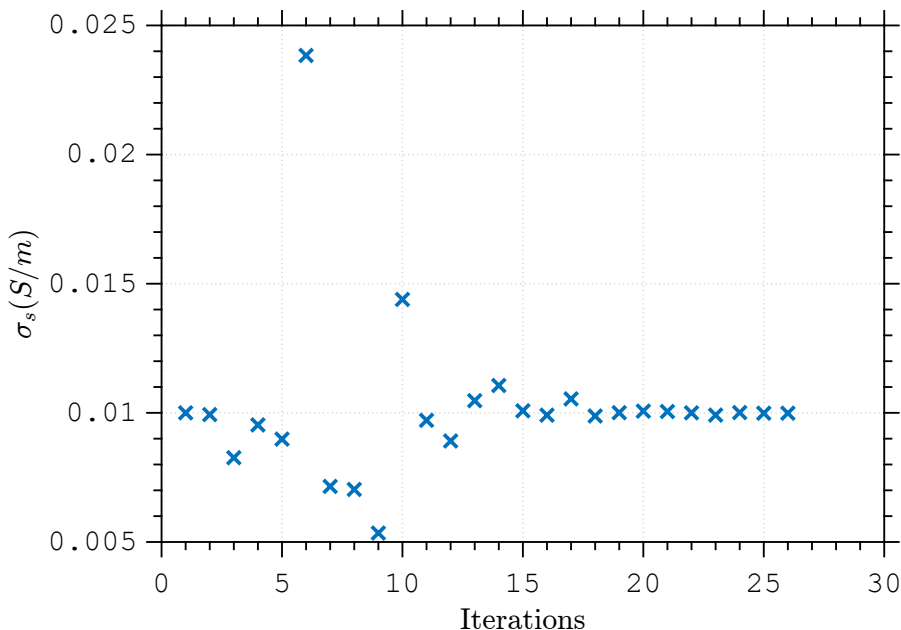


Figure 5.118: Evolution of the optimization parameter as a function of the number of iterations using linear functional. Convergence was achieved after 26 iterations at $\sigma_s = 0.01$.

PUC-Rio - Certificação Digital N° 2012321/CA

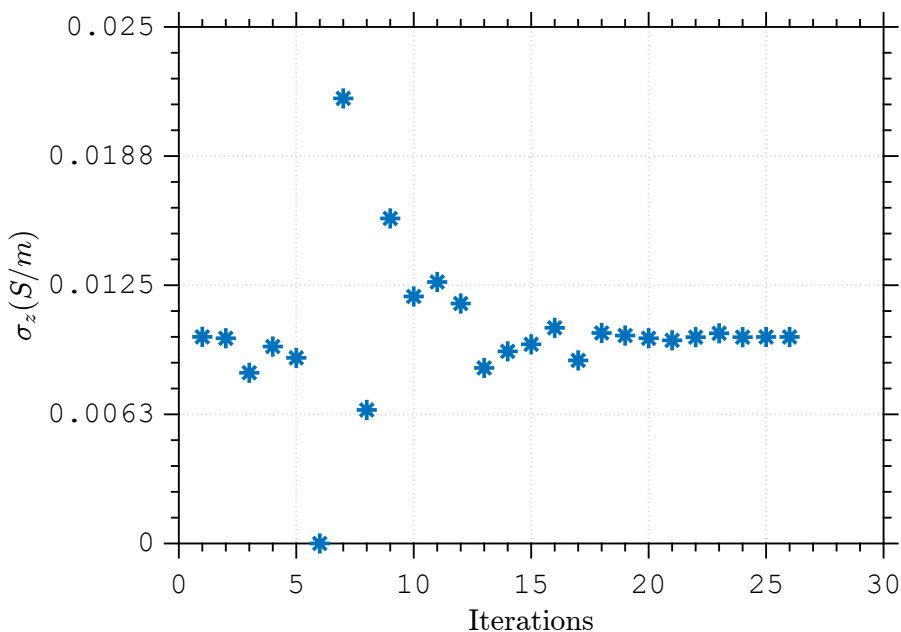


Figure 5.119: Evolution of the optimization parameter as a function of the number of iterations using linear functional. Convergence was achieved after 26 iterations at $\sigma_z = 0.01$.

Table 5.70: Initial guess, CPU time, and the number of iterations to achieve convergence by using the parameters Table 5.69 using linear functional.

x_0	Time	Iterations
[2.51 3.01 0.01 0.01]	197 min 36 seconds	26

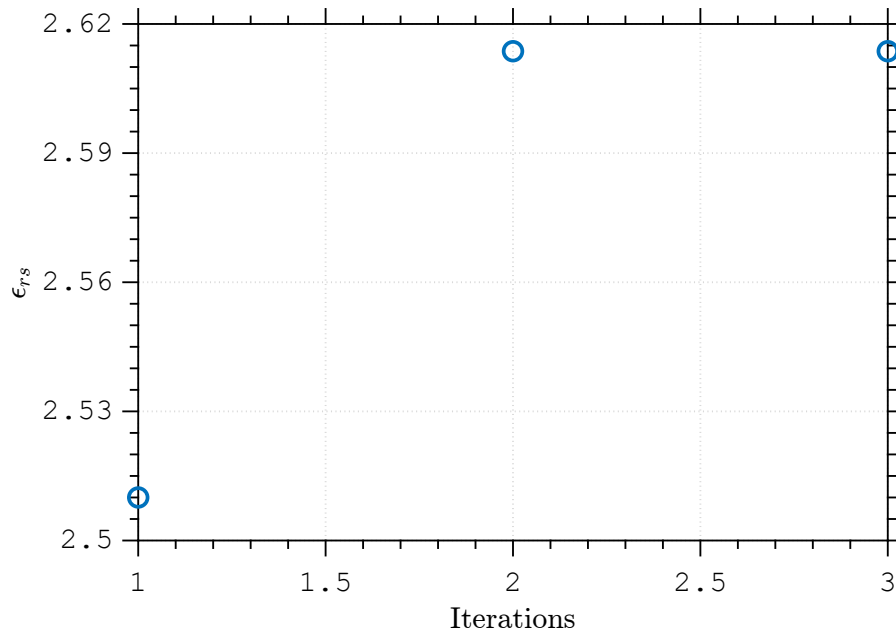


Figure 5.120: Evolution of the optimization parameter as a function of the number of iterations using decibel functional. Convergence was achieved after 3 iterations at $\epsilon_{rs} = 2.61$.

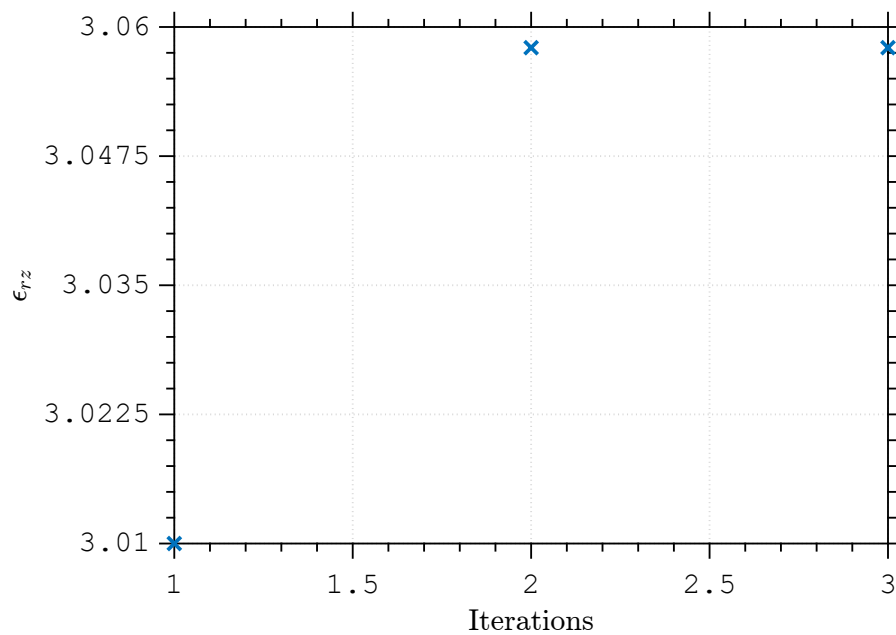


Figure 5.121: Evolution of the optimization parameter as a function of the number of iterations using decibel functional. Convergence was achieved after 3 iterations at $\epsilon_{rz} = 3.05$.

Table 5.71: Initial guess, CPU time, and the number of iterations to achieve convergence by using the parameters Table 5.69 using decibel functional.

x_0	Time	Iterations
[2.51 3.01 0.01 0.01]	156 min 33 seconds	3

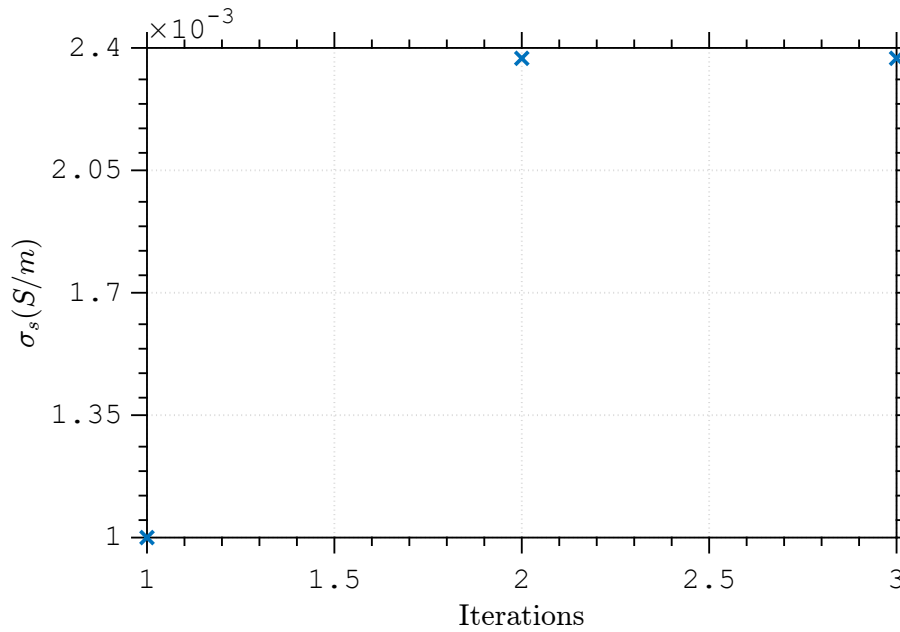


Figure 5.122: Evolution of the optimization parameter as a function of the number of iterations using decibel functional. Convergence was achieved after 3 iterations at $\sigma_s = 0.002$.

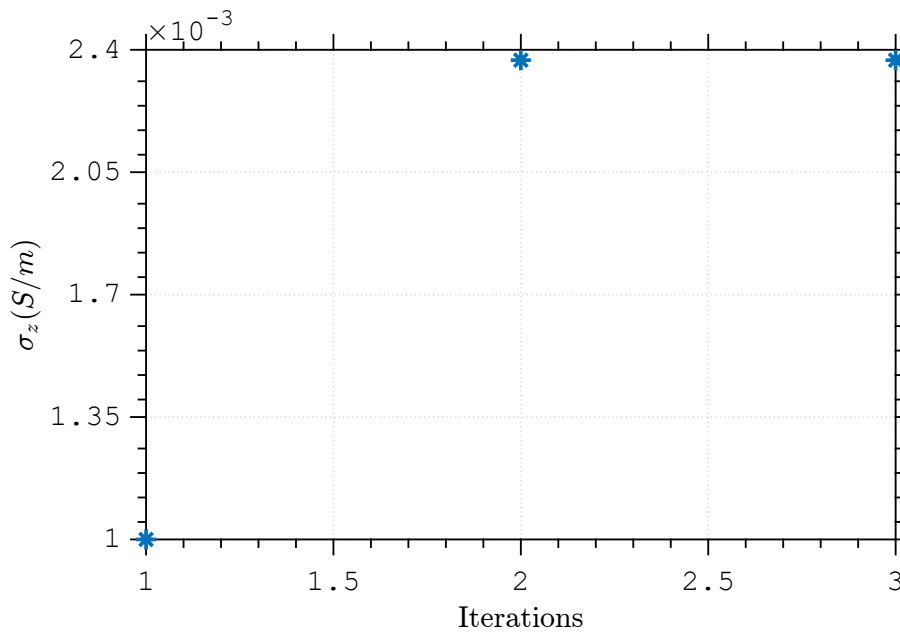


Figure 5.123: Evolution of the optimization parameter as a function of the number of iterations using decibel functional. Convergence was achieved after 3 iterations at $\sigma_z = 0.002$.

5.2.2.5

Anisotropic sample with anisotropic loss

The last case, with an lossy anisotropic material, parameters are in Table 5.72 and results for linear functional are in Fig. 5.124, 5.125, 5.126 and 5.127 and in Table 5.73. The decibel functional has results presented

in Fig. 5.128, 5.129, 5.130 and 5.131 and in Table 5.74. We observe that the convergence was achieved after 23 iterations for linear functional and 4 iterations for decibel functional for a value near $\epsilon_{rs} = 2.55$, $\epsilon_{rz} = 3$, $\sigma_s = 0.01$ and $\sigma_z = 0.02$ for linear functional with a good convergence from the ones used in simulation and $\epsilon_{rs} = 2.57$, $\epsilon_{rz} = 2.98$, $\sigma_s = 0.012$ and $\sigma_z = 0.012$ for decibel functional with a small difference from the ones used in simulation

Table 5.72: Geometric and constitutive parameters used on direct problem of a anisotropic lossy and anisotropic sample placed in second waveguide of a one-port homogeneous circular waveguide

Region	L(mm)	ρ_0 (mm)	ρ_1 (mm)	ρ_2 (mm)	ϵ_{rs1}	ϵ_{rz1}	σ_{s1}	σ_{z1}
1	-	6.3	10	18	1.01	1.01	10^{-6}	10^{-6}
2	30	0	19	-	2.55	3	10^{-2}	2×10^{-2}
3	30	6.3	10	18	1.01	1.01	10^{-6}	10^{-6}

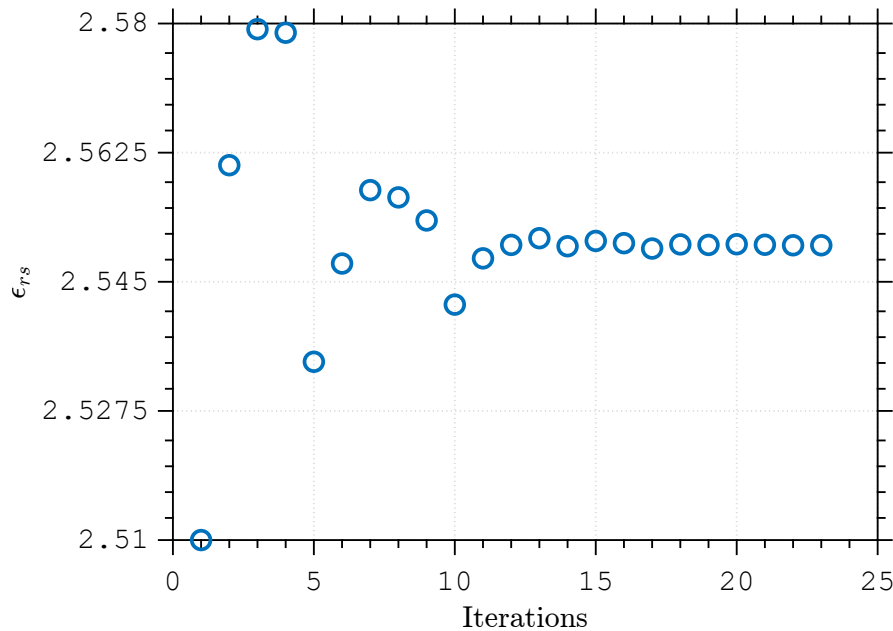


Figure 5.124: Evolution of the optimization parameter as a function of the number of iterations using linear functional. Convergence was achieved after 23 iterations at $\epsilon_{rs} = 2.55$.

Table 5.73: Initial guess, CPU time, and the number of iterations to achieve convergence by using the parameters Table 5.72 using linear functional.

x_0	Time	Iterations
[2.51 3.01 0.01 0.01]	200 min 41 seconds	23

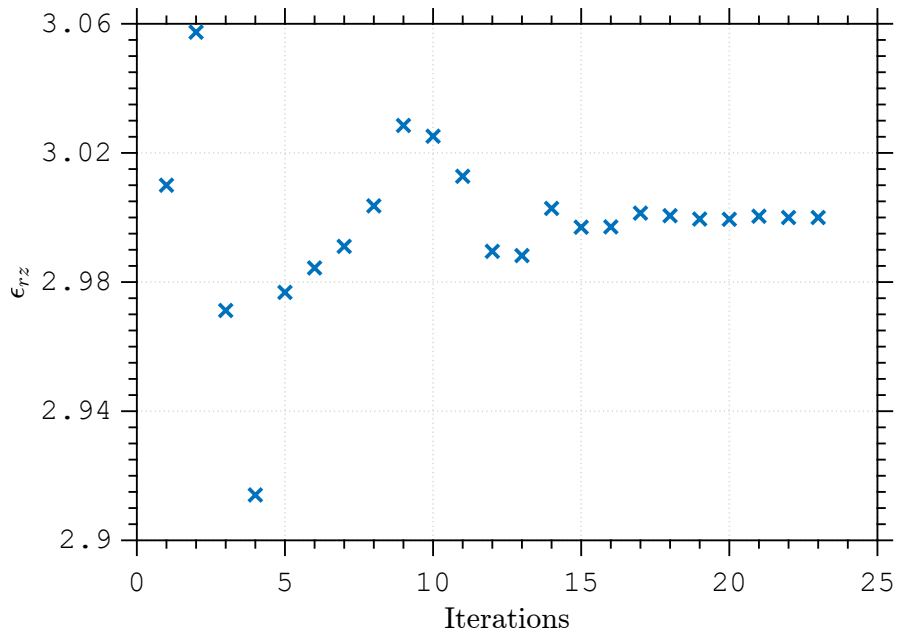


Figure 5.125: Evolution of the optimization parameter as a function of the number of iterations using linear functional. Convergence was achieved after 23 iterations at $\epsilon_{rz} = 3$.

PUC-Rio - Certificação Digital N° 2012321/CA

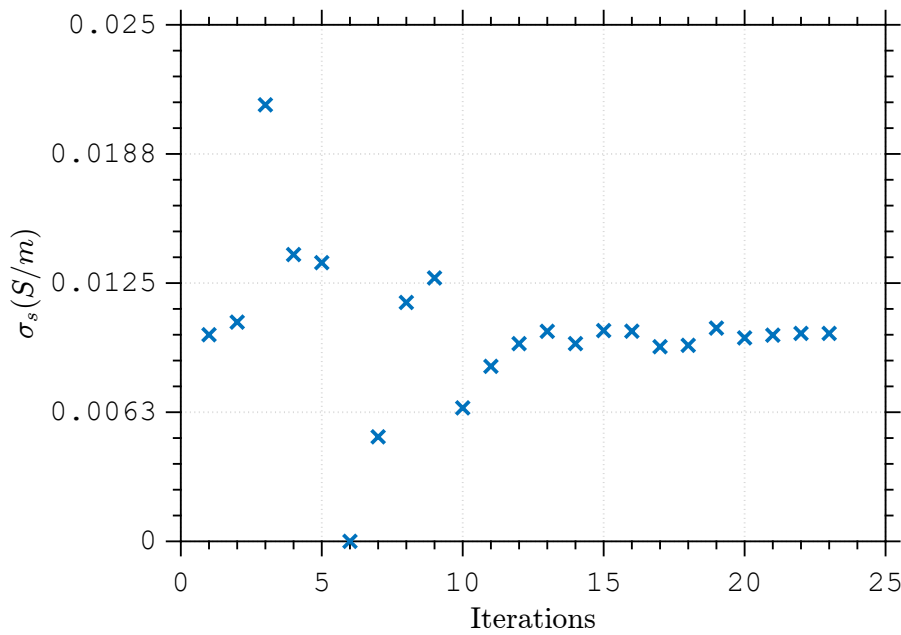


Figure 5.126: Evolution of the optimization parameter as a function of the number of iterations using linear functional. Convergence was achieved after 23 iterations at $\sigma_s = 0.01$.

Table 5.74: Initial guess, CPU time, and the number of iterations to achieve convergence by using the parameters Table 5.72 using decibel functional.

x_0	Time	Iterations
[2.51 3.01 0.01 0.01]	180 min 24 seconds	4

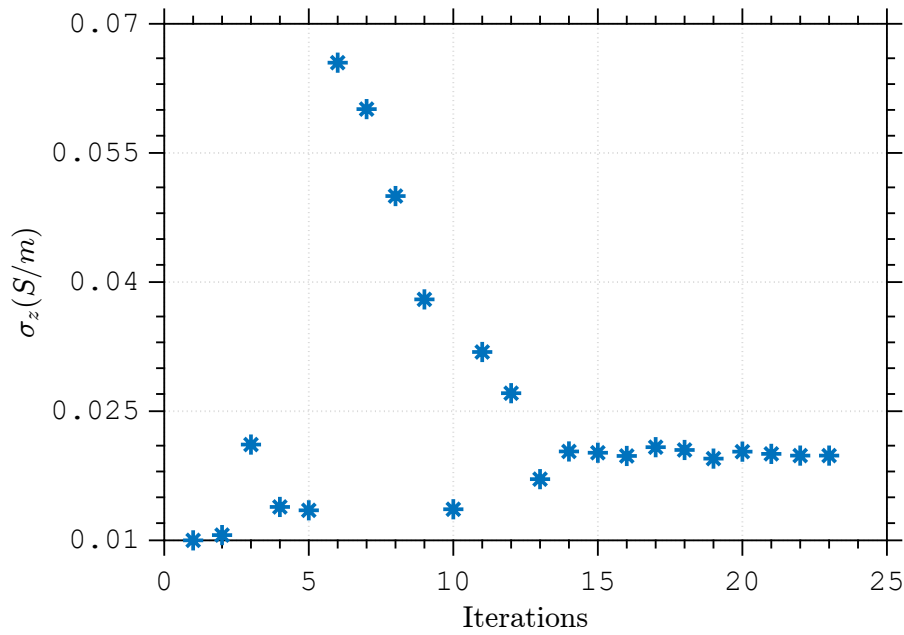


Figure 5.127: Evolution of the optimization parameter as a function of the number of iterations using linear functional. Convergence was achieved after 23 iterations at $\sigma_z = 0.02$.

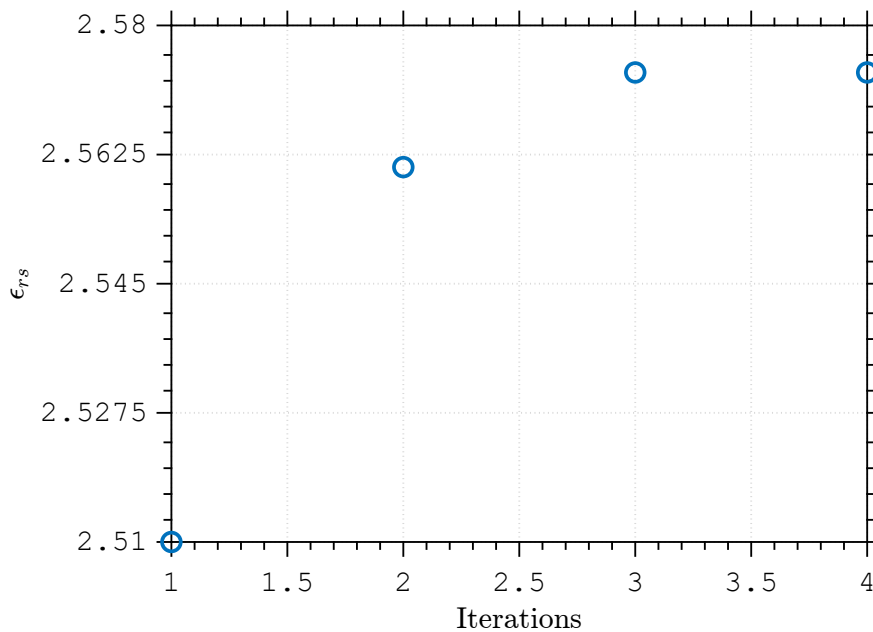


Figure 5.128: Evolution of the optimization parameter as a function of the number of iterations using decibel functional. Convergence was achieved after 4 iterations at $\epsilon_{rs} = 2.57$.

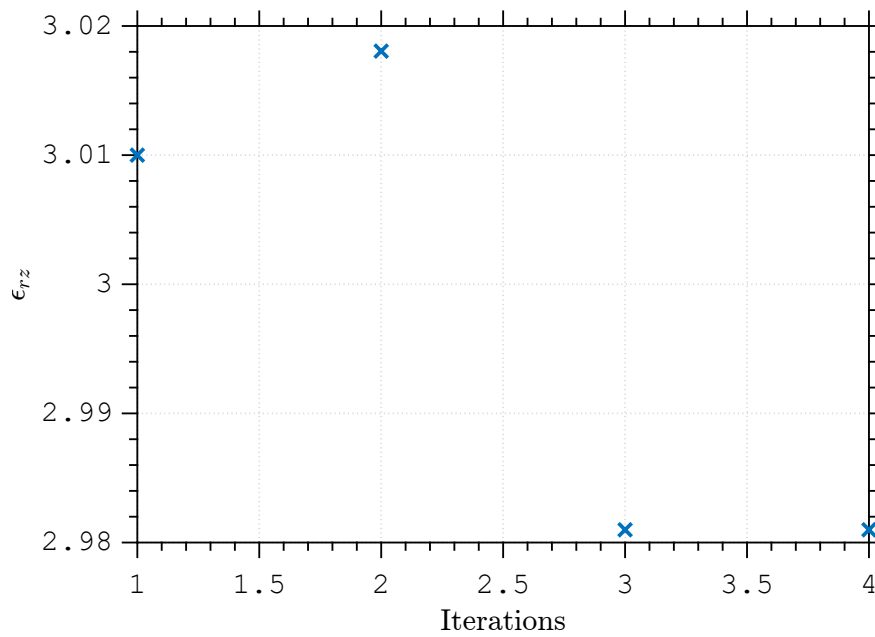


Figure 5.129: Evolution of the optimization parameter as a function of the number of iterations using decibel functional. Convergence was achieved after 4 iterations at $\epsilon_{rz} = 2.98$.

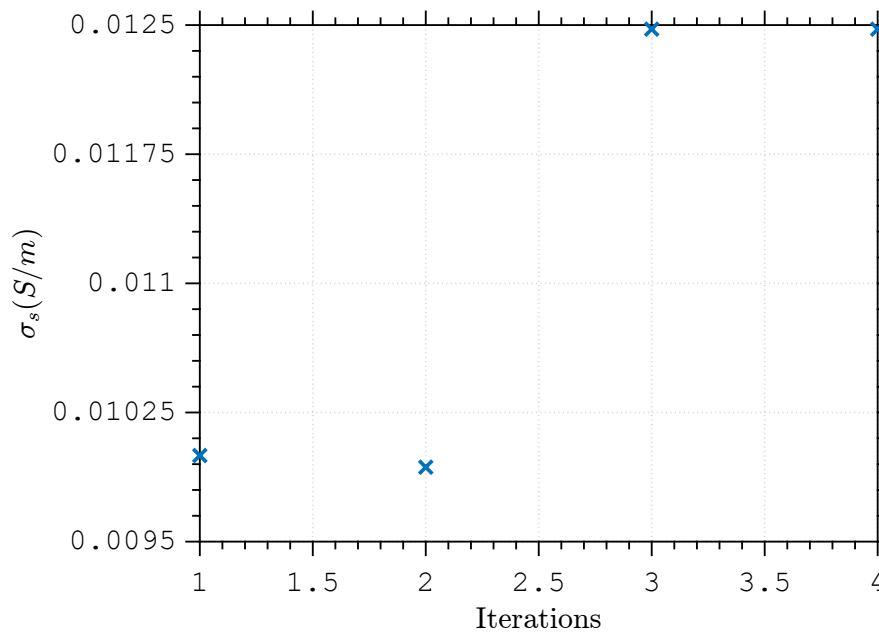


Figure 5.130: Evolution of the optimization parameter as a function of the number of iterations using decibel functional. Convergence was achieved after 4 iterations at $\sigma_s = 0.01$.

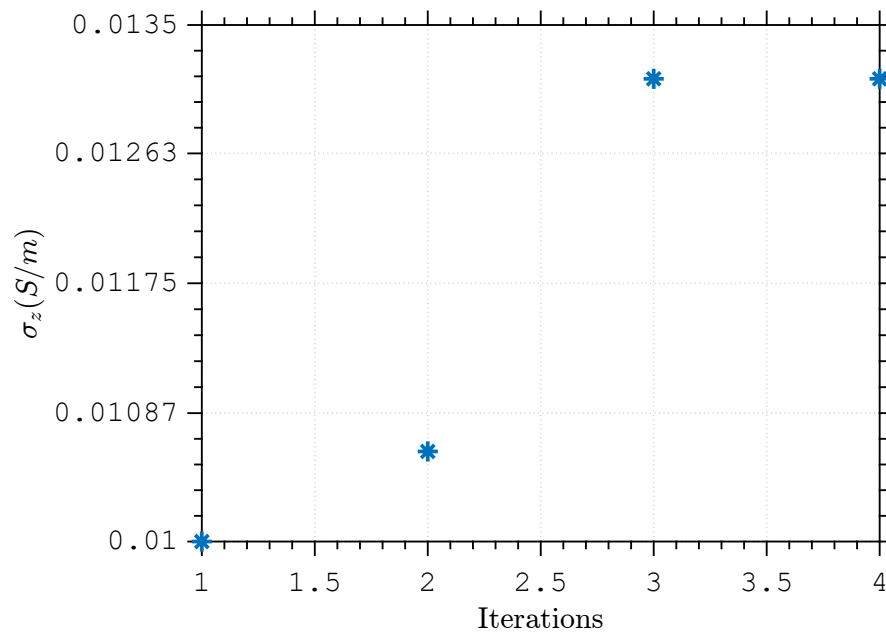


Figure 5.131: Evolution of the optimization parameter as a function of the number of iterations using decibel functional. Convergence was achieved after 4 iterations at $\sigma_z = 0.01$.

5.2.3 Heterogeneous Circular Waveguide

The second region is a circular waveguide, where the material is in the first layer and second layer is filled with vacuum.

5.2.3.1 Lossless isotropic sample

This first simulation used the parameters listed in Table 5.75. Results can be seen in Fig. 5.132 and in Table 5.76 for the linear functional while for the decibel one are in Fig. 5.133 and Table 5.77. We observe that the convergence was achieved after 8 iterations for linear functional and 4 iterations for decibel functional for a value near $\epsilon_r = 2.55$ for linear functional with a good convergence from the ones used in simulation and $\epsilon_r = 2.55$ for decibel functional with a good convergence from the ones used in simulation.

Table 5.75: Geometric and constitutive parameters used on direct problem of a lossless isotropic sample placed in second waveguide of a one-port heterogeneous circular waveguide

Region	L(mm)	ρ_0 (mm)	ρ_1 (mm)	ρ_2 (mm)	ϵ_{rs1}	ϵ_{rz1}	σ_{s1}	σ_{z1}
1	-	6.3	10	18	1.01	1.01	10^{-6}	10^{-6}
2	30	0	12.6	19	2.55	2.55	10^{-6}	10^{-6}
3	30	6.3	10	18	1.01	1.01	10^{-6}	10^{-6}

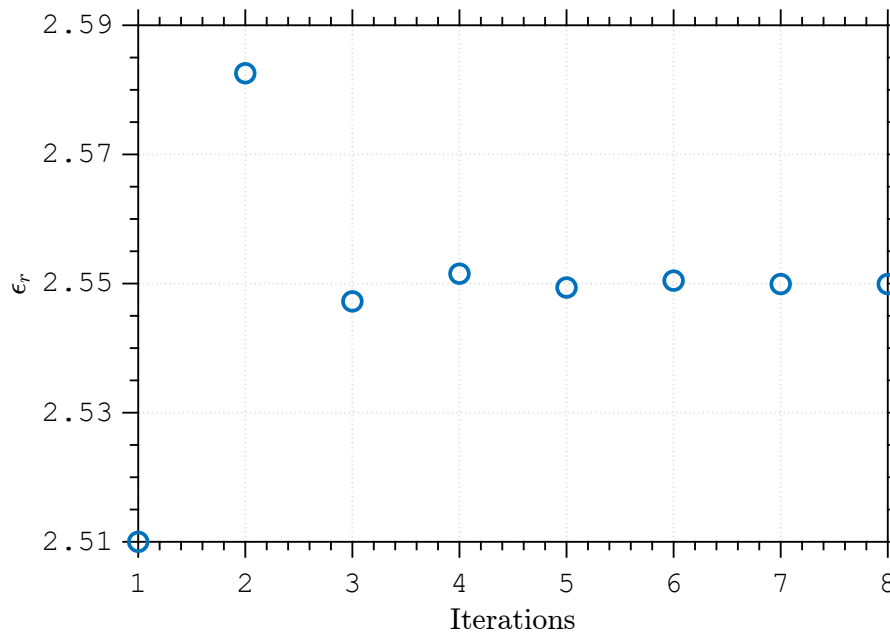


Figure 5.132: Evolution of the optimization parameter as a function of the number of iterations using linear functional. Convergence was achieved after 8 iterations at $\epsilon_r = 2.55$.

Table 5.76: Initial guess, CPU time, and the number of iterations to achieve convergence by using the parameters Table 5.75 using linear functional.

x_0	Time	Iterations
2.51	43 min 25 seconds	8

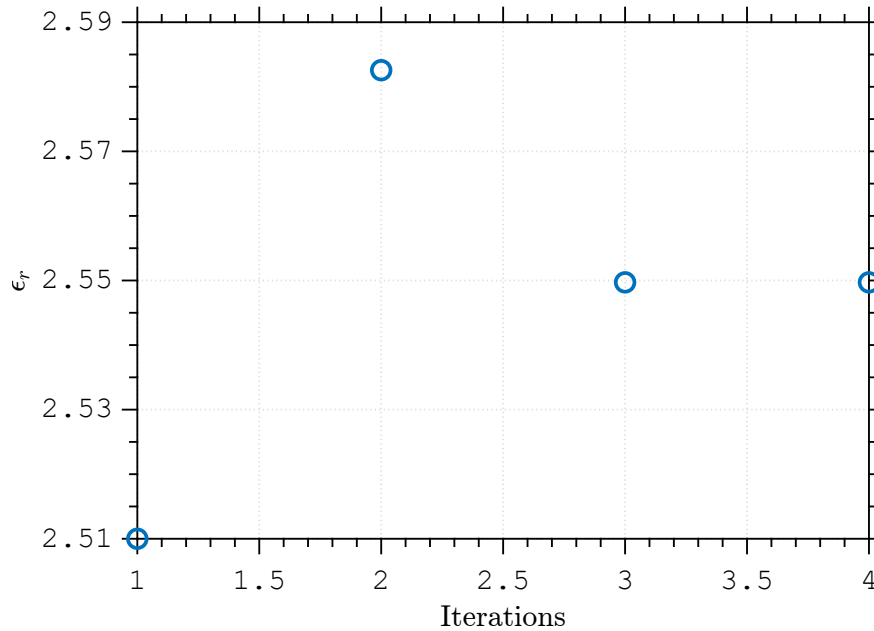


Figure 5.133: Evolution of the optimization parameter as a function of the number of iterations using decibel functional. Convergence was achieved after 4 iterations at $\epsilon_r = 2.55$.

Table 5.77: Initial guess, CPU time, and the number of iterations to achieve convergence by using the parameters table 5.75 of Fig. 5.133 using decibel functional

x_0	Time	Iterations
2.51	40 min 21 seconds	4

5.2.3.2

Lossy isotropic sample

For this case, parameters can be seen in Table 5.78 and results for linear functional are in Fig. 5.134 and 5.135 and in Table 5.79. The decibel functional has its results on Fig. 5.136 and 5.137 and in Table 5.80. We observe that the convergence was achieved after 5 iterations for linear functional and 3 iterations for decibel functional for a value near $\epsilon_r = 2.53$ and $\sigma = 0.015$ for linear functional with a small difference from the ones used in simulation and $\epsilon_r = 2.58$ and $\sigma = 0.01$ for decibel functional with a small difference from the ones used in simulation.

Table 5.78: Geometric and constitutive parameters used on direct problem of a lossy isotropic sample placed in second waveguide of a one-port heterogeneous circular waveguide

Region	L(mm)	ρ_0 (mm)	ρ_1 (mm)	ρ_2 (mm)	ϵ_{rs1}	ϵ_{rz1}	σ_{s1}	σ_{z1}
1	-	6.3	10	18	1.01	1.01	10^{-6}	10^{-6}
2	30	0	12.6	19	2.55	2.55	10^{-2}	10^{-2}
3	30	6.3	10	18	1.01	1.01	10^{-6}	10^{-6}

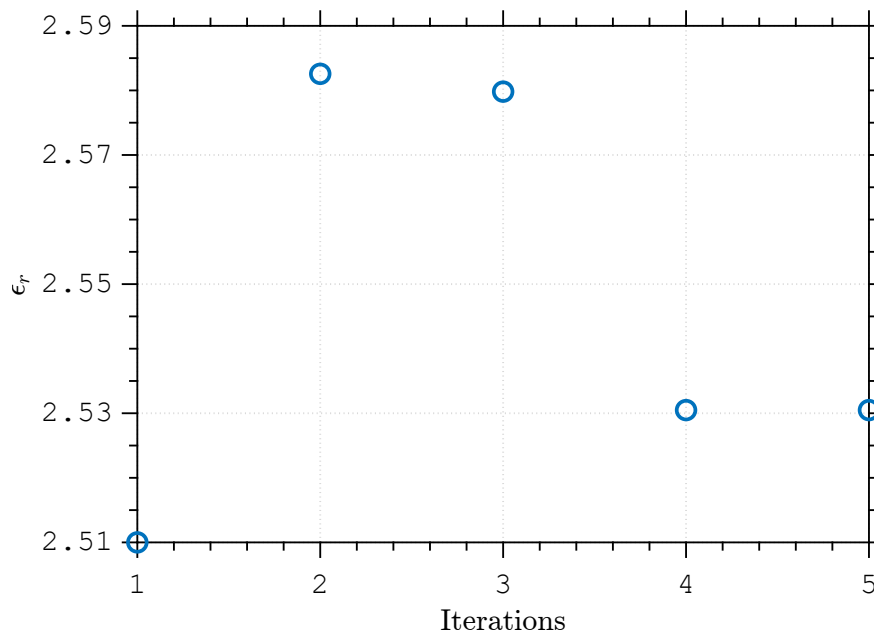


Figure 5.134: Evolution of the optimization parameter as a function of the number of iterations using linear functional. Convergence was achieved after 5 iterations at $\epsilon_r = 2.53$.

Table 5.79: Initial guess, CPU time, and the number of iterations to achieve convergence by using the parameters Table 5.78 using linear functional.

x_0	Time	Iterations
[2.51 0.01]	119 min 13 seconds	5

Table 5.80: Initial guess, CPU time, and the number of iterations to achieve convergence by using the parameters Table 5.78 using decibel functional.

x_0	Time	Iterations
[2.51 0.01]	98 min 55 seconds	3

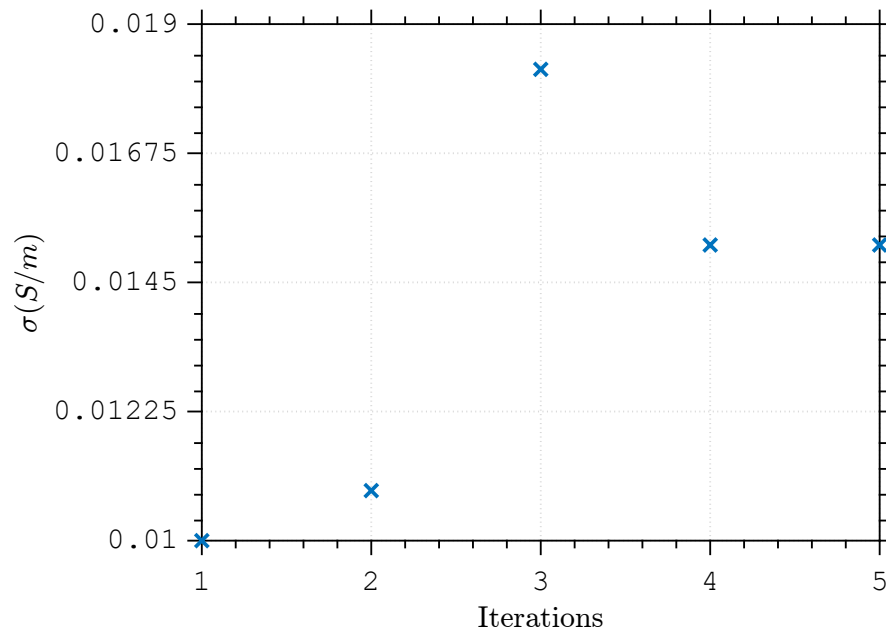


Figure 5.135: Evolution of the optimization parameter as a function of the number of iterations using linear functional. Convergence was achieved after 5 iterations at $\sigma = 0.015$.

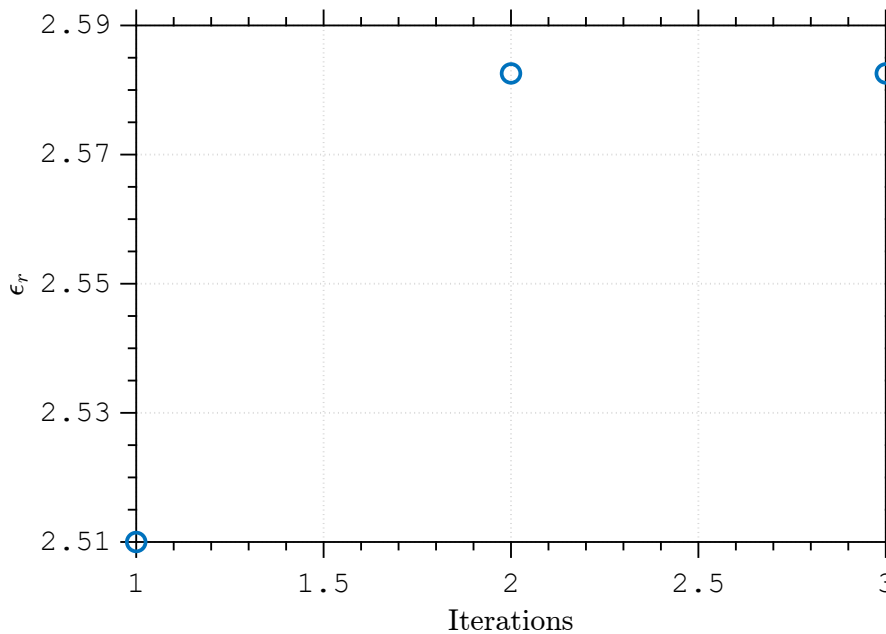


Figure 5.136: Evolution of the optimization parameter as a function of the number of iterations using decibel functional. Convergence was achieved after 3 iterations at $\epsilon_r = 2.58$.

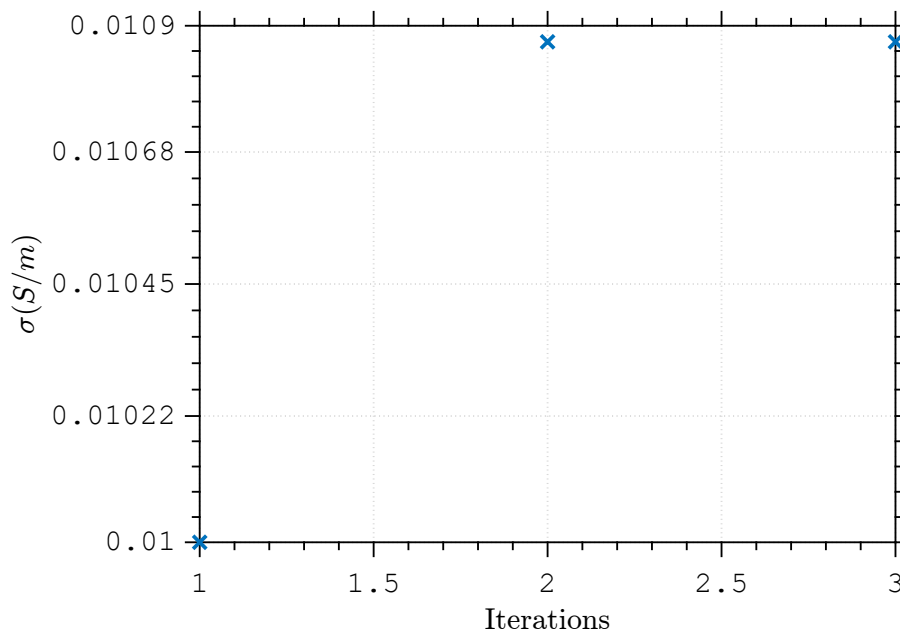


Figure 5.137: Evolution of the optimization parameter as a function of the number of iterations using decibel functional. Convergence was achieved after 3 iterations at $\sigma = 0.01$.

5.2.3.3

Lossless anisotropic sample

For the lossless anisotropic material case, parameters are in Table 5.81. Results for the linear functional are in Fig. 5.138 and 5.139 and in Table 5.82. For decibel functional they are in Fig. 5.140 and 5.141 and in Table 5.83. We observe that the convergence was achieved after 3 iterations for linear functional and 7 iterations for decibel functional for a value near $\epsilon_{rs} = 2.72$ and $\epsilon_{rz} = 3.2$ for linear functional with a relatively difference from the ones used in simulation and $\epsilon_{rs} = 2.55$ and $\epsilon_{rz} = 3$ for decibel functional with a small difference from the ones used in simulation

Table 5.81: Geometric and constitutive parameters used on direct problem of a lossless anisotropic sample placed in second waveguide of a one-port heterogeneous circular waveguide

Region	L(mm)	ρ_0 (mm)	ρ_1 (mm)	ρ_2 (mm)	ϵ_{rs1}	ϵ_{rz1}	σ_{s1}	σ_{z1}
1	-	6.3	10	18	1.01	1.01	10^{-6}	10^{-6}
2	30	0	12.6	19	2.55	3	10^{-6}	10^{-6}
3	30	6.3	10	18	1.01	1.01	10^{-6}	10^{-6}

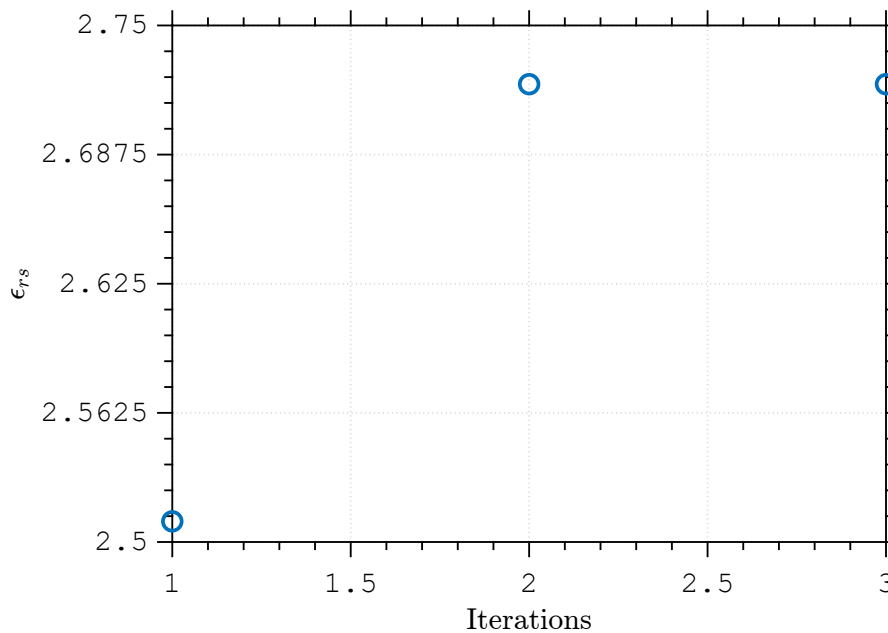


Figure 5.138: Evolution of the optimization parameter as a function of the number of iterations using linear functional. Convergence was achieved after 14 iterations at $\epsilon_{rs} = 2.72$.

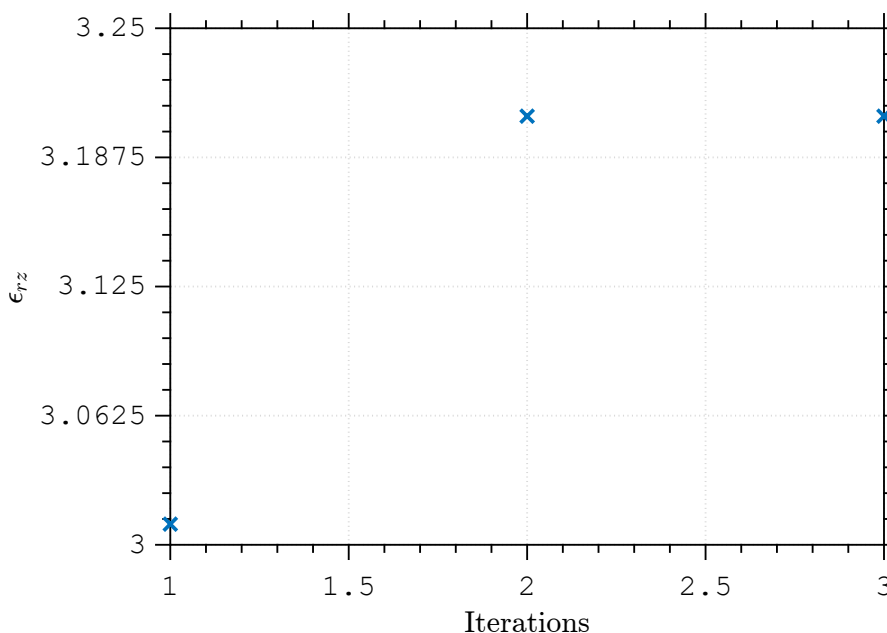


Figure 5.139: Evolution of the optimization parameter as a function of the number of iterations using linear functional. Convergence was achieved after 14 iterations at $\epsilon_{rz} = 3.2$.

Table 5.82: Initial guess, CPU time, and the number of iterations to achieve convergence by using the parameters Table 5.81 using linear functional.

x_0	Time	Iterations
[2.51 3.01]	243 min 18 seconds	3

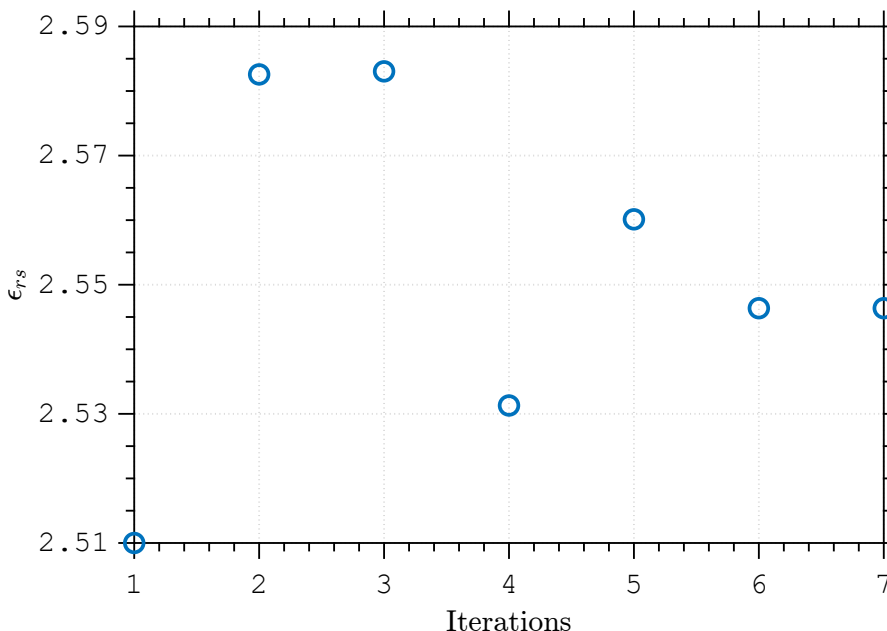


Figure 5.140: Evolution of the optimization parameter as a function of the number of iterations using decibel functional. Convergence was achieved after 7 iterations at $\epsilon_{rs} = 2.55$.

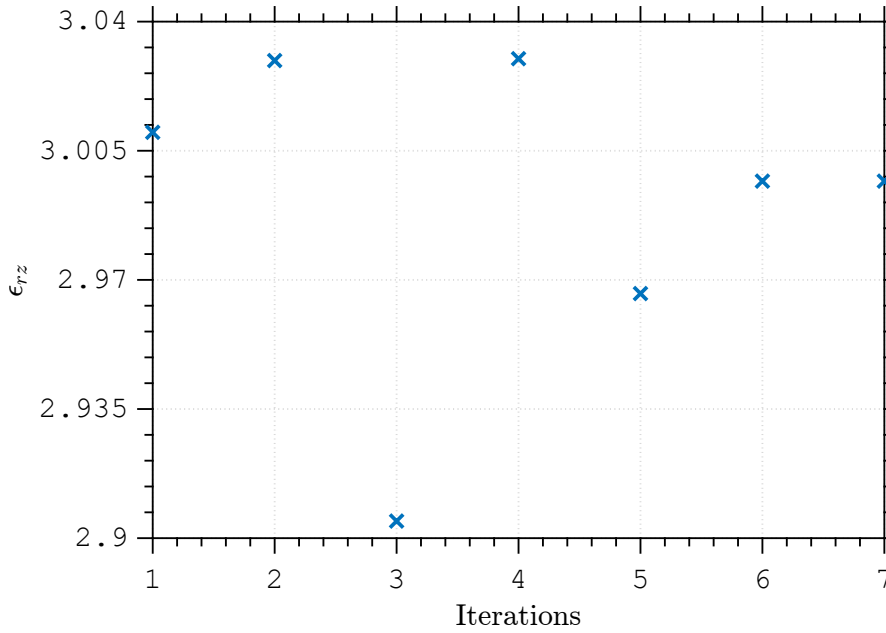


Figure 5.141: Evolution of the optimization parameter as a function of the number of iterations using decibel functional. Convergence was achieved after 7 iterations at $\epsilon_{rz} = 3$.

Table 5.83: Initial guess, CPU time, and the number of iterations to achieve convergence by using the parameters Table 5.81 using decibel functional.

x_0	Time	Iterations
[2.51 3.01]	213 min 3 seconds	7

5.2.3.4

Anisotropic sample with isotropic loss

In this simulation parameters used are in Table 5.84. Results for the linear functional are in Fig. 5.142, 5.143, 5.144 and 5.145 and Table 5.85. For the decibel one, results are in Fig. 5.146, 5.147, 5.148 and 5.149 and Table 5.86. We observe that the convergence was achieved after 24 iterations for linear functional and 2 iterations for decibel functional for a value near $\epsilon_{rs} = 2.55$, $\epsilon_{rz} = 3$, $\sigma_s = 0.02$ and $\sigma_z = 0.02$ for linear functional with a good convergence from the ones used in simulation and $\epsilon_{rs} = 2.51$, $\epsilon_{rz} = 3.01$, $\sigma_s = 0.01$ and $\sigma_z = 0.01$ for decibel functional with a small difference from the ones used in simulation

Table 5.84: Geometric and constitutive parameters used on direct problem of a isotropic lossy and anisotropic sample placed in second waveguide of a one-port heterogeneous circular waveguide

Region	L(mm)	ρ_0 (mm)	ρ_1 (mm)	ρ_2 (mm)	ϵ_{rs1}	ϵ_{rz1}	σ_{s1}	σ_{z1}
1	-	6.3	10	18	1.01	1.01	10^{-6}	10^{-6}
2	30	0	12.6	19	2.55	3	2×10^{-2}	2×10^{-2}
3	30	6.3	10	18	1.01	1.01	10^{-6}	10^{-6}

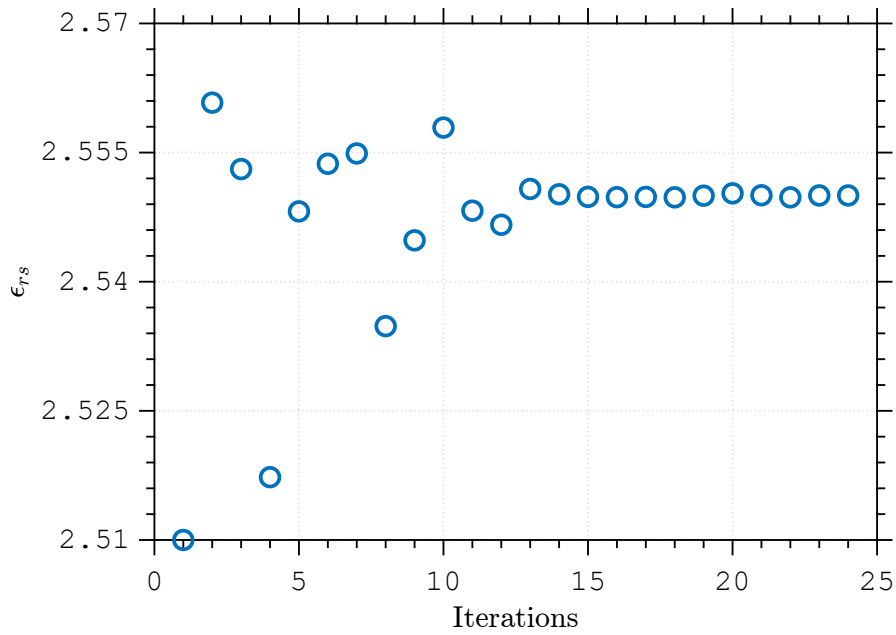


Figure 5.142: Evolution of the optimization parameter as a function of the number of iterations using linear functional. Convergence was achieved after 24 iterations at $\epsilon_{rs} = 2.55$.

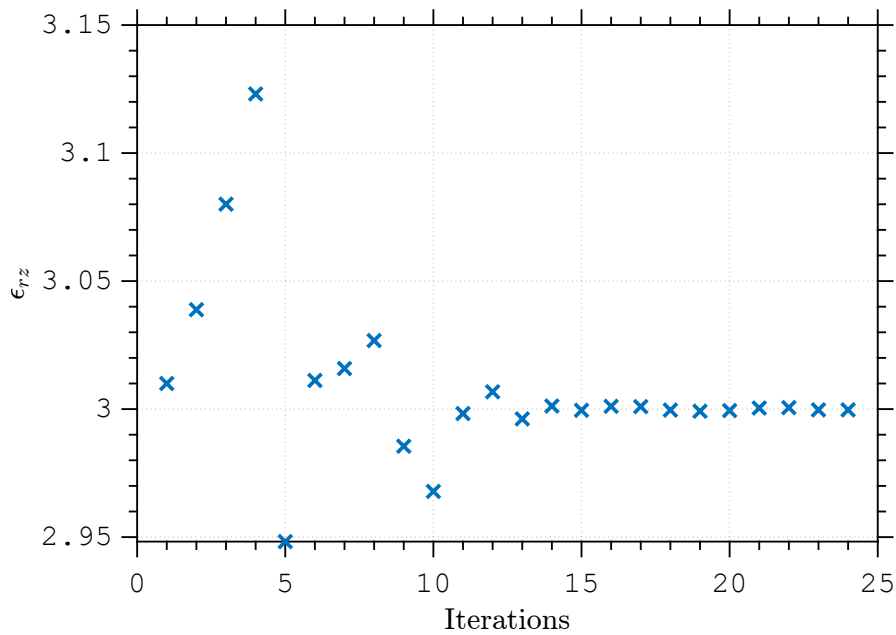


Figure 5.143: Evolution of the optimization parameter as a function of the number of iterations using linear functional. Convergence was achieved after 24 iterations at $\epsilon_{rz} = 2.99$.

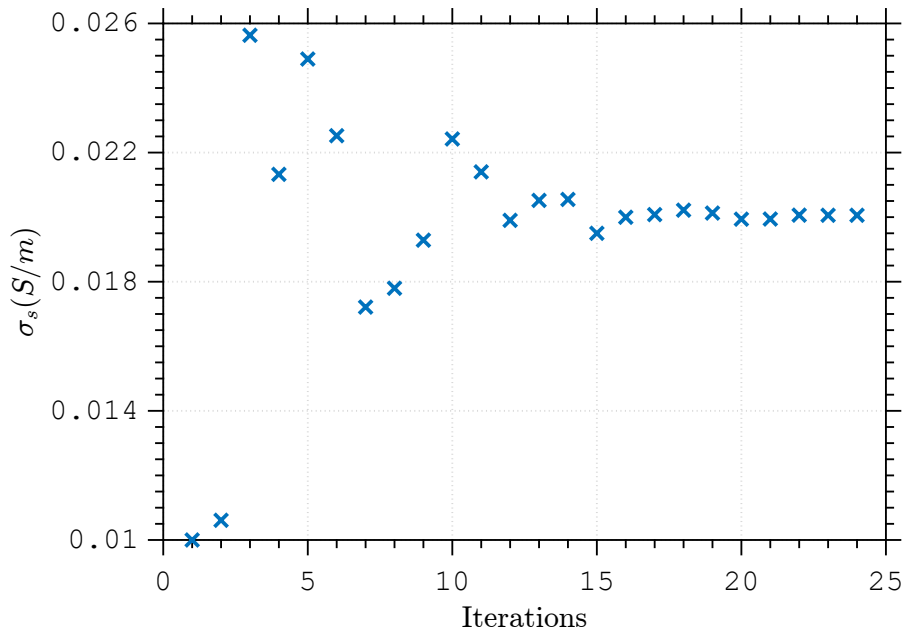


Figure 5.144: Evolution of the optimization parameter as a function of the number of iterations using linear functional. Convergence was achieved after 24 iterations at $\sigma_s = 0.02$.

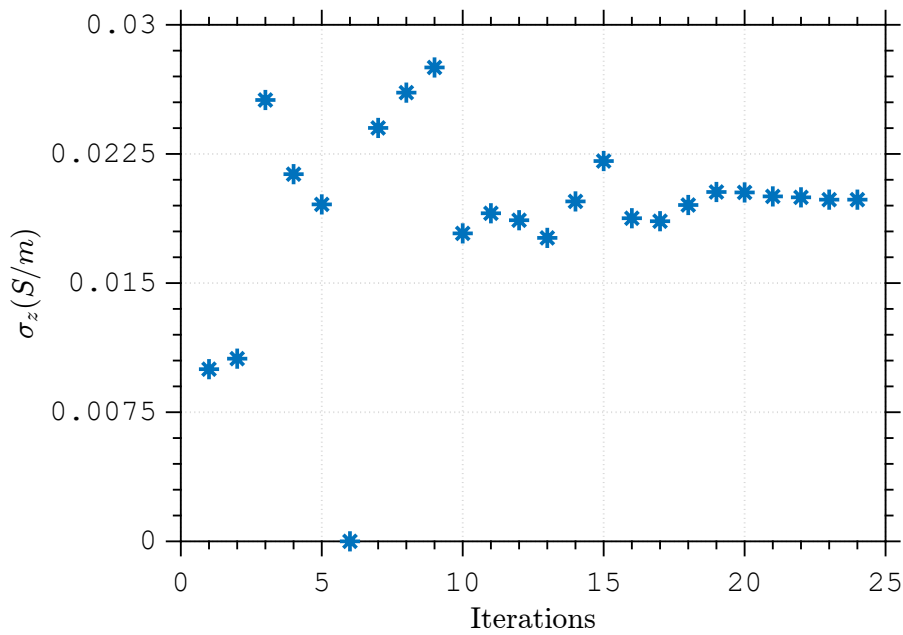


Figure 5.145: Evolution of the optimization parameter as a function of the number of iterations using linear functional. Convergence was achieved after 24 iterations at $\sigma_z = 0.02$.

Table 5.85: Initial guess, CPU time, and the number of iterations to achieve convergence by using the parameters Table 5.84 using linear functional.

x_0	Time	Iterations
[2.51 3.01 0.01 0.01]	230 min 53 seconds	24

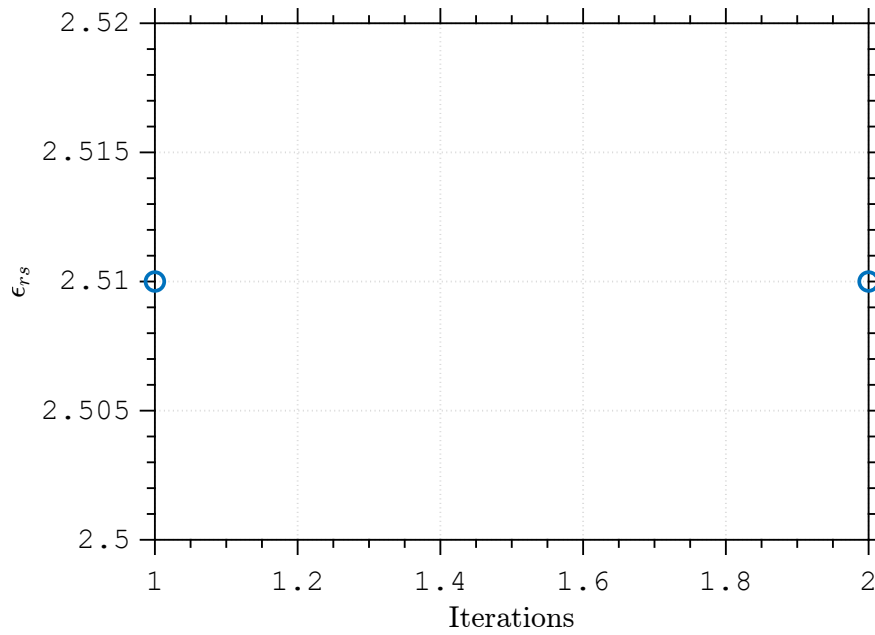


Figure 5.146: Evolution of the optimization parameter as a function of the number of iterations using decibel functional. Convergence was achieved after 2 iterations at $\epsilon_{rs} = 2.51$.

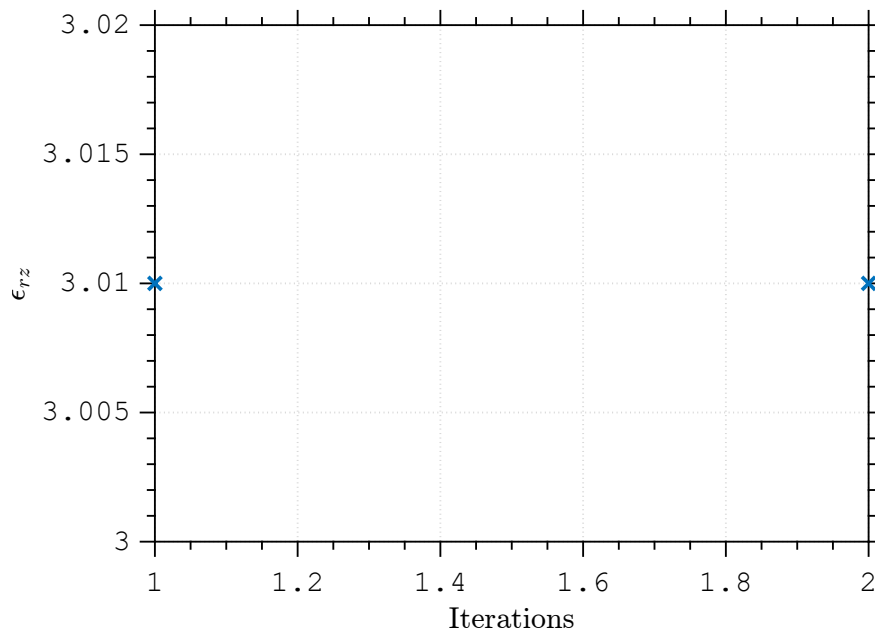


Figure 5.147: Evolution of the optimization parameter as a function of the number of iterations using decibel functional. Convergence was achieved after 2 iterations at $\epsilon_{rz} = 3.01$.

Table 5.86: Initial guess, CPU time, and the number of iterations to achieve convergence by using the parameters Table 5.84 using decibel functional.

x_0	Time	Iterations
[2.51 3.01 0.01 0.01]	156 min 36 seconds	2

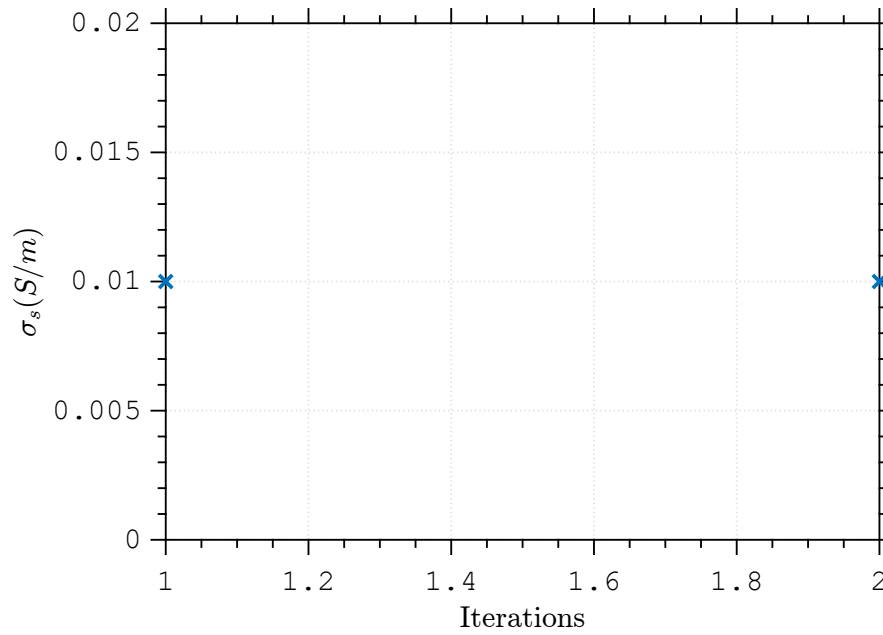


Figure 5.148: Evolution of the optimization parameter as a function of the number of iterations using decibel functional. Convergence was achieved after 2 iterations at $\sigma_s = 0.01$.

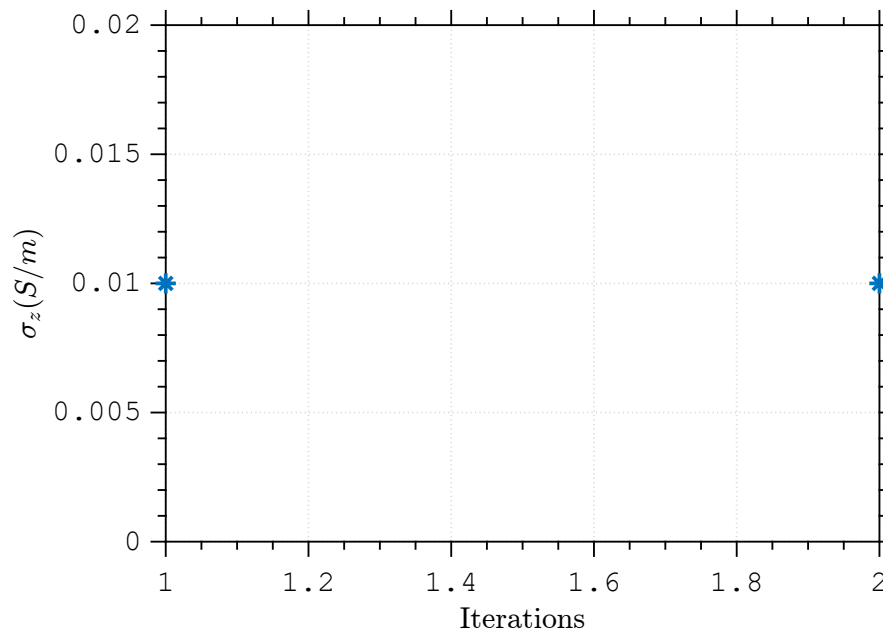


Figure 5.149: Evolution of the optimization parameter as a function of the number of iterations using decibel functional. Convergence was achieved after 2 iterations at $\sigma_z = 0.01$.

5.2.3.5

Anisotropic sample with anisotropic loss

The last case, with an lossy anisotropic material, parameters are in Table 5.87 and results for linear functional are in Fig. 5.150, 5.151, 5.152 and 5.153 and in Table 5.88. The decibel functional has results presented

in Fig. 5.154, 5.155, 5.156 and 5.157 and in Table 5.89. We observe that the convergence was achieved after 21 iterations for linear functional and 4 iterations for decibel functional for a value near $\epsilon_{rs} = 2.55$, $\epsilon_{rz} = 3$, $\sigma_s = 0.01$ and $\sigma_z = 0.02$ for linear functional with a good convergence from the ones used in simulation and $\epsilon_{rs} = 2.57$, $\epsilon_{rz} = 2.98$, $\sigma_s = 0.012$ and $\sigma_z = 0.013$ for decibel functional with a small difference from the ones used in simulation

Table 5.87: Geometric and constitutive parameters used on direct problem of a anisotropic lossy and anisotropic sample placed in second waveguide of a one-port heterogeneous circular waveguide

Region	L(mm)	ρ_0 (mm)	ρ_1 (mm)	ρ_2 (mm)	ϵ_{rs1}	ϵ_{rz1}	σ_{s1}	σ_{z1}
1	-	6.3	10	18	1.01	1.01	10^{-6}	10^{-6}
2	30	0	12.6	19	2.55	3	10^{-2}	2×10^{-2}
3	30	6.3	10	18	1.01	1.01	10^{-6}	10^{-6}

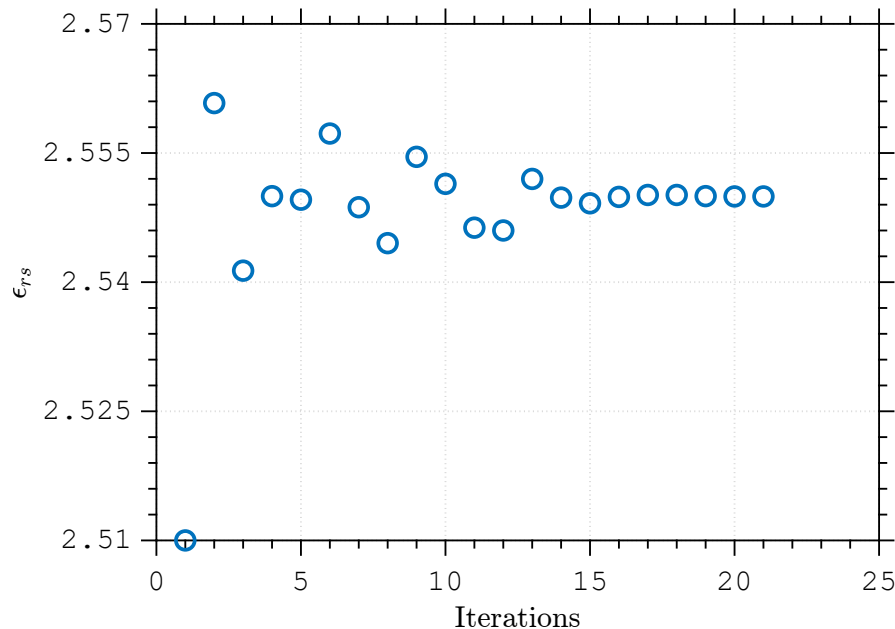


Figure 5.150: Evolution of the optimization parameter as a function of the number of iterations using linear functional. Convergence was achieved after 21 iterations at $\epsilon_{rs} = 2.55$.

Table 5.88: Initial guess, CPU time, and the number of iterations to achieve convergence by using the parameters Table 5.87 using linear functional.

x_0	Time	Iterations
[2.51 3.01 0.01 0.01]	217 min 14 seconds	21

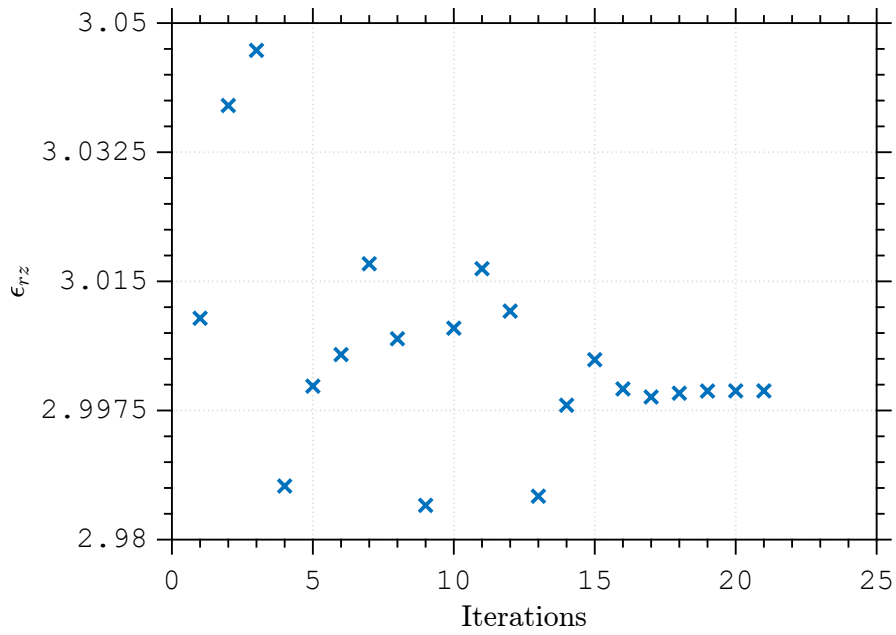


Figure 5.151: Evolution of the optimization parameter as a function of the number of iterations using linear functional. Convergence was achieved after 21 iterations at $\epsilon_{rz} = 3.00$.

PUC-Rio - Certificação Digital N° 2012321/CA

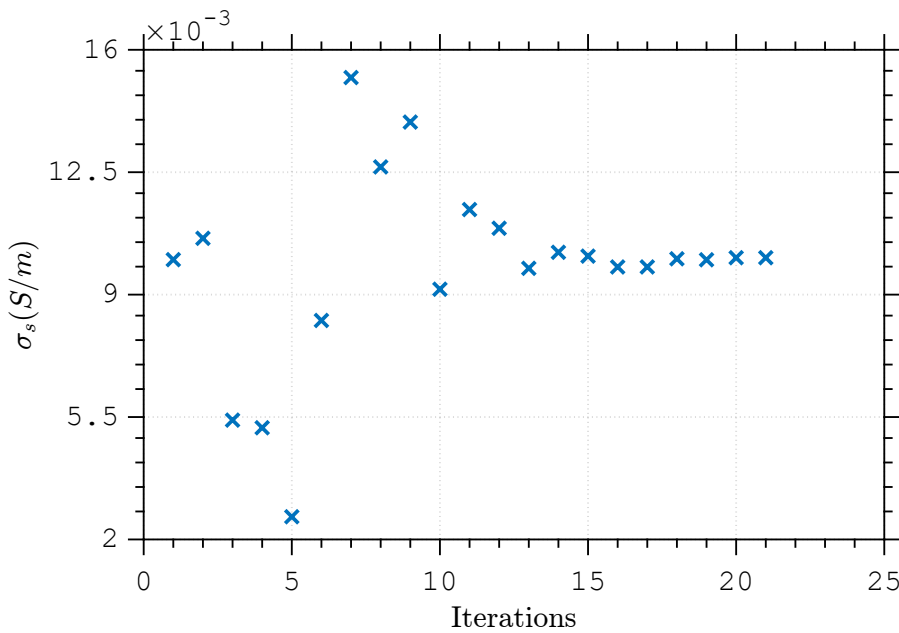


Figure 5.152: Evolution of the optimization parameter as a function of the number of iterations using linear functional. Convergence was achieved after 21 iterations at $\sigma_s = 0.01$.

Table 5.89: Initial guess, CPU time, and the number of iterations to achieve convergence by using the parameters Table 5.87 using decibel functional.

x_0	Time	Iterations
[2.51 3.01 0.01 0.01]	180 min 24 seconds	4

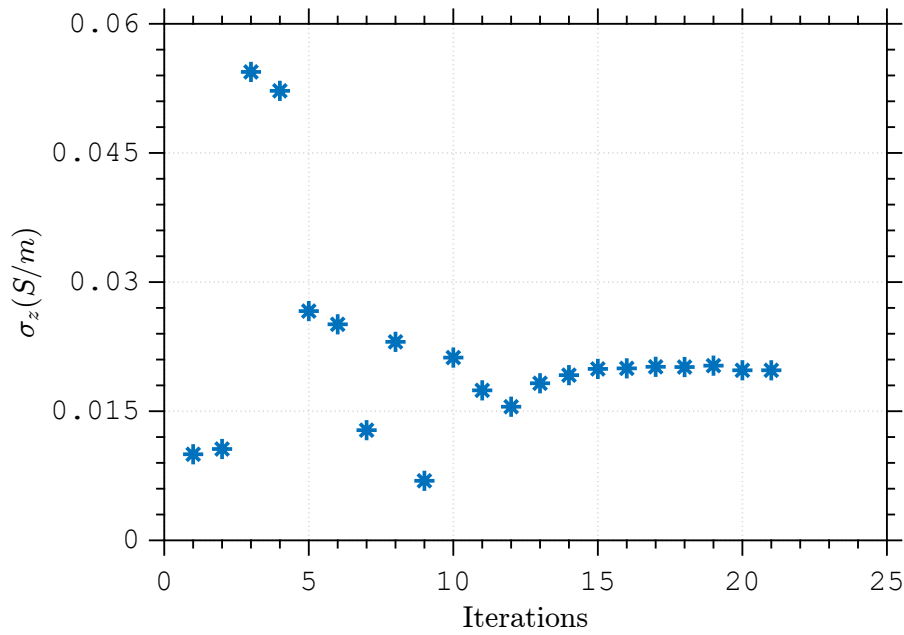


Figure 5.153: Evolution of the optimization parameter as a function of the number of iterations using linear functional. Convergence was achieved after 21 iterations at $\sigma_z = 0.02$.

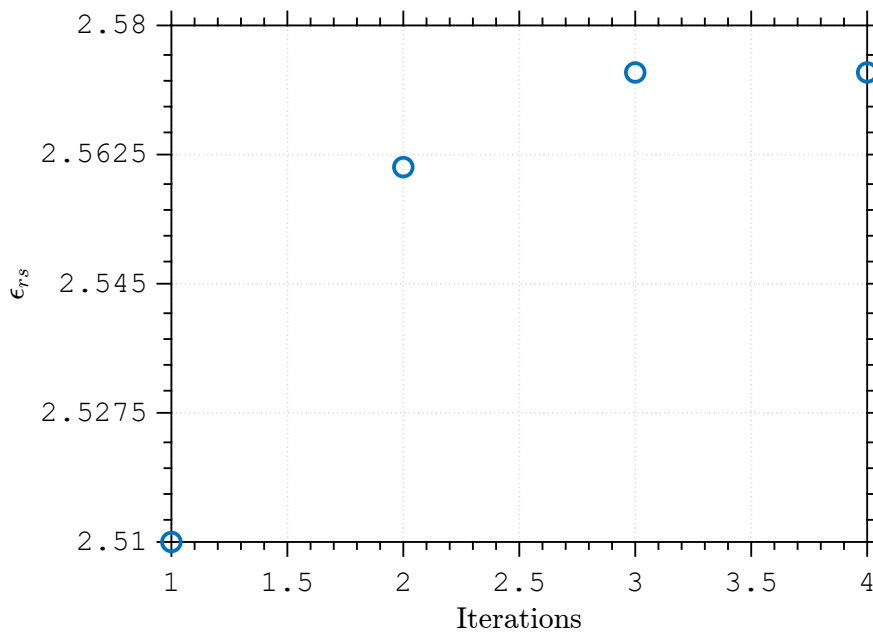


Figure 5.154: Evolution of the optimization parameter as a function of the number of iterations using decibel functional. Convergence was achieved after 2 iterations at $\epsilon_{rs} = 2.57$.

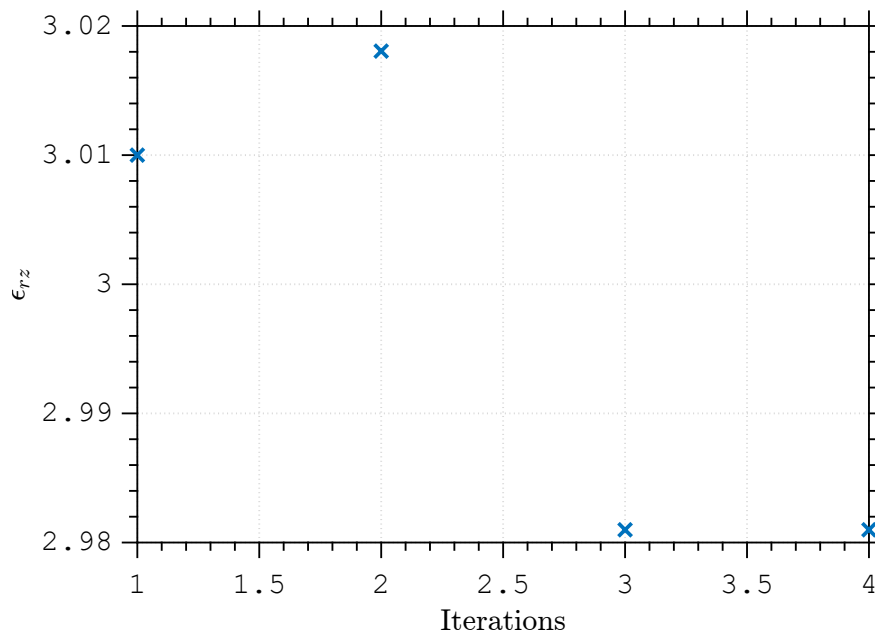


Figure 5.155: Evolution of the optimization parameter as a function of the number of iterations using decibel functional. Convergence was achieved after 4 iterations at $\epsilon_{rz} = 2.98$.

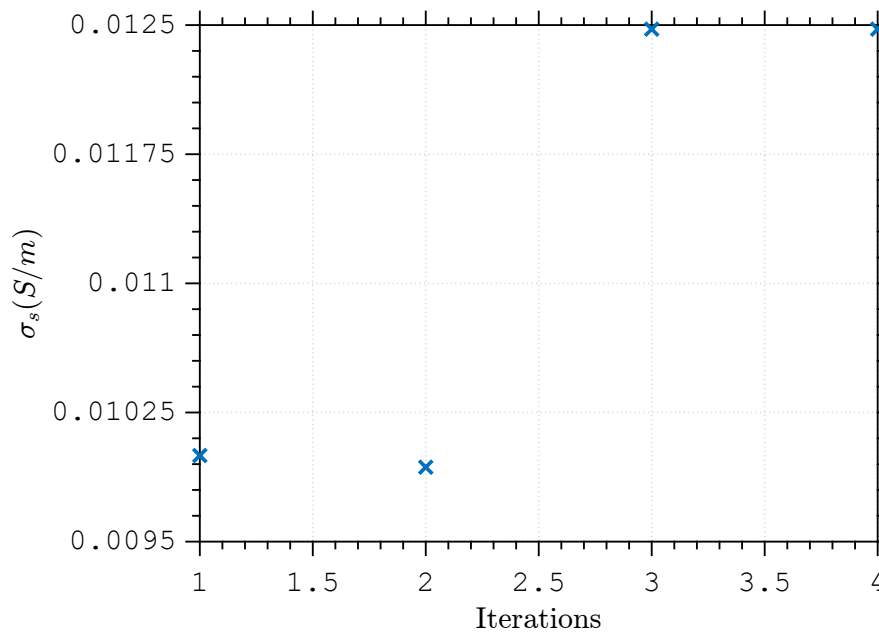


Figure 5.156: Evolution of the optimization parameter as a function of the number of iterations using decibel functional. Convergence was achieved after 4 iterations at $\sigma_s = 0.012$.

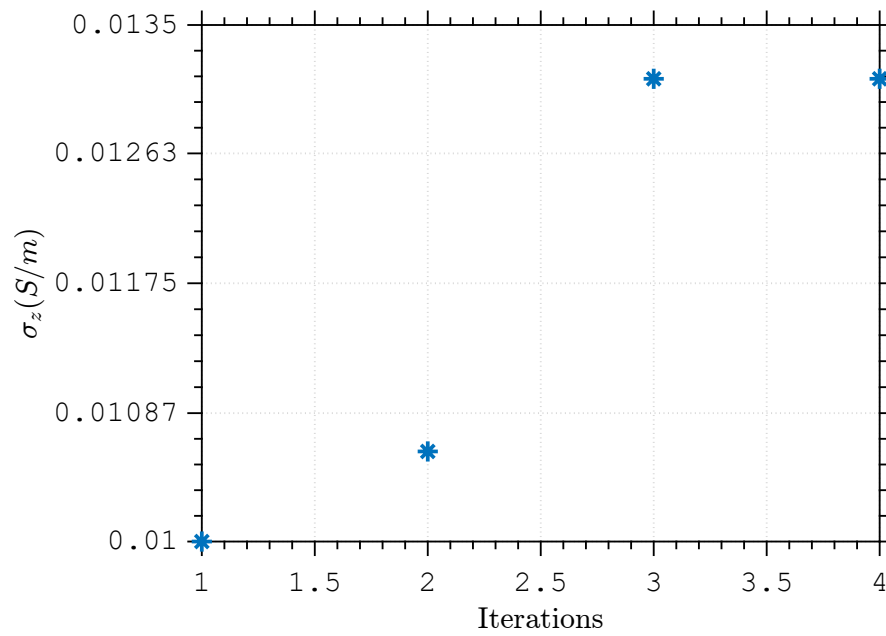


Figure 5.157: Evolution of the optimization parameter as a function of the number of iterations using decibel functional. Convergence was achieved after 4 iterations at $\sigma_z = 0.013$.

5.3

Open-ended Coaxial Measurement Cells

For the inverse problem using open-ended coaxial measurement cells it was used the following cases:

- lossless isotropic sample
- lossless anisotropic sample

All of them were tested using an homogeneous circular waveguide.

5.3.1

Homogeneous Circular Waveguide

The material has a circular shape, and is not inside an waveguide, as in the previous case.

5.3.1.1

Lossless isotropic sample

This first simulation used the parameters listed in Table 5.90. Results can be seen in Fig. 5.158 and in Table 5.91 for the linear functional while for the decibel one are in Fig. 5.159 and Table 5.92. We observe that the convergence was achieved after 6 iterations for linear functional and 4 iterations for decibel functional for a value near $\epsilon_r = 2.55$ for linear functional with a good convergence from the ones used in simulation and $\epsilon_r = 2.55$ for decibel functional with a good convergence from the ones used in simulation.

Table 5.90: Geometric and constitutive parameters used on direct problem of a lossless isotropic sample placed in second waveguide of a one-ended homogeneous circular waveguide

Region	$L(\text{mm})$	$\rho_0(\text{mm})$	$\rho_1(\text{mm})$	$\rho_2(\text{mm})$	ϵ_{rs1}	ϵ_{rz1}	σ_{s1}	σ_{z1}
1	0	6.3	10	18	1.01	1.01	10^{-6}	10^{-6}
2	∞	0	54	-	2.55	2.55	10^{-6}	10^{-6}

Table 5.91: Initial guess, CPU time, and the number of iterations to achieve convergence by using the parameters Table 5.90 using linear functional.

x_0	Time	Iterations
2.51	18 min 13 seconds	6

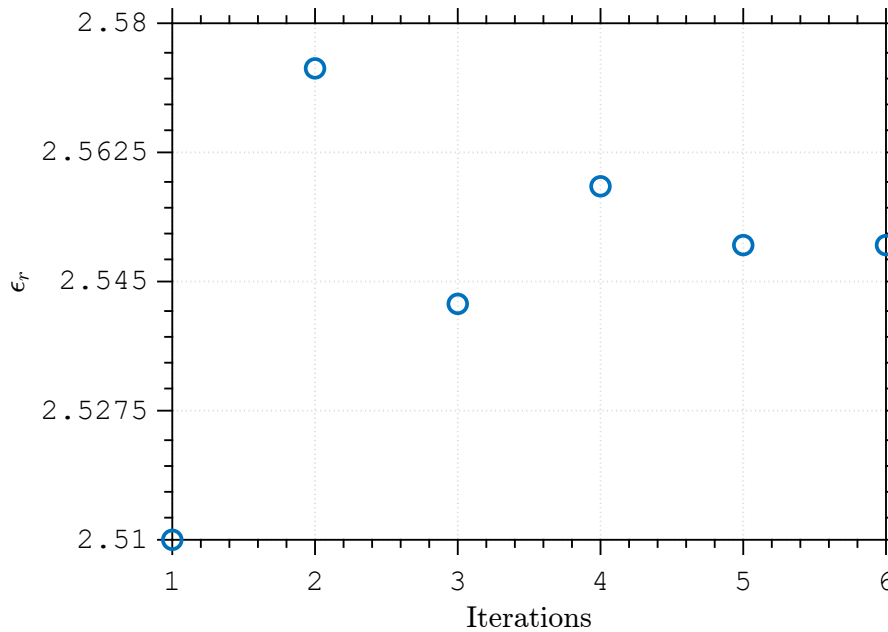


Figure 5.158: Evolution of the optimization parameter as a function of the number of iterations using linear functional. Convergence was achieved after 6 iterations at $\epsilon_r = 2.55$.

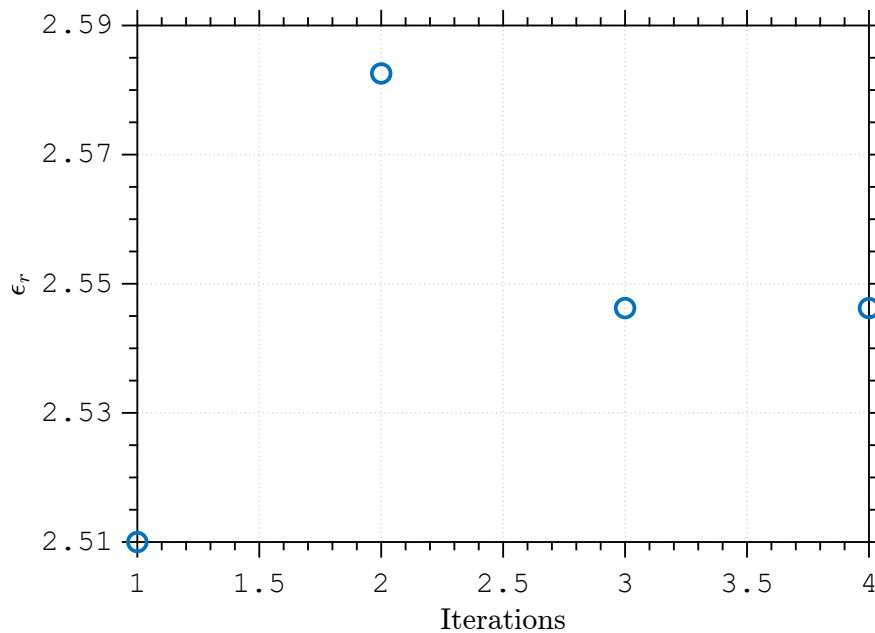


Figure 5.159: Evolution of the optimization parameter as a function of the number of iterations using decibel functional. Convergence was achieved after 4 iterations at $\epsilon_r = 2.55$.

Table 5.92: Initial guess, CPU time, and the number of iterations to achieve convergence by using the parameters Table 5.90 using decibel functional.

x_0	Time	Iterations
2.51	16 min 31 seconds	4

5.3.1.2

Lossless anisotropic sample

For the lossless anisotropic material case, parameters are in Table 5.93. Results for the linear functional are in Fig. 5.160 and 5.161 and in Table 5.94. For decibel functional they are in Fig. 5.162 and 5.163 and in Table 5.95. We observe that the convergence was achieved after 10 iterations for linear functional and 3 iterations for decibel functional for a value near $\epsilon_{rs} = 2.55$ and $\epsilon_{rz} = 3$ for linear functional with a good convergence from the ones used in simulation and $\epsilon_{rs} = 2.58$ and $\epsilon_{rz} = 2.99$ for decibel functional with a small difference from the ones used in simulation.

Table 5.93: Geometric and constitutive parameters used on direct problem of a lossless anisotropic sample placed in second waveguide of a one-ended homogeneous circular waveguide

Region	$L(\text{mm})$	$\rho_0(\text{mm})$	$\rho_1(\text{mm})$	$\rho_2(\text{mm})$	ϵ_{rs1}	ϵ_{rz1}	σ_{s1}	σ_{z1}
1	0	6.3	10	18	1.01	1.01	10^{-6}	10^{-6}
2	∞	0	54	-	2.55	3.00	10^{-6}	10^{-6}

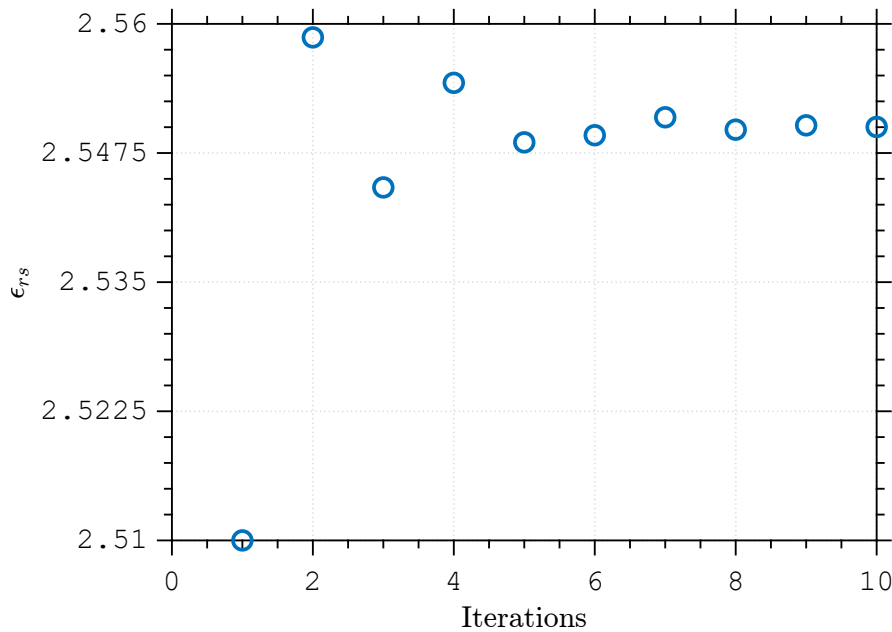


Figure 5.160: Evolution of the optimization parameter as a function of the number of iterations using linear functional. Convergence was achieved after 10 iterations at $\epsilon_{rs} = 2.55$.

Table 5.94: Initial guess, CPU time, and the number of iterations to achieve convergence by using the parameters Table 5.93 using linear functional.

x_0	Time	Iterations
[2.51 3.01]	125 min 52 seconds	10

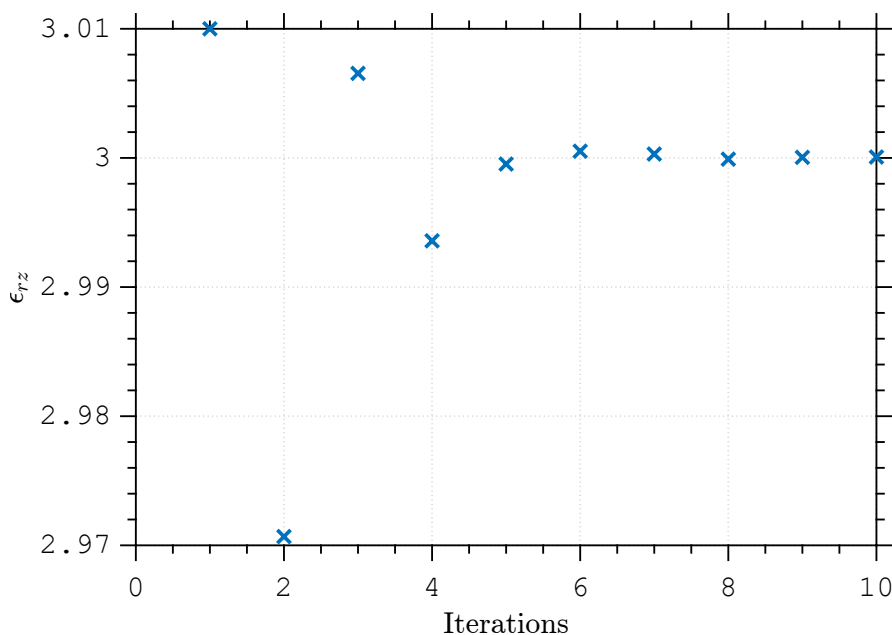


Figure 5.161: Evolution of the optimization parameter as a function of the number of iterations using linear functional. Convergence was achieved after 10 iterations at $\epsilon_{rz} = 3$.

PUC-Rio - Certificação Digital N° 2012321/CA

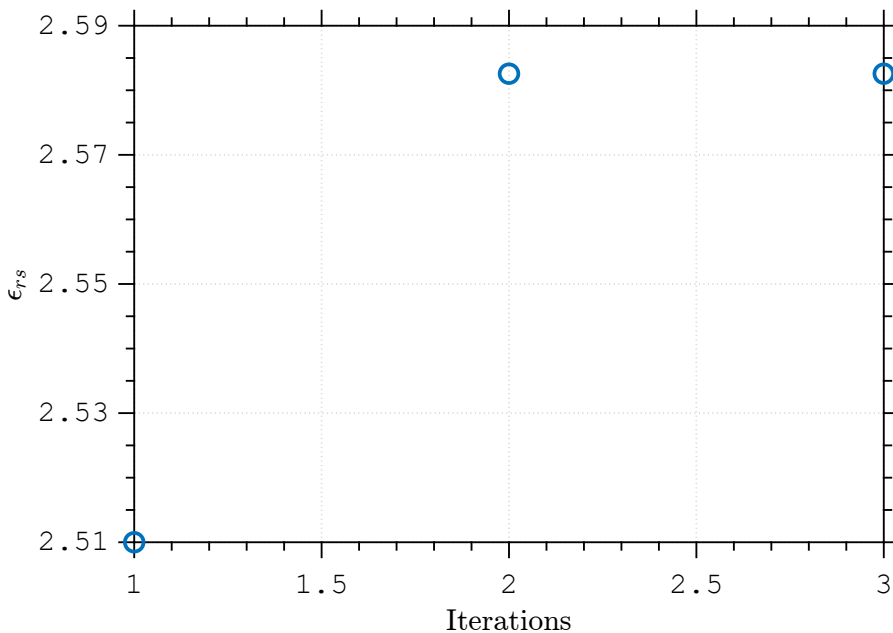


Figure 5.162: Evolution of the optimization parameter as a function of the number of iterations using decibel functional. Convergence was achieved after 3 iterations at $\epsilon_{rs} = 2.58$.

Table 5.95: Initial guess, CPU time, and the number of iterations to achieve convergence by using the parameters Table 5.93 using decibel functional.

x_0	Time	Iterations
[2.51 3.01]	106 min 34 seconds	3

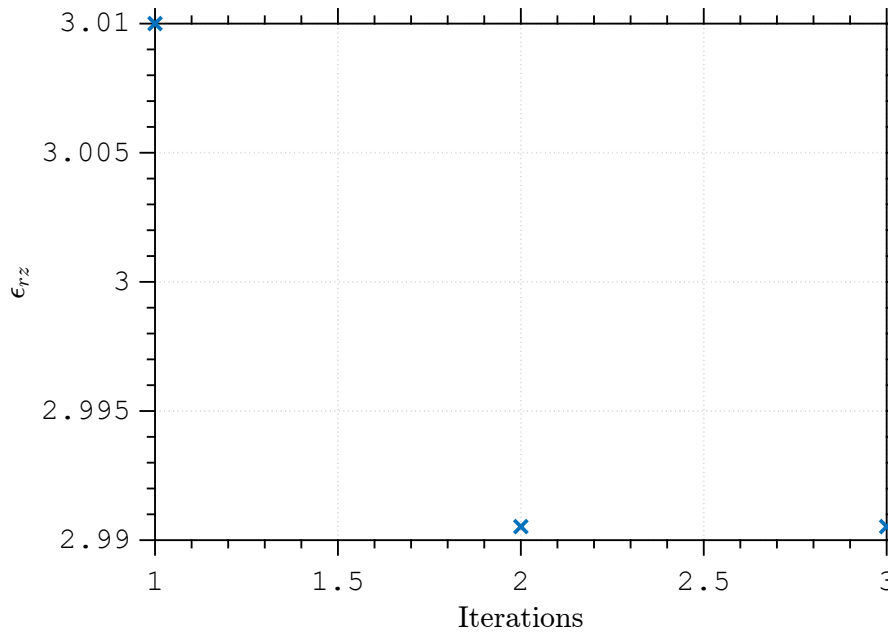


Figure 5.163: Evolution of the optimization parameter as a function of the number of iterations using decibel functional. Convergence was achieved after 3 iterations at $\epsilon_{rz} = 2.99$.

As conclusion for this chapter, it is possible to notice that the linear functional has a better convergence when compared to decibel functional this was due the fact of a scale problem when the numerical difference on amplitude was small, also due to matching phase difficulty which was presented on chapter 4.

This problem was also the reason why was also possible to observe that the decibel functional converged to an answer with a much smaller number of iterations in `fmincon` optimization than linear functional.

Since the coaxial waveguide has TEM propagation mode, it covers a larger frequency range when compared to circular waveguide, for this reason, for future workers, i advice to use the coaxial waveguide measurement cell for electromagnetic characterization purposes.

6

Conclusion

In this final chapter, a review and a resume about the subjects presented in this work will be addressed, followed by comments on the results and proposal of future works.

On Chapter 1, we discussed the importance and the evolution until nowadays of researches using microwave measurement cells for material characterization. The techniques presented still are highly used by researchers to find the constitutive parameters of samples. Some electromagnetic models are popular in applications as structural monitoring of components [84], underwater electromagnetic communication [85], nondestructive testing [86, 87] and design and evaluation of well-logging sensors in the oil and gas industry [88–91]. However, in the present days, more computationally efficient algorithms must be developed to faster converge to an answer. In this sense, we proposed the MMT, with a small sight of direct and inverse problem. Also, we presented a new technique using PML and the virtual combination of PEC + PMC boundary in order to converge to a better and faster solution.

Methods for material characterization were reviewed on Chapter 2, from resonant methods, such as resonator cavity, to non resonant methods, as free space and scatter parameters measurements. The advantages and drawbacks for each of them were presented. On further sections, techniques to extract the material parameters for one and two probes were analyzed.

In Chapter 3 the electromagnetic fields and its characteristic equations was presented, as well as the expressions for radially layered waveguides. The MMT was also explained and the reaction integrals were derived. Additionally, the particular case for PEC truncation which was used later to validate the one port measurement cell confined was shown.

On Chapter 4, the direct problem using MMT and the developed algorithm was validated when compared to CST, for two-port, one-port and open-ended with PML and truncated by PEC, PMC and PEC and PMC together. Then, the inverse problem functionals used to obtain the constitutive parameters were presented, and a review of global and local minimum was studied to avoid convergence errors.

On Chapter 5, the results for the linear and decibel functionals were

presented. The linear functional demonstrated to be more efficient and more accurate than decibel one, since there were some results in decibel that presented convergence problem. This was due some scale problem presented when the functional were working with small numerical difference on amplitude, also, the difficulty on matching the phase difference on the direct problem and the phase obtained through the iterative optimization functional may have influenced on this problem. Also, our new technique using combined PEC and PMC truncations on circular waveguide with PML presented very good results to mimic an open space radiation boundaries. This approach proved to be more efficient than PEC or PMC alone, since it converged better when compared to the CST simulation.

For future works, we suggest the investigation of more reliable decibel functionals for mitigating the convergence errors we have observed in this work. In special on the phase comparison which is a hard thing to work on. Additionally, we propose that our inverse algorithm is tested with real samples where the S parameters are extracted using VNA and the constutive parameters of this material is obtained.

7

Bibliography

- [1] A. Nicolson and G. Ross, "Measurement of the intrinsic properties of materials by time-domain techniques," *IEEE Transactions on instrumentation and measurement*, vol. 19, no. 4, pp. 377–382, 1970.
- [2] W. B. Weir, "Automatic measurement of complex dielectric constant and permeability at microwave frequencies," *Proceedings of the IEEE*, vol. 62, no. 1, pp. 33–36, 1974.
- [3] J. Baker-Jarvis, R. G. Geyer, J. Grosvenor, M. D. Janezic, C. A. Jones, B. Riddle, C. M. Weil, and J. Krupka, "Dielectric characterization of low-loss materials a comparison of techniques," *IEEE Transactions on Dielectrics and Electrical insulation*, vol. 5, no. 4, pp. 571–577, 1998.
- [4] E. Tanabe and W. T. Joines, "A nondestructive method for measuring the complex permittivity of dielectric materials at microwave frequencies using an open transmission line resonator," *IEEE Transactions on Instrumentation and Measurement*, no. 3, pp. 222–226, 1976.
- [5] K. Y. You, F. B. Esa, and Z. Abbas, "Macroscopic characterization of materials using microwave measurement methods—a survey," in *2017 Progress in Electromagnetics Research Symposium-Fall (PIERS-FALL)*. IEEE, 2017, pp. 194–204.
- [6] O. Tantot, M. Chatard-Moulin, and P. Guillon, "Measurement of complex permittivity and permeability and thickness of multilayered medium by an open-ended waveguide method," *IEEE transactions on instrumentation and measurement*, vol. 46, no. 2, pp. 519–522, 1997.
- [7] B. Sanadiki and M. Mostafavi, "Inversion of inhomogeneous continuously varying dielectric profiles using open-ended waveguides," *IEEE transactions on antennas and propagation*, vol. 39, no. 2, pp. 158–163, 1991.
- [8] M. Mostafavi and W.-C. Lan, "Polynomial characterization of inhomogeneous media and their reconstruction using an open-ended waveguide," *IEEE transactions on antennas and propagation*, vol. 41, no. 6, pp. 822–824, 1993.

- [9] S. I. Ganchev, S. Bakhtiari, and R. Zoughi, "A novel numerical technique for dielectric measurement of generally lossy dielectrics," *IEEE Transactions on Instrumentation and Measurement*, vol. 41, no. 3, pp. 361–365, 1992.
- [10] C.-L. Li and K.-M. Chen, "Determination of electromagnetic properties of materials using flanged open-ended coaxial probe-full-wave analysis," *IEEE Transactions on Instrumentation and Measurement*, vol. 44, no. 1, pp. 19–27, 1995.
- [11] P. De Langhe, K. Blomme, L. Martens, and D. De Zutter, "Measurement of low-permittivity materials based on a spectral-domain analysis for the open-ended coaxial probe," *IEEE transactions on instrumentation and measurement*, vol. 42, no. 5, pp. 879–886, 1993.
- [12] D. P. Wibowo and A. Munir, "3d artificial material characterization using rectangular waveguide," in *2014 6th International Conference on Information Technology and Electrical Engineering (ICITEE)*. IEEE, 2014, pp. 1–4.
- [13] N. Rogers, M. Havrilla, M. W. Hyde, and A. Knisely, "Nondestructive electromagnetic characterization of uniaxial sheet media using a two-flanged rectangular waveguide probe," *IEEE Transactions on Instrumentation and Measurement*, vol. 69, no. 6, pp. 2938–2947, 2019.
- [14] K. J. Bois, L. F. Handjojo, A. D. Benally, K. Mubarak, and R. Zoughi, "Dielectric plug-loaded two-port transmission line measurement technique for dielectric property characterization of granular and liquid materials," *IEEE Transactions on Instrumentation and Measurement*, vol. 48, no. 6, pp. 1141–1148, 1999.
- [15] D. P. Martínez, D. R. Somolinos, and B. P. Gallardo, "Electromagnetic characterization of materials through high accuracy free space measurements," in *2021 15th European Conference on Antennas and Propagation (EuCAP)*. IEEE, 2021, pp. 1–5.
- [16] E. Marouby, M. Aubourg, and P. Guillon, "Application of the finite element method to the design of transitions between coaxial lines," in *IEE Proceedings H-Microwaves, Antennas and Propagation*, vol. 137, no. 4. IET, 1990, pp. 219–225.
- [17] W. Scott, "Accurate modeling of axisymmetric two-port junctions in coaxial lines using the finite element method," *IEEE transactions on microwave theory and techniques*, vol. 40, no. 8, pp. 1712–1716, 1992.

- [18] W. Yu, R. Mittra, and S. Dey, "Application of the nonuniform fdtd technique to analysis of coaxial discontinuity structures," *IEEE Transactions on Microwave Theory and Techniques*, vol. 49, no. 1, pp. 207–209, 2001.
- [19] W. K. Gwarek, "Computer-aided analysis of arbitrarily shaped, coaxial discontinuities," *IEEE transactions on microwave theory and techniques*, vol. 36, no. 2, pp. 337–342, 1988.
- [20] C.-W. Chang, K.-M. Chen, and J. Qian, "Nondestructive determination of electromagnetic parameters of dielectric materials at x-band frequencies using a waveguide probe system," *IEEE Transactions on Instrumentation and Measurement*, vol. 46, no. 5, pp. 1084–1092, 1997.
- [21] M. Hyde and M. J. Havrilla, "A clamped dual-ridged waveguide measurement system for the broadband, nondestructive characterization of sheet materials," *Radio Science*, vol. 48, no. 5, pp. 628–637, 2013.
- [22] W. C. Chew, *Waves and Fields in Inhomogeneous Media*. IEEE press, 1995.
- [23] G. S. Rosa, J. R. Bergmann, and F. L. Teixeira, *Full-Wave Pseudoanalytical Methods for Cylindrically Symmetric Electromagnetic Structures: Applications in Sensing and Telemetry for Geophysical Exploration*. World Scientific Publishing Co Pte Ltd, 2020, ch. 10, pp. 385–431.
- [24] J.-P. Berenger, "A perfectly matched layer for the absorption of electromagnetic waves," *Journal of computational physics*, vol. 114, no. 2, pp. 185–200, 1994.
- [25] W. C. Chew and W. H. Weedon, "A 3d perfectly matched medium from modified maxwell's equations with stretched coordinates," *Microwave and optical technology letters*, vol. 7, no. 13, pp. 599–604, 1994.
- [26] N. Raveu, B. Byrne, L. Claudepierre, and N. Capet, "Modal theory for waveguides with anisotropic surface impedance boundaries," *IEEE Transactions on Microwave Theory and Techniques*, vol. 64, no. 4, pp. 1153–1162, 2016.
- [27] F. L. Teixeira and W. C. Chew, "General closed-form pml constitutive tensors to match arbitrary bianisotropic and dispersive linear media," *IEEE microwave and guided wave letters*, vol. 8, no. 6, pp. 223–225, 1998.
- [28] F. Teixeira and W. C. Chew, "Systematic derivation of anisotropic pml absorbing media in cylindrical and spherical coordinates," *IEEE microwave and guided wave letters*, vol. 7, no. 11, pp. 371–373, 1997.

- [29] I. V. Lindell, A. H. Sihvola, S. Tretyakov, and A. J. Viitanen, *Electromagnetic Waves in Chiral and Bi-Isotropic Media*. London, England: Artech House, 1994.
- [30] EMTS 2019, URSI Commission B International Symposium on Electromagnetic Theory - 2019 URSI Commission B School for Young Scientists, Field and Potential Based Methods in Anisotropic and Bianisotropic Electromagnetics, San Diego, CA, USA, 2019, Lecture Notes.
- [31] J. A. Kong, "Theorems of bianisotropic media," *Proceedings of the IEEE*, vol. 60, no. 9, pp. 1036–1046, 1972.
- [32] J. Kong, *Electromagnetic Wave Theory*. New York, NY, USA: Wiley, 1986.
- [33] T. Gric and O. Hess, "Electromagnetics of metamaterials," *Phenomena of Optical Metamaterials, Micro and Nano Technologies*, pp. 41–73, 2019.
- [34] X. Chen, T. M. Grzegorzczak, B.-I. Wu, J. Pacheco Jr, and J. A. Kong, "Robust method to retrieve the constitutive effective parameters of metamaterials," *Physical review E*, vol. 70, no. 1, p. 016608, 2004.
- [35] W. Hua-Qiang, L. Chang-Yang, L. Hong-Ming, and Q. He, "Graphene applications in electronic and optoelectronic devices and circuits," *Chinese Physics B*, vol. 22, no. 9, p. 098106, 2013.
- [36] E. Guerriero, L. Polloni, M. Bianchi, A. Behnam, E. Carrion, L. G. Rizzi, E. Pop, and R. Sordan, "Gigahertz integrated graphene ring oscillators," *ACS nano*, vol. 7, no. 6, pp. 5588–5594, 2013.
- [37] C. Gao, Y. Jiang, J. Zhang, W. Cao, X. Gao, X. Yu, and J. Wang, "Graphene-based wideband absorbing screen with radar cross section reduction," in *2016 11th International Symposium on Antennas, Propagation and EM Theory (ISAPE)*. IEEE, 2016, pp. 686–689.
- [38] B. Chaudhury and S. Chaturvedi, "Study and optimization of plasma-based radar cross section reduction using three-dimensional computations," *IEEE Transactions on Plasma Science*, vol. 37, no. 11, pp. 2116–2127, 2009.
- [39] H. A. Malhat and S. H. Zainud-Deen, "Reconfigurable plasma circularly polarized magneto-electric dipole antenna," in *2018 35th National Radio Science Conference (NRSC)*. IEEE, 2018, pp. 14–21.
- [40] A. Moazami, M. Hashemi, and N. C. Shirazi, "High efficiency tunable graphene-based plasmonic filter in the thz frequency range," *Plasmonics*, vol. 14, no. 2, pp. 359–363, 2019.

- [41] S. W. Tsai and H. T. Hahn, *Introduction to composite materials*. Routledge, 2018.
- [42] Y. T. Aladadi and M. A. Alkanhal, "Classification and characterization of electromagnetic materials," *Scientific Reports*, vol. 10, no. 1, pp. 1–11, 2020.
- [43] T. G. Mackay and A. Lakhtakia, *Electromagnetic anisotropy and bianisotropy: a field guide*. World Scientific, 2010.
- [44] J. S. Seybold, *Introduction to RF propagation*. John Wiley & Sons, 2005.
- [45] K. L. Kaiser, *Electromagnetic shielding*. Crc Press, 2005.
- [46] H. Fellner-Feldegg, "Measurement of dielectrics in the time domain," *The Journal of Physical Chemistry*, vol. 73, no. 3, pp. 616–623, 1969.
- [47] M. VANGEMERT, "High-frequency time-domain methods in dielectric spectroscopy," *Philips Research Reports*, vol. 28, no. 6, pp. 530–572, 1973.
- [48] A. Suggett, "Time domain spectroscopic measurements," in *High Frequency Dielectric Measurement*. IPC, 1973, pp. 98–103.
- [49] M. N. Afsar, J. R. Birch, R. Clarke, and G. Chantry, "The measurement of the properties of materials," *Proceedings of the IEEE*, vol. 74, no. 1, pp. 183–199, 1986.
- [50] A. Kazemipour, M. Hudlicka, S.-K. Yee, M. Salhi, T. Kleine-Ostmann, and T. Schrader, "Wideband frequency-domain material characterization up to 500 ghz," in *2014 39th International Conference on Infrared, Millimeter, and Terahertz waves (IRMMW-THz)*. IEEE, 2014, pp. 1–2.
- [51] A. K. Klein, P. S. Stefanova, A. Gallant, and C. Balocco, "Material characterization with frequency domain thz ellipsometry," in *2018 43rd International Conference on Infrared, Millimeter, and Terahertz Waves (IRMMW-THz)*. IEEE, 2018, pp. 1–2.
- [52] D. Stock, A. K. Wigger, and P. H. Bolívar, "Reducing errors in thz material parameter determination by model-based time-domain extraction methods," *JOSA B*, vol. 38, no. 3, pp. 815–824, 2021.
- [53] M. T. Khan and S. M. Ali, "A brief review of measuring techniques for characterization of dielectric materials," *International Journal of Information Technology and Electrical Engineering*, vol. 1, no. 1, 2012.

- [54] S. N. Jha, K. Narsaiah, A. L. Basediya, R. Sharma, P. Jaiswal, R. Kumar, and R. Bhardwaj, "Measurement techniques and application of electrical properties for nondestructive quality evaluation of foods—a review," *Journal of food science and technology*, vol. 48, no. 4, pp. 387–411, 2011.
- [55] K. Y. You, "Materials characterization using microwave waveguide system," *Microwave systems and applications*, pp. 341–358, 2017.
- [56] F. H. Wee, P. J. Soh, A. Suhaizal, H. Nornikman, and A. Ezanuddin, "Free space measurement technique on dielectric properties of agricultural residues at microwave frequencies," in *2009 SBMO/IEEE MTT-S International Microwave and Optoelectronics Conference (IMOC)*. IEEE, 2009, pp. 183–187.
- [57] T. Tosaka, K. Fujii, K. Fukunaga, and A. Kasamatsu, "Development of complex relative permittivity measurement system based on free-space in 220–330-ghz range," *IEEE Transactions on Terahertz science and Technology*, vol. 5, no. 1, pp. 102–109, 2014.
- [58] Z. Abbas, R. D. Pollard, and R. W. Kelsall, "Complex permittivity measurements at ka-band using rectangular dielectric waveguide," *IEEE Transactions on instrumentation and measurement*, vol. 50, no. 5, pp. 1334–1342, 2001.
- [59] E. Kemptner and S. Thurner, "Free space material characterization for microwave frequencies," in *2012 6th European Conference on Antennas and Propagation (EUCAP)*. IEEE, 2012, pp. 3513–3515.
- [60] V. Varadan, R. Hollinger, D. Ghodgaonkar, and V. Varadan, "Free-space, broadband measurements of high-temperature, complex dielectric properties at microwave frequencies," *IEEE Transactions on Instrumentation and Measurement*, vol. 40, no. 5, pp. 842–846, 1991.
- [61] A. P. Gregory and R. N. Clarke, "A review of rf and microwave techniques for dielectric measurements on polar liquids," *IEEE Transactions on Dielectrics and Electrical Insulation*, vol. 13, no. 4, pp. 727–743, 2006.
- [62] K. Y. You and Y. L. Then, "Simple calibration and dielectric measurement technique for thin material using coaxial probe," *IEEE Sensors Journal*, vol. 15, no. 10, pp. 5393–5397, 2015.
- [63] K. You, Z. Abbas, M. Malek, and E. Cheng, "Non-destructive dielectric measurements and calibration for thin materials using waveguide-coaxial adaptors," *Measurement Science Review*, vol. 14, no. 1, p. 16, 2014.

- [64] R. Compton Jr, "The aperture admittance of a rectangular waveguide radiating into a lossy half-space," *NASA Tech. Rep*, no. 64, p. 19608, 1963.
- [65] G. S. Rosa, "Pseudo-analytical modeling for electromagnetic well- logging tools in complex geophysical formations," PhD Thesis, Dept. Elect. Eng., Pontifical Catholic University of Rio de Janeiro, Rio de Janeiro, RJ, Brasil, 2017.
- [66] V. B. Cosenza, "Electromagnetic characterization of inhomogeneous cylindrical waveguides using mode-matching-based methods," Master Thesis, Dept. Elect. Eng., Pontifical Catholic University of Rio de Janeiro, Rio de Janeiro, RJ, Brasil, 2020.
- [67] R. F. Harrington, *Time-harmonic electromagnetic fields*. New York, NY, USA: McGraw-Hill, 1961.
- [68] G. S. Rosa, "Propagação de ondas eletromagnéticas em estruturas coaxiais carregadas com meios não homogêneos excitadas pelo modo TEM," Master Thesis, Dept. Elect. Eng., Pontifical Catholic University of Rio de Janeiro, Rio de Janeiro, RJ, Brasil, 2013.
- [69] G. S. Rosa, J. R. Bergmann, and F. L. Teixeira, "A robust mode-matching algorithm for the analysis of triaxial well-logging tools in anisotropic geophysical formations," *IEEE Trans. Geosci. Remote Sens.*, vol. 55, no. 5, pp. 2534–2545, May 2017.
- [70] G. S. Rosa, "A novel mode-matching formulation of multifurcated waveguide junctions," *J. Microw. Optoelectron. Electromagn. Appl.*, vol. 20, no. 3, pp. 675–688, Sept. 2021.
- [71] G. S. Rosa, F. L. Teixeira, and W. C. Chew, "High-frequency transmission lines," in *Encyclopedia of RF and Microwave Engineering*, "In production."
- [72] G. S. Rosa and J. R. Bergmann, "An efficient mode-matching solution for open-ended coaxial waveguides via analytic continuation of the radial space," in *2018 IEEE International Symposium on Antennas and Propagation & USNC/URSI National Radio Science Meeting*. IEEE, 2018, pp. 721–722.
- [73] CST AG, CST Studio Suite 2016, Darmstadt, Germany, 2020.
- [74] J. Esteban and J. M. Rebolgar, "Characterization of corrugated waveguides by modal analysis," *IEEE transactions on microwave theory and techniques*, vol. 39, no. 6, pp. 937–943, 1991.

- [75] MATLAB, *version 9.10.0.1649659 (R2021a)*. Natick, Massachusetts: The MathWorks Inc., 2021.
- [76] MathWorks. fmincon. [Online]. Available: <https://www.mathworks.com/help/optim/ug/fmincon.html>
- [77] ——. Choosing the algorithm. [Online]. Available: <https://www.mathworks.com/help/optim/ug/choosing-the-algorithm.html>
- [78] R. Fletcher, “Practical methods of optimization john wiley & sons,” *New York*, vol. 80, p. 4, 1987.
- [79] P. E. Gill, W. Murray, and M. H. Wright, *Practical optimization*. SIAM, 2019.
- [80] W. Hock and K. Schittkowski, “A comparative performance evaluation of 27 nonlinear programming codes,” *Computing*, vol. 30, no. 4, pp. 335–358, 1983.
- [81] M. J. Powell, “Variable metric methods for constrained optimization,” in *Mathematical programming the state of the art*. Springer, 1983, pp. 288–311.
- [82] M. Sevaux, “Metaheuristics: strategies for the optimisation of the production of goods and services,” 07 2004.
- [83] MathWorks. Local vs. global optima. [Online]. Available: <https://www.mathworks.com/help/optim/ug/local-vs-global-optima.html#brhl2e0>
- [84] Y. Lugovtsova, J. Bulling, C. Boller, and J. Prager, “Analysis of guided wave propagation in a multi-layered structure in view of structural health monitoring,” *Applied Sciences*, vol. 9, no. 21, p. 4600, 2019.
- [85] Y. Tian, D. Zhou, S. Kong, W. Zhang, B. Li, and J. Qi, “Modeling and simulation on three-layer media propagation characteristics of underwater electromagnetic field in shallow sea area,” in *2019 IEEE 4th Advanced Information Technology, Electronic and Automation Control Conference (IAEAC)*, vol. 1, 2019, pp. 1515–1518.
- [86] X. Wang, H. Zhang, and C. Ying, “Acoustic field in a borehole within a horizontally layered formation,” in *1995 IEEE Ultrasonics Symposium. Proceedings. An International Symposium*, vol. 2. IEEE, 1995, pp. 1121–1124.
- [87] M. W. Hyde IV, M. J. Havrilla, and A. E. Bogle, “Nondestructive determination of the permittivity tensor of a uniaxial material using a two-port clamped

- coaxial probe," *IEEE Transactions on Microwave Theory and Techniques*, vol. 64, no. 1, pp. 239–246, 2015.
- [88] G. S. Rosa, M. S. Canabarro, J. R. Bergmann, and F. L. Teixeira, "A comparison of two numerical mode-matching methodologies for the analysis of inhomogeneous media with radial and vertical stratifications," *IEEE Transactions on Antennas and Propagation*, vol. 66, no. 12, pp. 7499–7504, 2018.
- [89] L. Saavedra, G. S. Rosa, and J. R. Bergmann, "A novel semi-analytical mode-matching technique for modeling realistic electromagnetic well-logging sensors immersed in dissipative inhomogeneous media," in *2019 URSI International Symposium on Electromagnetic Theory (EMTS)*. IEEE, 2019, pp. 1–4.
- [90] —, "An accurate technique for modeling realistic well-logging sensors inside complex media," in *2019 International Applied Computational Electromagnetics Society Symposium (ACES)*. IEEE, 2019, pp. 1–2.
- [91] D. Hong, S. Yang, Y. Zhang, W.-F. Huang, and Q. H. Liu, "Pseudoanalytical formulations for modeling the effect of an insulating layer in electromagnetic well logging," *IEEE Transactions on Geoscience and Remote Sensing*, vol. 56, no. 12, pp. 7022–7029, 2018.